Relaxation Behaviour and Mechanical Properties of Aluminosilicate Glasses

Bechgaard, Tobias Kjær

DOI (link to publication from Publisher):
10.5278/vbn.phd.eng.00066

Publication date:
2018

Document Version
Publisher's PDF, also known as Version of record

RELAXATION BEHAVIOR AND MECHANICAL PROPERTIES OF ALUMINOSILICATE GLASSES

BY
TOBIAS KJÆR BECHGAARD

DISSERTATION SUBMITTED 2018

AALBORG UNIVERSITY
DENMARK

RELAXATION BEHAVIOR AND MECHANICAL PROPERTIES OF ALUMINOSILICATE GLASSES

by

Tobias Kjær Bechgaard

AALBORG UNIVERSITY
DENMARK

Dissertation submitted 2018

Dissertation submitted:	October 2018
PhD supervisor:	Professor MSO Morten M. Smedskjær, Aalborg University, Denmark
PhD committee:	Associate Professor Casper Steinmann Svendsen (chair.) Aalborg University
	Professor Edgar D. Zanotto Universidade Federal de São Carlos
	Professor Dominique de Ligny Universität Erlangen
PhD Series:	Faculty of Engineering and Science, Aalborg University
Department:	Department of Chemistry and Bioscience

ISSN (online): 2446-1636
ISBN (online): 978-87-7210-341-9

Published by:
Aalborg University Press
Langagervej 2
DK – 9220 Aalborg Ø
Phone: +45 99407140
aauf@forlag.aau.dk
forlag.aau.dk

Printed in Denmark by Rosendahls, 2018

ENGLISH SUMMARY

Glasses are fascinating materials with a wide range of applications. Glasses within the aluminosilicate family are relatively inexpensive to manufacture and can be tailored with superior properties, making them of special industrial interest. Understanding the composition-structure-property relations in aluminosilicate glasses can accelerate the design of new compositions with tailored performances. The goal of this Ph.D. project is to understand the compositional and structural origins of structure, relaxation behavior, and selected mechanical properties of aluminosilicate glasses.

First, we have studied the glass structure of aluminosilicates with three different modifier cations at varying concentration by Raman and nuclear magnetic resonance spectroscopy. The short and intermediate range order of the glasses depends on the modifier-aluminum ratio and the field strength of the modifier.

Second, we have used temperature-modulated differential scanning calorimeters, which function at high temperature (>1000°C), to study relaxation behavior in calcium aluminosilicate glasses. To do so, we first developed experimental protocols for the use of the equipment and then applied them to determine the liquid fragility index and study the enthalpy relaxation through determination of the non-reversing heat capacity. We found that the accuracy of the activation energy approach for the determination of liquid fragility is comparable to the Moynihan method known from linear differential scanning calorimetry. Moreover, a correction is needed to remove the systematic error in the Arrhenius approximation in the fragility determination. By comparing the non-reversing heat capacity to molecular dynamics simulations, we find an apparent correlation between extent of relaxation and network topology in calcium aluminosilicate glasses.

Third, we studied the effect of time and humidity on the crack initiation probability (CIP) upon Vicker's indentation of aluminosilicate glasses. As expected, humid conditions and longer time result in the initiation of a larger number of radial/median cracks. We show that the CIP increases drastically when the humidity increases and that cracks can form at least 24 h after indentation. The study has quantified the time-scale of indentation cracking and highlighted the need for a general experimental protocol for crack resistance data to be comparable, as the environmental humidity greatly affects the crack resistance. Finally, we studied the pressure dependence of the photoelastic response of aluminosilicate glasses. Today, photoelasticity is predicted by an empirical model, but we found that the model cannot account for the structural changes associated with compression at high temperature and pressure.

DANSK RESUME

Glas er et fascinerende materiale med en bred vifte af applikationer. Glas i aluminosilikatfamilien er relativt billige at fremstille og kan skræddersyes med overlegne egenskaber, hvilket gør dem af særlig industriel interesse. Forståelse af det indbyrdes forhold mellem komposition, struktur og egenskaber i aluminosilikatglas kan fremme udviklingen af nye kompositioner med skræddersyede egenskaber. Formålet med dette Ph.d. projekt er at forstå struktur, relaksation og udvalgte mekaniske egenskaber af aluminosilikatglas på baggrund af deres kemiske sammensætning and struktur.

Vi har studeret glasstrukturen i aluminosilikater med tre forskellige modificerende kationer i varierende koncentration ved Raman- og kernemagnetisk resonans spektroskopi. Den korte og middellange orden i glasstrukturen afhænger af forholdet imellem aluminium og modificerende kationer og de modificerende kationers feltstyrke.

Derudover har vi brugt temperaturmoduleret differentiel scanningskalorimetri, som fungerer ved høj temperatur (> 1000 °C), til at studere relaksation i calcium aluminiumsilikatglas. Først udviklede vi en eksperimentel protokol til anvendelsen af udstyret og anvendte derefter protokollen til at bestemme fragilitet og studere relaksationsentalpien gennem bestemmelse af den ikke-reversible varmekapacitet. Vi opdagede, at nøjagtigheden af aktiveringsenergimetoden til bestemmelse af fragilitet er sammenlignelig med Moynihan-metoden kendt fra lineær differentiel scanningskalorimetri. Det er nødvendigt at korrigere de bestemte fragilitetsværdier for at fjerne den systematiske fejl i Arrhenius-tilnærmelsen i bestemmelsen af fragilitet. Ved at sammenligne den ikke-reversible varmekapacitet med molekylærdynamiske simulationer finder vi tilsyneladende en sammenhæng mellem omfanget af relaksation og netværkstopologien i calcium aluminosilikatglas.

Desuden undersøgte vi indvirkningen af tid og fugtighed på sandsynligheden for revnedannelse ved Vickers indentering af aluminosilikatglas. Som forventet resulterer fugtige betingelser og længere tid i dannelsen af et større antal radial- og/eller medianrevner. Vi viser, at sandsynligheden for revnedannelse stiger drastisk, når fugtigheden stiger, og at revner kan dannes mindst 24 timer efter indentering. Undersøgelsen har kvantificeret tidsafhængigheden af revnedannelse og understreget behovet for en generel eksperimentel protokol for at revnedannelsesdata kan sammenlignes, da luftens fugtighed i høj grad påvirker modstanden mod revnedannelse. Endelig studerede vi trykafhængigheden af den fotoelastiske respons i aluminosilikatglas. I dag forudses fotoelasticitet ved en empirisk model, men vi har beskrevet hvordan modellen ikke tager højde for de strukturelle ændringer, der er forbundet med kompression ved høje temperaturer og tryk.

ACKNOWLEDGEMENTS

This thesis has been submitted for assessment in partial fulfilment of the PhD degree. The thesis is based on published scientific papers listed in Section 1.3. The work was carried out from October 2015 to September 2018. The work was conducted at the Section of Chemistry at Aalborg University. The project was partially funded by Aalborg University and partially by Corning Incorporated.

First of all I want to express my gratitude to my supervisor Morten M. Smedskjær for being the inspiration that led me to pursue research in glass science. Thank you for your belief, encouragement and dedicated supervision. Thank you for always taking the time and for valuable discussions and helpful suggestions.

My acknowledgements also go to Corning Incorporated for the financial support and for providing and characterizing glass samples. Special thanks go employee Ozgur Gulbiten and former employee John C. Mauro. Thanks to Ozgur Gulbiten for his knowledge and helpful suggestions in relation to the temperature-modulated differential scanning calorimetry experiments. Thanks to Professor John C. Mauro, now at Pennsylvania State University, for his insight, his inspiring nature and for the meticulous revision of my drafts.

Thanks go to all present and former members of the Section at Chemistry at Aalborg University for your comradery, colleagueship and fruitful discussions. You have provided a pleasant professional and social working environment. I have enjoyed every scientific discussion and every piece of cake.

A special thanks to my family. Thank you to my parents Else-Marie and Niels for their life-long encouragement and confidence in my ability. Thanks to my siblings Christoffer and Sofie for their support. Thank you to Ella, Jens, Poul, and Solveig for their unconditional love and for teaching me about the meaning of life.

Finally, special thanks to my fiancée Camilla for her patience, understanding and continuous support. You are my greatest inspiration.

TABLE OF CONTENTS

CHAPTER 1. INTRODUCTION

Glass is a fascinating state of matter, resulting in numerous low- and high-tech applications [1,2]. Historically, glass was primarily used for decorative or practical applications, such as the glass beads and containers of ancient Mesopotamia [3]. Later, glass was used as a medium for the sun to light up the inside of manmade buildings, while simultaneous shielding the occupants from wind and weather. Arguably, the most beautiful examples are the stained glass mosaics in the European cathedrals [4]. However, during the last two centuries, glass has become an increasingly high-tech material and its presence in the average human life has rapidly increased. Most notably as cover and display glasses in our televisions, computers, and smartphones [5]. However, glass also plays a vital role in, e.g., global communication, energy production, and medical technology [6]. The usage of glass in increasingly advanced applications requires a proportional increase in the understanding of the underlying chemistry and physics that control the disordered glass structure and ultimately its macroscopic properties [3].

1.1. BACKGROUND AND CHALLENGES

Most people recognize 'glass' as the material windows is made of and therefore mistakenly consider silicate glass to be the only type of glass. However, glass is a state of matter and can theoretically be made from any material that can be liquefied [1,2] and even directly from the solid state [7,8]. Instead, glasses are characterized as having an amorphous structure and exhibiting a glass transition. Very recently, Zanotto and Mauro proposed a revised definition of glass [9]:

> "*Glass is a nonequilibrium, noncrystalline condensed state of matter that exhibits a glass transition. The structure of glasses is similar to that of their parent supercooled liquids (SCL), and they spontaneously relax toward the SCL state. Their ultimate fate, in the limit of infinite time, is to crystallize*."

By considering this definition, the origin of the most well-known glass myth can be understood. That is, the myth that glass flows. The myth originates from the conical shape of the individual glass pieces in medieval stained glass mosaics, which are thicker at the bottom than at the top. This has been disproved several times [4,10–13] as it would have taken billions of years for the glass to adopt its current conical shape. However, as just indicated, glass does actually flow. According to the definition above, glass is not in equilibrium and will continuously relax. That is, glasses will continuously change their shape and decrease their volume; otherwise it would not be a glass. The reason that glass scientists argue that the shape of the medieval stained glass is frozen and not flowing is the impact of temperature and observation time on the dynamics and relaxation of glass. Although relaxation was irrelevant in relation to the shape of medieval stained glass [4,10–13], it has

attracted increasing interest from glass scientists in recent years, promoted by the increase in the size and resolution of display screens [14]. Glass relaxation can, e.g., occur as density fluctuations on the nanoscale, and the increase in display screen size increases the effect of glass shrinkage, causing pixel misalignment. The penetration of electronic devices with 4K and eventually 8K screen resolution lowers the pixel sizes, further enhancing the effect of relaxation. Furthermore, the production of liquid crystal and light-emitting diode displays requires the use of high temperature, enhancing relaxation [5,14–17]. Despite its importance for such applications, the atomistic mechanism controlling relaxation in glasses remains poorly understood. An improved understanding of relationship between glass composition and relaxation will allow both prediction and control of the magnitude of relaxation [17,18].

For the average glass user, 'brittle' is probably the term most intimately related to glass [9,16]. Despite its versatile properties and high intrinsic strength [19], a major drawback of glass is its inherent brittleness and tendency to form surface cracks [20,21]. End-users experience this, e.g., when a stone flings into the wind shield of their car or when a smart phone is accidentally dropped. The resistance against cracking has been increased by both optimized composition design and post-treatments (e.g., thermal tempering, lamination, partial crystallization, and ion exchange) [1,19]. Historically, the development of more crack-resistant glasses was based on a trial-and-error approach, with emphasis on quantifying properties. However, in order to accelerate the design of continuously stronger and more damage resistant glasses, the current approach is based on understanding the underlying chemical and physical origin of glass deformation. An example of this is the structural characterizations of glass compacted by either high isostatic pressure or indentation in order to understand the structural changes occurring in the glass when a dropped smartphone hits the ground [22,23].

This Ph.D. project has been partially funded by Corning Incorporated, a company specializing in the production of specialty glasses. For industrial producers of display screens for, e.g., televisions and smart phones, the aluminosilicate glass family is particularly important [24,25], as the introduction of the Al_2O_3 has a positive impact on relevant properties, such as hardness and thermal endurance [26]. Moreover, the present Ph.D. study has also been partially funded by a grant focusing on glass deformation under high stress from the Danish Council for Independent Research. Therefore, the content of this thesis covers both the relaxation behavior and mechanical properties of industrially relevant aluminosilicate glass compositions.

1.2. OBJECTIVES

The objectives of this Ph.D. study are summarized as follows:

1. Achieve an improved understanding of the structural change occurring in aluminosilicate glasses under simultaneous high pressure/high temperature conditions.
2. Clarify the relationship between configurational heat capacity and the "fragility" of aluminosilicate glass-forming liquids.
3. Explore the applicability of temperature-modulated differential scanning calorimetry to study glass relaxation of oxide glasses and glass-forming liquids.
4. Reveal the effect of humidity and time on the kinetics of crack initiation in aluminosilicate glasses.
5. Clarify the physical origin of the pressure-induced changes in the photo-elastic properties of aluminosilicate glasses.

1.3. THESIS CONTENT

This thesis is presented as plurality of seven papers together with an extended summary as recommended by the Doctoral School of Engineering and Science at Aalborg University. The papers constitute the main body of this thesis and will be referred to by their roman numerals:

I. T.K. Bechgaard, A. Goel, R.E. Youngman, J.C. Mauro, S.J. Rzoska, M. Bockowski, L.R Jensen, and M.M. Smedskjaer, Structure and mechanical properties of compressed sodium aluminosilicate glasses: role of non-bridging oxygens. *Journal of Non-Crystalline Solids*, **441** (2016), 49-57.

II. T.K. Bechgaard, G. Scannell, L. Huang, R.E. Youngman, J.C. Mauro, and M.M. Smedskjaer. Structure of MgO/CaO sodium aluminosilicate glasses: Raman spectroscopy study. *Journal of Non-Crystalline Solids*, **470** (2017), 145-151

III. T.K. Bechgaard, J.C. Mauro, M. Bauchy, Y. Yue, L.A. Lamberson, L.R. Jensen, and M.M Smedskjaer. Fragility and configurational heat capacity of calcium aluminosilicate glass-forming liquids. *Journal of Non-Crystalline Solids*, **461** (2017), 24-34.

IV. T.K. Bechgaard, O. Gulbiten, J.C. Mauro, and M.M. Smedskjaer. Parametric study of temperature-modulated differential scanning calorimetry for high-temperature oxide glasses with varying fragility. *Journal of Non-Crystalline Solids*, **484** (2018), 84-94.

V. T.K. Bechgaard, O. Gulbiten, J.C. Mauro, Yuanzheng Yue, Mathieu Bauchy, and M.M. Smedskjaer. Liquid Fragility Determination of Oxide Glass-Formers Using Temperature-Modulated DSC, *International Journal of Applied Glass Science*, (under review)

VI. T.K. Bechgaard, J.C. Mauro, and M.M Smedskjaer. Time and humidity dependence of indentation cracking in aluminosilicate glasses. *Journal of Non-Crystalline Solids*, **491** (2018), 64-70.

VII. T.K. Bechgaard, J.C. Mauro, L.M. Thirion, S.J. Rzoska, M. Bockowski, and M.M Smedskjaer. Photoelastic response of permanently densified oxide glasses. *Optical Materials*, **67** (2017), 155-161.

CHAPTER 2. ALUMINOSILICATE GLASSES: FORMATION AND STRUCTURE

Glass is a state of matter and it can therefore be convenient to group glasses according to their chemical constituents as the glass chemistry controls its properties. Typically, glasses have been grouped into organic, metallic, chalcogenide, and oxide glasses, and more recently also the hybrid metal-organic framework glass group. The majority of the industrial glass production [18] continues to be within the silicate subgroup of the oxide glasses. Glasses in this subgroup has silica (SiO_2) as the main component, but can also contain various other cation oxides, such as, e.g., soda (Na_2O), lime (CaO), or alumina (Al_2O_3) [1,2]. The group of aluminosilicate glasses is of especial industrial interest as their properties can be optimized for a range of applications e.g. flat panel display glass [16,27], scratch resistant cover glass [12], and nuclear waste glass [28]. The addition of Al_2O_3 to e.g. soda-lime-silica glass drastically changes a broad range of properties, such as optical properties, chemical resistance, molar volume, thermal properties, mechanical properties, and thermodynamic behavior [27,29,30], typically resulting in improved properties.

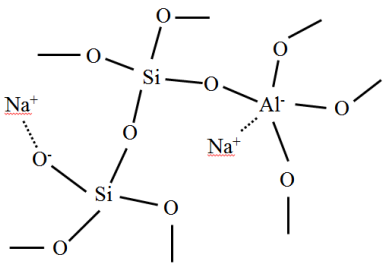

Figure 1. Schematical 2D representation of the structure of a peralkaline sodium aluminosilicate glass. The sodium cations can both create non-bridging oxygens (left) or charge-compensate Al^{3+} in tetrahedral confirmation. The dotted lines between Na^+ and O^- and Al^- represent the ionic attraction.

The oxides present in silicate glasses can be separated into three categories, depending on their structural role: network formers, network modifiers, and intermediates. The group of networks formers consists of, e.g., SiO_2, GeO_2, and B_2O_3, which are distinguished by forming relative covalent bonds with oxygen [1,2]. As their classification name implies, these species form the backbone of the glassy

network. Network modifiers have a low electronegativity and forms highly ionic bonds with oxygen. Typical modifiers include alkali or alkaline earth oxides, such as Na_2O, K_2O, and CaO. The structural role of the network modifier is typically to depolymerize the structural network, through ionic bonds between the cation and tetrahedral oxygen on a network former, creating a negatively charged dangling oxygen, known as a non-bridging oxygen (NBO) [1,2,31] (Figure 1). The intermediates can undertake the structural role of either the network former or the network modifier, depending on the chemical environment. The typical intermediate is Al_2O_3, but can also be, e.g., TiO_2 and ZnO. By itself, an intermediate such as Al_2O_3 is not able to form a glass using normal melt-quench conditions and when added to pure SiO_2, the intermediate will act as a modifier. However, an additional modifier cation is able to charge-compensate the Al^{3+} ion, allowing it to assume tetragonal configuration and enter the network analogous to true network formers [1,2,26].

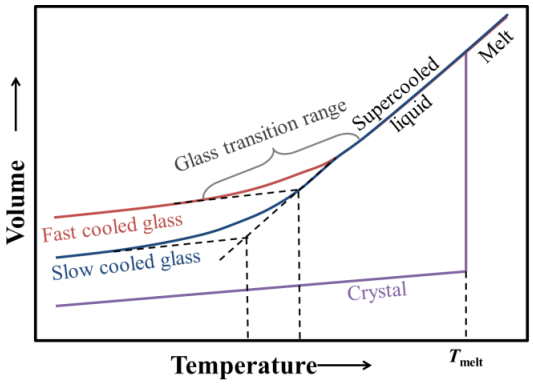

Figure 2. The temperature dependence of glass and melt volume. The atomic mobility is high in the melt and the supercooled liquid, allowing instantaneous structural adaptations to changes in temperature. Upon further cooling, the increasing viscosity causes an abrupt change in the slope of the volume-temperature curve during the transition from liquid to solid.

Glasses are typically produced by avoiding crystallization when cooling a melt from the liquid to the solid glass state. This can be described by the volume-temperature diagram, which describes the thermal history dependence of the melt volume (Figure 2). Cooling a melt below its melting point typically results in a phase transition, where the liquid melt is converted into a solid crystal. However, when the cooling rates is sufficiently large, liquids with good glass-forming ability can be cooled below their melting point without crystallization and enter the supercooled state. During cooling, the viscosity of the liquid is sufficiently low for structural rearrangement to occur instantaneously allowing the liquid volume to be in equilibrium. As the temperature decreases, the atomic mobility decreases simultaneously and at a certain temperature, the atomic mobility is too low for the

structure to adapt to the decreasing temperature and the glass transition occurs [1,2]. The time allowed for structural relaxation depends on the cooling rate and therefore the glass volume decreases with decreasing cooling rate. Understanding the thermal history dependence of the glass volume is crucial for understanding the propensity for glass to relax. In the glassy state, the structure and volume is frozen-in. Subsequent heating can allow sufficient atomic mobility to enable relaxation of the glass resulting in volume reduction.

2.1. SILICATE GLASSES

Silica glass is the compositionally simplest of the oxide glasses, partially due to the low number of different structural configurations. In its nature, silica glass is amorphous and, contrary to its crystalline analogue, it completely lacks a periodic atomic structure [1,2,26]. However, considerable structural order exists on the short-range scale. For example, the Si coordination number at ambient pressure is always four and it features narrow distributions of Si-O bond lengths and O-Si-O angles, with the latter exhibiting a maximum at 109.7° similar to the SiO_2 crystal [6,32]. The considerable structural order at this length-scale is termed short-range order. With increasing observation length scale, the extent of disorder increases. For example, the distribution of Si-O-Si angles varies from 120° to 180°, due to the presence of Si-O-Si rings of varying size and shape [6,33,34]. The ring size is not entirely random, as most of the rings contain 5, 6, or 7 silicon atoms, with a smaller number of 3- and 4-membered rings [35,36]. This length scale is termed intermediate-range order.

2.2. ALUMINOSILICATE GLASSES

The properties of aluminosilicate glasses depend on the presence of modifying cations that can charge-balance Al^{3+}, as this determines the concentration of the dangling non-bridging oxygens (NBO) [26]. Aluminosilicate glasses are thus divided into peralkaline, meta-aluminous, and peraluminous regimes, in which the concentration of modifying cations is either lower, equal to, or higher than that of Al^{3+}, respectively. Using an ideal structural model about the interaction between Al^{3+} and modifiers, the excess modifiers in peralkaline results in all Al^{3+} in tetrahedral coordination and the presence of some amount of NBO-forming modifier [37–40].

2.2.1. ALUMINIUM COORDINATION NUMBER

The prevailing models of the structure of aluminosilicate glasses predict that the structural role of Al^{3+} is determined by the aluminum/modifier concentration ratio ($[Al^{3+}]/[M]$) [37–40]. Peralkaline glasses have an excess of modifier compared to Al^{3+} ($[Al^{3+}]/[M] \leq 1$) and all Al^{3+} will ideally be charge-compensated by modifier cations into a tetrahedral configuration (Al^{IV}). The excess modifiers will

depolymerize the network through NBOs [41]. In tectosilicates ($[Al^{3+}]/[M] = 1$) all Al^{3+} are expected to be fully charge-compensated and in tetrahedral configuration with no NBOs present. Peraluminous compositions have a deficit of modifier ions and the prevailing model cannot account for the structural configuration of the excess Al^{3+}. From nuclear magnetic resonance (NMR) spectroscopy studies, peraluminous compositions have been found to contain Al^{3+} in higher coordination states [42,43].

The model for peralkaline compositions is too simple to describe the structure of some peralkaline glasses. For highly peralkaline sodium aluminosilicate glasses, all Al^{3+} is expected to be in tetrahedral configuration. In Paper I, we consider a series of $(75\text{-}x)SiO_2\text{-}xAl_2O_3\text{-}25Na_2O$ glasses with x = 5, 10, 15, 20, and 25. We found non-negligible contents of Al^{3+} in five-fold coordination (Al^V), thus violating the simple model (Figure 3). In the ^{27}Al magic angle spinning nuclear magnetic resonance (MAS NMR) signal, the two compositions with x = 5 an 10 exhibit a resonance signal at 20 ppm typically associated with Al^V groups. This phenomenon has been described before and is believed to be a result of the high concentration of NBOs, shifting the equilibrium $Al^{IV} + NBO \leftrightarrow Al^V$ towards the Al^V side [44].

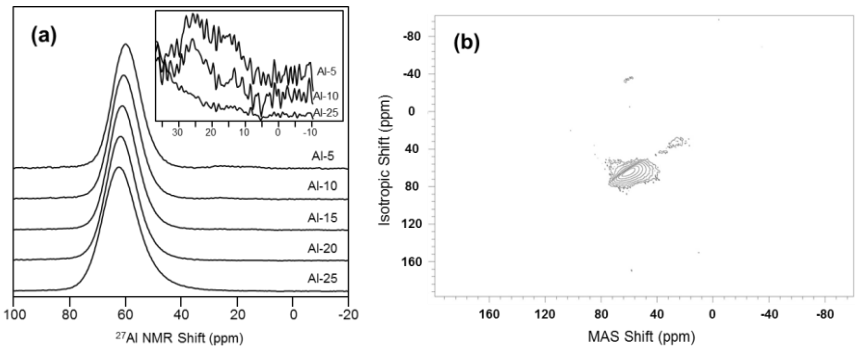

Figure 3. (a) ^{27}Al MAS NMR spectra for $(75\text{-}x)SiO_2\text{-}xAl_2O_3\text{-}25Na_2O$ compositions with x = 5, 10, 15, 20, and 25. The inset shows the resonances for Al^V and Al^{VI} structural units. (b) ^{27}Al 3QMAS NMR spectrum for the $70SiO_2\text{-}5Al_2O_3\text{-}25Na_2O$ glass with Al^{IV} and Al^V peaks. Figures taken from Paper I.

This equilibrium effect can be shifted further by densifying the glasses at high pressure and temperature, as also discussed in Paper I. High pressure and temperature have previously been shown to result in increases in the coordination number of network formers such as B^{3+} [45–47] and Al^{3+} [48–50]. Here we find that pressure increases the coordination of Al^{3+}, but that it only occurs in glasses with a high concentration of NBOs (Figure 4). Furthermore, the pressure-induced increase in Al^V increases with increasing NBO concentration. We note that the Al^{3+} concentration increases across the series and the reported fraction in Figure 4 is related to the specific concentration. However, no change occurs for the glasses with

high Al^{3+} concentration and few or no NBOs. This indicates that the presence of Al^{V} in peralkaline compositions is intimately related to high NBO concentrations. Furthermore, we observe trace amounts of six-fold coordinated Al^{3+} (Al^{VI}), although too small to quantify (not shown). The conversion of Al^{IV} to Al^{VI} is believed to follow the equilibrium $Al^{IV} + 2NBO \leftrightarrow Al^{VI}$.

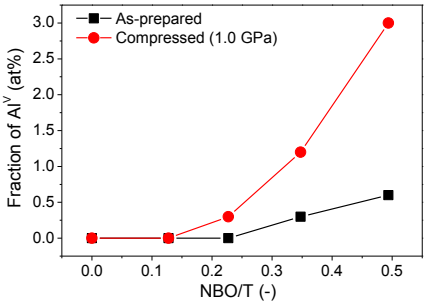

Figure 4. Fraction of five-fold coordinated aluminium (Al^{V}) in the $(75\text{-}x)SiO_2\text{-}xAl_2O_3\text{-}25Na_2O$ glass series as a function on the number of non-bridging oxygens per network tetrahedral (NBO/T). Al^{V} structural units are found in the most peralkaline compositions and their fraction increases after hot compression. Figures taken from Paper I.

In the ideal model, the role of Al^{3+} in tectosilicates is to be fully charge-compensated, with no NBOs present. This is the case for sodium aluminosilicate glasses, as found for the fully charge-compensated compositions (NBO/T = 0) in Figure 4. However, the ability to charge-compensate Al^{3+} is affected by the field strength (charge-to-size ratio) of the modifier. Monovalent modifiers are able to charge-compensate Al^{3+} approximately independent of the spatial distribution of the Al^{3+}, while divalent modifiers requires Al^{3+} to be in immediate vicinity [51]. Consequently, tectosilicates with divalent modifier are more likely to show deviations from ideality, as for the tectosilicate with calcium as the modifier, whereAl^{V} concentrations can be up to 6% [25,52]. The glass structure is also affected by the size of the modifier, as the ionic radius affect the local environment around the modifier cation [53,54]. The coordination number of the large Ca^{2+} is around six to seven [55,56], while the coordination numbers around the smaller Mg^{2+} is reported to be four-, five-, and six-fold [57–65]. This causes Mg^{2+} to behave partly as network modifier and partly as network former [66].

The structural role of Al^{3+} in peraluminous compositions is not described by the model. The modifier concentration is too low for charge-compensation of Al^{3+}, and instead some of the Al^{3+} must act as modifier having a coordination number of five- or six [42,67]. Alternatively, the formation of oxygen triclusters (three-fold coordinated oxygen), known from crystalline analogues, is required to charge-compensate Al^{3+} [28,68,69].

2.2.2. Q^N SPECIATION

The bond strength in covalent bridging oxygen is higher than for the ionic bond between modifying cations and non-bridging oxygens. This can be probed by Raman spectroscopy. For aluminosilicate glasses, the region 850-1200 cm^{-1} in the Raman spectrum gives information on the distribution of NBOs on the network formers, which is described by the Q^n speciation. In this terminology *n* equals the number of bridging oxygens per tetrahedra (T). Thus a fully polymerized Si^{4+} would be in Q^4 speciation and if with one NBO the Si^{4+} would be a Q^3. The wavenumber of the Raman shift depends on the bond strength. Thus, the signal from structural units with many NBOs is found at lower wavenumber than fully polymerized species. Deconvolution of the Raman peak in the 850-1200 cm^{-1} region allows estimation of the distribution of NBO in the network, as discussed in Paper I. However, it is challenging to distinguish between Al^{3+} or Si^{4+} tetrahedra. Figure 5 shows an example of such a deconvolution for the $65SiO_2$-$10Al_2O_3$-$25Na_2O$ glass. The Raman spectrum contains the signals from three types of tetrahedral units without any NBOs: $Q^{4,I}$ (~1125 cm^{-1}), $Q^{4,II}$ (~1100 cm^{-1}), and Q^n (~1000 cm^{-1}) [41,70]. Furthermore, excess concentration of modifiers relative to the Al^{3+} concentration results in signals from tetrahedra with one (Q^3 at ~1050 cm^{-1}) and two NBOs (Q^2 at ~950 cm^{-1}) [41,70].

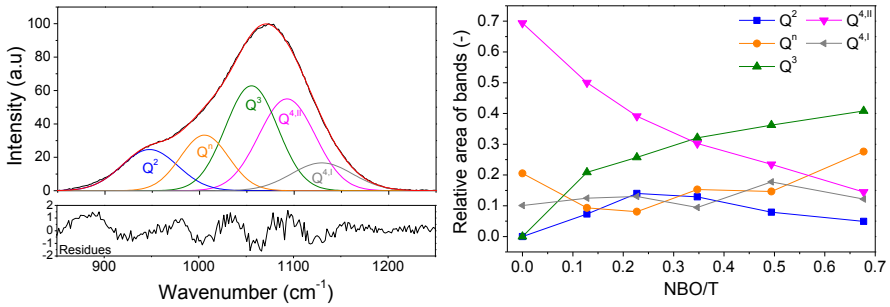

Figure 5. (a) Deconvolution of the Q^n species in the 850-1250 cm^{-1} frequency range of the Raman spectra for the $65SiO_2$-$10Al_2O_3$-$25Na_2O$ glasses. (b) Relative areas of the Q^n Raman bands for $65SiO_2$-$10Al_2O_3$- glasses as a function of the predicted NBO/T content. Figures taken from Paper I.

The area of each Gaussian fitting peak does not give the "true" concentration of the structural units, as it also depends on the local environment around the tetrahedra. However, deconvolution of the peak allows for a qualitative description of the relationship between NBO/T and different structural units [70]. The summary of the deconvolution of the peralkaline $(75\text{-}x)SiO_2$-xAl_2O_3-$25Na_2O$ glass series is given in Figure 5b, showing the relative variation of the structural species throughout the peralkaline region of the sodium aluminosilicate glass series. As the expected NBO/T ratio increases, fully polymerized structural units are substituted for

depolymerized species. Interestingly, the deconvolution shows that the Q^2 concentration goes through a maximum instead of having the highest concentration when the NBO/T ratio is highest.

Some information about Q^3 and Q^4 species can also be found from another region in the Raman spectrum. Sodium silicate glasses are characterized by a high concentration of Q^3 species see as the signal at 540 cm^{-1} (Figure 6) [41]. This signal disappears when Al_2O_3 is added to the glass as the Q^3 species are continuously converted to Q^4, which are found at ~500 cm^{-1}. It is also a consequence of the higher proportion of Al-O bonds, which are weaker than Si-O bonds, shifting the Raman band to lower wavenumbers.

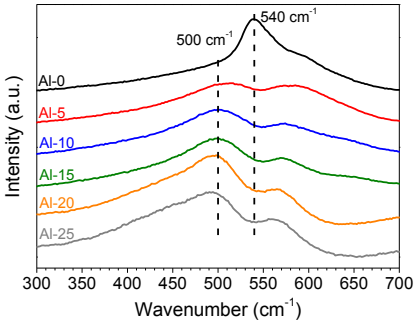

Figure 6. Raman spectra of the 300 to 700 cm^{-1} frequency range for the (75-*x*)SiO_2-*x*Al_2O_3-25Na_2O glass series, with x = 0, 5, 10, 15, 20, and 25. The Raman peaks associated with Q^3 species decrease as modifier ions charge-compensate the increasing amount of Al^{3+}. Figure modified from Paper I.

2.2.3. INTERMEDIATE RANGE STRUCTURE

The intermediate-range order of silicate glasses consist of Si-O-Si rings with varying ring size. The ring size can be evaluated by Raman spectroscopy, as small membered rings (3 and 4) typically can be found at specific frequencies between 450 and 650 cm^{-1}. Larger rings (≥5) are found at lower frequencies and due to their larger geometric flexibility, they have wider bond angle distributions resulting in wider signal peaks. The distribution of ring size and bond angles is dependent on the modifying cations. Silicate glass with sodium as the modifier tends to have a rather narrow distribution of structural units, as seen from the narrow signal at ~540 cm^{-1}. When divalent modifiers are substituted for sodium, the band broadens. The divalent modifier presumably results in a larger extent of disorder, as their better ability to stabilize the network allows for a larger distribution of bond angles and lengths [71].

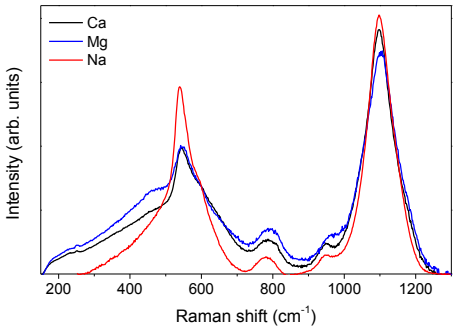

Figure 7. Raman spectra of the three Al-free glasses with similar silica content and varying modifier cations. The nominal compositions are $8CaO\text{-}16Na_2O\text{-}76SiO_2$ (Ca) and $8MgO\text{-}16Na_2O\text{-}76SiO_2$ (Mg), and $25Na_2O\text{-}75SiO_2$ (Na). Some of the intensity different can be explained by different baseline-correction procedures. Figure taken from Paper II.

2.2.4. AL-AVOIDANCE

Although glasses are random networks, the distribution of network formers in aluminosilicates is not completely random [72]. The stability of tetrahedral linkages depends on the coordination of the cations and if the cations can enter a higher coordination state the stability can be increased. Consequently, Al-O-Al linkages are stable when at least one of the Al^{3+} is in a higher coordination state, which is atypical especially in peralkaline glasses. Thus, Al-O-Si linkages are generally more energetically favorable than Al-O-Al linkages [73]. The energetic resistance against Al-O-Al linkages is termed the Al-avoidance [72]. Al-avoidance can be violated, e.g., in peraluminous compositions with Al^{3+} in five- or six-fold coordination. The field strength of the modifier cations can also affect the Al^{3+}/Si^{4+} mixing. The presence of divalent modifiers allows for violation of the Al-avoidance and the fraction of Al-O-Al linkages increases with increasing Mg/Ca ratio [74,75].

Experimental evidence for a small proportion of Al-O-Al linkages can be found from the ^{27}Al MAS NMR data (Figure 3). In glasses with low Al^{3+}-content, the resonance of Al^{IV} is found around 60 ppm. This resonance suggests that Al-O-Al bonds do not exist. For glasses with higher Al^{3+}-content, the resonance shifts to 62 ppm, which is an indication that the Al^{3+} concentration is so high that the principle of Al-avoidance is violated. Violation of Al-avoidance also depends on the nature of the divalent modifier. For example, in Paper II we find that both Ca^{2+} and Mg^{2+} facilitate a more disordered network than the monovalent Na^{+} through a greater violation of Al-avoidance. The smaller Mg^{2+} has been reported to increase the fraction of Al-O-Al bonds more than Ca^{2+} due to its higher ability to stabilize the network [74,75].

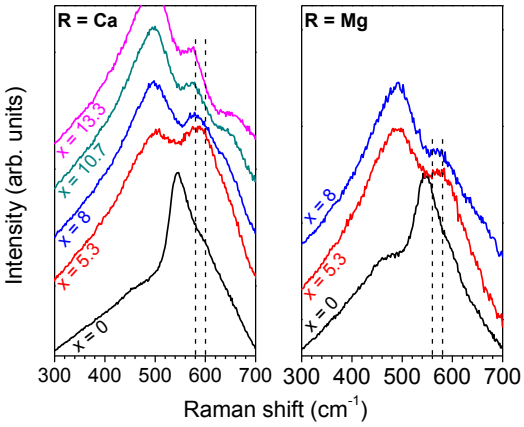

Figure 8. Raman spectra of 300-700 frequency range for (76-x)SiO2-xAl_2O_3-16Na_2O-8RO glasses, with R = Ca or Mg. The Al-O-Al linkage peak is found at ~560 cm^{-1}. The Al-avoidance occurs at lower modifier concentration in Mg^{2+} containing glasses than in Ca^{2+} containing glasses. Figure modified from Paper II.

In Paper II, we have compared the ability of Ca^{2+} and Mg^{2+} to create Al-O-Al in glasses of the (76-*x*)SiO_2 – *x*Al_2O_3 – 16Na_2O – 8RO composition, with R = Ca and Mg. The stabilizing ability can be evaluated through a Raman peak around 560 cm^{-1}, which is attributed to Al-O-Al bridges [41,76]. The appearance of this peak occurs at lower Al^{3+} concentration for Mg^{2+} containing glasses, than for the Ca^{2+} containing glasses. This suggests that Mg^{2+} has a better stabilizing ability and thus facilities Al-avoidance better than the larger Ca^{2+}.

CHAPTER 3. GLASS RELAXATION

Glasses are thermodynamically unstable and continuously relax towards their supercooled liquid state. Thus, glasses always relax, albeit at different rates depending on the composition, temperature, thermal history etc. [77]. The mechanism of glass relaxation typically involves small intermolecular rearrangements, resulting in slight shrinkage [14]. Glass relaxation affects various glass properties, e.g., density [78], hardness [78], refractive index [79], etc. For applications such as window glasses, relaxation is not a major problem, whereas it often needs to be controlled or accounted for in more high-tech applications. For example, the production of flat-panel displays involves high-temperature processes, which increase the relaxation rate. This causes problems related to both the extent and variability in the density fluctuations [5,14]. The extent of the compaction can be compensated for during the fabrication process, while density fluctuations must be controlled by composition design. Insufficient control of the relaxation processes can result in a nonfunctioning display due to pixel misalignment [12].

The simplest method to quantify glass relaxation is arguably by quantifying the amount of volume shrinkage. However, the structural rearrangements of glass relaxation occur at the nano-scale. The magnitude of the macroscopic volume changes is typically too small for precise quantification in standard laboratory samples sizes using conventional techniques. For example, this can be overcome by increasing the sample size to above, e.g., 1x1 m^2 area, allowing precise quantification of the volume relaxation [12]. However, generally it is not a suitable approach to quantify volume relaxation, as the production of homogenous samples of that size requires industrial-scale melting facilities. Therefore, the prediction of glass relaxation either from other properties or from simulations is needed.

In literature, several approaches have been used for the prediction of glass relaxation. The magnitude of volume relaxation has, for example, been found to scale with the enthalpy relaxation during the glass transition [80]. The latter has been widely studied [77,79,81–83], with attempt to predict it from the liquid fragility [84–92]. Fragility classifies glass-forming liquids according to the extent of their non-Arrhenius temperature dependence of either viscosity or relaxation time [93]. The liquid fragility index m, which varies with composition (x), is defined as the slope of the logarithmic viscosity (η) versus T_g-scaled inverse temperature (T) curve at T_g, where T_g is the glass transition temperature (10^{12} Pa s isokom temperature):

$$m(x) = \left.\frac{d \log_{10}\eta(T,x)}{d(T_g(x)/T)}\right|_{T=T_g(x)} . \quad (1)$$

Elsewhere, the relationship between glass composition and the enthalpic driving force for relaxation have been studied. By designing compositions with low fragility, the thermodynamic driving force for relaxation can be minimized. This has been utilized in the studies of Boolchand and co-workers on glasses exhibiting so-called intermediate phases. In those studies, relaxation effects are claimed to be minimized through an optimized network topology and low fragility [94–98]. The relaxation can also be controlled by designing glass compositions with large activation energy barriers for structural rearrangements. Glasses whose parent glass-forming liquids are fragile will have a large thermodynamics driving for relaxation, but a large activation energy results in slow relaxation [14,83]. Minimized structural relaxation from high fragility compositions have also be found in the reversibility windows [14]. Recently, molecular dynamics simulations have been used to gain insights into the dynamics of oxide glass relaxation [15,99].

3.1. FUNDAMENTALS OF DIFFERENTIAL SCANNING CALORIMETRY ANALYSIS

Physical transitions, such as the glass transition, typically involve the exchange of heat with the surroundings. Calorimetry is the measurement of heat and often used to measure the amount of heat required to increase the temperature of a sample. Calorimetric analyses can therefore be used to study relaxation processes through quantification of their endothermic processes. In differential scanning calorimetry (DSC), the change of the difference in heat flow rate to the sample and a reference material is measured, while subjected to a temperature program. The isobaric heat capacity (C_p) (unit: J K^{-1}) of the sample determines the amount of heat required to increase its temperature. The heat capacity of glasses is fairly constant in the glassy and liquid states, but undergoes an abrupt change during the glass transition. Typically, a DSC temperature program involves linear heating/cooling at fixed rates:

$$T = T_0 + \beta t, \tag{2}$$

where T_0 is the initial temperature at time $t = 0$, and β is the heating rate. DSC is a versatile probe for determination of, e.g., transition temperatures (glass transition, crystallization, melting) and the temperature dependence of heat capacity [100]. Despite its success, complications arise, e.g., when analyzing SiO_2-rich compositions. This can result in low signal-to-noise ratio due to the small change in heat capacity during glass transition and the typical low instrument sensitivity at high temperature.

Temperature-modulated DSC (TM-DSC) might be a solution to some of these challenges. In TM-DSC, a superior sensitivity is achieved by superimposing a sinusoidal heating rate on the standard linear heating rate from DSC with increased measurement duration as the only drawback [101]. The resulting temperature program is described by

$$T = T_0 + \beta t + A\sin(\omega t), \tag{3}$$

where T_0 is the initial temperature at time t = 0, β is the heating rate, A is the amplitude of the modulation and ω is the angular frequency of the modulation ($\omega = 2\pi/P$, where P is period). An example of the raw TM-DSC data is found in

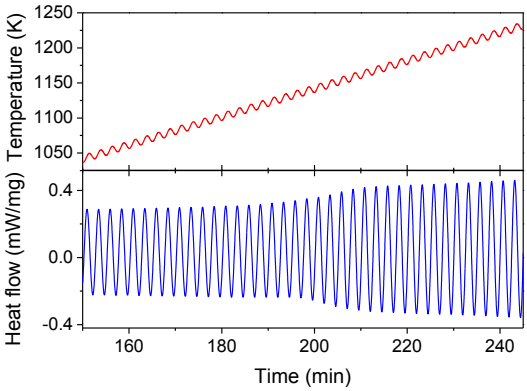

Figure 9. Standard raw data from TM-DSC for the 39.8SiO_2-31.6Al_2O_3-28.7CaO (mol%) glass. Both the temperature profile and the heat flow curve are sinusoidal according to Eq. (3).

The post-treatment of raw TM-DSC data is more complicated than for DSC data, but also provides more information. Through a deconvolution, the raw data can be separated into a kinetic component and a heat capacity component, identified by the imaginary heat capacity (Cp″) and real heat capacity (Cp′), respectively [101]. The kinetic component gives information about, e.g., relaxation and crystallization processes [101–103]. These transitions are filtered out in the heat capacity component, which describes the heat capacity of the sample itself. For glasses, the kinetic component contains the endothermic enthalpy relaxation [101]. The real and imaginary heat capacities can be obtained by dividing the amplitude of the heat flow by the amplitude of the heating rate, giving the modulus of the complex heat capacity (C_p^*):

$$C_p^* = C_p'(\omega) + iC_p'' \tag{4}$$

Due to thermal inertia effects, there is a time delay between input and output defined by the phase angle (θ), which can be used to obtain real and imaginary parts of Cp* [104]:

$$C_p' = \left|C_p^*(\omega)\right| \cos\varphi \tag{5}$$

$$C_p'' = \left|C_p^*(\omega)\right| \sin\varphi \tag{6}$$

For glasses, the imaginary heat capacity is equal to zero far away from the glass transition, as the timescale of the atomic and molecular motions are much faster than the temperature modulation (typically 90-200 s). This permits exploration and characterization of structural relaxation processes in the glass from the phase lag or the imaginary heat capacity [105–109]. An example of the deconvoluted data is found in Figure 10.

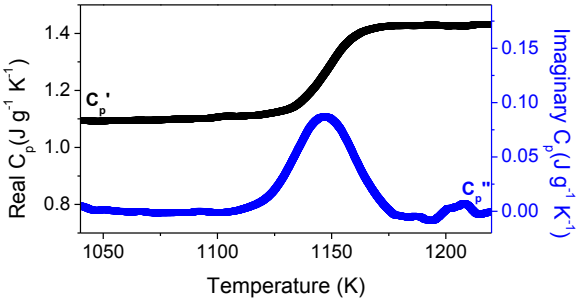

Figure 10. Deconvoluted TM-DSC data for $39.8SiO_2$-$31.6Al_2O_3$-28.7CaO (mol%) glass. The glass exhibits a sigmoidal change in the real heat capacity during the glass transition, while the imaginary heat capacity and phase lag are Gaussian-shaped.

In order for the deconvolution procedure to be valid, the input and output (heating rate and heat flow) must exhibit a linear response [102,110–112]. The linearity can be evaluated by Lissajous curves that describe the heat flow as a function of heating rate [113,114]. When the heat transfer is ideal and instantaneous, the Lissajous curve is linear. However, the heat transfer in glass is not ideal and as a result of thermal inertia, a linear response results in elliptical shaped Lissajous curves. Linearity can be lost if the underlying heat rate or the amplitude is too high. Too high instantaneous heating rate (dT/dt) will result in discrepancies between input (heating rate) and output (heat flow)

3.2. PREDICTING CONFIGURATIONAL HEAT CAPACITY

Predicting the composition dependence of the magnitude of enthalpy relaxation is of industrial interest, as it have been found to scale with the magnitude of volume relaxation [80]. Several studies have attempted to estimate the enthalpy relaxation from the liquid fragility index [84–92]. In Paper III, we have used a recent model that attempts to combine topology and thermodynamics to predict the extent of enthalpy relaxation [115].

The heat capacity of the super-cooled liquid consists of both vibrational and configurational contributions. When cooling from the super-cooled liquid to the glassy state, the configurational degrees of freedom are lost as a result of the

increase in viscosity. The heat capacity of the glassy state primarily contains vibrational degrees of freedom [91], and the heat capacity of the glass (C_{pg}) is thus approximately equal to the vibrational heat capacity of the liquid at T_g. For relatively strong glass-forming liquids, the vibrational degrees of freedom change only slightly going from the liquid to the glass and thus the vibrational heat capacity is the same in the liquid and glassy state. Therefore, the configurational heat capacity is approximately equal to the difference in heat capacity between the glass and the liquid. In the model, the configurational heat capacity ($C_{p,conf}$) is therefore approximated to be the isobaric heat capacity jump (ΔC_p) between the heat capacity of the super-cooled liquid (C_{pl}) and heat capacity of the glass (C_{pg}) at T_g ($C_{p,conf} \approx C_{pl} - C_{pg} = \Delta C_p$). The derivation of the model defines the configurational heat capacity as changes in the configurational enthalpy and entropy, and then combines the Adam-Gibbs model for equilibrium viscosity with Angell's definition of fragility. This is used to establish a relation between the kinetics (m) and thermodynamics (C_p) (See Ref. [115] for full derivation),

$$\Delta C_p\left[x, T_g(x)\right] = \frac{A(x_R)}{T_g(x)}\left(\frac{m(x)}{m_0} - 1\right), \tag{7}$$

where $A((x,y,z)_R)$ is a proportionality constant and m_0 is the fragility of a strong liquid (m = 14.97). The model in Eq. (7) was found to successfully predict $C_{p,conf}$ in a series of borosilicate glasses [115]. Here, we apply it to aluminosilicate glasses.

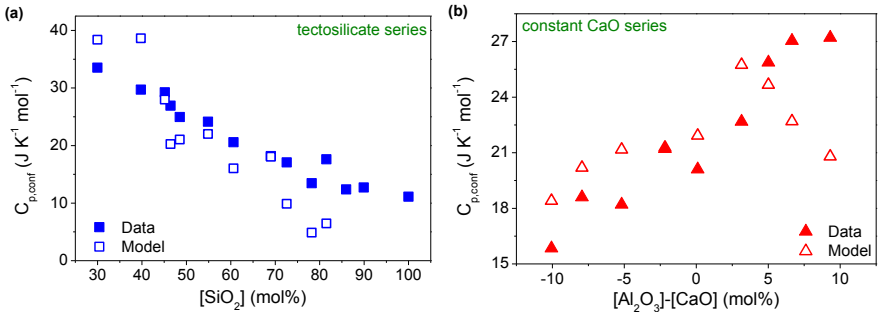

Figure 11. Configurational heat capacity ($C_{p,conf}$) as a function of (a) SiO_2 content for the (100-2x)SiO_2-$x$$Al_2O_3$-$x$CaO series and (b) [$Al_2O_3$]-[CaO] for the (80-$y$)$SiO_2$-$y$$Al_2O_3$-20CaO series. The experimental $C_{p,conf}$ values was determined by differential scanning calorimetry and the modeled $C_{p,conf}$ values was calculated using Eq. (7). Figures taken from Paper III.

The validity of the model was here tested using two series of calcium aluminosilicate glasses; a tectosilicate series ((100-2x)SiO_2-$x$$Al_2O_3$-$x$CaO) and a series with constant CaO content ((80-y)SiO_2-$y$$Al_2O_3$-20CaO). The model in Eq. (7) predicts $C_{p,conf}$ to be proportional to m and inversely proportional to T_g. This was the case for the tectosilicate series and therefore good agreement between data and model is observed (Figure 11a). The fitting is best for relatively fragile glass formers

while we find some discrepancies for strong compositions. We suspect these discrepancies to be a result of the difficulties in obtaining accurate *m* values for strong glass formers using calorimetric methods. The constant CaO series exhibited constant T_g and a decrease in *m* for peraluminous compositions, without a corresponding drop in $C_{p,conf}$, resulting in a poorer correlation between model and data (Figure 11b).

The model predicts $C_{p,conf}$ using the scaling factor *A*. For the tectosilicate series and the constant CaO series we find *A* to be 16.0 and 11.8 kJ/mol, respectively. *A* was found to be 19 kJ/mol for the series of borosilicate glasses [115] and using literature data for aluminosilicate, we find *A* to be 12.7, 13.3, and 16.5 kJ/mol for sodium aluminosilicate, calcium aluminosilicate, and sodium calcium aluminosilicate glasses, respectively [116]. These differences between compositions suggest that *A* is dependent on the chemical composition.

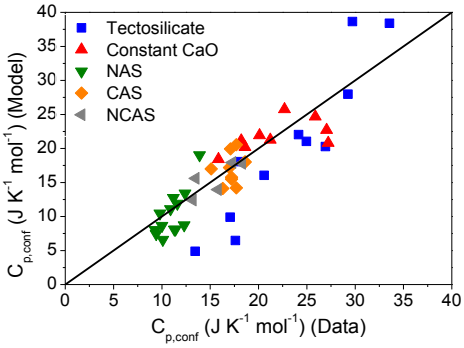

Figure 12. $C_{p,conf}$modelled from Eq. (7) as a function of experimental $C_{p,conf}$. The tectosilicate and constant CaO series data are from Paper III and the data for sodium aluminosilicate (NAS), calcium aluminosilicate (CAS), and sodium calcium aluminosilicate (NCAS) glasses are from Ref. [116]. Figure taken from Paper III.

3.3. ANALYZING HIGH-T_G GLASSES USING TM-DSC

Temperature-modulated DSC has been used to analyze organic, chalcogenide, metallic, and oxide glasses. The applications range from determination of T_g [117–119] and liquid fragility index [120–122] to the study of relaxation behavior [120–126] and identifying rigidity transitions [94–97]. All previous studies have been performed on calorimeters limited to ~1000 K, thereby only allowing analysis of a minor fraction of silicate glasses [127,128]. Recently, the TM-DSC technique has become available in commercial high-temperature calorimeters, enabling the analysis of silicate glass with high T_g. However, the design of these calorimeters is different from the low-temperature ones, thus complicating the data collection and analysis procedures.

The usable measurement parameters (β, A, P) cannot be directly transferred from low- to high-temperature experiments. For example, the furnace design is different, resulting in different sensitivity. The appropriate underlying heat rate depends on the sample characteristics, especially the fragility and the width of the glass transition. Therefore, a universally suitable β value cannot be given. To decrease the measurement duration, a high underlying heating rate is desired. To study the different experimental parameters, we thoroughly analyzed a $55SiO_2$-$25Al_2O_3$-20CaO (mol%) composition (m = 48) in Paper IV. However, too high heating rates result in sharp and distorted phases due to the shorter observation time (Figure 13a). Lower β values result in smooth phases with a nearly Gaussian shape, as expected for homogeneous systems with a normal distribution of relaxation times (Figure 13b).

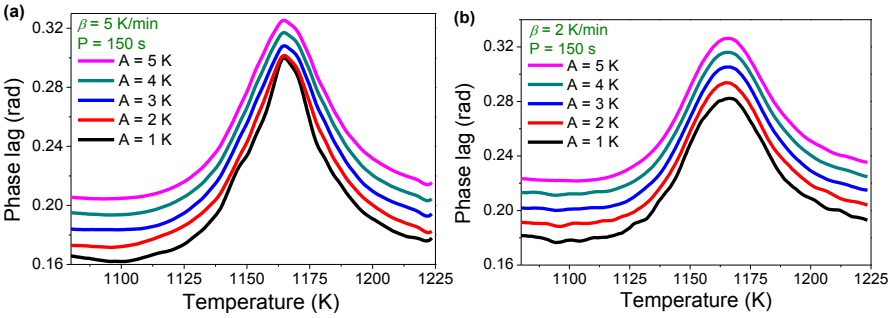

Figure 13. Phase lag for the $55SiO_2$-$25Al_2O_3$-20CaO (mol%) glass around the glass transition with constant modulation period (P = 150 s) and varying modulation amplitude (A) for heating rates of (a) 5 K/min and (b) 2 K/min. The phase lag curves are shifted by 0.01 rad for an easier comparison. Figures taken from Paper IV.

As a rule of thumb, an underlying heating rate of 2 K/min is appropriate for silicate glasses, as it allows for a sufficient number of periods to be cycled during the transition from glass to supercooled liquid. However, for strong glass-forming liquids, a higher underlying heating rate is needed to ensure a sufficient signal-to-noise ratio. For the strong $86SiO_2$-$7Al_2O_3$-7CaO (mol%) composition (m < 22), we observe substantial noise using β = 3 K/min. The noise is decreased when increasing β to 5 K/min (Figure 14). The same difficulties with low signal-to-noise ratio for strong glass forming melts are known from linear DSC.

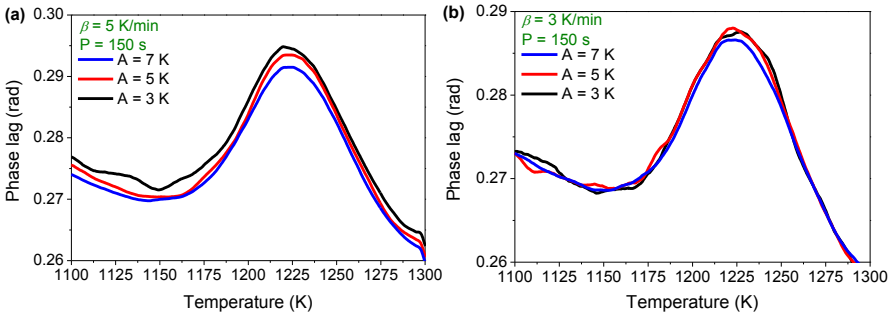

Figure 14. Phase lag curve for the $86SiO_2$-$7Al_2O_3$-7CaO glass around the glass transition with constant modulation period (P = 150 s) and varying modulation amplitude (A) for heating rates of (a) 5 K/min and (b) 3 K/min. Figures taken from Paper IV.

The selection of the amplitude value is less affected by the sample properties. A relatively high amplitude is desirable as it provides increased sensitivity, due to the larger changes in instantaneous heating rate (dT/dt). However, too high amplitudes will decrease the resolution. For the $55SiO_2$-$25Al_2O_3$-20CaO (mol%) composition, we found that a small A value of 1 K results in noise, while increasing it to 5 K decreases the noise with no loss of resolution (Figure 13b). An amplitude of 5 K thus appears to be a good initial value for compositions with m = 30-60 (not shown), while stronger glass-forming liquids can require amplitudes around 7 K (Figure 14).

In order for the deconvolution of raw data to be valid, the sample must respond linearly to the thermal perturbations. We observe a linear response for the $55SiO_2$-$25Al_2O_3$-20CaO (mol%) composition, when using a heating rate of 2 K/min in combination with amplitudes of both 1 and 5 K (Figure 15a-b). For heating rates of 5 K/min, the response is linear when the amplitude is high, but loses linearity at low amplitude (Figure 15c-d). For the combinations of experimental parameters exhibiting a linear response, the number of modulation periods during the glass transitions is sufficiently high. However, then a linear response should also be found for the data in Figure 15c. We suspect that the origin of the non-linear response in Figure 15c is the low amplitude, indicating that the calorimeter is not able to accurately control such small perturbations in the heat flow. This highlights the sensitivity issues for high-temperature calorimeters, which must be solved through careful experimental design, as described above.

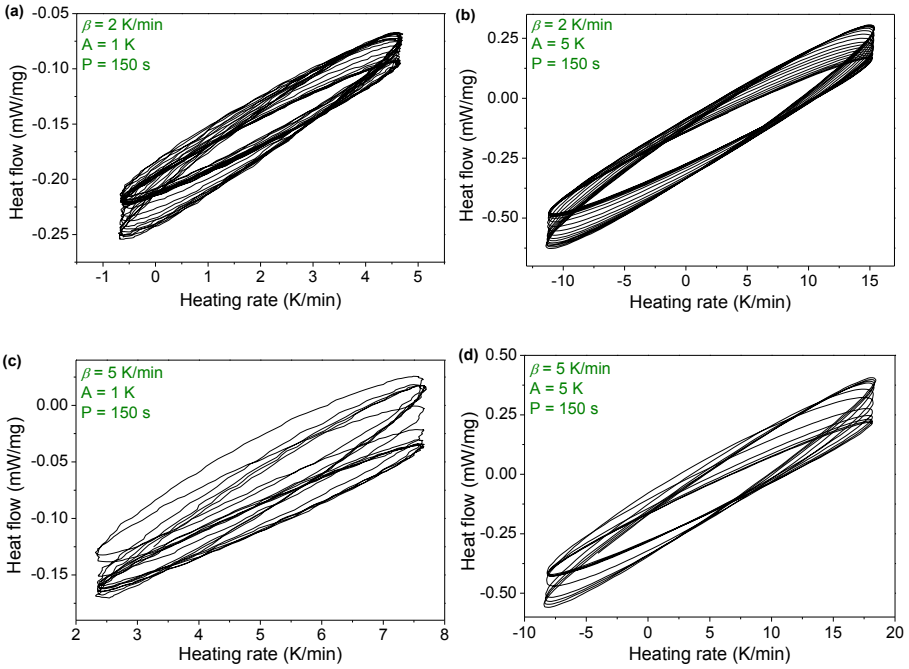

Figure 15. Lissajous curves for the $55SiO_2$-$25Al_2O_3$-20CaO (mol%) glass for four combinations of parameters with constant modulation period (P = 150 s): (a) β = 2 K/min and A = 1 K; (b) β = 2 K/min and A = 5 K; (c) β = 5 K/min and A = 1 K; (d) β = 5 K/min and A = 5 K. The curves been smoothed using a Savitzky-Golay algorithm [129] without any change in the overall shape. Figures taken from Paper IV.

3.4. DETERMINATION OF FRAGILITY USING TM-DSC

Fragility is typically determined directly from viscosity-temperature data. However, this requires relatively large sample volume of a certain shape, which can be difficult to obtain for poor glass-formers [130]. Instead fragility can be determined by DSC using the Moynihan method [131–134], in which the activation energy for structural relaxation is estimated by varying the cooling/heating rate. However, the relatively low sensitivity of high-temperature calorimeters complicates the determination of the fragility index for strong glass-forming liquids and liquids with high T_g. The activation energy for structural relaxation is estimated from the fictive temperatures at different heating rates.

An alternative approach to determine m of strong glass-forming liquids could be TM-DSC, as discussed in Paper V. The technique has two advantages over the Moynihan approach using linear DSC: (i) the superimposed sinusoidal heating rate gives superior sensitivity and signal-to-noise ratio at high temperatures; (ii) the

determination of the characteristic temperature (here T_g^{ω}, T_f in Moynihans method) is more reliable, as T_g^{ω} is determined at the peak maximum temperature from the imaginary heat capacity data. The C_p'' curve scales relative to the phase lag (φ) (Eq. (6)) [101] andT_g^{ω} can be determined directly from the phase lag (Figure 16). The characteristic temperature is more reliable, as more data points are used to establish T_g^{ω} in the Gaussian fit to the phase lag curve compared to determining T_f from the two data point on either side of T_g as by the Moynihan method.

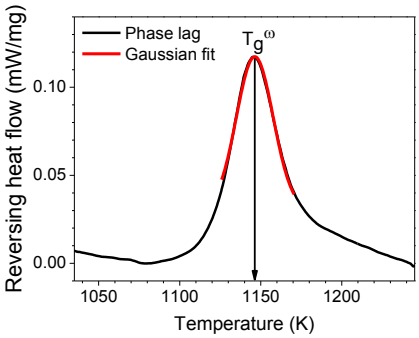

Figure 16. Temperature dependence of the phase lag scanned through the glass transition for 39.8SiO_2-31.6 Al_2O_3-28.7CaO (mol %) glass with β = 2 K/min, A = 5 K, and P = 180 s. The maximum in the phase lag peak (T_g^{ω}) is determined from the Gaussian fit. Figure modified from Paper V.

In previous studies, TM-DSC has been used to determine fragility of chalcogenide and oxide compositions [120–122], but only for glass-forming systems with low T_g under 800 K. Typically, the fragility is determined using an activation energy approach analogous to the Moynihan approach. However, instead of changing cooling/heating rates, the oscillation frequency is changed in the TM-DSC method, shifting the response to higher temperature. The slope of the frequency dependence of T_g^{ω} is then used to estimate the fragility [122] (Figure 17).

Another method to determine fragility by TM-DSC is to construct an Angell plot, by estimating the relaxation time (τ) at T_g^{ω}. The fragility can then be determined as:

$$m(x) = \left.\frac{d \log_{10}\tau(T,x)}{d(T_g(x)/T)}\right|_{T=T_g(x)} . \quad (8)$$

The shear relaxation time (τ) dependence of temperature (T_g^{ω}) and the glass transition temperature (T_g) is needed to construct the Angell plot. T_g^{ω} is found from the phase lag data, while τ at T_g^{ω} can be approximated by $\tau = P/2\pi$ [120,121]. Traditionally, T_g is defined as the temperature at which the equilibrium viscosity $\eta = 10^{12}$ Pa s [135], while we here define it in terms of the shear relaxation time. τ depends on the shear modulus and follows the Maxwell equation ($\tau = \eta/G$). It is

usually taken to be ~100 s at T_g [136–138]. T_g must be determined by extrapolation, as the period needed to determine T_g^{ω} directly (~628 s) results in too few modulation cycles through the glass transition for a valid deconvolution of the raw data [101]. The extrapolation exploits the linear relationship between T_g^{ω} and τ at each modulation frequency [139]. We not that the shear modulus is composition dependent and therefore τ is not equal to ~100 s at T_g for all glasses. The fragility can then be calculated from the slope in the Angell plot constructed from T_g^{ω}, the estimated τ, and the extrapolated $T_g^{\tau = 100}$ (Figure 18).

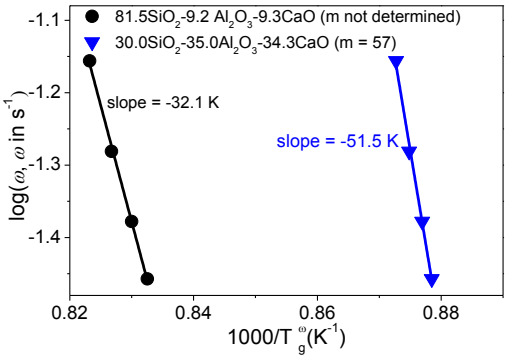

Figure 17. Liquid fragility determination using the activation energy approach. The logarithmic frequency is plotted as a function ofthe inverse phase peak temperature. The phase lag and the T_g^{ω} shifts to higher temperature as the frequency increases. Figure modified from Paper V.

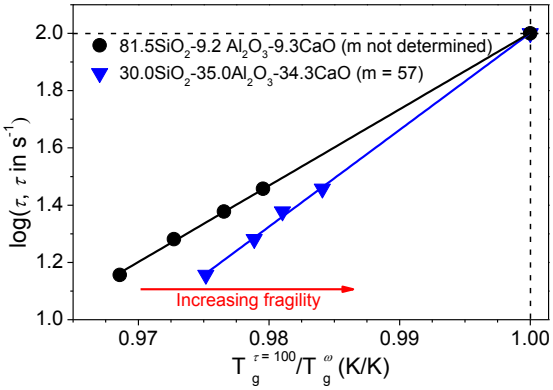

Figure 18. Angell plot of the relaxation time slightly above the glass transition temperature. The relaxation times have been determined using $\tau = 1/\omega = P/2\pi$ rad/s. The straight lines are the linear fits to the data. Figure modified from Paper V.

The validity of the fragility values determined by the two TM-DSC methods is checked by comparison with values from viscometric data for the same glasses (Figure 19). The compositions cover tellurites, borates, and silicates, with a wide range of fragilities (*m* from 25 to 97) [140,141]. The calorimetric fragilities are corrected according to the correction procedure in Ref. [130]. The correction is needed to correct for the systematic DSC underestimation of *m*, as a result of the inherent error in the Arrhenian approximation in the fragility determination. After correction, the activation energy and relaxation time approaches give approximately identical *m* values. The fragilities values from viscometry and TM-DSC scale approximately linearly. The data are comparable to fragility values obtained by the Moynihan method, suggesting that TM-DSC probes the same type of relaxation as DSC.

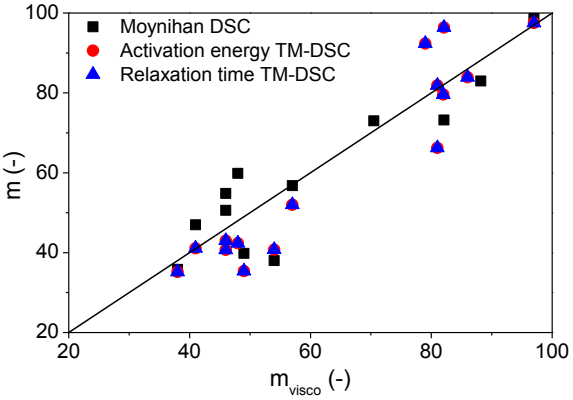

Figure 19. Corrected fragility values (*m*) from the Moynihan approach and the two TM-DSC procedures as a function of the fragility of the same compositions determined from viscometry (m_{visco}). The data are corrected according to the procedure in Ref. [130]. After the correction, the fragility values from the two TM-DSC procedures become identical. Figure taken from Paper V.

For the tectosilicate calcium aluminosilicate system, the 81.5SiO_2-9.2 Al_2O_3-9.3CaO composition is the strongest we have successfully determined the fragility of using the Moynihan method (*m* = 22). Using TM-DSC, the improved sensitivity compared to standard DSC has allowed determination of fragility of the 88.9SiO_2-4.6 Al_2O_3-5.5CaO glass-forming liquid and potentially even the strong SiO_2 composition. However, it should also be noted that the determination of fragility by TM-DSC has two main disadvantages: (i) the experiment duration is increased compared to the Moynihan method; (ii) while the composition-dependent trend in fragility can be successfully reproduced by TM-DSC, there is a tendency to underestimate fragility values for high-*m* compositions and overestimate for low-*m* compositions (data not shown).

3.5. UNDERSTANDING GLASS RELAXATION FROM NETWORK TOPOLOGY

The concept of so-called reversibility windows, which describe compositional regimes with tailored topology, resulting in non-aging glasses with a minimal propensity for relaxation, has received significant attention [96]. The concept is based on a counting of bond stretching and angular constraints, as originally introduced by Phillips [142]. The concept filters out some chemical details, while focusing on the network topology. The compositional regimes with minimal relaxation are found when the network topology results in isostatic networks through a mean coordination number of 2.4. Networks with a mean coordination number lower than 2.4 contain floppy modes, making them flexible. If the mean coordination number is above 2.4, redundant constraints are introduced to the network, causing the network to be stressed-rigid.

Following these ideas, the extent of glass relaxation should be predictable from the network topology, i.e., the number of bond constraints per atom. In flexible networks, the floppy modes result in entropic stress and low kinetic barriers against relaxation, while the enthalpic stress in the stressed-rigid network results in a high enthalpic driving force for relaxation [96]. The intermediate isostatic networks provide the best resistance against relaxation. Experimentally, the reversibility window can be identified based on Brillouin [143] and neutron scattering [144], Raman [145] and Mössbauer spectroscopy [146], molar volume [147], and TM-DSC [98] experiments. However, it should be noted that it has also be criticized, as no convincing structural origin of the reversibility window has hitherto been reported [126,148]. Furthermore, the compositional regime of the reversibility window cannot always be predicted from the mean coordination number [148].

Today, the glass compositions with an identified reversibility window are not industrially relevant [149]. Therefore, there is an interest in identifying silicate glasses of industrial relevance that exhibit minimal structural relaxation, e.g., for high-performance display glasses. In some unpublished work, we have used TM-DSC as a probe to investigate the existence of a reversibility window in the fully charge-compensated calcium aluminosilicate series. This glass series is chosen based on molecular dynamics simulations [150], which suggest a mean coordination number of 2.4 and a minimum in the enthalpy relaxation around the $76SiO_2$-$12Al_2O_3$-12CaO composition (Figure 20). Through the magnitude of the non-reversing heat flow in the TM-DSC experiment, the enthalpy relaxation can be approximated. The compositional range exhibiting a minimum in relaxation (ΔH_{max}) from molecular dynamics simulations coincides with a minimum in the non-reversing heat flow from TM-DSC, suggesting that there is a correlation between

network topology and propensity for relaxation. We propose that the origin of the minimal relaxation in this narrow compositional regime is due to a combination of high activation energy barrier against relaxation through low atomic mobility, as the glass network is isostatic, and low enthalpic driving force for relaxation through low internal stress.

This can, however, not explain the existence of a second minimum around the $50SiO_2$-$25Al_2O_3$-25CaO composition (Figure 20). This origin of this minimum is still under investigation, but we note that it coincides with the minimum in molar volume, which has previously been suggested as experimental evidence of the reversibility window [96,147]. Regardless of the physical origin of the two minima, they coincide with reported probes for identifying the reversibility window and the results indicate that the relaxation in glass is indeed correlated to network topology.

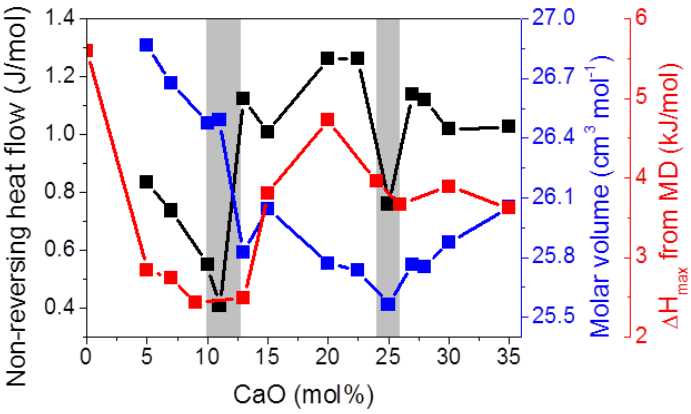

Figure 20. Non-reversing heat flow from TM-DSC experiments, molar volume, and magnitude of relaxation (ΔH_{max}) from molecular dynamics (MD) simulations in the (100-2x)SiO_2-xAl_2O_3-xCaO glass system. The experimental non-reversing heat flow data exhibit two minima, coinciding with the minimum in ΔH_{max} and molar volume, respectively.

CHAPTER 4. GLASS UNDER STRESS

The mechanical behavior of glasses covers a wide range of properties, including strength, toughness, crack resistance, hardness, and elasticity. All of these properties affect the product performance experienced by end-users and must be considered in the development of new glass compositions and products. For example is the risk of catastrophic fracture decreased by high toughness and crack resistance [151,152].Here we describe three phenomena that have remained relatively unexplored, namely the time- and humidity-dependence of crack initiation and pressure-induced changes in hardness, crack resistance, and photoelasticity. The kinetics of crack initiation is almost unexplored, although it profoundly affects, e.g., determination of the crack resistance and frangibility of glass. The manipulation of glass structure and properties at high pressure can guide the development of glasses with improved mechanical properties through an improved understanding of the densification mechanism. The photoelastic effect can result in birefringence in glass, which can be an issue for various optical glasses. Understanding the effect of pressure is important for understanding the densification mechanism of these materials under pressure and the corresponding changes in macroscopic properties.

4.1. CRACK INITIATION

Oxide glasses are intrinsically among the strong materials [19], but have the disadvantage of being brittle [19,153–155]. The brittleness originates from stress-intensifying surface flaws. The concentrated stress around the flaw results in brittle failure, as the amorphous structure of glass does not allow for a stable shearing mechanism to dissipate the stress [156]. Preventing the initiation and propagation of cracks in glassy materials is one of the most important tasks for producers of displays for portable devices. In order to develop stronger and tougher glasses, the nature of crack initiation and propagation must be understood, including the effect of composition, thermal history, post-treatment, etc.

Much effort have been put into studying crack propagation [154,157,158], while crack initiation have received less attention. Hirao and Tomozawastudied the effect of liquid water on crack initiation [159], Striepe *et al.* [160] showed that the crack initiation probability depends on the relative humidity and Lawn *et al.* [161] showed that the crack initiation probability is a function of both time and atmospheric environment. The origin of this humidity dependence is reported to be the hydrolysis of strained network former (T) oxygen bonds [162,163]:

$$\equiv T–O–T\equiv + H_2O \rightarrow 2\equiv TOH$$

In order to study crack initiation, Vickers indentation is often used. Originally designed to measure hardness and utilized for its reproducibility and simple sample

preparation, Vickers indentation have become a preferred tool for determination of the resistance against cracking in the glass community [151,164–166], as it simulates real-life failures for many applications. In Vickers indentation, a pyramidal diamond of 136° angle is loaded onto a polished, flat surface. Normally, the Vickers hardness is determined from the size of the indent relative to the applied load. However, when studying crack initiation, the number of initiated cracks is counted instead. The resistance to crack initiation can be quantified by the crack resistance (CR) [167], defined as the indentation load that generates an average of two radial/median crack from the corners of the pyramidal indent. This definition impedes the determination of crack resistance for anomalous glasses with low Poisson's ratio, as their cracking behavior favors ring/cone cracking over radial/median cracks [168].

Determining crack resistance has become an increasingly popular method for evaluation of crack initiation [22,23,46,151,160,165,166,169–191]. However, the experimental procedure varies between research groups and details about the atmospheric conditions or the time between indentation and crack counting are often missing, even though these have a large effect on the measured CR values. In order to compare data from different research group, the crack resistance studies could be performed in a dry glove box purged with N_2. However, in real-life situations, various concentrations of water vapor is always present and the property testing must thus ideally also be performed in the presence of gaseous water.

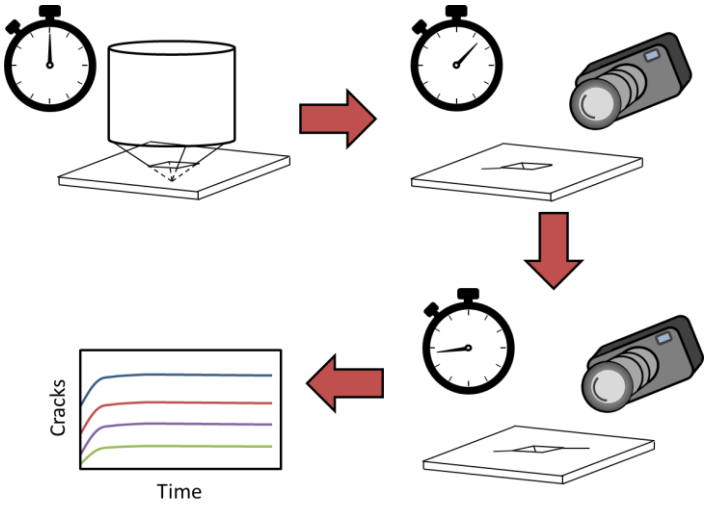

Figure 21: Experimental procedure for determining the time (t) dependence of crack initiation. After the indenter is unloaded at $t = 0$, images are continuously collected for 6 h. Consequently, the time of each pop-in of cracks can be determined. Figure taken from Paper VI.

In Paper VI we attempted to elucidate the effect of the atmospheric conditions and the time between indentation and crack counting on crack initiation. To do so, the exact time of the pop-in of individual crack was continuously monitored for at least 6 h and counted again after 24 h. In order to test the effect of humidity on crack initiation, the same glass was indented during winter (relative humidity of 39±8%) and summer (relative humidity of 70±9%). The experimental setup is visualized in Figure 21, showing indentation at time $t_0 = 0$ and continuously monitoring of each crack pop-in in order to establish the time-dependence of the crack probability.

When determining crack resistance of glasses, delayed cracking is often observed. In literature it has been reported to occur at least during the initial 10 min after indentation [161]. Recently, delayed cracking was studied for 24 h for titanosilicate glasses and found to cease after 2 h [175]. An example of delayed cracking in our data can be found in Figure 22. The indent is found to exhibit no crack immediately after indentation, with the pop-in of two cracks occurring after 353 s. One additional crack pop-in is observed after both 363 s and 393 s. This example of a single indent is not representative and the behavior depends on both indentation load and humidity, but Figure 22 highlights the importance of considering and reporting the time period between indentation and crack counting when determining the crack resistance. If the crack initiation probability was compiled from this indent alone, during a 50 s time span it would be observed to be 0%, 50%, 75%, or 100%.

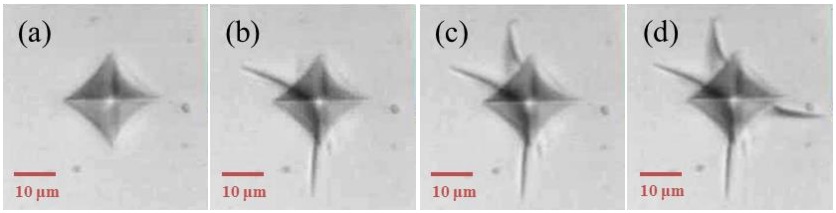

Figure 22: Time-dependence of the pop-in of crack for single indent at four different periods after indentation at a load of 1.96 N with RH = 37.2%. The images show an indent (a) immidiately after indentation and after 343 s (identical), (b) after 353 s, (c) after 363 s, and (d) after 393 s. Figures taken from Paper VI.

The effect on the time between indentation and crack counting is visualized in Figure 23 for a $67.5SiO_2$-$12.5Al_2O_3$-$20CaO$ glass. The crack resistance is determined 35 s and 24 h after indentation from at least 20 indents. For low relative humidity conditions (LRH), the crack resistance is found to be 2.5 N after 35 s. After 24 h the CR drops by >30% to 1.4 N, as a results of the prolonged time for the pop-in of cracks to occur. A similar effect is observed under more humid conditions with a drop in the CR from 1.7 to 1.0 N when counting the cracks after 35 s and 24 h, respectively. The similar pattern is found when changing the humidity instead of the time between indentation and crack counting. Increased humidity increases the crack initiation dramatically, resulting in decreasing crack resistance. The effect of

increasing humidity depends on the applied indentation load. For low load (<1 N), the residual stress around the indents is low and often insufficient to facilitate the pop-in of a crack. At high loads (>5 N) the crack initiation probability is very high regardless of humidity, as the applied stress is sufficiently high to facilitate cracking.The largest effect of increased humidity is found in the intermediate load range (1-5 N), where the crack initiation probability can be increased by >20 percentage points when comparing high- to low-humidity conditions as an effect of the hydrolysis reaction [159,192]. When increasing the humidity, the crack resistance decrease from 2.5 to 1.7 N and 1.4 to 1.0 N when cracks have been counted after 35 s and 24 h, respectively.

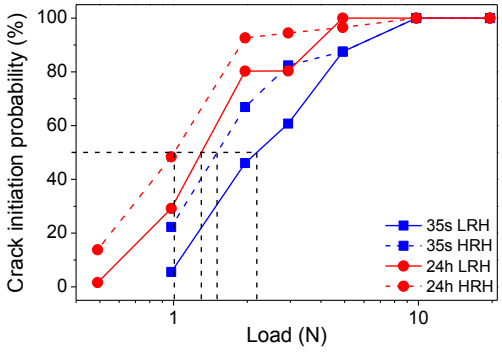

Figure 23. Crack initiation probability for the $67.5SiO_2$-$12.5Al_2O_3$-20CaO (mol%) composition at low relative humidity (LRH) (full line) and high relative humidity (HRH) (dashed line) after 35 s (blue line) and 24 h (red line). Figure taken from Paper VI.

To understand the time dependence of the crack initiation, the pop-in of cracks were counted continuously for several hours (Figure 24). We find that the rate of cracks initiation is highest within the first seconds and minutes, but a substantial amount of cracks continue to initiate minutes and hours after indentation. An example is the curve for the 0.98 N load (full red line) under the low humidity conditions. The number of cracks after 24 h has more than doubled compared to the initial few seconds. A similar behavior is also found for the same indentation load at higher humidity (dashed red line) and for other loads.

Independent of load and humidity, the crack initiation rate decreases with time. The crack initiation probability rate is high within the first ~300 s after indentation and most of the crack initiation occurs within the first 3 h, more or less in agreement with the cease of crack initiation found by Scannell *et al.* [175]. However, crack initiation was observed after more than 19 h and when revisiting the indents 1.5 year after indentation several additional cracks had formed. The decrease in crack initiation rate with time is directly related to the stress release after the initiation of new cracks and the depletion of uncracked indent corners.

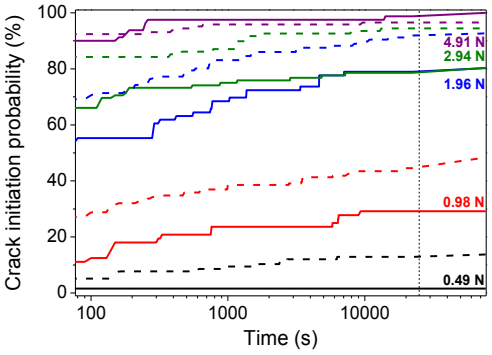

Figure 24. Crack initiation probability determined at up to 24 h after indentation at various load and humidity for the $67.5SiO_2$-$12.5Al_2O_3$-20CaO glass. The applied loads are 0.49 (black), 0.98 (red), 1.96 (blue), 2.94 (green), and 4.91 N (purple). The data are obtained under both low (solid lines) and high (dashed) relative humidity conditions. The continuous data collected was stopped after 22,000 s and therefore the crack initiation probability between 22,200 (vertical dashed line) and 76,500 s has been extrapolated. Figure taken from Paper VI.

Indentation crack resistance is becoming an increasingly popular method to compare the resistance to surface damage among different glass compositions. However, the data highlight the importance of a rigorous control of the experimental conditions, namely the humidity and the time between indentation and crack counting. Currently, cracks are counted after different time across research groups and the effect of humidity (either due to geographical location, time of year, or even the local weather during an experiment) will highly affect the crack resistance values, as the humidity will fluctuate accordingly. Therefore, we recommend that standardized protocols must be developed, ideally involving measurements of crack resistance at a controlled humidity.

Our results also suggest that cracks should not be counted within the first 5 min, as small variations in the time between t_0 and the time of crack counting will result in an erroneous determination of crack initiation probability and crack resistance. It appears that 3 h is a more appropriate minimum waiting time between indentation and crack counting, but for practical purposes, a waiting period of 24 h might be the best option. In addition to time and humidity, the chemical composition of the glass also needs to be considered, as the reactivity between atmospheric water and glass greatly depends on the type of network former.

4.2. EFFECT OF DENSIFICATION ON HARDNESS AND CRACK RESISTANCE

Surface damage is the Achilles heel of glass display screens for portable electronic devices. An approach to understand the underlying structural origin of a glass being resistant to cracking is hot compression, in which the glass sample is simultaneously

exposed to high pressure and high temperature around T_g [45–47,182,193]. The relatively low viscosity at high temperature results in large structural changes in e.g. coordination number of network cations. The structural changes occurring during hot compression are often comparable to those obtained during real-life surface damage and at the same time enable preparation of bulk samples (unlike, e.g., diamond anvil cell densification experiments). This enables ex-situ analyses of the structural change by e.g. Raman and NMR spectroscopy, facilitating an improved understanding of the compositional and structural origins of mechanical properties [23].

Two of the relevant mechanical properties are Vickers hardness and crack resistance of the glasses. During indentation, the glass deforms through three different deformation mechanisms: elastic deformation, densification, and shear flow. In Paper I, to understand the effect of pressure on the mechanical properties, we choose a sodium aluminosilicate series with varying NBO/T ratio ($25Na_2O$-xAl_2O_3-$(75-x)SiO_2$. with x = 0, 5, 10, 15, 20, and 25). During indentation all three deformation mechanisms occur. Initially, the response is purely elastic. Then both densification of the glass volume beneath the indenter tip and pile-up caused by shear flow occur. For uncompressed samples, the hardness increases with increasing Al_2O_3 content, as a result of the reduction in the NBO/T ratio [194] (Figure 25). The network rigidity increases as a results of incorporation of Al^{3+} tetrahedra in the network structure, which increase the resistance against elastoplastic deformation [195].

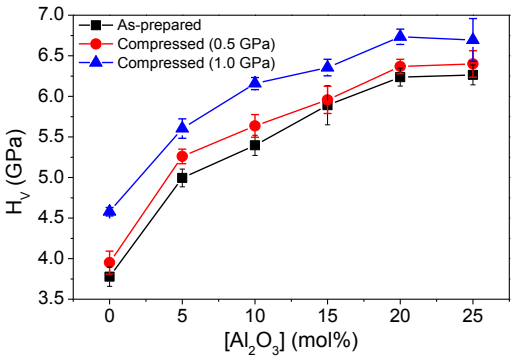

Figure 25. Vickers hardness (H_V) measured at an indentation load of 0.98 N for as-prepared and compressed glasses in the $25Na_2O$-xAl_2O_3-$(75-x)SiO_2$ system as a function of Al_2O_3 content. Figure taken from Paper I.

After a HP/HT treatment, the hardness is increased for all compositions (Figure 25). The deformation occurring under the indenter tip still cover all three deformation mechanisms, but due to the 'pre-densification' occurring during the HP/HT

treatment, the volume available for densification during indentation is decreased. This is manifested as an increase in hardness, as the ability to deform has decreased [173].

While hardness is negatively influenced by the presence of NBOs for these sodium aluminosilicate glasses, the tendency for cracks to initiate is lower in more flexible glasses. Thus, the crack resistance decreases with increasing Al/Na ratio and increasing rigidity (Figure 6). The flexible compositions with many NBOs easily densify, leading to lower residual stress around the indents. This results in a low driving force for crack initiation and a high crack resistance. The resistance to densification in rigid low-NBO compositions leads to higher residual stress, high crack initiation, and low crack resistance [177]. The crack initiation has previously been attributed to a mismatch between the plastically deformed volume and the surrounding elastically deformed matter [178,196,197]. In the compressed samples, the ability to densify and dissipate stress has been reduced. This limits the ability to further deform during subsequent indentation, resulting in higher residual stress and decreasing crack resistance for all compositions[173,177].It is clear from the crack resistance data that high crack resistance is intimately related to the ability of the glass to adapt through structural change and densification [23].

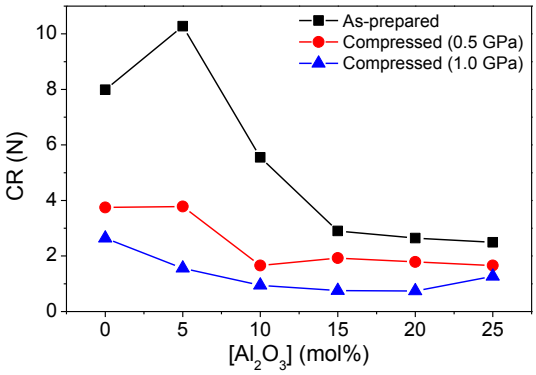

Figure 26. Crack resistance (CR) of the as-prepared and compressed glasses in the $25Na_2O$-xAl_2O_3-$(75-x)SiO_2$ (mol%) system as a function of Al_2O_3 content. Hot compression results in decreasing CR for all glasses. Figure taken from Paper I.

4.3. EFFECT OF DENSIFICATION ON PHOTOELASTICITY

Oxide glasses are well-known for their light transparency, which is exploited in windows, lightbulbs, display screens, solar-energy glass, microscopes etc. For most of these applications, the optical pathway of light through the glass is less important, but for, e.g., the microscope glass, rigorous control of refractive index and specimen shape is essential for its application. Another example is the optical response of the

glass to elastic strain, known as the photoelastic effect. Glasses are random networks that are inherently isotropic due to their lack of long-range order. However, under a deviatoric stress, glass can exhibit an anisotropic response, including optical birefringence, which can lead to undesired rotations of polarized light in the glass. This is of importance for, e.g., display glasses [198–200] and fiber current sensors [201] to maintain the color rendering or sensing properties [202]. The magnitude of stress-induced optical birefringence is quantified by the proportionally constant between applied stress and birefringence, the stress optic coefficient (*C*):

$$\delta = C\sigma l, \tag{9}$$

where δ is the difference in the optical path length for light polarization along the stress axis and the orthogonal direction, σ is the applied uniaxial stress, and l is the sample thickness.

The major component in silicate glasses, SiO_2, has a relatively large positive *C* value of $+3.5 \times 10^{-12}\,Pa^{-1}$, which is a problem for advanced optical applications [16,198,201,203]. Other typical components (e.g., Na_2O and CaO) can decrease *C*, but not sufficiently to reduce *C* to zero to avoid birefringence. Instead, PbO have typically been added to counter-balance the *C* contribution from SiO_2, as the electronic structure of Pb^+ contributes to decrease *C* substantially [204–206].However, recent legislation aims at reducing the presence of lead, as it has large negative effect on both health and environment. This has motivated research in the compositional and structural origins of the photoelastic response [198,207,208], leading to the discovery of new lead-free glass compositions, exhibiting zero-stress optic response when strained anisotropically [198,206,208–212].

The stress optic coefficient is controlled by the structural response of the glass to anisotropic stress. If the chemical bonds in the glass are highly directional, such as the low-coordinated Si^{4+} species, the glass tends to distort anisotropically, while the more highly coordinated modifier ions can be distorted isotropically. Furthermore, the less directional metallic bonds can be distorted in both the direction of the anisotropic stress and in the orthogonal direction.

Aiming at developing a predictive model for photoelasticity, Zwanziger and co-workers [198] used the relations between distortion mechanisms and bonding types. Relating these through the cation-anion bond length (d) and the cation coordination number (N_c) of the glass components, Zwanziger and co-workers proposed an empirical model, stating that glasses exhibiting no photoelastic effect have a d/N_c ratio of approximately 0.5 Å. Negative birefringence occurs for d/N_c ratios > 0.5 Å and positive values occur when the d/N_c ratio is < 0.5 Å. By studying the glass structure in detail using both simulations [30,213] and experimental structural probes [206–208,213,214], the model has shown good qualitative agreement with data [198].

In Paper VII we investigated if the structural and topological basis for the empirical by using hot compression to alter the glass structure. As discussed in Paper VII, the model cannot accurately predict the change in C when a glass is hot compressed, suggesting that changes must be made to the empirical model. Recent studies describe how hot compression results in changes in both bond length and coordination numbers.The coordination numbers of network formers, such as boron [45–47] and aluminum [48–50,182] has been found to increase, while hot compression does not impact the coordination number of modifiers [45]. The bond length of modifier-oxygen bonds decreases [45,46,49,50,215], while the increasing coordination numbers of the network-forming cations [48,50,182,216] should increase the bond length, in order to accommodate the higher-coordinated species in the coordination sphere. Overall, the hot compression is expected in result in decreasing d and increasing N_c. This results in a decrease in the d/N_c ratio and therefore an expected increase in C following the Zwanziger model. However, hot compression of ten aluminosilicate glasses show that C always increases.

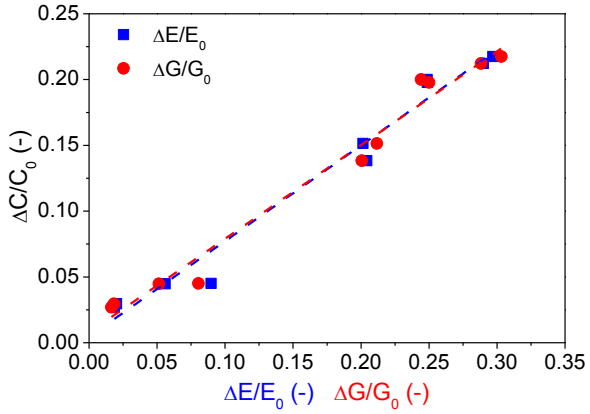

Figure 27. Pressure-induced relative change in stress optic coefficient ($\Delta C/C_0$) as a function of pressure-induced relative change in both Young's ($\Delta E/E_0$) and shear ($\Delta G/G_0$) moduli. Figure taken from Paper VII.

As the Zwanziger model cannot account for the observed change in C, the origin of the increase in C might be related to the pressure-induced change in elastic moduli, as a recent study showed that birefringence is related to the resistance of a material to elastic shear deformation [217]. Both the Young's and the shear modulus are found to increase approximately linearly with C (Figure 27). Following its definition, C is a function of shear modulus (G) through therelation [1],

$$C = \frac{n^3}{4G}(p_{12} - p_{11}). \qquad (10)$$

where p_{12} and p_{11} are the Pockels strain-optical coefficients and n is the refractive index. The Pockels strain-optical coefficients describe the response of the glass when strained.

From experimental data of shear modulus, refractive index, and stress optic coefficient, we can easily determine the sum of the Pockels strain-optical coefficients using Eq. (10) and find that the effect of hot compression on (p_{12}-p_{11}) is negligible (Figure 28). The magnitude of the Pockels strain coefficients are hardly affected by the hot compression.

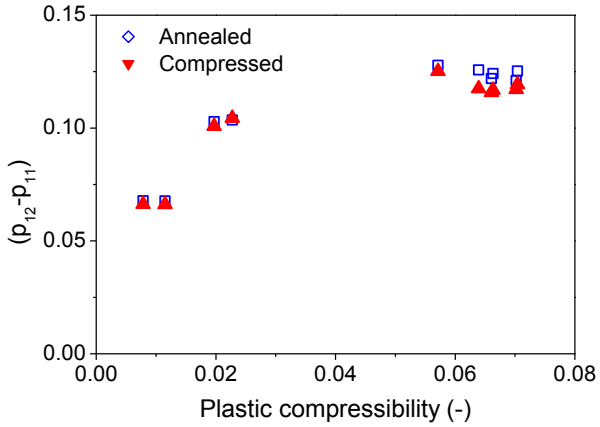

Figure 28. The sum of the Pockel's strain-optical coefficients of as-prepared and compressed glasses as a function of the plastic compressibility, which is the relative volume (V) change measured after hot compression described by $-(1/V)(\mathrm{d}V/\mathrm{d}p)$. The strain-optical coefficients are calculated from Eq. (10) using stress optic coefficient and refractive index values obtained from experiments. Figure modified from Paper VII.

As the Pockels strain-optical coefficients are approximately unaffected by pressure, the change in C cannot be explained by structural change nor by Zwanziger's model. As the pressure-induced change in refractive index is also small (not shown), the only major property change in Eq. (10) is in the shear modulus. The pressure-induced decrease in C must therefore primarily be governed by the increase in shear modulus according to Eq. (10). By considering the C and G values for the studied aluminosilicate glasses, we find a linear relationship (R^2=0.997) between C and G for both uncompressed and compressed glasses for G values below 30 GPa (Figure 29). This relationship can be rationalized by the glasses having similar compositions and therefore all glasses have approximately identical Pockels strain-optical coefficients. Thus, they will behave similarly when strained. The extent of the strain is mostly controlled by elastic moduli; hence, the stress-optic coefficient will be controlled by the shear modulus. The two glass compositions with G values around 41-43 GPa stand out by having a high modifier content. The high modifier content

(>50 mol%) acts to increase the shear modulus, but also introduces a higher ability to distort isotropically. This results in decreasing Pockels strain-optical coefficients (seen in Figure 28), changing the proportionality between *C* and *G*. In summary, the Zwanziger model cannot predict the effect of hot compression on the stress optic coefficient, as the magnitude of *C* is largely dependent on the shear modulus.

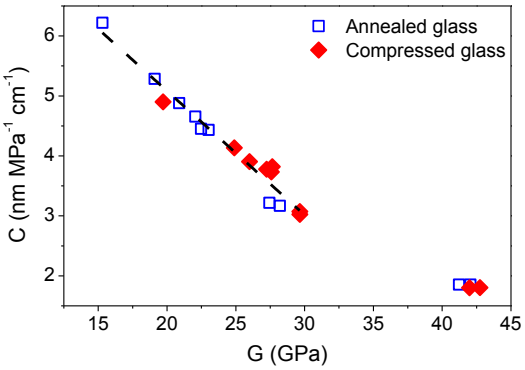

Figure 29. The relationship between the stress optic coefficient (*C*) andthe shear modulus (*G*) for both annealed (not-compressed) and compressed glasses. The dashed line (R^2 = 0.997) represent the linear fit to the dependence of *C* on *G* for the glasses with similar Pockels strain-optical coefficients. The remaining two compositions do not match the linear fit as they have vastly different Pockels strain-optical coefficients compared to the remaining eigth compositions. Figure taken from Paper VII.

CHAPTER 5. GENERAL DISCUSSION AND PERSPECTIVE

Aluminosilicate glasses form the basis for a wide variety of industrial glass products. Understanding their composition-structure-property relations is important, as it can allow prediction of properties directly from the chemical composition. This enables tailoring the glass properties to match specific applications. In this Ph.D. thesis, we have investigated various composition-structure-property relations in aluminosilicate glasses.

In the study of aluminosilicate glass structure, we found links between the field strength of modifier cation and the fraction of various structural units. For example, we found a violation of both the standard model for aluminum coordination and Al-avoidance depending on the modifier cations. We argued that both violations are positively correlated to the field strength and valence of the modifiers. Understanding the rheological properties of glasses and glass-forming melts is based on understanding this intimate relationship between composition and structure.

A universal understanding of all types of relaxation in glass is important for many optical applications. The volume relaxation is especially important for producers of display screens. Studying the relationship between configurational heat capacity and liquid fragility is relevant, due to the possible proportionality between configurational heat capacity and volume relaxation. Therefore, a full understanding of relations between these properties can enable prediction of volume relaxation directly from fragility. We found good agreement between model predictions of configurational heat capacity from fragility and experimental data. However, a better understanding of this relationship is needed to use it actively in the design of glass compositions with minimal relaxation during re-heating.

To the best of our knowledge, this thesis is the first to use high-temperature temperature-modulated differential scanning calorimetry (TM-DSC) to oxide glasses. TM-DSC is a promising technique to study the dynamic behavior of these materials at high-temperature, as it, compared to standard DSC, provides superior sensitivity. We have developed experimental protocols for this technique, which effectively expands the range of glass compositions that are available for temperature modulated analysis, enabling a deeper understanding of, e.g., relaxation effects in glasses. The potential applications of TM-DSC include the study of relaxation and crystallization under isothermal conditions at high temperature and quantification and separation of thermal events in hyper-quenched mineral fibers.

Understanding the humidity and time dependence of crack initiation is important for industrial producers of damage-resistant glasses, as their products are used in humid

environments. As expected, we found a higher tendency for cracks to initiate in a humid environment and after longer time. A better understanding of the mechanism of water-assisted initiation of cracks in glass and its relationship with the glass composition will help improve the design of crack-resistant aluminosilicate glasses. Our results also give insight to the kinetics of frangibility determination [218], as the experiment requires delayed fracture as a result of internally stored energy.

For a range of optical applications, tailoring of the photoelastic properties through glass composition design is needed. Understanding this composition-property relationship is important for discovering new glass compositions with a minimized photoelastic effect. Currently the photoelastic effect is predicted from the glass structure through coordination numbers and bond lengths. We showed that this empirical model was unable to predict the effect of the structural changes associated with hot compression on the photoelastic effect. Consequently, the model is insufficient in predicting the photoelastic effect for aluminosilicate glasses. To improve the development of zero-stress optic glasses, a model with a physical basis must be developed. For example, understanding the effect of compression on photoelasticity affects the determination of compressive stress in ion exchange glasses. We showed that the substitution of cations during ion exchange hardly changes the photoelastic properties. We also highlighted the pressure-induced change in shear modulus, which must be known in order to determine surface compressive stress in ion-exchanged glasses. Without an accurate quantification of the change in shear modulus during ion-exhange, the determined surface compressive stress may be artificially high.

CHAPTER 6. CONCLUSION

The topic of this thesis has been to study the composition-structure-property relations in industrial relevant aluminosilicate glasses. Common for all our studies is the desire to understand the interplay between composition, structure, and properties in order to accelerate the design of glass compositions for high-tech applications through the ability to predict properties from either composition and/or structure.

The glass structure is controlled by its chemical composition and thermal and pressure history. We have investigated the structural dependence on the modifier cations in aluminosilicate glasses with various amounts of sodium, calcium, and magnesium using both Raman and nuclear magnetic resonance spectroscopy. We found strong correlations between the field strength of the modifier and the presence of 'forbidden' structural units, namely Al^V in peralkaline compositions and Al-O-Al linkages. In glasses containing divalent calcium or magnesium, Al-O-Al linkages were detected by Raman spectroscopy, suggesting that the high field strength modifiers have an excellent charge-stabilizing ability. The higher field strength of magnesium over calcium leads to the appearance of Al-O-Al linkages at lower modifier concentration and probably also in higher concentration. From NMR spectroscopy, we found evidence of unexpected five-coordinated aluminum (Al^V) in peralkaline sodium aluminosilicate glasses and found the concentration of Al^V to increase after hot compression. This change in the pressure history causes an increase in Al^V for highly peralkaline glasses only, emphasizing the role of NBOs in the formation of higher coordinated aluminum species.

The compositional and structural origins of relaxation in glass are not fully understood. We have investigated the relationship between the configurational heat capacity and fragility, due to the expected relationship with volume relaxation. We found that the investigated model predicts configurational heat capacity from fragility reasonably well with some discrepancies. The scaling factor between these two quantities appears to be composition dependent, but more studies are needed to achieve a deeper understanding of the relationship.

A different approach to study relaxation is through measuring the non-reversing heat capacity from temperature-modulated differential scanning calorimetry. This technique was hitherto limited to low temperature (< 600°C). In order to use the TM-DSC for relaxation studies, we first developed an experimental protocol for the use of TM-DSC at high temperature. Our results highlight the challenges and importance of ensuring a sufficiently high signal-to-noise ratio through high amplitudes (5 K). Furthermore, we have shown that for glasses with intermediate

fragility values (m = 30-50) the underlying heating rate should be ~2 K/min. For strong compositions with high glass transition temperatures, the underlying heating rates can be increased up to 5-7 K/min.

Using this experimental protocol for TM-DSC, we successfully determined liquid fragility of oxide glasses. The technique has an accuracy, which is comparable to the Moynihan approach for calorimetric determination of fragility, while the error is smaller due to an easier and more reliable determination of characteristic temperature. However, there is a tendency for under- and overestimation of the m values for fragile and strong compositions, respectively, using this technique. A correction of the calorimetric fragility values is presumably needed, but requires a larger pool of fragility values determined by TM-DSC.

We have also used the TM-DSC method to determine the non-reversing heat flow of a series of tectosilicate calcium aluminosilicate glasses in order to investigate non-aging compositions in the so-called reversibility window. We also compared the data to molecular dynamics simulations of identical glasses. We find minima in non-reversing heat flow in both experiments and simulations, indicating some correlation between the number of topological constraints and the non-reversing heat capacity.

The mechanical properties of aluminosilicates are also very important for their high-tech applications. It is, for example, essential to prevent the propensity of the display glasses to form strength-limiting cracks. To achieve a better understanding of environmental effects, we quantified the load-time-humidity dependence of the initiation of cracks in aluminosilicate glasses. Increasing the time and humidity will both increase the propensity of cracks to initiate and therefore affect the crack resistance negatively. Our results highlight how experimental conditions affect apparent glass properties. Therefore, when using the crack resistance methodology as a probe of damage-resistant glasses, we have suggested the use of a standardized experimental protocol.

Finally, we have evaluated Zwanziger's model of photoelasticity in glass. The model suggests that photoelasticity can be predicted from the average coordination numbers and bond lengths in the glass. As such, the model predicts that the structural change occurring as a results of hot compression will results in an increase in the stress optic coefficient. However, hot compression results in a decrease in the stress optic coefficient. We argue that the empirical model must be revised and in order to fully understand the phenomenon of photoelasticity, a revised model with a basis in physics should be developed.

BIBLIOGRAPHY

[1] A.K. Varshneya, Fundamentals of Inorganic Glasses, Elsevier, 2011.

[2] J.E. Shelby, Introduction to Glass Science and Technology, 2nd ed., The Royal Society of Chemistry, Cambridge, 2005.

[3] J.C. Mauro, E.D. Zanotto, Two Centuries of Glass Research: Historical Trends, Current Status, and Grand Challenges for the Future, Int. J. Appl. Glas. Sci. 5 (2014) 313–327.

[4] O. Gulbiten, J.C. Mauro, X. Guo, O.N. Boratav, Viscous flow of medieval cathedral glass, J. Am. Ceram. Soc. 101 (2018) 5–11.

[5] A.J. Ellison, I.A. Cornejo, Glass Substrates for Liquid Crystal Displays, Int. J. Appl. Glas. Sci. 1 (2010) 87–103.

[6] G.N. Greaves, S. Sen, Inorganic glasses, glass-forming liquids and amorphizing solids, Adv. Phys. 56 (2007) 1–166.

[7] J.F. Willart, A. De Gusseme, S. Hemon, G. Odou, F. Danede, M. Descamps, Direct crystal to glass transformation of trehalose induced by ball milling, Solid State Commun. 119 (2001) 501–505.

[8] M. Tatsumisago, S. Hama, A. Hayashi, H. Morimoto, T. Minami, New lithium ion conducting glass-ceramics prepared from mechanochemical Li_2S-P_2S_5 glasses, Solid State Ionics. 154–155 (2002) 635–640.

[9] E.D. Zanotto, J.C. Mauro, The glassy state of matter: Its definition and ultimate fate, J. Non. Cryst. Solids. 471 (2017) 490–495.

[10] E.D. Zanotto, Do cathedral glasses flow?, Am. J. Phys. 66 (1998) 392–395.

[11] E.D. Zanotto, Do cathedral glasses flow?—Additional remarks, Am. J. Phys. 67 (1999) 260.

[12] R.C. Welch, J.R. Smith, M. Potuzak, X. Guo, B.F. Bowden, T.J. Kiczenski, D.C. Allan, E.A. King, A.J. Ellison, J.C. Mauro, Dynamics of glass relaxation at room temperature, Phys. Rev. Lett. 110 (2013) 1–4.

[13] M.O.J.Y. Hunault, V. Vinel, L. Cormier, G. Calas, Thermodynamic insight into the evolution of medieval glassworking properties, J. Am. Ceram. Soc. 100 (2017) 2363–2367.

[14] Q. Zheng, J.C. Mauro, Variability in the relaxation behavior of glass: Impact of thermal history fluctuations and fragility, J. Chem. Phys. 146 (2017) 074504.

[15] Y. Yu, M. Wang, D. Zhang, B. Wang, G. Sant, M. Bauchy, Stretched Exponential Relaxation of Glasses at Low Temperature, Phys. Rev. Lett. 115 (2015) 1–5.

[16] Y.S. Choi, J.U. Yun, S.E. Park, Flat panel display glass : Current status and future, J. Non. Cryst. Solids. 431 (2016) 2–7.

[17] M. Potuzak, R.C. Welch, J.C. Mauro, Topological origin of stretched exponential relaxation in glass, J. Chem. Phys. 135 (2011) 214502.

[18] J.C. Mauro, C.S. Philip, D.J. Vaughn, M.S. Pambianchi, Glass science in the United States: Current status and future directions, Int. J. Appl. Glas. Sci. 5 (2014) 2–15.

[19] L. Wondraczek, J.C. Mauro, J. Eckert, U. Kühn, J. Horbach, J. Deubener, T.

Rouxel, Towards ultrastrong glasses, Adv. Mater. 23 (2011) 4578–4586.
[20] C. Brodmann, Einige Beobachtungen über die Festigkeit von Glasstäben, Nachrichten von Der Gesellschaft Der Wissenschaften Zu Göttingen, Math. Klasse. 1894:1 (1895).
[21] A. Tandia, K.D. Vargheese, J.C. Mauro, A.K. Varshneya, Atomistic understanding of the network dilation anomaly in ion-exchanged glass, J. Non. Cryst. Solids. 358 (2012) 316–320.
[22] K. Januchta, R.E. Youngman, A. Goel, M. Bauchy, S.J. Rzoska, M. Bockowski, M.M. Smedskjaer, Structural origin of high crack resistance in sodium aluminoborate glasses, J. Non. Cryst. Solids. 460 (2017) 54–65.
[23] K. Januchta, R.E. Youngman, A. Goel, M. Bauchy, S.L. Logunov, S.J. Rzoska, M. Bockowski, L.R. Jensen, M.M. Smedskjaer, Discovery of Ultra-Crack-Resistant Oxide Glasses with Adaptive Networks, Chem. Mater. 29 (2017) 5865–5876.
[24] J.C. Mauro, M.M. Smedskjaer, Unified physics of stretched exponential relaxation and Weibull fracture statistics, Phys. A Stat. Mech. Its Appl. 391 (2012) 6121–6127.
[25] M. Bauchy, Structural, vibrational, and elastic properties of a calcium aluminosilicate glass from molecular dynamics simulations: The role of the potential, J. Chem. Phys. 141 (2014) 024507.
[26] B.O. Mysen, P. Richet, Silicate glasses and melts: Properties and structure, 1st ed., Elsevier Science, Amsterdam, 2005.
[27] Q. Zheng, M. Potuzak, J.C. Mauro, M.M. Smedskjaer, R.E. Youngman, Y. Yue, Composition–structure–property relationships in boroaluminosilicate glasses, J. Non. Cryst. Solids. 358 (2012) 993–1002.
[28] M.J. Toplis, D.B. Dingwell, T. Lenci, Peraluminous viscosity maxima in Na2O-Al2O3-SiO2 liquids: The role of triclusters in tectosilicate melts, Geochim. Cosmochim. Acta. 61 (1997) 2605–2612.
[29] M.M. Smedskjaer, L. Huang, G. Scannell, J.C. Mauro, Elastic interpretation of the glass transition in aluminosilicate liquids, Phys. Rev. B - Condens. Matter Mater. Phys. 85 (2012) 1–10. doi:10.1103/PhysRevB.85.144203.
[30] M.M. Smedskjaer, S. a. Saxton, A.J. Ellison, J.C. Mauro, Photoelastic response of alkaline earth aluminosilicate glasses, Opt. Lett. 37 (2012) 293.
[31] R. Kerner, J.C. Phillips, Quantitative principles of silicate glass chemistry, Solid State Commun. 117 (2000) 47–51.
[32] J.R.G. Da Silva, D.G. Pinatti, C.E. Anderson, M.L. Rudee, A refinement of the structure of vitreous silica, Philos. Mag. 31 (1975) 713–717.
[33] P.F. McMillan, B.T. Poe, P. Gillet, B. Reynard, A study of SiO_2 glass and supercooled liquid to 1950 K via high-temperature Raman spectroscopy, Geochim. Cosmochim. Acta. 58 (1994) 3653–3664.
[34] R.F. Pettifer, R. Dupree, I. Farnan, U. Sternberg, NMR determinations of Si-O-Si bond angle distributions in silica, J. Non. Cryst. Solids. 106 (1988) 408–412.
[35] S. Kohara, K. Suzuya, Intermediate-range order in vitreous SiO_2 and GeO_2, J. Phys. Condens. Matter. 17 (2005) S77.
[36] J.P. Rino, I. Ebbsjö, R.K. Kalia, A. Nakano, P. Vashishta, Structure of rings

in vitreous SiO_2, Phys. Rev. B. 47 (1993) 3053–3062.

[37] D.E. Day, G.E. Rindone, Properties of Soda Aluminosilicate Glasses: II, Internal Friction, J. Am. Ceram. Soc. 45 (1962) 489–496.

[38] D.A. McKeown, F.L. Galeener, G.E. Brown Jr., Raman studies of Al coordination in silica-rich sodium aluminosilicate glasses and some related minerals, J. Non. Cryst. Solids. 68 (1984) 361–378.

[39] M. Taylor, G.E. Brown, Structure of mineral glasses-II. The SiO_2-$NaAlSiO_4$ join, Geochim. Cosmochim. Acta. 43 (1979) 1467–1473.

[40] P.F. McMillan, B. Piriou, A. Navrotsky, A Raman Spectroscopic Study of Glasses Along the Join Silica-Calcium Aluminate, Silica-Sodium Aluminate, and Silica-Potassium Aluminate, Geochim. Cosmochim. Acta. 46 (1982) 2021–2037.

[41] F.A. Seifert, B.O. Mysen, D. Virgo, Three-dimensional network structure of quenched melts (glass) in the systems SiO_2-$NaAlO_2$, SiO_2-$CaAl_2O_4$ and SiO_2-$MgAl_2O_4$, Am. Mineral. 67 (1982) 696–717.

[42] D.R. Neuville, L. Cormier, D. Massiot, Al environment in tectosilicate and peraluminous glasses: A ^{27}Al MQ-MAS NMR, Raman, and XANES investigation, Geochim. Cosmochim. Acta. 68 (2004) 5071–5079.

[43] S. Sen, R.E. Youngman, High-resolution multinuclear NMR structural study of binary aluminosilicate and other related glasses, J. Phys. Chem. B. 108 (2004) 7557–7564.

[44] W.J. Malfait, R. Verel, P. Ardia, C. Sanchez-Valle, Aluminum coordination in rhyolite and andesite glasses and melts: Effect of temperature, pressure, composition and water content, Geochim. Cosmochim. Acta. 77 (2012) 11–26.

[45] M.M. Smedskjaer, R.E. Youngman, S. Striepe, M. Potuzak, U. Bauer, J. Deubener, H. Behrens, J.C. Mauro, Y. Yue, Irreversibility of pressure induced boron speciation change in glass., Sci. Rep. 4 (2014) 3770.

[46] M.N. Svenson, T.K. Bechgaard, S.D. Fuglsang, R.H. Pedersen, A.O. Tjell, M.B. Østergaard, R.E. Youngman, J.C. Mauro, S.J. Rzoska, M. Bockowski, M.M. Smedskjaer, Composition-Structure-Property Relations of Compressed Borosilicate Glasses, Phys. Rev. Appl. 2 (2014) 1–9.

[47] M.B. Østergaard, R.E. Youngman, M.N. Svenson, S.J. Rzoska, M. Bockowski, L.R. Jensen, M.M. Smedskjaer, Temperature-dependent densification of sodium borosilicate glass, RSC Adv. 5 (2015) 78845–78851.

[48] S.K. Lee, G.D. Cody, Y. Fei, B.O. Mysen, Nature of polymerization and properties of silicate melts and glasses at high pressure, Geochim. Cosmochim. Acta. 68 (2004) 4189–4200.

[49] J.R. Allwardt, J.F. Stebbins, B.C. Schmidt, D.J. Frost, A.C. Withers, M.M. Hirschmann, Aluminum coordination and the densification of high-pressure aluminosilicate glasses, Am. Mineral. 90 (2005) 1218–1222.

[50] J. Wu, J. Deubener, J.F. Stebbins, L. Grygarova, H. Behrens, L. Wondraczek, Y. Yue, Structural response of a highly viscous aluminoborosilicate melt to isotropic and anisotropic compressions, J. Chem. Phys. 131 (2009) 1–10.

[51] L.M. Thompson, J.F. Stebbins, Non-stoichiometric non-bridging oxygens and five-coordinated aluminum in alkaline earth aluminosilicate glasses: Effect of modifier cation size, J. Non. Cryst. Solids. 358 (2012) 1783–1789.

[52] M.J. Toplis, S.C. Kohn, M.E. Smith, I.J.F. Poplett, Fivefold-coordinated aluminum in tectosilicate glasses observed by triple quantum MAS NMR, Am. Mineral. 85 (2000) 1556–1560.

[53] A. Navrotsky, H.D. Zimmermann, R.L. Hervig, Thermochemical study of glasses in the system $CaMgSi_2O_6$-$CaAl_2SiO_6$, Geochim. Cosmochim. Acta. 47 (1983) 1535–1538.

[54] M. Li, B.N. Roy, A. Navrotsky, Thermochemistry of Charge-Coupled Substitutions in Silicate Glasses: The Systems $M_{1/n}^{n+}AlO_2$-SiO_2 (M = Li, Na, K, Rb, Cs, Mg, Ca, Sr, Ba,Pb), J. Am. Ceram. Soc. 67 (1984) 606–610.

[55] L. Cormier, D. Ghaleb, D.R. Neuville, J.-M. Delaye, G. Calas, Chemical dependence of network topology of calcium aluminosilicate glasses: A computer simulation study, J. Non. Cryst. Solids. 332 (2003) 255–270.

[56] D.R. Neuville, L. Cormier, A. Flank, V. Briois, D. Massiot, Al speciation and Ca environment in calcium aluminosilicate glasses and crystals by Al and Ca K-edge X-ray absorption spectroscopy, Chem. Geol. 213 (2004) 153–163.

[57] L. Cormier, G.J. Cuello, Mg coordination in a $MgSiO_3$ glass using neutron diffraction coupled with isotopic substitution, Phys. Rev. B - Condens. Matter Mater. Phys. 83 (2011) 1–8.

[58] Y. Tabira, Local structure around oxygen atoms in $CaMgSi_2O_6$ glass by O K-edge EXELFS, Mater. Sci. Eng. B. 41 (1996) 63–66.

[59] D. Li, M. Peng, T. Murata, Coordination and local structure of magnesium in silicate minerals in glasses: Mg K-Edge XANES study, Can. Mineral. 37 (1999) 199–206.

[60] S. Kroeker, J.F. Stebbins, Magnesium coordination environments in glasses and minerals: New insight from high-field magnesium-25 MAS NMR, Am. Mineral. 85 (2000) 1459–1464.

[61] M.C. Wilding, C.J. Benmore, J.A. Tangeman, S. Sampath, Evidence of different structures in magnesium silicate liquids: Coordination changes in forsterite- to enstatite-composition glasses, Chem. Geol. 213 (2004) 281–291.

[62] K. Shimoda, Y. Tobu, M. Hatakeyama, T. Nemoto, K. Koji Saito, Structural investigation of Mg local environments in silicate glasses by ultra-high field ^{25}Mg 3QMAS NMR spectroscopy, Am. Mineral. 92 (2007) 695–698.

[63] K. Shimoda, T. Nemoto, K. Saito, Local structure of magnesium in silicate glasses: A ^{25}Mg 3QMAS NMR study, J. Phys. Chem. B. 112 (2008) 6747–6752.

[64] M. Guignard, L. Cormier, Environments of Mg and Al in MgO-Al_2O_3-SiO_2 glasses: A study coupling neutron and X-ray diffraction and Reverse Monte Carlo modeling, Chem. Geol. 256 (2008) 110–117.

[65] N. Trcera, D. Cabaret, S. Rossano, F. Farges, A.-M. Flank, P. Lagarde, Experimental and theoretical study of the structural environment of magnesium in minerals and silicate glasses using X-ray absorption near-

edge structure, Phys. Chem. Miner. 36 (2009) 241–257.
[66] M.M. Smedskjaer, J.C. Mauro, Y. Yue, Ionic diffusion and the topological origin of fragility in silicate glasses, J. Chem. Phys. 131 (2009) 1–9.
[67] D.R. Neuville, L. Cormier, D. Massiot, Al coordination and speciation in calcium aluminosilicate glasses: Effects of composition determined by ^{27}Al MQ-MAS NMR and Raman spectroscopy, Chem. Geol. 229 (2006) 173–185.
[68] E. Lacy, Aluminum in glasses and melts, Phys. Chem. Glas. 4 (1963) 234–238.
[69] D. Iuga, C. Morais, Z. Gan, D.R. Neuville, L. Cormier, D. Massiot, NMR heteronuclear correlation between quadrupolar nuclei in solids, J. Am. Chem. Soc. 127 (2005) 11540–11541.
[70] C. Le Losq, D.R. Neuville, P. Florian, G.S. Henderson, D. Massiot, The role of Al^{3+} on rheology and structural changes in sodium silicate and aluminosilicate glasses and melts, Geochim. Cosmochim. Acta. 126 (2014) 495–517.
[71] S.A. Brawer, W.B. White, Raman Spectroscopic Investigation of the Structure of Silicate Glasses (II). Soda-Alkaline Earth-Alumina Ternary and Quaternary Glasses, J. Non. Cryst. Solids. 23 (1977) 261–278.
[72] W. Loewenstein, The distribution of aluminum in the tetrahedra of silicates and aluminates., Am. Mineral. 39 (1954) 92–96.
[73] S.K. Lee, J.F. Stebbins, The degree of aluminum avoidance in aluminum silicate glasses, Am. Mineral. 84 (1999) 937–945.
[74] S.K. Lee, G.D. Cody, B.O. Mysen, Structure and the extent of disorder in quaternary (Ca-Mg and Ca-Na) aluminosilicate glasses and melts, Am. Mineral. 90 (2005) 1393–1401.
[75] K.E. Kelsey, J.R. Allwardt, J.F. Stebbins, Ca-Mg mixing in aluminosilicate glasses: An investigation using ^{17}O MAS and 3QMAS and ^{27}Al MAS NMR, J. Non. Cryst. Solids. 354 (2008) 4644–4653.
[76] P.F. McMillan, B. Piriou, The structures and vibrational spectra of crystals and glasses in the silica-alumina system, J. Non. Cryst. Solids. 53 (1982) 279–298.
[77] C.T. Moynihan, P.B. Macedo, C.J. Montrose, C.J. Montrose, P.K. Gupta, M.A. DeBolt, J.F. Dill, B.E. Dom, P.W. Drake, A.J. Easteal, P.B. Elterman, R.P. Moeller, H. Sasabe, J.A. Wilder, Structural Relaxation in Vitreous Materials, Ann. N. Y. Acad. Sci. 279 (1976) 15–35.
[78] T.M. Gross, M. Tomozawa, Indentation-induced microhardness changes in glasses: Possible fictive temperature increase caused by plastic deformation, J. Non. Cryst. Solids. 354 (2008) 4056–4062.
[79] L. Boesch, A. Napolitano, P.B. Macedo, Spectrum of volume relaxation times in B_2O_3, J. Am. Ceram. Soc. 53 (1970) 148–153.
[80] K. Adachi, T. Kotaka, Volume and Enthalpy Relaxation in Polystyrene, Polym. J. 14 (1982) 959–970.
[81] M.A. DeBolt, A.J. Easteal, P.B. Macedo, C.T. Moynihan, Analysis of structural relaxation in glass using heating rate data, J. Am. Ceram. Soc. 59 (1975) 16–21.

[82] I.M. Hodge, Enthalpy relaxation and recovery in amorphous materials, J. Non. Cryst. Solids. 169 (1994) 211–266.
[83] J.C. Mauro, R.J. Loucks, Impact of fragility on enthalpy relaxation in glass, Phys. Rev. E. 78 (2008) 1–8.
[84] L.-M. Wang, C.A. Angell, Response to "Comment on 'direct determination of the fragility indices of glassforming liquids by differential scanning calorimetry: Kinetic versus thermodynamic fragilities'" [J. Chem. Phys. 118, 10351 (2003)] (Journal of Chemical Physics (2003), J. Chem. Phys. 124 (2006) 10353–10355.
[85] C.A. Angell, Strong and fragile liquids, in: K. Ngai, G.B. Wright (Eds.), Relaxations Complex Syst., National Technical Information Service, U.S. Department of Commerce, Springfield, VA 22161, 1985: pp. 3–11.
[86] D. V. Matyushov, C.A. Angell, Two-Gaussian excitations model for the glass transition, J. Chem. Phys. 123 (2005).
[87] D. Huang, G.B. McKenna, New insights into the fragility dilemma in liquids, J. Chem. Phys. 114 (2001) 5621–5630.
[88] G. Ruocco, F. Sciortino, F. Zamponi, C. De Michele, T. Scopigno, Landscapes and fragilities, J. Chem. Phys. 120 (2004) 10666–10680.
[89] F.H. Stillinger, P.G. Debenedetti, Energy landscape diversity and supercooled liquid properties, J. Chem. Phys. 116 (2002) 3353–3361.
[90] C.A. Angell, Ten questions on glassformers, and a real space 'excitations' model with some answers on fragility and phase transitions C, J. Phys. Condens. Matter. 12 (2000) 6463–6475.
[91] L.M. Martinez, C.A. Angell, A thermodynamic connection to the fragility of glass-forming liquids., Nature. 410 (2001) 663–667.
[92] J.D. Stevenson, P.G. Wolynes, Thermodynamic- Kinetic Correlations in Supercooled Liquids: A Critical Survey of Experimental Data and Predictions of the Random First Order Transition Theory of Glasses, J. Phys. Chem. B. 109 (2005) 1–15.
[93] K. Ito, C.T. Moynihan, C.A. Angell, Thermodynamic determination of fragility in liquids and a fragile-to-strong liquid transition in water, Nature. 398 (1999) 492–495.
[94] D.G. Georgiev, P. Boolchand, M. Micoulaut, Rigidity transitions and molecular structure of As_xSe_{1-x} glasses, Phys. Rev. B. 62 (2000) 9228–9231.
[95] D. Selvanathan, W.J. Bresser, P. Boolchand, Stiffness transitions in Si_xSe_{1-x} glasses from Raman scattering and temperature-modulated differential scanning calorimetry, Phys. Rev. B. 61 (2000) 61–76.
[96] P. Boolchand, D.G. Georgiev, B. Goodman, Discovery of the Intermediate Phase in Chalcogenide Glasses, J. Optoelectron. Adv. Mater. 3 (2001) 703–720.
[97] X. Feng, W.J. Bresser, P. Boolchand, Direct Evidence for Stiffness Threshold in Chalcogenide Glasses, Phys. Rev. Lett. 78 (1997) 4422.
[98] Y. Vaills, T. Qu, M. Micoulaut, F. Chaimbault, P. Boolchand, Direct evidence of rigidity loss and self-organisation in silicate glasses, J. Phys. Condens. Matter. 17 (2005) 4889.
[99] Y. Yu, J.C. Mauro, M. Bauchy, Stretched Exponential Relaxation of

Glasses: Origin of the Mixed Alkali Effect, Am. Ceram. Soc. Bull. 96 (2017) 34–36.

[100] G. Höhne, W.F. Hemminger, H.-J. Flammersheim, Differential scanning calorimetry − An Introduction for Practitioners, Springer-Verlag, Berlin, 1996.

[101] M. Reading, D.J. Hourston, Modulated temperature differential scanning calorimetry: theoretical and practical applications in polymer characterisation, 6th ed., Springer, 2006.

[102] J.E.K. Schawe, Modulated temperature DSC measurements : the influence of the experimental conditions[1], Thermochim. Acta. 271 (1996) 127–140.

[103] O. Gulbiten, J.C. Mauro, P. Lucas, Relaxation of enthalpy fluctuations during sub-Tg annealing of glassy selenium, J. Chem. Phys. 138 (2013) 244504.

[104] J.E.K. Schawe, A comparison of different evaluation methods in modulated temperature DSC, Thermochim. Acta. 260 (1995) 1–16.

[105] C. Alvarez, J.J. Moura-Ramos, The glass transition relaxation in a side-chain liquid crystalline polymer studied by modulated temperature differential scanning calorimetry, Phys. Chem. Chem. Phys. 2 (2000) 4743–4747.

[106] L. Carpentier, O. Bustin, M. Descamps, Temperature-modulated differential scanning calorimetry as a specifig heat spectroscopy, J. Phys. D. Appl. Phys. 35 (2002) 402–408.

[107] O. Bustin, M. Descamps, Slow structural relaxations of glass-forming Maltitol by modulated DSC calorimetry, J. Chem. Phys. 110 (1999) 10982–10992.

[108] E. Hempel, G. Hempel, A. Hensel, C. Schick, E. Donth, Characteristic Length of Dynamic Glass Transition near T_g for a Wide Assortment of Glass-Forming Substances, J. Phys. Chem. B. 104 (2000) 2460–2466.

[109] E. Donth, Characteristic length of the glass transition, J. Polym. Sci. Part B Polym. Phys. 34 (1996) 2881–2892.

[110] S.L. Simon, Temperature-modulated differential scanning calorimetry : theory and application, Thermochim. Acta. 374 (2001) 55–71.

[111] J.M. Hutchinson, A.B. Tong, Z. Jiang, Aging of polycarbonate studied by temperature modulated differential scanning calorimetry, Thermochim. Acta. 335 (1999) 27–42.

[112] S.L. Simon, G.B. McKenna, The effects of structural recovery and thermal lag in temperature-modulated DSC measurements, Thermochim. Acta. 307 (1997) 1–10.

[113] B. Wunderlich, Y. Jin, A. Boller, Mathematical description of differential scanning calorimetry based on periodic temperature modulation, Thermochim. Acta. 236 (1994) 277–293.

[114] A. Boller, Y. Jin, B. Wunderlich, Heat Capacity Measurement by Modulated DSC at constant temperature, J. Therm. Anal. Calorim. 42 (1994) 307–330.

[115] M.M. Smedskjaer, J.C. Mauro, R.E. Youngman, C.L. Hogue, M. Potuzak, Y. Yue, Topological principles of borosilicate glass chemistry, J. Phys. Chem. B. 115 (2011) 12930–12946.

[116] S.L. Webb, Configurational heat capacity of Na_2O-CaO-Al_2O_3-SiO_2 melts,

Chem. Geol. 256 (2008) 91–100.
[117] H. McPhillips, D.Q.M. Craig, P.G. Royall, V.L. Hill, Characterisation of the glass transition of HPMC using modulated temperature differential scanning calorimetry, Int. J. Pharm. 180 (1999) 83–90.
[118] J.E.K. Schawe, Investigations af the glass transitions of organic and inorganic substances: DSC and temperature-modulated DSC, J. Therm. Anal. Calorim. 47 (1996) 475–484.
[119] Z.P. Lu, Y. Li, S.C. Ng, Y.P. Feng, K. Lu, Glass transition of rare-earth based metallic glasses: Temperature modulated differential scanning calorimetry, J. Non. Cryst. Solids. 250–252 (1999) 689–693.
[120] Y. Matsuda, Y. Fukawa, M. Kawashima, S. Mamiya, S. Kojima, Dynamic glass transition and fragility of lithium borate binary glass, Solid State Ionics. 179 (2008) 2424–2427.
[121] Y. Fukawa, Y. Matsuda, M. Kawashima, S. Kojima, Determination of complex-specific heat and fragility of sodium borate glasses by temperature-modulated DSC, J. Therm. Anal. Calorim. 99 (2010) 39–44.
[122] G. Yang, O. Gulbiten, Y. Gueguen, B. Bureau, J.-C. Sangleboeuf, C. Roiland, E.A. King, P. Lucas, Fragile-strong behavior in the As_xSe_{1-x} glass forming system in relation to structural dimensionality, Phys. Rev. B. 85 (2012) 144107.
[123] Y. Matsuda, C. Matsui, Y. Ike, M. Kodama, S. Kojima, Non-debye nature in thermal relaxation and thermal properties of lithium borate glasses studied by modulated DSC, J. Therm. Anal. Calorim. 85 (2006) 725–730.
[124] Y. Matsuda, Y. Fukawa, C. Matsui, Y. Ike, M. Kodama, S. Kojima, Calorimetric study of the glass transition dynamics in lithium borate glasses over a wide composition range by modulated DSC, Fluid Phase Equilib. 256 (2007) 127–131.
[125] P. Lucas, E.A. King, A.D. Horner, B.R. Johnson, S.K. Sundaram, Photostructural relaxation in As–Se–S glasses: Effect of network fragility, J. Non. Cryst. Solids. 352 (2006) 2067–2072.
[126] P. Lucas, E.A. King, O. Gulbiten, J.L. Yarger, E. Soignard, B. Bureau, Bimodal phase percolation model for the structure of Ge-Se glasses and the existence of the intermediate phase, Phys. Rev. B. 80 (2009) 214114.
[127] R. Brüning, On the glass transition in vitreous silica by differential thermal analysis measurements, J. Non. Cryst. Solids. 330 (2003) 13–22.
[128] C.T. Moynihan, Correlation between the width of the glass transition region and the temperature dependence of the viscosity of high-Tg glasses, J. Am. Ceram. Soc. 76 (1993) 1081–1087.
[129] A. Savitzky, M.J.E. Golay, Smoothing and Differentiation of Data by Simplified Least Squares Procedures, Anal. Chem. 36 (1964) 1627–1639.
[130] Q. Zheng, J.C. Mauro, Y. Yue, Reconciling calorimetric and kinetic fragilities of glass-forming liquids, J. Non. Cryst. Solids. 456 (2017) 95–100.
[131] C.T. Moynihan, A.J. Easteal, M.A. DeBolt, J. Tucker, Dependence of the Fictive Temperture of Glass on Cooling Rate, J. Am. Ceram. Soc. 59 (1976) 12–16.

[132] C.T. Moynihan, Structural relaxation and the glass transition, Rev. Mineral. Geochemistry. 32 (1995) 1–19.
[133] C.T. Moynihan, S.K. Lee, M. Tatsumisago, T. Minami, Estimation of activation energies for structural relaxation and viscous flow from DTA and DSC experiments, Thermochim. Acta. 280–281 (1996) 153–162.
[134] A.Q. Tool, Relation Between Inelastic Deformability and Thermal Expansion of Glass in Its Annealing Range, J. Am. Ceram. Soc. 29 (1946) 240–253.
[135] Y. Yue, Characteristic temperatures of enthalpy relaxation in glass, J. Non. Cryst. Solids. 354 (2008) 1112–1118.
[136] C.A. Angell, Relaxation in liquid, polymers and plastic crystal - strong/fragile patterns and problems, J. Non. Cryst. Solids. 131 (1991) 13–31.
[137] R. Bohmer, K.L. Ngai, C.A. Angell, D.J. Plazek, Nonexponential relaxations in strong and fragile glass formers, J. Chem. Phys. 99 (1993) 4201.
[138] C.A. Angell, K.L. Ngai, G.B. McKenna, P.F. McMillan, S.W. Martin, Relaxation in glassforming liquids and amorphous solids, J. Appl. Phys. 88 (2000) 3113.
[139] N.O. Birge, S.R. Nagel, Specific-Heat Spectroscopy of the Glass Transition, Phys. Rev. Lett. 54 (1985) 2674–2677.
[140] T.K. Bechgaard, J.C. Mauro, M. Bauchy, Y. Yue, L.A. Lamberson, L.R. Jensen, M.M. Smedskjaer, Fragility and configurational heat capacity of calcium aluminosilicate glass-forming liquids, J. Non. Cryst. Solids. 461 (2017) 24–34.
[141] M.L.F. Nascimento, C. Aparicio, Viscosity of strong and fragile glass-forming liquids investigated by means of principal component analysis, J. Phys. Chem. Solids. 68 (2007) 104–110.
[142] J.C. Phillips, Topology of covalent non-crystalline solids I: Short-range order in chalcogenide allloys, October. 34 (1981) 153–181.
[143] Y. Vaills, Y. Luspin, G. Hauret, Two opposite effects of sodium on elastic constants of silicate binary glasses, Mater. Sci. Eng. B. 40 (1996) 199–202.
[144] A. Feltz, H. Aust, A. Blayer, Glass formation and properties of chalcogenide systems XXVI: Permittivity and the structure of glasses As_xSi_{1-x} and Ge_xSe_{1-x}, World. 2 (1982) 1–16.
[145] Y. Wang, M. Nakamura, O. Matsuda, K. Murase, Raman-spectroscopy studies on rigidity percolation and fragility in Ge–(S,Se) glasses, J. Non. Cryst. Solids. 266–269 (2000) 872–875.
[146] P. Boolchand, W. Bresser, M. Zhang, Y. Wu, J. Wells, R.N. Enzweiler, Lamb-Mössbauer factors as a local probe of floppy modes in network glasses, J. Non. Cryst. Solids. 182 (1995) 143–154.
[147] R. Bhageria, K. Gunasekera, P. Boolchand, M. Micoulaut, Fragility and molar volumes of non-stoichiometric chalcogenides: The crucial role of melt/glass homogenization, Phys. Status Solidi Basic Res. 251 (2014) 1322–1329.
[148] A. Zeidler, P.S. Salmon, D.A.J. Whittaker, K.J. Pizzey, A.C. Hannon,

Topological Ordering and Viscosity in the Glass-Forming Ge-Se System: The Search for a Structural or Dynamical Signature of the Intermediate Phase, Front. Mater. 4 (2017) 32.
[149] M. Bauchy, M. Micoulaut, Densified network glasses and liquids with thermodynamically reversible and structurally adaptive behaviour, Nat. Commun. 6 (2015) 1–8.
[150] M. Bauchy, Personal communication, (n.d.).
[151] T.M. Gross, M. Tomozawa, A. Koike, A glass with high crack initiation load: Role of fictive temperature-independent mechanical properties, J. Non. Cryst. Solids. 355 (2009) 563–568.
[152] J. Sehgal, S. Ito, A New Low-Brittleness Glass in the Soda–Lime–Silica Glass Family, J. Am. Ceram. Soc. 81 (1998) 2485–2488.
[153] J.E. Ritter, C.L. Sherburne, Dynamic and Static Fatigue of Silicate Glasses, J. Am. Ceram. Soc. 54 (1971) 601–605.
[154] C.R. Kurkjian, P.K. Gupta, R.K. Brow, The Strength of Silicate Glasses: What Do We Know, What Do We Need to Know?, Int. J. Appl. Glas. Sci. 1 (2010) 27–37.
[155] S.M. Wiederhorn, L.H. Bolz, Stress corrosion and static fatigue of glass, J. Am. Soc. Ceram. 53 (1970) 543–548.
[156] A.A. Griffith, The Phenomena of Rupture and Flow in Solid, Philos. Trans. R. Soc. London. Ser. A, Contain. Pap. a Math. or Phys. Character. 221 (1921) 163–198.
[157] S.M. Wiederhorn, Influence of Water Vapor on Crack Propagation in Soga-Lime Glass, J. Am. Ceram. Soc. 50 (1967) 407–414.
[158] C. Gurney, Delayed fracture in glass, Proc. Phys. Soc. 59 (1947) 169.
[159] K. Hirao, M. Tomozawa, Microhardness of SiO_2 Glass in Various Environments, J. Am. Ceram. Soc. 70 (1987) 497–502.
[160] S. Striepe, J. Deubener, M.M. Smedskjaer, M. Potuzak, Environmental effects on fatigue of alkaline earth aluminosilicate glass with varying fictive temperature, J. Non. Cryst. Solids. 379 (2013) 161–168.
[161] B.R. Lawn, T.P. Dabbs, C.J. Fairbanks, Kinetics of shear-activated indentation crack initiation in soda-lime glass, J. Mater. Sci. 18 (1983) 2785–2797.
[162] T.A. Michalske, S.W. Freiman, A Molecular Mechanism for Stress Corrosion in Vitreous Silica, J. Am. Ceram. Soc. 66 (1983) 284–288.
[163] T.M. Gross, M. Tomozawa, Crack-free high load Vickers indentation of silica glass, J. Non. Cryst. Solids. 354 (2008) 5567–5569.
[164] J.J. Price, G.S. Glaesemann, D.A. Clark, T.M. Gross, K.L. Barefoot, A Mechanics Framework for Ion-Exchanged Cover Glass with a Deep Compression Layer, SID Symp. Dig. Tech. Pap. 40 (2009) 1049–1051.
[165] C. Hermansen, J. Matsuoka, S. Yoshida, H. Yamazaki, Y. Kato, Y. Yue, Densification and Plastic Deformation under Microindentation in Silicate Glasses and the Relation to Hardness and Crack Resistance, J. Non. Cryst. Solids. 364 (2013) 40–43.
[166] S. Yoshida, Y. Nishikubo, A. Konno, T. Sugawara, Y. Miura, J. Matsuoka, Fracture- and Indentation-Induced Structural Changes of Sodium

Borosilicate Glasses, Int. J. Appl. Glas. Sci. 3 (2012) 3–13.
[167] M. Wada, H. Furukawa, K. Fujita, Crack Resistance of Glass on Vickers Indentation, Proc. Int. Congr. Glas. 10th. 11 (1974) 39–46.
[168] T. Rouxel, Driving force for indentation cracking in glass: composition, pressure and temperature dependence, Philos. Trans. A. Math. Phys. Eng. Sci. 373 (2015) 20140140.
[169] H. Morozumi, H. Nakano, S. Yoshida, J. Matsuoka, Crack Initiation Tendency of Chemically Strengthened Glasses, Int. J. Appl. Glas. Sci. 6 (2015) 64–71.
[170] G.A. Rosales-Sosa, A. Masuno, Y. Higo, H. Inoue, Crack-resistant Al_2O_3–SiO_2 glasses, Sci. Rep. 6 (2016) 23620.
[171] A. Koike, S. Akiba, T. Sakagami, K. Hayashi, S. Ito, Difference of cracking behavior due to Vickers indentation between physically and chemically tempered glasses, J. Non. Cryst. Solids. 358 (2012) 3438–3444.
[172] Y. Kato, H. Yamazaki, Y. Kubo, S. Yoshida, J. Matsuoka, T. Akai, Effect of B2O3 Content on Crack Inititation under Vickers Indentation Test, J. Ceram. Soc. Japan. 118 (2010) 792–798.
[173] Y. Kato, H. Yamazaki, S. Yoshida, J. Matsuoka, Effect of densification on crack initiation under Vickers indentation test, J. Non. Cryst. Solids. 356 (2010) 1768–1773.
[174] S. Striepe, M.M. Smedskjaer, J. Deubener, U. Bauer, H. Behrens, M. Potuzak, R.E. Youngman, J.C. Mauro, Y. Yue, Elastic and micromechanical properties of isostatically compressed soda–lime–borate glasses, J. Non. Cryst. Solids. 364 (2013) 44–52.
[175] G. Scannell, L. Huang, T. Rouxel, Elastic properties and indentation cracking behavior of Na_2O-TiO_2-SiO_2 glasses, J. Non. Cryst. Solids. 429 (2015) 129–142.
[176] M. Barlet, J.-M. Delaye, T. Charpentier, M. Gennisson, D. Bonamy, T. Rouxel, C.L. Rountree, Hardness and toughness of sodium borosilicate glasses via Vickers's indentations, J. Non. Cryst. Solids. 417–418 (2015) 66–79.
[177] K.G. Aakermann, K. Januchta, J.A.L. Pedersen, M.N. Svenson, S.J. Rzoska, M. Bockowski, J.C. Mauro, M. Guerette, L. Huang, M.M. Smedskjaer, Indentation deformation mechanism of isostatically compressed mixed alkali aluminosilicate glasses, J. Non. Cryst. Solids. 426 (2015) 175–183.
[178] R. Limbach, A. Winterstein-Beckmann, J. Dellith, D. Möncke, L. Wondraczek, Plasticity, crack initiation and defect resistance in alkali-borosilicate glasses: From normal to anomalous behavior, J. Non. Cryst. Solids. 417 (2015) 15–27.
[179] S. Striepe, M. Potuzak, M.M. Smedskjaer, J. Deubener, Relaxation kinetics of the mechanical properties of an aluminosilicate glass, J. Non. Cryst. Solids. 362 (2013) 40–46.
[180] G.D. Sorarù, M. Guglielmi, R. Dal Maschio, Influence of sol-gel coatings on crack initiation by vickers indentation in soda-lime glass, J. Non. Cryst. Solids. 100 (1988) 440–446.
[181] A. Pönitzsch, M. Nofz, L. Wondraczek, J. Deubener, Bulk elastic properties,

hardness and fatigue of calcium aluminosilicate glasses in the intermediate-silica range, J. Non. Cryst. Solids. 434 (2016) 1–12.

[182] T.K. Bechgaard, A. Goel, R.E. Youngman, J.C. Mauro, S.J. Rzoska, M. Bockowski, L.R. Jensen, M.M. Smedskjaer, Structure and mechanical properties of compressed sodium aluminosilicate glasses: Role of non-bridging oxygens, J. Non. Cryst. Solids. 441 (2016) 49–57.

[183] S. Yoshida, A. Hidaka, J. Matsuoka, Crack initiation behavior of sodium aluminosilicate glasses, J. Non. Cryst. Solids. 344 (2004) 37–43.

[184] A. Talimian, V.M. Sglavo, Can annealing improve the chemical strengthening of thin borosilicate glass?, J. Non. Cryst. Solids. 465 (2017) 1–7.

[185] S. Kapoor, N. Lönnroth, R.E. Youngman, S.J. Rzoska, M. Bockowski, L.R. Jensen, M.M. Smedskjaer, Pressure-driven structural depolymerization of zinc phosphate glass, J. Non. Cryst. Solids. 469 (2017) 31–38.

[186] S. Kapoor, X. Guo, R.E. Youngman, C.L. Hogue, J.C. Mauro, S.J. Rzoska, M. Bockowski, L.R. Jensen, M.M. Smedskjaer, Network Glasses under Pressure: Permanent Densification in Modifier-Free Al_2O_3-B_2O_3-P_2O_5-SiO_2 Systems, Phys. Rev. Appl. 7 (2017) 1–16.

[187] S. Striepe, N. Da, J. Deubener, L. Wondraczek, Micromechanical properties of (Na,Zn)-sulfophosphate glasses, J. Non. Cryst. Solids. 358 (2012) 1032–1037.

[188] G.A. Rosales-Sosa, A. Masuno, Y. Higo, H. Inoue, Y. Yanaba, T. Mizoguchi, T. Umada, K. Okamura, K. Kato, Y. Watanabe, High Elastic Moduli of a $54Al_2O_3$-$46Ta_2O_5$ Glass Fabricated via Containerless Processing, Sci. Rep. 5 (2015) 1–8.

[189] I. Hasdemir, S. Striepe, J. Deubener, K. Simon, A 2000-year perspective on indentation crack resistance and brittleness of glass, J. Non. Cryst. Solids. 408 (2015) 51–56.

[190] S. Sperimentale, Crack Nucleation In Ultrathin Blown Silicate Glasses, J. Non. Cryst. Solids. 80 (1986) 481–486.

[191] H. Morozumi, S. Yoshida, J. Matsuoka, Composition dependence of crack formation probability in aluminoborosilicate glass, J. Non. Cryst. Solids. 444 (2016) 31–37.

[192] M. Tomozawa, W.-T. Han, W.A. Lanford, Water Entry into Silica Glass During Slow Crack Growth, J. Am. Ceram. Soc. 74 (1991) 2573–2576.

[193] M.M. Smedskjaer, S.J. Rzoska, M. Bockowski, J.C. Mauro, Mixed alkaline earth effect in the compressibility of aluminosilicate glasses, J. Chem. Phys. 140 (2014) 054511.

[194] J.E. Shelby, Viscosity and thermal expansion of lithium aluminosilicate glasses, J. Appl. Phys. 49 (1978) 5885.

[195] M.M. Smedskjaer, J.C. Mauro, Y. Yue, Prediction of Glass Hardness Using Temperature-Dependent Constraint Theory, Phys. Rev. Lett. 105 (2010) 115503.

[196] Z. Zhang, N. Soga, K. Hirao, Indentation deformation and fracture of densified silicate glass, J. Mater. Sci. 30 (1995) 6359–6362.

[197] R.F. Cook, G.M. Pharr, Direct Observation of Indentation Cracking in Glass

and Ceramics, J. Am. Ceram. Soc. 73 (1990) 787.
[198] M. Guignard, L. Albrecht, J.W. Zwanziger, Zero-stress optic glass without lead, Chem. Mater. 19 (2007) 286–290.
[199] K. Ramesh, R. Vivek, P. Tarkes Dora, D. Sanyal, A simple approach to photoelastic calibration of glass using digital photoelasticity, J. Non. Cryst. Solids. 378 (2013) 7–14.
[200] K. Ramesh, V. Ramakrishnan, Digital photoelasticity of glass: A comprehensive review, Opt. Lasers Eng. 87 (2016) 59–74.
[201] K. Kurosawa, K. Yamashita, T. Sowa, Y. Yamada, Flexible Fiber Faraday Effect Current Sensor Using Flint Glass Fiber and Reflection Scheme, Ieice Trans. Electron. 83 (2000) 326–330.
[202] A. Saitoh, U. Hoppe, R.K. Brow, G. Tricot, Y. Hashida, H. Takebe, The structure and properties of xZnO–(67-x)SnO–P_2O_5 glasses: (III) Photoelastic behavior, J. Non. Cryst. Solids. 484 (2018) 173–176.
[203] K. Kusama, T. Matano, Y. Ohashi, M. Kobayashi, K. Nagamoto, P-72 : Is the Photo-elasticity of PSAs for LCD Panels Reducible?, in: SID Symp. Dig. Tech. Pap., 2008: pp. 1457–1460.
[204] F. Pockels, Über die Änderung des optischen Verhaltens verschiedener Gläser durch elastische Deformation, Ann. Phys. 312 (1902) 745–771.
[205] A.I. Rabukhin, Photoelastic constants of germanate glasses containing lead and bismuth oxides, Glas. Ceram. 51 (1994) 15–18.
[206] V. Martin, B. Wood, U. Werner-Zwanziger, J.W. Zwanziger, Structural aspects of the photoelastic response in lead borate glasses, J. Non. Cryst. Solids. 357 (2011) 2120–2125.
[207] M. Guignard, U. Werner-Zwanziger, J.W. Zwanziger, Glass-former/glass-modifier interactions and the stress-optic response, J. Non. Cryst. Solids. 354 (2008) 79–83.
[208] M. Guignard, J.W. Zwanziger, Zero stress-optic barium tellurite glass, J. Non. Cryst. Solids. 353 (2007) 1662–1664.
[209] M. Itadani, A. Saitoh, Y. Masaoka, H. Takebe, Low photoelastic and optical properties in RO–SnO–P_2O_5 (R = Zn, Ba, Sr) glasses, Opt. Lett. 41 (2016) 45–48.
[210] A. Saitoh, K. Nakata, G. Tricot, Y. Chen, N. Yamamoto, H. Takebe, Zero photoelastic and water durable ZnO–SnO-P_2O_5–B_2O_3 glasses, APL Mater. 3 (2015) 046102.
[211] N. Yamamoto, A. Saitoh, H. Takebe, Zero photoelastic zinc tin phosphate glass without lead oxide, Opt. Lett. 37 (2012) 4203–4205.
[212] J. Galbraith, J.W. Zwanziger, Designing glass with non-dispersive stress-optic response, J. Non. Cryst. Solids. 433 (2016) 82–86.
[213] V. Martin, U. Werner-Zwanziger, J.W. Zwanziger, R.A. Dunlap, Correlation of Structure and Photoelastic Response in Tin Phosphate Glass, Int. J. Appl. Glas. Sci. 2 (2011) 282–289.
[214] J.G. Thorbahn, J.W. Zwanziger, Compositional dependence of the stress-optic response in zinc tellurite glasses, J. Non. Cryst. Solids. 381 (2013) 48–53.
[215] S.K. Lee, J.F. Stebbins, The distribution of sodium ions in aluminosilicate

glasses: A high-field Na-23 MAS and 3Q MAS NMR study, Geochim. Cosmochim. Acta. 67 (2003) 1699–1709.

[216] L.S. Du, J.R. Allwardt, B.C. Schmidt, J.F. Stebbins, Pressure-induced structural changes in a borosilicate glass-forming liquid: Boron coordination, non-bridging oxygens, and network ordering, J. Non. Cryst. Solids. 337 (2004) 196–200.

[217] M.M. Smedskjaer, M. Potuzak, X. Guo, J.C. Mauro, Compositional control of the photoelastic response of silicate glasses, Opt. Mater. (Amst). 35 (2013) 2435–2439.

[218] Z. Tang, Y.Z. Mauro, C. Gee, D.L.J. Duffy, T.E. Meyer, M.B. Abrams, K.A. Walker, J.C. Mauro, Methods for measurement and statistical analysis of the frangibility of strengthened glass, Front. Mater. 2 (2015) 1–8.

LIST OF PUBLICATIONS

Publications in peer-reviewed journals:

I. T.K. Bechgaard, A. Goel, R.E. Youngman, J.C. Mauro, S.J. Rzoska, M. Bockowski, L.R Jensen, and M.M. Smedskjaer, Structure and mechanical properties of compressed sodium aluminosilicate glasses: role of non-bridging oxygens. *Journal of Non-Crystalline Solids*, **441** (2016), 49-57.

II. T.K. Bechgaard, G. Scannell, L. Huang, R.E. Youngman, J.C. Mauro, and M.M. Smedskjaer. Structure of MgO/CaO sodium aluminosilicate glasses: Raman spectroscopy study. *Journal of Non-Crystalline Solids*, **470** (2017),145-151

III. T.K. Bechgaard, J.C. Mauro, M. Bauchy, Y. Yue, L.A. Lamberson, L.R. Jensen, and M.M Smedskjaer. Fragility and configurational heat capacity of calcium aluminosilicate glass-forming liquids. *Journal of Non-Crystalline Solids*, **461** (2017), 24-34.

IV. T.K. Bechgaard, O. Gulbiten, J.C. Mauro, and M.M. Smedskjaer. Parametric study of temperature-modulated differential scanning calorimetry for high-temperature oxide glasses with varying fragility. *Journal of Non-Crystalline Solids*, **484** (2018), 84-94.

V. T.K. Bechgaard, O. Gulbiten, J.C. Mauro, Yuanzheng Yue, Mathieu Bauchy, and M.M. Smedskjaer. Liquid Fragility Determination of Oxide Glass-Formers Using Temperature-Modulated DSC, *International Journal of Applied Glass Science*, (under review)

VI. T.K. Bechgaard, J.C. Mauro, and M.M Smedskjaer. Time and humidity dependence of indentation cracking in aluminosilicate glasses. *Journal of Non-Crystalline Solids*, **491** (2018), 64-70.

VII. T.K. Bechgaard, J.C. Mauro, L.M. Thirion, S.J. Rzoska, M. Bockowski, and M.M Smedskjaer. Photoelastic response of permanently densified oxide glasses. *Optical Materials*, **67** (2017), 155-161.

Publications in Non peer-reviewed journals:

I. T.K.Bechgaard and M.M Smedskjaer. Jagten på skrumpefrit glas (in Danish). *Aktuel Naturvidenskab*, **6** (2017), 20-23.

II. T.K. Bechgaard, O. Gulbiten, J.C. Mauro, Y. Hu, M. Bauchy, and M.M Smedskjaer. Temperature-modulated differential scanning calorimetry analysis of high-temperature silicate glasses. *American Ceramic Society Bulletin*, **97**[4] (2018), 31-33.

Conference contributions

I. T.K. Bechgaard, A. Goel, R.E. Youngman, J.C. Mauro, S.J. Rzoska, M. Bockowski, L.R. Jensen, M.M Smedskjaer. Structure and Mechanical Properties of Compressed Sodium Aluminosilicate Glasses. Oral presentation: *Materials Science & Technology 2016*, Salt Lake City, USA (2016).

II. T.K. Bechgaard, J. C. Mauro, M. Bauchy, Y. Z. Yue, L. R. Jensen, M.M. Smedskjaer. Correlation between Fragility and Configurational Heat Capacity in Calcium Aluminosilicate Glasses. Oral presentation: *12th Pacific Rim Conference on Ceramic and Glass Technology*, Hawaii, USA (2017).

III. T. K. Bechgaard, L. M. Thirion, S. J. Rzoska, M. Bockowski, J. C. Mauro, M. M. Smedskjaer. Impact of Hot Compression on the Stress Optic Coefficient of Oxide Glasses. Poster: *12th Pacific Rim Conference on Ceramic and Glass Technology*, Hawaii, USA (2017).

IV. T. K. Bechgaard, K. Januchta, S. Kapoor, M. M. Smedskjaer. Indentation Behavior of Permanently Densified Oxide Glasses. Oral presentation: *7th International Workshop on Flow and Fracture of Advanced Glasses*, Aalborg, Denmark (2017).

V. T. K. Bechgaard, J. C. Mauro, M. M. Smedskjaer. Time and Humidity Dependence of Indentation Cracking in Aluminosilicate Glasses. Poster: *2018 Glass & Optical Materials Division Meeting*, San Antonio, USA (2018).

VI. T. K. Bechgaard, O. Gulbiten, J. C. Mauro, M. M. Smedskjaer Temperature-Modulated Differential Scanning Calorimetry Analysis of High-Temperature Silicate Glasses. Norbert J. Kreidl award lecture: *2018 Glass & Optical Materials Division Meeting*, San Antonio, USA (2018).

Paper I

Journal of Non-Crystalline Solids 441 (2016) 49–57

Contents lists available at ScienceDirect

Journal of Non-Crystalline Solids

journal homepage: www.elsevier.com/locate/jnoncrysol

Structure and mechanical properties of compressed sodium aluminosilicate glasses: Role of non-bridging oxygens

Tobias K. Bechgaard [a], Ashutosh Goel [b], Randall E. Youngman [c], John C. Mauro [c], Sylwester J. Rzoska [d], Michal Bockowski [d], Lars R. Jensen [e], Morten M. Smedskjaer [a,*]

[a] Department of Chemistry and Bioscience, Aalborg University, Aalborg, Denmark
[b] Department of Materials Science and Engineering, Rutgers, The State University of New Jersey, Piscataway, NJ, USA
[c] Science and Technology Division, Corning Incorporated, Corning, USA
[d] Institute of High-Pressure Physics, Polish Academy of Sciences, Warsaw, Poland
[e] Department of Mechanical and Manufacturing Engineering, Aalborg University, Aalborg, Denmark

ARTICLE INFO

Article history:
Received 2 February 2016
Received in revised form 15 March 2016
Accepted 16 March 2016
Available online 2 April 2016

Keywords:
Aluminosilicate glass
Structure
Non-bridging oxygen
Pressure
Indentation

ABSTRACT

Clarifying the effect of pressure on the structure of aluminosilicate glasses is important for understanding the densification mechanism of these materials under pressure and the corresponding changes in macroscopic properties. In this study, we examine changes in density, network structure, indentation hardness, and crack resistance of sodium aluminosilicate glasses with varying Al/Si ratio and thus non-bridging oxygen (NBO) content before and after 1 GPa isostatic compression at elevated temperature. With increasing NBO content, the silicate network depolymerizes, resulting in higher atomic packing density, lower hardness, and higher crack resistance. The ability of the glasses to densify under isostatic compression is higher in the high-NBO glasses, and these glasses also exhibit more pronounced pressure-induced changes in mechanical properties. The ^{27}Al NMR data show a surprising presence of five-fold aluminum in the as-made high-NBO glasses, with additional formation upon compression. Our study therefore provides new insights into the complicated relationship between Al coordination and NBO content in aluminosilicate glasses and how it affects their densification behavior.

1. Introduction

The relationship between structure and properties for sodium aluminosilicate (Na_2O-Al_2O_3-SiO_2) glasses and glass-forming liquids with varying thermodynamic variables (e.g., composition, temperature, and pressure) are important for both industrial and geological processes. These glasses are commercially used for various products, such as flat panel display glass, scratch resistant cover glass, and nuclear waste glass. The three oxides constitute >80% of andesitic and granitic magmatic systems and therefore also have important implications for magma dynamics and properties.

Several structural models have proposed that for Al/Na ratio ≤1, i.e., excess Na^+ ions, all Al^{3+} is found in tetrahedral configuration (Al^{IV}) [1–4]. Addition of Al_2O_3 to an alkali silicate glass ideally leads to the removal of the network-modifying Na^+ ions from their original role in the network until no more non-bridging oxygen (NBO) atoms remain [5]. For Al/Na ratio ≥1, some Al^{3+} ions can no longer be charge balanced in tetrahedral configuration and some excess Al^{3+} is forced into higher coordination number (five-fold Al^V or six-fold Al^{VI}) as a means of charge-balancing additional Al tetrahedra [6–8]. An alternative hypothesis is that Al^{IV} can be incorporated, even in peraluminous compositions, without the need for a charge-balancing cation through association with a three-coordinated oxygen (oxygen tricluster) [9–11]. In any case, it is well accepted that a range of macroscopic properties (e.g., transport and mechanical) depend on the Al/Na ratio and thus the network connectivity [12–15], i.e., the fraction of NBOs.

Clarifying the effect of pressure on the structure of aluminosilicate glasses is important for understanding the densification mechanism of these materials under pressure and the corresponding changes in macroscopic properties. However, high-pressure experiments are challenging, partly due to the typical small sample volumes [16], prohibiting characterization of post-compression properties. In this work, we investigate sodium aluminosilicate glasses quenched under isostatic pressure from the glass transition temperature in a nitrogen gas pressure chamber. Although this approach is relatively modest in both temperature and pressure (~T_g and ≤1 GPa), it permits permanent densification of relatively large glass pieces (cm^2) that are suitable for characterization of, e.g., mechanical properties [17,18]. This is because permanent densification of glass occurs at significantly lower pressures for compression at elevated temperature compared to that at room temperature [19,20].

Pressure-induced structural changes of aluminosilicates are manifested by changes at both short- and intermediate-range length scales,

* Corresponding author.
E-mail address: mos@bio.aau.dk (M.M. Smedskjaer).

http://dx.doi.org/10.1016/j.jnoncrysol.2016.03.011
0022-3093/

including increase in the local coordination numbers of the network forming Al and Si cations from 4 to 5 and 6, enabling closer packing of the structural units. This coordination number change has been reported to involve conversion of NBO to bridging oxygen (BO) [21–24], but in the absence of NBOs, it can also occur through the formation of oxygen triclusters [25,26]. The densification mechanism of sodium aluminosilicate glasses has also been suggested to include decrease of Na—O bond distances [23,27,28], decrease of inter-tetrahedral bond angles [29,30], decrease of average ring size [31], and increase in distribution of Si—O and Al—O bond lengths [30].

In this work, we study the structure and micromechanical properties of a series of Na_2O-Al_2O_3-SiO_2 glasses before and after isostatic compression at elevated temperature. Specifically we study the influence of NBOs on the changes in structure and properties by varying the Al/Si ratio at constant Na_2O concentration. Our results provide insight into the composition-dependent structural changes that facilitate densification of the aluminosilicate network during compression and the consequence for the micromechanical properties. Improved understanding of the link between structure and mechanical properties is important due to the need for more scratch-resistant and mechanically durable glasses to enable new advanced glass applications.

2. Experimental section

2.1. Sample preparation

We have prepared six glasses in the (75-x)SiO_2-xAl_2O_3-25Na_2O system with $x = 0$, 5, 10, 15, 20, and 25. In this series, the $[Al_2O_3]/[Na_2O]$ ratio is ≤1, and therefore prevailing models of network structure in peralkaline glasses would indicate sufficient charge-compensating Na^+ ions to keep all Al^{3+} in tetrahedral configuration. High purity powders of SiO_2 (Alfa Aesar; >99.5%), Na_2CO_3 (Sigma Aldrich; >99%), and Al_2O_3 (Sigma Aldrich; ≥99%) were used for glass melting. Homogeneous mixtures of batches (corresponding to ~70 g of oxides), obtained by ball milling, were melted in Pt-Rh crucibles at 1650 °C for 2 h in air. The melts were poured on a metallic table and were initially annealed at 600 °C for 1 h. The chemical compositions of the glasses were determined using flame emission spectroscopy and inductively coupled plasma mass spectroscopy. The results are given in Table 1. To ensure uniform thermal history, the glasses were annealed at their respective glass transition temperature (T_g) for ~2 h. T_g was determined using differential scanning calorimetry (DSC 449C, Netzsch) at 10 K/min (Table 1). The glasses were cut to dimensions of about $10 \times 10 \times 8$ mm^3 and polished to an optical finish.

The six glass compositions were isostatically compressed at 0.5 and 1.0 GPa at their respective ambient pressure T_g value (see Table 1) in a gas pressure reactor with nitrogen as the compression medium. The system was kept at the high-pressure/high-temperature condition for 30 min before cooling to room temperature at 60 K/min, followed by decompression at room temperature at 30 MPa/min. The setup used for this pressure treatment has been described in detail in Ref. [17]. X-ray diffraction analyses showed no evidence of crystallization following the pressure treatment.

Table 1
Analyzed chemical compositions (in mol%), calculated number of non-bridging oxygens per tetrahedrally coordinated cation (NBO/T), density (ρ), glass transition temperature (T_g), and plastic compressibility (β). Compositions are analyzed using inductively coupled plasma and flame emission spectroscopy, density determined using Archimedes method, T_g determined using differential scanning calorimetry at a rate of 10 K/min, and β calculated from the slopes of the linear fits to density vs. pressure for each composition.

Glass ID	Composition (mol%)			NBO/T	ρ	T_g	β
	SiO_2	Al_2O_3	Na_2O	(−)	(g cm^{-3})	(°C)	(GPa^{-1})
Al-0	74.7	0.0	25.3	0.677	2.437	470	0.0215
Al-5	70.0	5.1	24.9	0.494	2.456	500	0.0220
Al-10	64.8	10.2	25.0	0.347	2.471	534	0.0221
Al-15	59.6	15.1	25.3	0.227	2.484	595	0.0187
Al-20	54.6	19.7	25.7	0.128	2.494	638	0.0147
Al-25	49.7	25.2	25.1	0.000	2.498	797	0.0157

2.2. Density

The density values of the as-prepared and compressed glass samples were determined using Archimedes' principle with ethanol as the immersion medium. The weight of each glass sample in both air and ethanol was measured ten times.

2.3. Indentation

Vickers hardness (H_V) and crack resistance (CR) of as-prepared and isostatically compressed glasses were measured using a Vickers microindenter (Duramin 5, Struers A/S). The measurements were performed in air at room temperature with a dwell time of 15 s. Thirty indentations at each load (0.49, 0.98, 1.96, 2.94, 4.91, 9.81, and 19.6 N) were performed. H_V was calculated at 9.81 N from the length of the indentation diagonals. CR was determined as the load leading to an average of two radial/median cracks per indent [35].

2.4. Raman spectroscopy

Raman scattering spectra were measured in backscattering geometry with a Renishaw Invia Raman microscope on freshly polished samples. A diode laser with a wavelength of 532 nm was used as the excitation source. The collected Raman spectra were baseline-corrected using an asymmetric least square algorithm [32]. Afterwards the processed spectra were deconvoluted using Fityk software with Gaussian and Voigt lineshapes.

2.5. ^{27}Al NMR Spectroscopy

^{27}Al magic-angle spinning (MAS) nuclear magnetic resonance (NMR) and triple quantum magic-angle spinning (3QMAS) NMR experiments on both as-prepared and compressed (1.0 GPa) aluminosilicate glasses were conducted at 16.4 T using a commercial spectrometer (VNMRs, Agilent) and a 1.6 mm MAS NMR probe (Agilent) with spinning speeds of 25 kHz. MAS NMR data were acquired using radio frequency pulses of 0.6 μs (equivalent to a π/12 tip angle), relaxation delays of 2 s, and signal averaging of 1000 acquisitions. MAS NMR data were processed using commercial software, without additional apodization and referenced to aqueous aluminum nitrate at 0.0 ppm. A weak background signal from the zirconia MAS rotors was detected by ^{27}Al MAS NMR of an empty rotor and subsequently subtracted from the MAS NMR data of the glass samples. This signal, at approximately 16 ppm, is clearly distinct from the Al peaks in the glasses, but nonetheless has been removed to ensure higher accuracy in the ^{27}Al MAS NMR experiments. Unfortunately, this weak zirconia signal cannot be removed from ^{27}Al 3QMAS NMR data, and appears in some of the spectra as a weak set of contours around 16 ppm in the MAS NMR dimension.

MQMAS NMR spectra were measured using the three pulse, zero quantum filtering method [33]. The hard 3π/2 and π/2 pulse widths were calibrated to 1.8 and 0.7 μs, and the soft reading pulse of the z-filter was optimized to 10 μs. 48 scans were collected for each of 88 t_1 points, using a recycle delay of 1 s. Spectra were processed using commercial software (VNMRJ, Agilent) and modest line broadening (100 Hz) was used in processing the ^{27}Al 3QMAS NMR data. For each resonance in the 3QMAS NMR spectra, the centers of gravity in the MAS and isotropic

dimensions, δ_2^{CG} and δ_{iso}^{CG}, were used to calculate the isotropic chemical shift (δ_{CS}) and the quadrupolar coupling product (P_q) according to

$$\delta_{CS} = \frac{10}{27}\delta_2^{CG} + \frac{17}{27}\delta_{iso}^{CG} \quad (1)$$

and

$$P_q = \left(\delta_{iso}^{CG} - \delta_2^{CG}\right)^{1/2} * f(S) * \nu_0 * 10^{-3}, \quad (2)$$

where $f(S) = 10.244$ for spin-5/2 nuclei (^{27}Al), and ν_0 is the resonance frequency of the quadrupolar nucleus in MHz [34]. P_q from Eq. (2) can be related to the quadrupolar coupling constant (C_q) as $P_q = C_q(1 + \eta_{|q}^2/3)^{1/2}$, where η_q is the quadrupolar coupling asymmetry parameter. P_q and C_q are often used interchangeably, with small errors introduced when neglecting the contribution of η_q.

3. Results and discussion

3.1. Glass transition temperature and density

As given in Table 1, T_g increases with increasing Al_2O_3/Na_2O ratio. This is because the number of non-bridging oxygens per tetrahedrally coordinated cation (NBO/T) decreases with increasing Al_2O_3/Na_2O ratio, i.e., the network connectivity increases. Values of NBO/T are also given in Table 1, which have been calculated from the analyzed compositions by assuming that all available Na^+ ions are used for charge-balancing Al tetrahedra and by neglecting the presence of oxygen triclusters and free oxide. The compositional variation of density is shown in Fig. 1a. Density increases with increasing Al_2O_3 content throughout the studied peralkaline composition space. The measured values of T_g and densities are generally in agreement with those reported previously [1,36].

For all glass compositions, the density increases approximately linearly with the applied pressure (Fig. 1a). Since the Al_2O_3-for-SiO_2 substitution changes the average molar mass of the glasses, we calculated the atomic packing factor (APF) of the glasses to evaluate differences in free volume. APF is the ratio between the minimum theoretical volume occupied by the ions (assumed to be spherical) and the corresponding molar volume of the glass. The assumed coordination numbers (2 for O, 4 for Si and Al^{IV}, 5 for Al^{V}, and 6 for Na) along with the corresponding effective ionic radii of Shannon [37] have been used to calculate the minimum theoretical volume occupied by the ions. We note that the average coordination number of Na in peralkaline aluminosilicate glasses is in the range 6–8 [38–40], which would change the absolute values of APF by maximum 1–2%. The molar volume is calculated as the ratio between the molar mass and measured density from Table 1. We find that SiO_2-rich glasses have a larger atomic packing factor and thus smaller free volume than the Al_2O_3-rich compositions (Fig. 1b).

Based on the linear relation between density and applied pressure for each glass (Fig. 1a), we calculate the irreversible plastic compressibility, which is defined as $-(1/V)(dV/dp)$. This is the volume change measured after decompression to ambient pressure. We find that the plastic compressibility is larger in the SiO_2-rich glasses (Table 1). This is not in agreement with the observed trend in APF, since the glasses with smaller free volume are more prone to network compaction upon pressure treatment at elevated temperature. Instead, it appears that the plastic compressibility of the glasses is positively correlated to NBO/T as shown in Fig. 1c. That is, flexible glasses containing NBOs exhibit a larger capability to undergo densification.

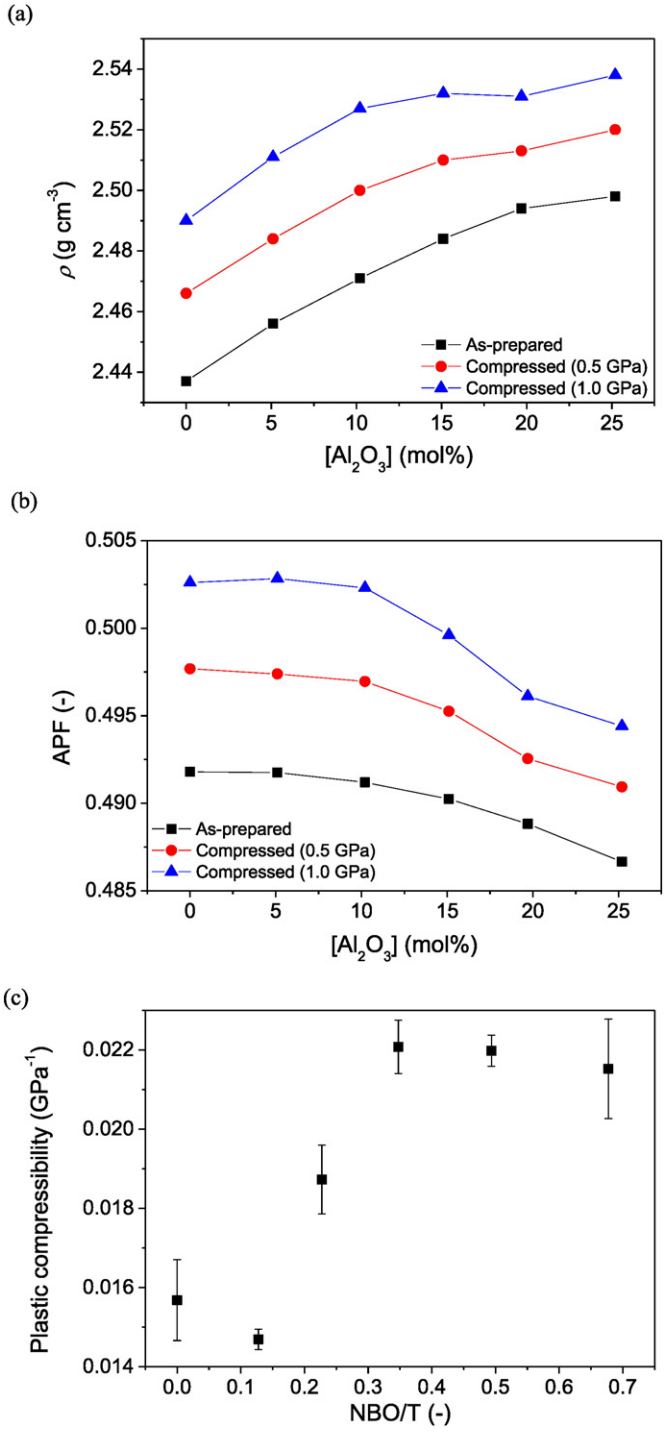

Fig. 1. (a) Density ρ and (b) atomic packing factor APF of the as-prepared and compressed sodium aluminosilicate glasses as a function of the Al_2O_3 content. Errors associated with the ρ and APF results are smaller than the size of the symbols. APF is calculated as the ratio between the minimum theoretical volume occupied by the ions and the corresponding molar volume of the glass. (c) Plastic compressibility as a function of the calculated number of non-bridging oxygens per tetrahedrally coordinated cation NBO/T. Plastic compressibility is calculated from the slopes of the linear fits to density vs. pressure for each composition.

3.2. Hardness and crack resistance

Vickers hardness has been determined by micro-indentation at 9.81 N and is a measure of the ability of the glasses to resist elastoplastic deformation. Hardness increases with increasing Al/Na ratio and then appears to saturate around $[Al_2O_3] = [Na_2O] = 25$ mol% (Fig. 2). This composition dependence is likely caused by the reduction in the number of NBOs with increasing Al/Na ratio [36]. The reduction in the number of NBOs increases the rigidity of the network [41], which in turn decreases the ability of the glass to deform. Isostatic compression

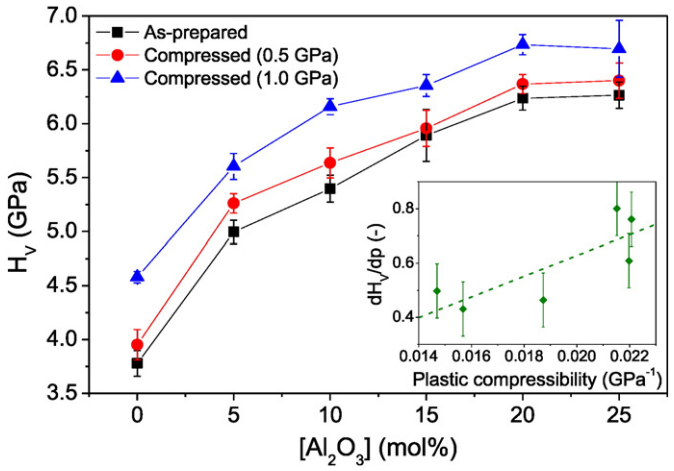

Fig. 2. Vickers hardness (H_V) of the as-prepared and compressed sodium aluminosilicate glasses as a function of the Al_2O_3 content. H_V was measured at an indentation load of 0.98 N. Inset: dependence of the slopes of the hardness vs. pressure curves (dH_V/dp) on the plastic compressibility for the six glasses. The dashed line is a guide for the eye.

increases the hardness of all compositions (Fig. 2). The pressure-induced increase in hardness has been shown to be related to the ability of the glass to deform under the indentation tip. The glass volume available for densification beneath the indentation tip in the as-prepared glass is larger than that in the corresponding isostatically compressed glass, resulting in a larger resistance to densification and an increase in hardness [42]. As shown in the inset of Fig. 2, we find an apparent positive relation between the slope of the hardness vs pressure (dH_V/dp) and the plastic compressibility, suggesting that the overall network densification is responsible for the increase in hardness upon compression.

Crack initiation occurs at sufficiently high loads in a Vickers indentation test and has been attributed to the mismatch between the plastically deformed volume and the surrounding elastically deformed matter [43–45]. The crack resistance (CR) is derived as the load at which an average of two radial cracks form. CR decreases with increasing Al/Na ratio (Fig. 3), presumably due to a decrease in the densification ability of glass as NBOs are removed from the network. A glass that can be easily densified allows for decrease in the residual stress around the indent, which results in an increase in crack resistance [46]. Hence, the decrease in densification ability as the glass becomes more rigid decreases its crack resistance. The pressure-induced decrease in crack resistance is related to the densification of the glass during hot isostatic compression, which decreases the ability of the glass to deform further during subsequent indentation. The decrease in densification degree following isostatic compression increases the residual stress around the indent, which results in a decrease in crack resistance [42,46].

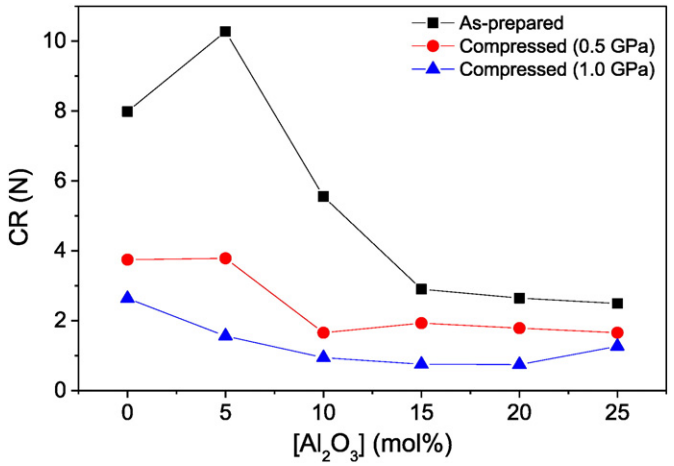

Fig. 3. Crack resistance (CR) of the as-prepared and compressed sodium aluminosilicate glasses as a function of the Al_2O_3 content. CR is defined as the load causing 50% radial crack probability.

3.3. Raman spectroscopy

Raman spectroscopy has been used to study the structural differences in the glass series due to differences in their composition and pressure history. The Raman spectra are all collected on glasses at ambient conditions and can be divided into three regions: low frequency region (250–700 cm^{-1}), intermediate frequency region (700–870 cm^{-1}), and high frequency region (870–1300 cm^{-1}). We note that when interpreting Raman spectra, it is not possible to distinguish between Al and Si based tetrahedra [38]. Q^n will refer to tetrahedrally coordinated Si^{4+} or Al^{3+} with n bridging oxygens and 4-n non-bridging oxygens. In general, our observations are in agreement with previous Raman results on related sodium aluminosilicate glasses [47–50].

First we consider the annealed glasses prior to isostatic compression (Fig. 4). In the low frequency region, two distinct bands are observed. The Raman shift and intensity of these signals depend on the Al/Na ratio. In the Al_2O_3-free glass (Al-0), they are located at ~540 cm^{-1} with a shoulder at ~600 cm^{-1}, corresponding to Q^3 units and three-membered tetrahedral rings in the glass, respectively [38]. When the Al_2O_3 content increases, the Raman shifts of the two bands decrease, approaching ~490 and ~560 cm^{-1}, respectively, in the Al-25 glass, which are illustrated in Fig. 5 for the band at ~500 cm^{-1}. For the Al_2O_3-containing glasses, the band at ~500 cm^{-1} likely corresponds to Q^4 units [50]. For Al-5, the higher frequency band is split into two peaks at ~580 and ~590 cm^{-1}, corresponding to three-membered rings containing one or more Al atoms and pure SiO_4 three-membered rings, respectively [48]. The existence of two distinct signals is explained by the substitution of Al_2O_3 into the glass, decreasing the bond strength in the Al-containing tetrahedral rings and therefore shifting the signal towards lower frequencies [38]. Furthermore, the intensity of the lower frequency band at ~540 cm^{-1} in the Al_2O_3-free glass indicates that a significant proportion of Q^3 units are present in the glass, whereas the intensity of the band at ~500 cm^{-1} in the Al_2O_3-containing glasses indicates the presence of an increasing proportion of Q^4 units with increasing Al_2O_3 content [38]. The long tail at lower frequencies (~250 to ~450 cm^{-1}), which is observed in all glasses (Fig. 4), is caused by the stretching of O atoms in large tetrahedral rings with five or more members [38].

In the intermediate frequency region, one broad band can be found. The contributions to the band in this region are strongly convoluted and poorly known [51], but we note that the peak position systematically

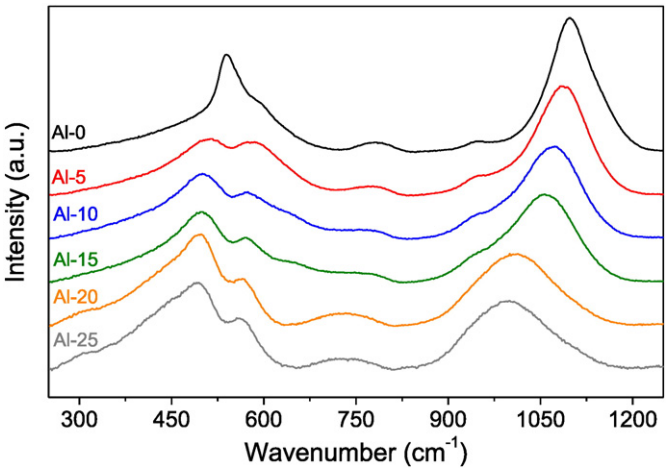

Fig. 4. Raman spectra of the as-prepared sodium aluminosilicate glasses.

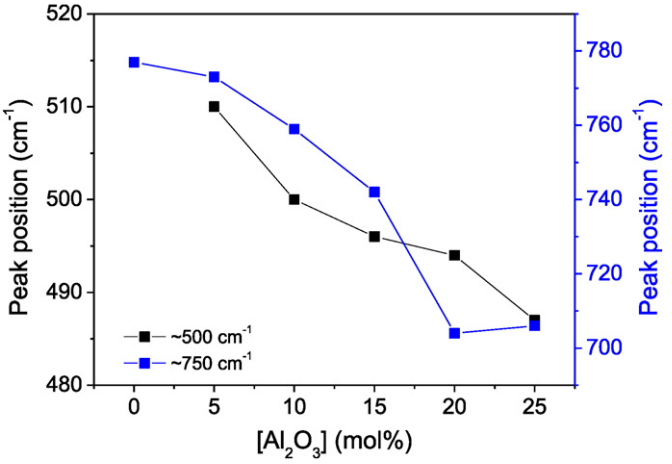

Fig. 5. Peak positions of the Raman bands around 500 and 750 cm^{-1}, respectively, for the as-prepared sodium aluminosilicate glasses as a function of the Al_2O_3 content.

shift towards lower frequencies when substituting Al_2O_3 for SiO_2 (Fig. 5). This is explained by a decrease in bond strength due to a decrease in the force constant as SiO_2 and Al_2O_3 mix [52]. In the high frequency region, two bands are visible in the Raman spectra of the low-Al_2O_3 glasses (Al-0 to Al-15), while only one band is evident in the high-Al_2O_3 glasses (Al-20 and Al-25) due to peak broadening and change of peak position. The position of these bands depend on the Al/Na ratio, i.e., for Al-0 the signals appear around 950 and 1100 cm^{-1} and then at lower frequencies as the Al_2O_3 content increases. These broad bands have been attributed to stretching vibrations of T-O bonds (T = Si, Al) [53,54] and different peaks are convoluted in them. Previously three to five Gaussian peaks have been used for fitting and deconvolution [55,56]. Such spectral deconvolution can reveal quantitative changes in the *Q*-speciation of the tetrahedral units, i.e., changes in connectivity as a function of the Al/Na ratio. An example of deconvolution of the high frequency band is shown in Fig. 6a for the Al-10 glass. The Gaussian peaks are Q^2 (~950 cm^{-1}), Q^3 (~1050 cm^{-1}), $Q^{4,I}$ (~1125 cm^{-1}), $Q^{4,II}$ (~1100 cm^{-1}), and Q^n (~1000 cm^{-1}) units, which originate from Si—O^- in Q^2 units [38], Si—O^- in Q^3 units [38], two Q^4 units with two different local environments [38], and TO_4 tetrahedra [48], respectively. The Q^2 and Q^3 peaks are not used to fit the spectrum for Al-25 since no NBOs are expected in this glass composition.

We note that the deconvolution does not give "true" concentrations as the intensity does not only depend on the concentration of the specific structural unit, but also on the local environment, such as next-nearest neighbors and number of NBOs etc. Instead, spectral fitting can be used to qualitatively describe variations in relative proportions of different structural units [51]. The relative areas of the Gaussian peaks used for the deconvolution of these high-frequency bands are shown in Fig. 6b, which reveals an increase in network connectivity with increasing Al/Na ratio. This is comparable to a recent study of compositionally similar glasses [38]. With the addition of alumina, the relative concentration of $Q^{4,II}$ increases at the expense of species with NBOs, i.e., Q^2 and Q^3, since Na^+ is used for charge-compensation of Al^{3+} in tetrahedral configuration rather than depolymerization of the network. This is coherent with the general structural model of modified aluminosilicate glasses and the changes in the Raman bands at 490 and 540 cm^{-1} as described above. The deconvolutions suggest that Al^{3+} will preferably enter the network as smaller-angle $Q^{4,II}$ units rather than larger-angle $Q^{4,I}$ units. This preference is explained by the smaller Al—O—Si tetrahedral angles relative to the Si—O—Si tetrahedral angles [38].

Compression of bulk glasses at elevated temperature has been shown to be associated with changes in short- and intermediate-range glass structure [57–60]. Pressure-induced changes in the Raman spectra

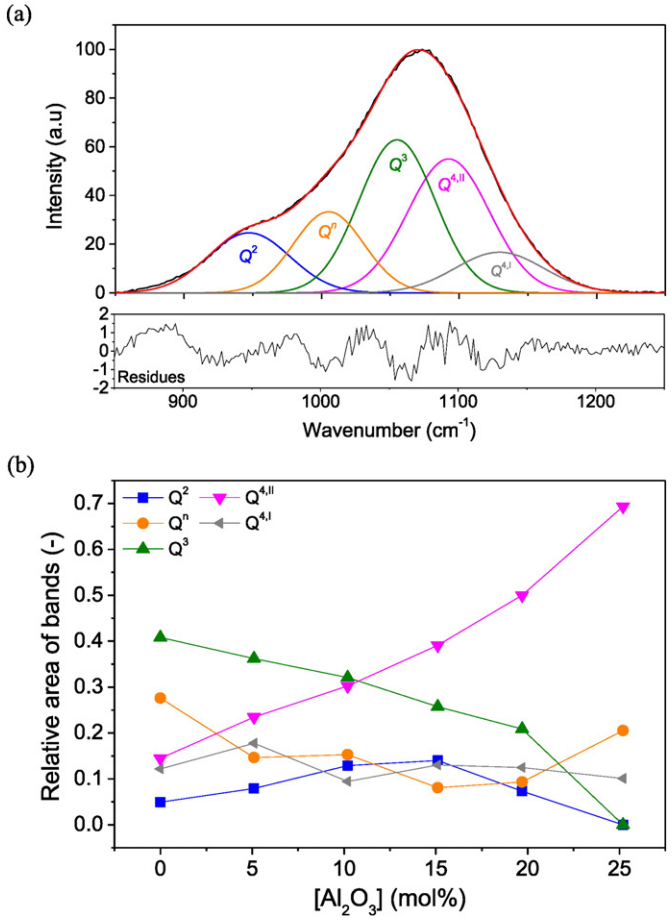

Fig. 6. Deconvolution of the 850–1250 cm^{-1} frequency range of the Raman spectra for the as-prepared sodium aluminosilicate glasses. (a) Example of deconvolution for the as-prepared Al-10 glass. Peaks near 950, 1000, 1050, 1100, and 1125 cm^{-1} are due to vibrations of Q^2, Q^n, Q^3, $Q^{4,II}$, and $Q^{4,I}$, respectively (see the text for details). (b) Relative areas of these Raman bands for the as-prepared glasses as a function of the Al_2O_3 content.

of aluminosilicate glasses have been found to involve decrease in the relative intensity of the low-frequency region compared to the high-frequency region and changes in the relative intensity of different peaks in the low-frequency region [26]. This effect has been attributed to a suppression of vibrational motion, either by the formation of triclusters, or by a development of bonding character between modifiers and BOs, both of which would inhibit vibrational motions of

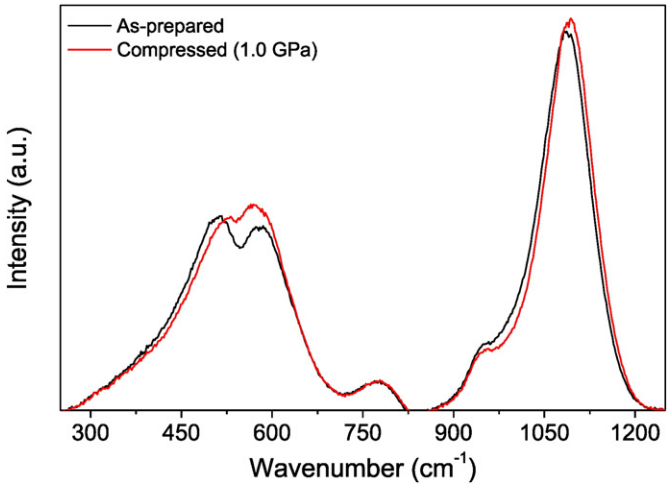

Fig. 7. Raman spectra of the as-prepared and compressed (at 1.0 GPa) Al-5 glass.

BOs resulting in a decrease in intensity [26]. Comparison of the acquired Raman spectra of all the as-prepared and compressed glasses in the present study generally does not reveal such decrease in intensity of the low-frequency region relative to the high-frequency region. We have illustrated this in Fig. 7 for the Al-5 glass, which exhibits the largest increase in density and hardness. Instead we next consider ^{27}Al NMR spectroscopy to study the pressure-induced structural changes.

3.4. ^{27}Al NMR Spectroscopy

Fig. 8a shows ^{27}Al MAS NMR spectra of the as-prepared aluminosilicate glasses. These spectra are characterized by an intense peak centered around 60 ppm, which moves to higher frequencies with increasing Al_2O_3 content. This resonance corresponds to four-fold coordinated aluminum (Al^{IV}), and the change in MAS NMR shift with Al_2O_3 content is consistent with the changes in next-nearest neighbor cations (Si or Al). The Al-5 glass, with smallest MAS NMR shift, has Al^{IV} surrounded by silicon, while the high Al_2O_3 glasses, with MAS NMR shifts approaching 62 ppm, have more instances where aluminum has replaced silicon as a next-nearest neighbor cation [61]. This is consistent with mixing of the Al and Si tetrahedra in these networks, as demonstrated by the Raman spectroscopy results discussed above.

In addition to Al^{IV} groups, there is some evidence for higher coordination sites (Al^{V}) in some of these as-prepared glasses. The two compositions with lowest Al_2O_3 content, Al-5 and Al-10, exhibit an additional MAS NMR signal around 20 ppm, as shown in the inset to Fig. 8a. This resonance is consistent with Al^{V} groups, which are unexpected for these highly peralkaline glasses. Furthermore, this Al^{V} resonance near 20 ppm is decreasing in intensity with increasing Al_2O_3 content, and is completely absent for the Al-25 glass, which is the only glass with $Al_2O_3 = Na_2O$. This behavior in Al^{V} concentration with glass composition is rather unusual given the prevailing models for Al^{IV} compensation in peralkaline aluminosilicate glasses. However, there have been a couple of related studies showing non-zero Al^{V} concentrations in highly peralkaline glasses, including the sodium aluminosilicate system [62]. This work by Malfait and co-workers suggested that the exchange between NBO and Al^{V} groups was at least partially responsible for the presence of Al^{V} in peralkaline compositions. In the case of Al-5 and Al-10 glasses in the present work, the NBO content is quite high (Table 1) and it is possible that more Al^{V} polyhedra can be energetically stabilized in such glasses. The presence of higher coordinated Al in the most peralkaline glasses is also consistent with an unexpected observation of Ga^{VI} groups in chalcogenide glasses having sufficient phosphorus content to fully stabilize Ga in tetrahedral coordination [63].

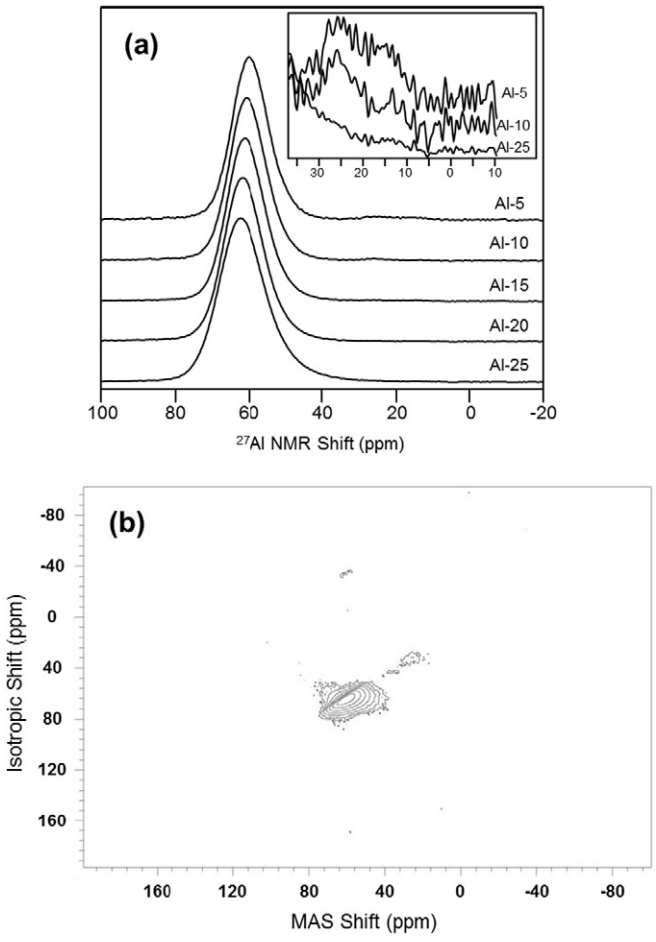

Fig. 8. (a) ^{27}Al MAS NMR spectra for the five as-made glasses with compositions shown to the right of each spectrum. The inset shows an expanded view of the shift region for Al^{V} and Al^{VI} for three as-made glasses having a range of Al_2O_3 content. (b) ^{27}Al 3QMAS NMR spectrum for the as-made Al-5 glass. Contours are drawn to display Al^{IV} and Al^{V} peaks, as well as a very weak Al^{IV} spinning sideband to the top of the main peaks.

A better understanding of the Al environments in these glasses is achieved through analysis of the ^{27}Al 3QMAS NMR spectra, where the positions in both MAS and isotropic dimensions are used to separate isotropic chemical shifts from quadrupolar coupling induced shifts, both of which contribute to the MAS NMR shifts in Fig. 8a. These data also provide enhanced spectral resolution and are often used to identify aluminum sites with different coordination numbers [64]. The two-dimensional contour plot in Fig. 8b, for the as-prepared Al-5 glass, shows two distinct resonances, assigned to Al^{IV} and Al^{V} groups, confirming the peak assignments in the corresponding MAS NMR data. The 3QMAS NMR spectra for these glasses also indicate that octahedral Al (Al^{VI} groups) do not appear to be present in any of the as-made glasses. This means that the extra intensity in the inset to Fig. 8a, attributed to Al^{V}, does indeed belong only to Al^{V} groups, with little to no contribution from Al^{VI}. δ_{CS} and P_q, the calculations of which are described in Section 2.5, are given in Table 2 for all of the as-prepared glasses. The trend in δ_{CS}, which accounts for the changing MAS NMR shifts of Fig. 8a, confirms an increase in chemical shielding of 4 ppm between the low and high Al_2O_3 glasses. Such changes in Al^{IV} environment are consistent with a gradual change in the local configuration of these tetrahedral network elements, especially in the identity of next-nearest neighbor cations. Previous NMR studies of glasses in the sodium aluminosilicate ternary indicate essentially no change in the chemical shift of Al^{IV} groups as Al_2O_3 content is increased [38]. Their interpretation was for Al^{IV} groups being surrounded entirely by silica tetrahedra, regardless of the glass composition and consistent with the Lowenstein rule of aluminum avoidance (i.e., no Al—O—Al connectivity) [65]. However, the data in Fig. 8a and Table 2 clearly indicate that the Al^{IV} groups are progressively deshielded with increasing [Al_2O_3] in the current study, suggesting some violation of the aluminum avoidance.

Table 2
^{27}Al NMR parameters determined from 3QMAS NMR spectroscopy. Uncertainties in δ_{CS}, P_q and Intensity are on the order of ±0.2 ppm, ±0.2 MHz and ±0.5%, respectively.

Glass	Al^{IV}			Al^{V}			Al^{VI}		
	δ_{CS} (ppm)	P_q (MHz)	Int (%)	δ_{CS} (ppm)	P_q (MHz)	Int (%)	δ_{CS} (ppm)	P_q (MHz)	Int (%)
Al-5	62.8	4.42	99.4	29.9	4.69	0.6			
Al-5, 1 GPa	62.8	4.69	97.0	29.3	4.98	3.0	−1	4.6	–
Al-10	63.6	4.54	99.7	31	5.28	0.3			
Al-10, 1 GPa	63.8	4.69	98.8	29.7	5.15	1.2			
Al-15	64.3	4.76							
Al-15, 1 GPa	64.5	4.83	99.7	29.6	4.73	0.3			
Al-20	65.3	5.01							
Al-20, 1 GPa	65.6	5.28							
Al-25	66.8	5.82							
Al-25, 1 GPa	67.0	5.94							

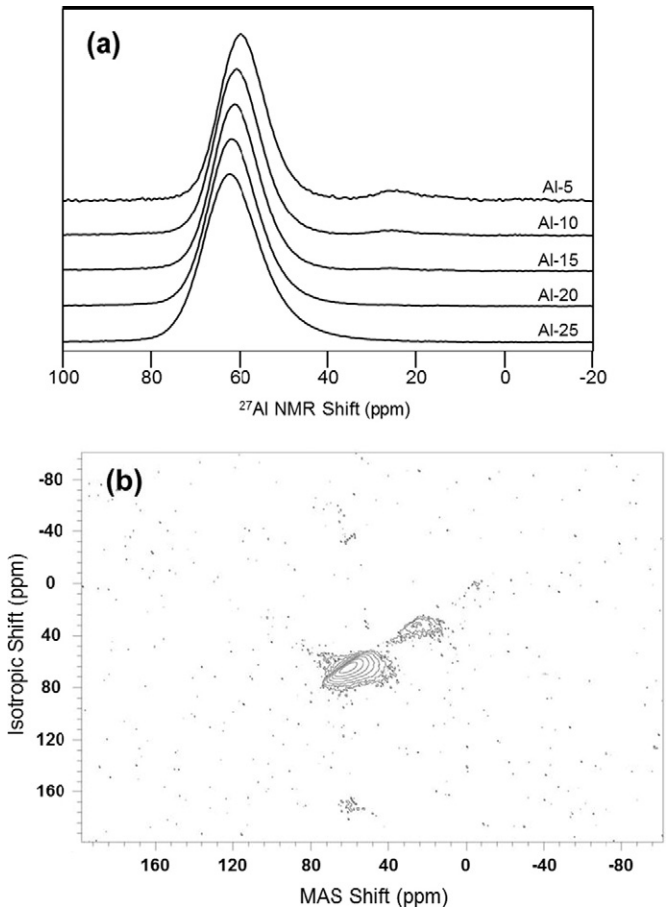

Fig. 9. (a) ^{27}Al MAS NMR spectra for the five compressed (at 1.0 GPa) glasses with compositions shown to the right of each spectrum. (b) ^{27}Al 3QMAS NMR spectrum for the compressed Al-5 glass. Contours are drawn to display Al^{IV} and Al^{V} peaks, as well as a very weak Al^{IV} spinning sideband to the top of the main peaks.

In addition to changes in isotropic chemical shift, the Al^{IV} groups in these glasses also are characterized by a progressively larger P_q (Table 2), pointing towards higher distortion of the tetrahedral units with increasing Al_2O_3. This has been associated with changing Al—O bond distances or possibly a change in interaction between the Al^{IV} tetrahedra and charge-compensating sodium cations [38].

Compressed analogues to these sodium aluminosilicate glasses have also been examined with ^{27}Al MAS and 3QMAS NMR spectroscopy. The ^{27}Al MAS NMR spectra for the five compressed glasses are plotted in Fig. 9a, showing that most aluminum remains in Al^{IV} polyhedra upon compression, but given the more apparent Al^{V} signal around 30 ppm, also shows that some aluminum has been forced into Al^{V} groups with compression. The increased intensity of the Al^{V} peak is also evident in ^{27}Al 3QMAS NMR spectra of these compressed glasses, as shown by the contour plot for Al-5 in Fig. 9b. The contours for Al^{V} are indeed more intense after compression of the glass. Full analysis of δ_{CS} and P_q for the compressed glasses are given in Table 2. The Al^{IV} groups in the compressed glasses exhibit nearly identical chemical shifts as in their as-made counterparts, indicating the close similarity in structural environment for Al^{IV} polyhedra before and after compression. In other words, compression does not appear to lead to any change in how Al^{IV} groups are connected into the glass network (e.g., Al—O—Si and Al—O—Al bonding). However, there are distinct changes in P_q with compression, where for all glass compositions, the P_q values increase with this treatment. This does indicate that the symmetry around Al^{IV} polyhedra is impacted by pressure, and the larger magnitude of the quadrupolar coupling parameter suggests more distortion after compression. Changes in Al^{V} parameters, both δ_{CS} and P_q, are less systematic with composition and in fact are probably insignificant given the low abundance of Al^{V} and correspondingly low signal-to-noise ratio in the NMR data. δ_{CS} is around 30 ppm for Al^{V} in both as-made and compressed glasses, consistent with other studies of Al^{V} in aluminosilicates [49,66]. Likewise, the P_q values around 5 MHz are also similar between as-made and compressed glasses.

The largest change in aluminum speciation due to glass compression is a change in Al^{IV} and Al^{V} site populations. The ^{27}Al NMR spectra in Figs. 8 and 9 indicate an increase in Al^{V} concentration with compression, which is quite apparent when comparing the isotropic projections from ^{27}Al 3QMAS NMR (Fig. 10). Here, isotropic data from the 3QMAS NMR experiments are overlaid for each glass composition, showing an increase in Al^{V} content for the two glasses with these polyhedra in their as-made forms (Al-5 and Al-10), as well as the appearance of Al^{V} in the Al-15 glass only after compression. All other compressed glasses do not exhibit Al^{V} resonances in their ^{27}Al MAS and 3QMAS NMR data, and thus the concentration of Al^{V} in these glasses is negligible. As shown by the comparisons in Fig. 10, aluminum coordination is sensitive to compression, similar to previous work on commercial aluminosilicates [18], and also the fictive temperature dependence of Al speciation in aluminosilicates [67]. The main change in Al coordination number occurs in glasses which already contained a non-zero Al^{V} population and high NBO content in their pre-compressed states (Fig. 11). Al-5 shows an increase of approximately 2.5%, compared to 1% and 0.3% in the Al-10 and Al-15 glasses, respectively (Table 2).

The effects of NBOs and compression on the generation of Al^{V} is shown in Fig. 11, where NBOs and pressure is positively correlated to the presence of Al^{V}. In agreement with our result, a larger pressure-

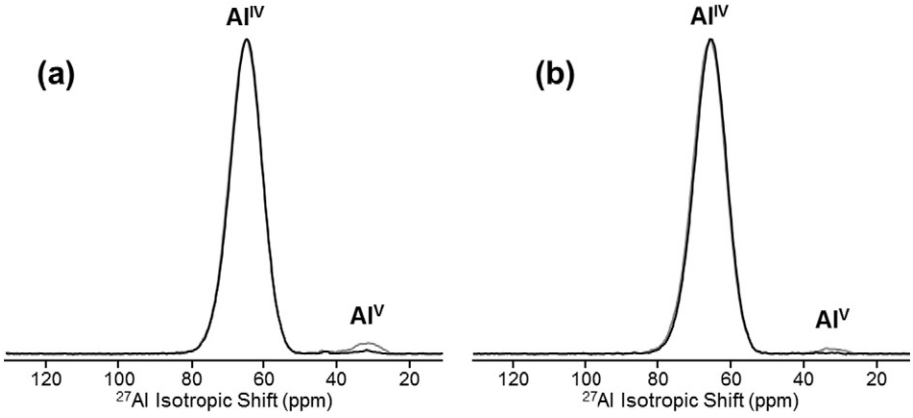

Fig. 10. Isotropic projections from the ^{27}Al 3QMAS NMR spectra of (a) Al-5 glasses and (b) Al-10 glasses, where as-made glasses are shown in black and compressed glasses (at 1.0 GPa) are shown in gray. Al^{IV} and Al^{V} resonances are denoted.

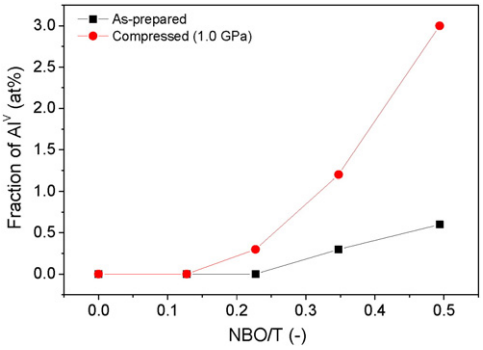

Fig. 11. Fraction of five-fold coordinated aluminum (Al^{V}) as a function of the calculated number of non-bridging oxygens per tetrahedrally coordinated cation NBO/T for as-prepared and compressed (at 1.0 GPa) sodium aluminosilicate glasses.

induced generation of Al^{V} in aluminosilicate glasses with NBOs has previously been reported in literature [68–70]. For such glasses, the simple proposed mechanism in the studied pressure range is $Al^{IV} + NBO \leftrightarrow Al^{V}$. This mechanism has been directly supported by changes in the oxygen speciation as probed by ^{17}O 3Q MAS NMR spectroscopy [68]. Although not observed herein at 1 GPa, pressure-induced formation of Al^{V} has also been reported in sodium aluminosilicate glasses with little or no NBO (e.g., albite $NaAlSi_3O_8$) [70,71], suggesting that alternative mechanisms could also be at play at higher pressure ranges, e.g., when most of the NBOs have already been consumed in increasing the aluminum coordination number. For example, this could involve formation of NBO and oxygen triclusters and subsequent consumption of NBO to form Al^{V} [10,64,70], or transformation of a BO to be coordinated with Al^{V} through formation of oxygen tricluster [70,71]. Finally, we note that in addition to changes in Al^{V} concentration, the most peralkaline glass (Al-5) also shows a small, but detectable amount of Al^{VI}, but only after compression (Fig. 8). This is the only glass, both as-made or compressed, showing any evidence for 6-fold coordinated Al, presumably because Al^{VI} could be formed by a similar mechanism to that of Al^{V}, i.e., $Al^{IV} + 2NBO \leftrightarrow Al^{VI}$.

4. Conclusion

We have investigated the effect of 1 GPa compression at elevated temperature on structure and mechanical properties of aluminosilicate glasses with varying Al/Si ratio and thus non-bridging oxygen content. Raman and ^{27}Al NMR spectroscopy, density, and Vickers indentation measurements have been performed. We find that the plastic compressibility (i.e., extent of permanent densification) is positively correlated to the number of non-bonding oxygens per tetrahedral (NBO/T), i.e., the network flexibility. Hardness increases while the resistance to initiate radial/median cracks decreases with decreasing NBO/T in the as-made glasses. Upon compression, hardness increases and crack resistance decreases as the ability of the glass to densify decreases upon compression and larger changes in these mechanical properties are found in the high-NBO compositions, consistent with the higher plastic compressibility of these glasses. The Raman spectroscopy measurements on the as-made glasses confirm the expected changes in Q speciation with Na/Al ratio, whereas no major pressure-induced structural changes are evident from the Raman spectra. The ^{27}Al NMR and Raman data both confirm the mixing of the aluminosilicate network, especially as evidenced by the change in chemical shift for the Al^{IV} resonance. Surprisingly, we find the presence of Al^{V} in the as-made glasses, especially when these polyhedra are present only in the most peralkaline glass compositions. Moreover, there is a larger pressure-induced generation of Al^{V}, and in one case Al^{VI}, in aluminosilicate glasses with NBOs. Their presence not only shows a more complicated relationship between Al coordination and NBO content, but also plays a substantial role in the compressibility of these glasses.

Acknowledgements

We thank Mouritz N. Svenson for assistance with Raman spectroscopy. M.M.S. acknowledges the financial support from the Danish Council for Independent Research under Sapere Aude: DFF-Starting Grant (1335-00051A). S.J.R. acknowledges the support from the National Science Center of Poland under Grant No. UMO-2011/03/B/ST3/02352. A part of the research was supported by U.S. Army Research Laboratory, under the direction of Dr. Parimal Patel.

References

[1] D.E. Day, G.E. Rindone, J. Am. Ceram. Soc. 45 (1962) 579–581.
[2] M. Taylor, G.E. Brown, Geochim. Cosmochim. Acta 43 (1979) 1467–1473.
[3] P. McMillan, B. Piriou, A. Navrotsky, Geochim. Cosmochim. Acta 46 (1982) 2021–2037.
[4] D.A. McKeown, F.L. Galeener, G.E. Brown, J. Non-Cryst. Solids 68 (1984) 361–378.
[5] F. Seifert, B.O. Mysen, D. Virgo, Am. Mineral. 67 (1982) 696–717.
[6] E.F. Riebling, J. Chem. Phys. 44 (1966) 2857–2865.
[7] S.H. Risbud, R.J. Kirkpatrick, A.P. Taglialavore, B. Montez, J. Am. Ceram. Soc. 70 (1987) C10–C12.
[8] M.J. Toplis, S.C. Kohn, M.E. Smith, I.J.F. Poplett, Am. Mineral. 85 (2000) 1556–1560.
[9] E.D. Lacy, Phys. Chem. Glasses 4 (1963) 234–238.
[10] M.J. Toplis, D.B. Dingwell, T. Lenci, Geochim. Cosmochim. Acta 61 (1997) 2605–2612.
[11] D. Iuga, C. Morias, Z. Gan, D.R. Neuville, L. Cormier, D. Massiot, J. Am. Chem. Soc. 127 (2005) 11540–11541.
[12] D.E. Day, G.E. Rindone, J. Am. Ceram. Soc. 45 (1962) 489–496.
[13] T.D. Taylor, G.E. Rindone, J. Am. Ceram. Soc. 53 (1970) 692–695.
[14] J.E. Shelby, R.J. Eagan, J. Am. Ceram. Soc. 59 (1976) 420–425.
[15] M.M. Smedskjaer, R.E. Youngman, J.C. Mauro, J. Non-Cryst. Solids 381 (2013) 58–64.
[16] P.S. Salmon, A. Zeidler, J. Phys. Condens. Matter 27 (2015) 133201.
[17] M.M. Smedskjaer, S.J. Rzoska, M. Bockowski, J.C. Mauro, J. Chem. Phys. 140 (2014) 054511.
[18] M.N. Svenson, L.M. Thirion, R.E. Youngman, J.C. Mauro, S.J. Rzoska, M. Bockowski, M.M. Smedskjaer, ACS Appl. Mater. Interfaces 6 (2014) 10436–10444.
[19] D.R. Uhlmann, J. Non-Cryst. Solids 13 (1973) 89–99.
[20] A. Yamada, S.J. Gaudio, C.E. Lesher, J. Phys. Conf. Ser. 215 (2010) 012085.
[21] J.L. Yarger, K.H. Smith, R.A. Nieman, J. Diefenbacher, G.H. Wolf, B.T. Poe, P.F. McMillan, Science 270 (1995) 1964–1967.
[22] S.K. Lee, G.D. Cody, Y.W. Fei, B.O. Mysen, Geochim. Cosmochim. Acta 68 (2004) 4189–4200.
[23] S.K. Lee, G.D. Cody, Y. Fei, B.O. Mysen, Chem. Geol. 229 (2006) 162–172.
[24] J.R. Allwardt, J.F. Stebbins, B.C. Schmidt, D.J. Frost, A.C. Withers, M.M. Hirschmann, Am. Mineral. 90 (2005) 1218–1222.
[25] G.H. Wolf, D.J. Durben, P.F. McMillan, J. Chem. Phys. 93 (1990) 2280–2288.
[26] B.T. Poe, C. Romano, N. Zotov, G. Cibin, A. Marcellli, Chem. Geol. 174 (2001) 21–31.
[27] N. Shimizu, I. Kushiro, Geochim. Cosmochim. Acta 48 (1984) 1295–1303.
[28] S.J. Gaudio, T.G. Edwards, S. Sen, Am. Mineral. 100 (2015) 326–329.
[29] D. Sykes, B.T. Poe, P.F. McMillan, R.W. Luth, R.K. Sato, Geochim. Cosmochim. Acta 57 (1993) 1753–1759.
[30] J.F. Stebbins, D. Sykes, Am. Mineral. 75 (1990) 943–946.
[31] M.F. Hochella, G.E. Brown, Geochim. Cosmochim. Acta 49 (1985) 1137–1142.
[32] P. H. Eilers, H. F. M. Boelens, Leiden University Medical Centre (2005).
[33] J.P. Amoureux, C. Fernandez, S. Steuernagel, J. Magn. Reson. Ser. A 123 (1996) 116.
[34] J.P. Amoureux, C. Huguenard, F. Engelke, F. Taulelle, Chem. Phys. Lett. 356 (2003) 497.
[35] M. Wada, H. Furukawa, K. Fujita, Ceram. Soc. Jpn. 11 (1974) 39.
[36] J.E. Shelby, J. Appl. Phys. 49 (1978) 5885–5891.
[37] R.D. Shannon, Acta Crystallogr. A 32 (1976) 751–767.
[38] D.A. McKeown, G.A. Waychunas, G.E. Brown, J. Non-Cryst. Solids 74 (1985) 325–348.
[39] X. Xue, J.F. Stebbins, Phys. Chem. Miner. 20 (1993) 297–307.
[40] A.M. George, J.F. Stebbins, Phys. Chem. Miner. 23 (1996) 526–534.
[41] M.M. Smedskjaer, J.C. Mauro, Y. Yue, Phys. Rev. Lett. 105 (2010) 115503.
[42] Y. Kato, Yoshinari, H. Yamazaki, S. Yoshida, J. Matsuoka, J. Non-Cryst. Solids 356 (2010) 1768.
[43] R. Limbach, A. Winterstein-Beckmann, J. Dellith, D. Möncke, L. Wondraczek, J. Non-Cryst. Solids 417 (2015) 15–27.
[44] R.F. Cook, G.M. Pharr, J. Am. Ceram. Soc. 73 (1990) 787–817.
[45] Z. Zhang, N. Soga, K. Hirao, J. Mater. Sci. 30 (1995) 6359–6362.
[46] K.G. Aakermann, K. Januchta, J.A. Pedersen, M.N. Svenson, S.J. Rzoska, M. Bockowski, J.C. Mauro, M. Guerette, L. Huang, M.M. Smedskjaer, J. Non-Cryst. Solids 426 (2015) 175–183.
[47] C. Le Losq, D.R. Neuville, P. Florian, G.S. Henderson, D. Massiot, Geochim. Cosmochim. Acta 126 (2014) 495–517.
[48] F.A. Seifert, B.O. Mysen, D. Virgo, Am. Mineral. 67 (1982) 696–717.
[49] D.R. Neuville, B.O. Mysen, Geochim. Cosmochim. Acta (1996) 1727–1737.
[50] P. McMillan, B. Piriou, J. Non-Cryst. Solids 53 (1982) 279–298.
[51] B.O. Mysen, A. Lucier, G.D. Cody, Am. Mineral. 88 (2003) 1668–1678.
[52] C. Le Losq, D.R. Neuville, Chem. Geol. 346 (2013) 57–71.
[53] R.J. Bell, N.F. Bird, P. Dean, J. Phys. C 1 (1968) 299–303.
[54] P.N. Sen, M.F. Thorpe, Phys. Rev. B 15 (1977) 4030–4038.

[55] P.F. McMillan, Am. Mineral. 69 (1984) 622–644.
[56] B.O. Mysen, Eur. J. Mineral. 15 (2003) 781–802.
[57] M.M. Smedskjaer, R.E. Youngman, S. Striepe, M. Potuzak, U. Bauer, J. Deubener, H. Behrens, J.C. Mauro, Y. Yue, Sci. Rep. 4 (2014).
[58] M.N. Svenson, T.K. Bechgaard, S.D. Fuglsang, R.H. Pedersen, A.Ø. Tjell, M.B. Østergaard, R.E. Youngman, J.C. Mauro, S.J. Rzoska, M. Bockowski, M.M. Smedskjaer, Phys. Rev. Appl. 2 (2014) 024006.
[59] M.B. Østergaard, R.E. Youngman, M.N. Svenson, S.J. Rzoska, M. Bockowski, L.R. Jensen, M.M. Smedskjaer, RSC Adv. 5 (2015) 78845–78851.
[60] J. Wu, J. Deubener, J.F. Stebbins, L. Grygarova, H. Behrens, L. Wondraczek, Y. Yue, J. Chem. Phys. 131 (2009) 104504.
[61] D.R. Neuville, L. Cormier, V. Montouillout, D. Massiot, J. Non-Cryst. Solids 353 (2007) 180–184.
[62] W.J. Malfait, R. Verel, P. Ardia, C. Sanchez-Valle, Geochim. Cosmochim. Acta 77 (2012) 11–26.
[63] R.E. Youngman, B.G. Aitken, J. Non-Cryst. Solids 345 (2004) 50–55.
[64] M.E. Smith, K.J.D. Mackenzie, Multinuclear solid state NMR of inorganic materials, Pergamon Mater. Ser. (2002).
[65] W. Loewenstein, Am. Mineral. 39 (1954) 92–96.
[66] D.R. Neuville, L. Cormier, D. Massiot, Chem. Geol. 229 (2006) 173–185.
[67] L.M. Thompson, J.F. Stebbins, Am. Mineral. 98 (2013) 1980–1987.
[68] S.K. Lee, G.D. Cody, Y. Fei, B.O. Mysen, Geochim. Cosmochim. Acta 68 (2004) 4189.
[69] J.R. Allwardt, J.F. Stebbins, H. Terasaki, L.S. Du, D.J. Frost, A.C. Withers, M.M. Hirschmann, A. Suzuki, E. Ohtani, Am. Mineral. 92 (2007) 1093.
[70] S.K. Lee, J. Phys. Chem. B 108 (2004) 5889–5900.
[71] S.J. Gaudio, C.E. Lesher, H. Maekawa, S. Sen, Geochim. Cosmochim. Acta 157 (2015) 28.

Paper II

Journal of Non-Crystalline Solids 470 (2017) 145–151

Contents lists available at ScienceDirect

Journal of Non-Crystalline Solids

journal homepage: www.elsevier.com/locate/jnoncrysol

Structure of MgO/CaO sodium aluminosilicate glasses: Raman spectroscopy study

Tobias K. Bechgaard[a], Garth Scannell[b], Liping Huang[b], Randall E. Youngman[c], John C. Mauro[c,*], Morten M. Smedskjaer[a,*]

[a] Department of Chemistry and Bioscience, Aalborg University, DK-9220 Aalborg, Denmark
[b] Department of Materials Science and Engineering, Rensselaer Polytechnic Institute, Troy, NY 12180, USA
[c] Science and Technology Division, Corning Incorporated, Corning, NY 14831, USA

ARTICLE INFO

Keywords:
Aluminosilicate glasses
Structure
Raman spectroscopy

ABSTRACT

Understanding the composition dependence of the atomic structure of multicomponent aluminosilicate glasses is a challenging problem. Aluminum has a crucial influence on the structure-property relations in these systems, but there are still questions regarding its local structural environment. Here, we present results detailing the network structure of twenty quaternary MgO/CaO-Na_2O-Al_2O_3-SiO_2 glasses upon Al_2O_3-for-SiO_2 and MgO-for-CaO substitutions using room temperature and in situ high-temperature Raman spectroscopy. The Raman spectra reveal that the Mg-containing glasses violate the Al-avoidance at lower Al_2O_3 concentration than the Ca-containing glasses. Furthermore, the alkaline earth ions acting as charge-compensators for tetrahedral aluminum are found to have a similar effect on the network structure (Q^n speciation and Al/Si mixing), while they affect the network differently when they are in a modifying role. Increasing cation field strength allows for stabilization of networks with a larger distribution of bond angles.

1. Introduction

Oxide glasses are synthesized by making use of at least one network-former (such as SiO_2, GeO_2, B_2O_3, or P_2O_5), which forms a continuous three-dimensional network, that is typically mixed with one or more network-modifying oxides (such as alkali or alkaline earth oxides). Understanding of the atomic structure of oxide glasses has advanced substantially in recent decades, primarily due to significant improvements in experimental methods and theoretical calculations [1–4]. Also, qualitative structure-property correlations in various glass systems have been demonstrated [1,5–16]. However, quantitative understanding of such correlations is still lacking for most multi-component glass-forming systems.

Silica (SiO_2) and alumina (Al_2O_3) are the two most important network-forming oxides for industrial glasses and also the two most abundant in natural magmatic liquids. Under ambient pressure conditions, Si^{4+} is in tetrahedral coordination in aluminosilicate glasses, while Al^{3+} can adopt various coordination states and thus possess different structural roles [1]. Early studies demonstrated the more complicated impact of Al_2O_3 on viscosity compared to that of SiO_2 [17,18]. A dual structural role of aluminum was suggested to explain this observation, i.e., Al^{3+} can act either as a network-former in tetrahedral coordination or in a charge compensating role in five- or six-fold coordination [19]. It is now well established that Al^{3+} is stabilized in tetrahedral coordination (Al^{IV}) when associated with charge balancing cations (such as Na^+ and Ca^{2+}) [1,20]. In the ideal case, addition of Al_2O_3 to an alkali silicate or alkaline earth silicate glass thus leads to the removal of network-modifying cations from their original role in the network until no more non-bridging oxygen (NBO) atoms remain [21]. When the concentration of Al_2O_3 exceeds that of the network-modifying oxides, Al^{3+} can no longer be charge balanced in tetrahedral configuration and some excess Al^{3+} is forced into higher coordination number as a means of charge-balancing additional Al tetrahedra [22–24]. Most such peraluminous glass systems exhibit a preference for the formation of five-fold over that of six-fold coordinated Al^{3+} [22,25,26]. We note that an alternative hypothesis is that Al^{IV} can be incorporated, even in peraluminous compositions, without the need for a charge-balancing cation through association with a three-coordinated oxygen [27]. A three-coordinated oxygen is shared by three tetrahedral network cations as found in crystalline $CaAl_4O_7$. Such oxygen triclusters have been found in molecular dynamics simulations [28], with additional evidence from viscosity data in the vicinity of the charge-balanced join [29] and nuclear magnetic resonance (NMR) studies on a calcium aluminate glass [30].

* Corresponding authors.
E-mail addresses: mauroj@corning.com (J.C. Mauro), mos@bio.aau.dk (M.M. Smedskjaer).

http://dx.doi.org/10.1016/j.jnoncrysol.2017.05.014
Received 24 March 2017; Received in revised form 11 May 2017; Accepted 12 May 2017
Available online 18 May 2017

The ability of a modifier to charge-compensate Al^{3+} is affected by its size and valence. While the structure of aluminosilicate glasses modified solely by sodium oxide is essentially equivalent to the ideal case with no Al^{V} or Al^{VI} present in peralkaline compositions, the structure of glasses modified by alkaline earth cations, such as Mg^{2+} and Ca^{2+}, is more complex since two charges are confined in the same position. The smaller ionic radius of Mg^{2+} in comparison with Ca^{2+} also causes it to have a different local environment, which affects the aluminosilicate network [31,32]. While the coordination number of Ca^{2+} is believed to be around six to seven [33,34], the local environment of Mg^{2+} is significantly different. Previous work has reached different conclusions and reported the presence of four-, five-, and six-fold coordinated Mg^{2+} [35–43]. The role of Mg^{2+} appears to be between a traditional network modifier and network former, but the detailed structural and topological role of Mg^{2+} remains relatively poorly understood, and its impact on the physical properties is therefore still unclear [44]. The modifier type also affects the mixing of Si^{4+} and Al^{3+} tetrahedra. Al—O—Al structural units have been found to be energetically unfavorable, which is termed Al-avoidance [45]. However, the fraction of Al—O—Al appears to increase with increasing Mg/Ca and Al/Si ratios [46,47]. Moreover, while much work has been done on the ternary alkali aluminosilicate and alkaline earth aluminosilicate systems [1], significantly less attention has been devoted to the more complicated quaternary alkali-alkaline earth aluminosilicate systems [46,48–50]. In these systems, the alkali and alkaline earth cations compete with each other in their interactions with the network forming units. A better understanding of the structural and topological roles of network modifiers and formers is important to provide the link between microscopic structure and the macroscopic properties.

In this study, we investigate the change in network structure upon Al_2O_3-for-SiO_2 and MgO-for-CaO substitutions in sodium aluminosilicate glasses (Fig. 1) using room temperature and in situ high-temperature Raman spectroscopy measurements to detect structural changes at ambient conditions and as a function of temperature. This investigation thus seeks to improve the understanding of the role of Al^{3+} in the silicate network in the presence of both alkali and alkaline earth cations and on the nature of the influence of these cations.

2. Experimental methods

2.1. Sample preparation

We prepared two sets of sodium aluminosilicate glasses with either calcium or magnesium (in mol%): $(76 - x)SiO_2 - xAl_2O_3 - 16Na_2O - 8RO$ with x = 0, 2.7, 5.3, 8, 10.7, 13.3, 16, 18.7, 21.3, and 24 for R = Ca and Mg [51,52]. We included 0.15 mol% SnO_2 as fining agent in all compositions. The batch materials (SiO_2, Al_2O_3, Na_2CO_3, $CaCO_3$, MgO, and SnO_2) were first thoroughly mixed for 60 min using a ball mill. The mixed batch materials were then melted in a covered Pt crucible for 5 h in air at a temperature between 1450 and 1600 °C depending on composition. In order to ensure chemical homogeneity, the melts were first quenched in water, and then the resulting glass pieces were crushed and remelted for 6 h at 1650 °C and finally poured onto a stainless steel plate in air. The homogeneity of the samples was subsequently confirmed through inspection under cross polarized light, showing no evidence of phase separation. The glasses were annealed for 2 h at their respective annealing points. The chemical compositions of the final glasses were determined using x-ray fluorescence and are reported in Table 1. The analyzed compositions were within 0.5 mol% of the nominal ones. All figures and calculations in this paper are made using the analyzed compositions, which are accurate within ± 0.1 mol %.

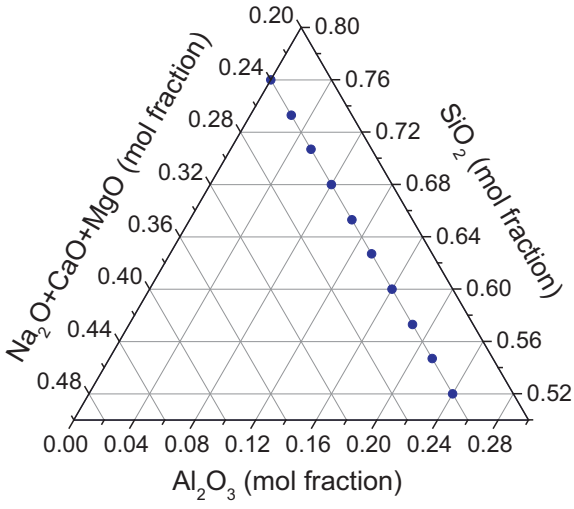

Fig. 1. Ternary molar diagram (SiO_2-Al_2O_3-[Na_2O + CaO + MgO]) showing the investigated glass compositions in this study.

Table 1
Analyzed chemical compositions (in mol%) of the twenty investigated aluminosilicate glasses as determined using x-ray fluorescence. The results are accurate within ± 0.1 mol %.

Glass		Chemical composition (mol%)					
R	x	SiO_2	Al_2O_3	Na_2O	MgO	CaO	SnO_2
Mg	0	75.8	0.1	15.6	8.1	0.2	0.2
Mg	2.7	73.7	2.7	15.7	7.6	0.1	0.2
Mg	5.3	70.9	5.3	15.7	7.9	0.1	0.2
Mg	8	68.1	8.0	15.7	8.0	0.1	0.2
Mg	10.7	65.3	10.7	15.7	8.0	0.1	0.2
Mg	13.3	62.8	13.3	15.8	7.9	0.1	0.2
Mg	16	59.9	16.0	15.8	8.1	0.1	0.2
Mg	18.7	56.6	18.6	15.6	8.9	0.1	0.2
Mg	21.3	54.6	21.3	15.8	8.0	0.1	0.2
Mg	24	52.0	24.0	15.8	8.0	0.1	0.2
Ca	0	75.9	0.0	15.7	0.1	8.1	0.2
Ca	2.7	73.2	2.7	15.8	0.1	8.1	0.2
Ca	5.3	70.7	5.3	15.8	0.1	7.9	0.2
Ca	8	68.1	8.0	15.7	0.1	7.9	0.2
Ca	10.7	65.2	10.7	15.8	0.1	8.0	0.2
Ca	13.3	62.6	13.3	15.8	0.1	8.1	0.2
Ca	16	59.8	16.0	15.8	0.1	8.1	0.2
Ca	18.7	57.2	18.7	15.7	0.1	8.2	0.2
Ca	21.3	54.2	21.3	15.7	0.1	8.4	0.2
Ca	24	51.8	24	15.8	0.1	8.1	0.2

2.2. Raman spectroscopy

Raman spectra were collected both at room temperature and in situ at higher temperatures. To do so, glass samples were optically polished to a thickness of 50–80 μm with two parallel top and bottom surfaces. Grinding and polishing were done using 600 grit SiC sand paper and cerium oxide slurry. The evolution of the glass structure as a function of temperature was monitored by heating up the polished thin samples in a Linkham TS1500 heating stage from room temperature to approximately 100 °C above the glass transition temperature (T_g) of each composition. T_g has been determined in a parallel study based on viscosity measurements [53].

Raman spectra were collected through the top fused quartz window of the Linkham TS1500 in air [54]. A LabRAM HR800 Raman microscope (Horiba Jobin Yvon) was used to carry out the in situ high-temperature light scattering experiments by using a 532 nm Verdi V2 DPSS green laser as the probing light source. In all experiments, a heating rate of 50 °C/min was used. After each temperature was reached, Raman spectra were collected after the temperature inside the heating stage had stabilized for 5 min. Following Refs. [55,56], we have removed the spectral background by fitting a second order

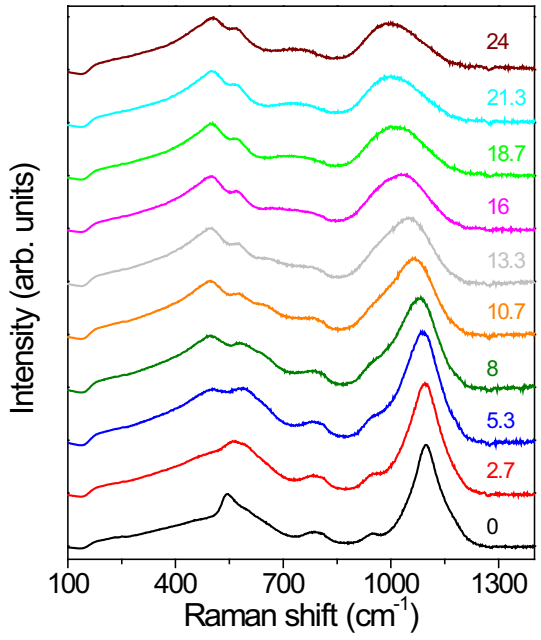

Fig. 2. Room temperature Raman spectra for the Ca-containing glasses. The spectra are shifted vertically for clarity. The numbers refer to the molar Al_2O_3 concentration.

polynomial to the spectral region between 1250 and 1550 cm^{-1} (where no Raman bands are present), extrapolating it to lower frequencies and subtracting it from each spectrum. We applied this empirical background removal protocol, since it results in the highest reproducibility for different spectra of the same sample [55]. A temperature-frequency correction was also applied for each spectrum after the background removal by using the approach described in Ref. [57].

3. Results

3.1. Room temperature Raman spectroscopy

Figs. 2 and 3 show room temperature Raman spectra of the Ca- and Mg-containing glasses, respectively. The Raman spectra exhibit relative strong bands around ~500 cm^{-1} and ~1100 cm^{-1}, in agreement with literature data of silicate glasses containing soda, calcia, magnesia, and alumina [58–62]. For these compositions, Raman spectra are traditionally divided into three regions: the low- (~400–700 cm^{-1}), intermediate- (~700–900 cm^{-1}) and high-frequency (~900–1200 cm^{-1}) regions, each region containing different structural information. The low-frequency regions contains information on ring sizes and their tetrahedral cations, the intermediate region is highly convoluted (i.e., contains several overlapping bands) and rarely used for anything but an evaluation of the change in average bond strength of the network, while the high-frequency region contains information about the concentration of NBO and on Al/Si mixing.

For both the R = Mg, Ca ternary silicate glasses without Al_2O_3 ($x = 0$) the Raman spectra exhibit a strong band around 545 cm^{-1} and a shoulder at ~580 cm^{-1}, typical of sodium-containing silicates. The 545 cm^{-1} band corresponds to a band in similar crystalline analogs [59] and has been assigned to the breathing vibrations of oxygens along T–O–T involving Q^3 species [58,60], that is network tetrahedra with one NBO. The shoulder at 580 cm^{-1} is normally designated to three-membered rings in silicate glasses [61]. In addition to the strong band and its shoulder, the Raman spectra of both the Ca- and Mg-containing glasses have a weak broad band at 650 cm^{-1} and the Mg-containing glasses a band at ~450 cm^{-1}. The band at ~650 cm^{-1} originates from Si–O–Si intertetrahedral linkages and can be found in both calcium silicates and magnesium silicates [63], while the ~450 cm^{-1} band has been reported to be an evidence of regions with very high SiO_2 content, possibly due to phase separation [59]. As seen from the Raman spectrum of a sodium silicate glass with a similar total modifier content as the Ca- and Mg-containing glasses in this study [62], the ~650 cm^{-1} band is not present in the alkaline earth-free glass (Fig. 4). Fig. 4 also indicates the presence of a larger extent of disorder in the alkaline earth-containing glasses, e.g., through larger distributions of bond angles and lengths [59].

With increasing Al_2O_3 concentration, the intense 545 cm^{-1} band separates into two bands near 500 and 560 cm^{-1}. The 500 cm^{-1} peak becomes narrower with increasing $[Al_2O_3]/[SiO_2]$ ratio. These bands are associated with motions of bridging oxygen in T–O–T linkages with T = Si, Al. For the high-Al_2O_3 glasses, the band at 580 cm^{-1} shifts to 560 cm^{-1} due to the presence of Al–O–Al bridges [21,64]. The shift occurs at lower Al-content for the Mg-containing glasses relative to the Ca-containing glasses as the greater stabilizing effect of Mg^{2+} allows for violation of the Al-avoidance principle [46,47].

With the substitution of Al_2O_3 for SiO_2, the relative intensity of the bands in the low-frequency region changes. The relative intensity increases in the favor of the 500 cm^{-1} band as $[Al_2O_3]$ increases in the range $[Al_2O_3] \leq [Na_2O]$, while the relative intensity decreases

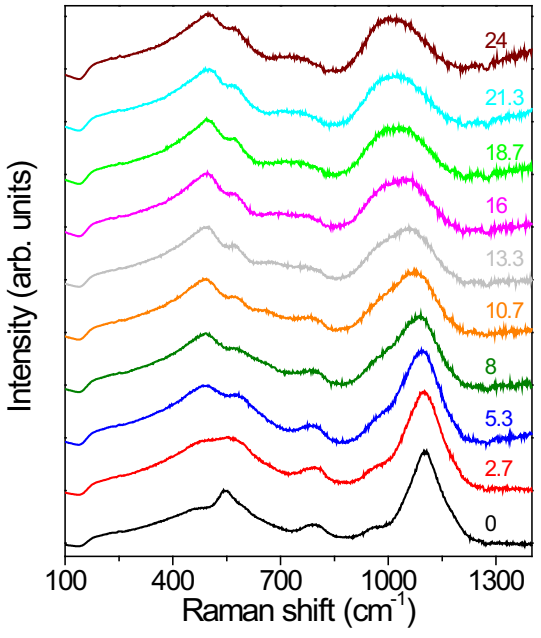

Fig. 3. Room temperature Raman spectra for the Mg-containing glasses. The spectra are shifted vertically for clarity. The numbers refer to the molar Al_2O_3 concentration.

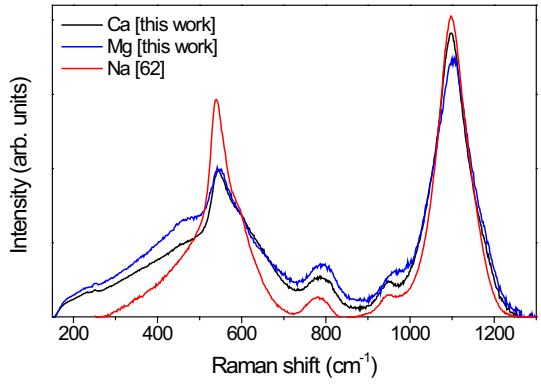

Fig. 4. Room temperature Raman spectra of the Al-free glasses ($x = 0$) with nominal compositions 8CaO-16Na_2O-76SiO_2 (Ca) and 8MgO-16Na_2O-76SiO_2 (Mg). The spectrum for an alkaline earth-free sodium silicate glass of composition 25Na_2O-75SiO_2 (Na) from Ref. [62] is also included for comparison. We note that the baseline-correction procedure is different for the spectra of the two glasses in this study and that from Ref. [62].

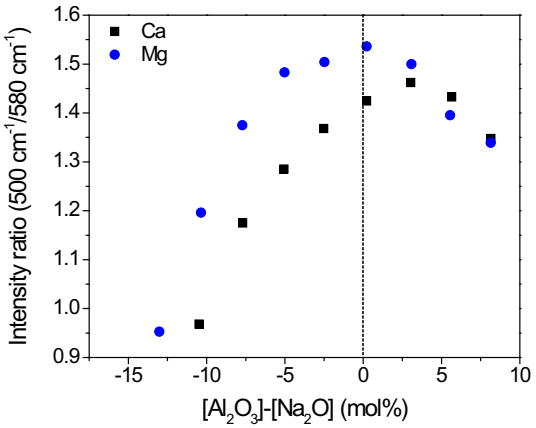

Fig. 5. Composition dependence of the relative intensity of the two main Raman bands of the low-frequency region at ~500 and ~580 cm^{-1}, respectively.

when $[Al_2O_3] > [Na_2O]$ as the role of the alkaline earth changes from network-modifying to charge-compensation (Fig. 5). In the $[Al_2O_3] \leq [Na_2O]$ range, the relative intensity of the peaks is different for the two glass series, indicating that the alkaline earth modifiers affect the structure differently due to differences in field strength. In the $[Al_2O_3] > [Na_2O]$ range, the relative intensity between the two bands converges for the two glass series, indicating a minimized effect of the alkaline earth cation on the network structure as they are used for charge-balancing. In the $[Al_2O_3] \leq [Na_2O]$ range, the band around 650 cm^{-1} decreases in intensity as the Al_2O_3 content is increased. This band is related to Si—O—Si angles [60,63] and the change in intensity might reflect changes in bond angles. A distinct peak near 790 cm^{-1} is also observed in the Al-free glasses ($x = 0$). As the SiO_2 concentration decreases, the peak broadens, its intensity decreases, and it shifts to lower frequencies. The peak nearly disappears in the Al_2O_3-rich glasses. It has been assigned to Si—O stretching involving oxygen motions [57] or to the motion of the Si atoms in their oxygen cage [65].

The high-frequency region (900 to 1200 cm^{-1}) is dominated by a broad band centered at 1100 cm^{-1} and a less intense band at 950 cm^{-1} for the glasses with $x = 0$. The position of the main band decreases as Al_2O_3 is substituted for SiO_2. This convoluted band is compiled from asymmetric and symmetric stretching vibrations of both completely polymerized tetrahedral network units (Q^4) and tetrahedra with one NBO (Q^3) [66]. These units can be described as $Si(OAl)_x$, where x is the number of Al tetrahedra connected to a SiO_4 tetrahedron [64] or to (Si,Al)-NBO and (Si,Al)-BO stretch bands (BO denotes bridging oxygens) [67]. With increasing Al_2O_3 concentration, the peak becomes broader and more asymmetric, shifts to lower frequencies, and the intensity decreases. The 950 cm^{-1} band is Si—O^- stretching of NBOs in Q^2 units [58,59,65,68]. This band is only present in low-Al_2O_3 composition due to the dual effect of Al_2O_3: the removal of NBOs results in a decrease in intensity, while the incorporation of Al^{3+} into the network decreases the average bond strength, resulting in a decrease in the Raman shift of the 1100 cm^{-1} band, and causing the two bands to merge. Due to the complex structure of these glasses with two different modifiers that allow many different structural conformations, we will not attempt to deconvolute the high-frequency region.

The composition dependence of the peak position of the 1100 cm^{-1} band is shown in Fig. 6(a), whereas the composition dependence of the width of the peak is shown in Fig. 6(b). We note that the largest changes in peak position and width with composition occur in the range where $[Al_2O_3] < [Na_2O]$. In addition, the peak position is following the same trend for the Ca- and Mg-containing glasses for $[Al_2O_3] < [Na_2O]$. However, for $[Al_2O_3] > [Na_2O]$, the band for the Mg-containing glasses is found at significantly higher Raman shift than the band for the Ca-containing glasses.

The peak width can be used as a measure of the relative order of the

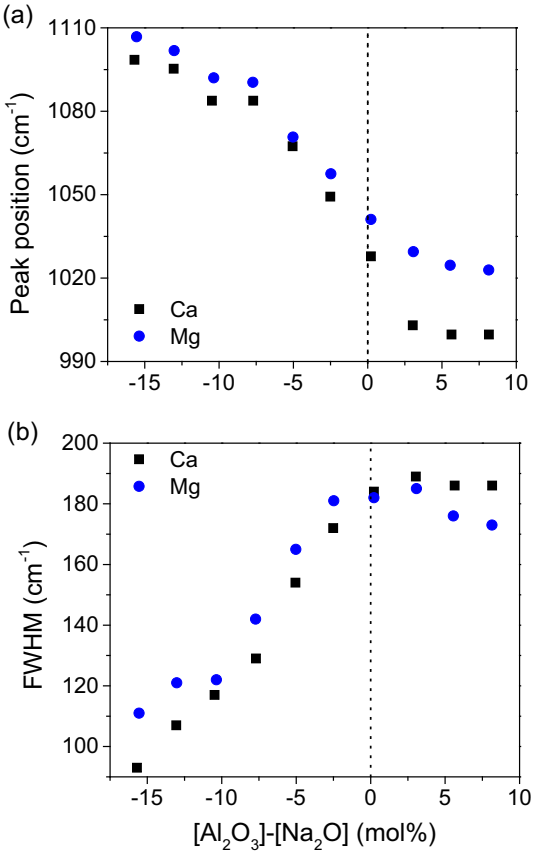

Fig. 6. (a) Position and (b) full width at half maximum (FWHM) of the room temperature Raman peak around 1000 to 1200 cm^{-1} for both Ca- and Mg-containing glasses.

Si—O network [59], as a larger distribution of bond angles results in a wider Raman band. For $[Al_2O_3] < [Na_2O]$, the larger full width at half maximum (FWHM) of the Mg-glasses as compared to the Ca-glasses in Fig. 6(b) indicates that the higher field strength of the Mg^{2+} modifier increases the structural disorder, consistent with observations in Ref. [59]. Finally, it should also be mentioned that the position and shape of this high-frequency peak is much more sensitive to the $[Al_2O_3]/[SiO_2]$ ratio than the peaks in the low-frequency region.

A difference in separation between the 950 and 1100 cm^{-1} bands in the spectra of the Ca- and Mg-containing glasses reveals differences in the modifying nature of the alkaline earths. For example, for the Ca-containing Al-free glass ($x = 0$) there is a clear separation between the bands, while the 950 cm^{-1} band appears as a shoulder for the Mg-containing glass. The broader 950 cm^{-1} band of the Mg-containing glass indicates that Mg^{2+} is better at stabilizing the network than Ca^{2+}, resulting in a structure with a larger distribution of bond lengths and angle fluctuations [4].

The intensity of Raman bands cannot be used for a quantitative analysis, as it is not only dependent on the concentration of the structural units, but also on the surrounding chemical environment. However, as the two series are isochemical in terms of modifier/network former ratio, we compare the effect of the two alkaline earth modifiers on the Raman spectra. Based on the peak widths and separation of the bands in the high-frequency region, we infer that the extent of disorder is different in the Ca- and Mg-containing glasses. Fig. 7 shows the composition dependence of relative intensity between the strongest signal in the low-frequency region (500, 545, or 580 cm^{-1} band, depending on composition) and the strongest signal (1100 cm^{-1} band) in the high-frequency region. A difference between the Ca- and Mg-glasses is observed when all alkaline earth cations are expected to act as network modifier when $[Al_2O_3] < [Na_2O]$, whereas the relative

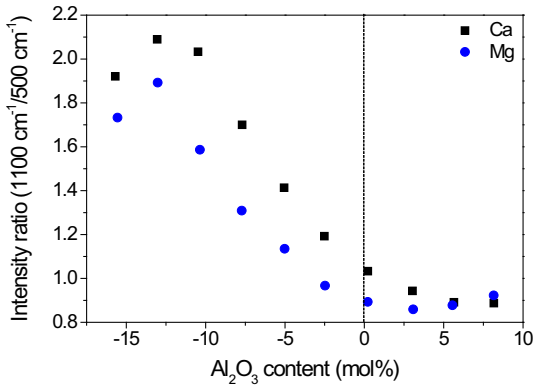

Fig. 7. Composition dependence of the relative intensity of the most intense Raman bands in the high- and low-frequency regions (at 1100 cm^{-1} and at 500, 545, or 580 cm^{-1} depending on composition, respectively).

intensity converges when the alkaline earth cations are mostly used for charge-compensation when $[Al_2O_3] > [Na_2O]$. This indicates that the impact of alkaline earths ions on the Q^n speciation and Al/Si mixing when acting as charge-compensator is similar, whereas they affect the network differently when acting as modifier.

3.2. In situ high temperature Raman spectroscopy

We have obtained in situ high temperature Raman spectra for eight selected glasses: $x = 0$, 8, 16, and 24 for R = Mg, Ca. Fig. 8 shows an example of the Raman spectra of the Ca-containing glass with $x = 16$ measured from room temperature to approximately 100 °C above its glass transition temperature. Qualitatively the changes in the Raman spectra with temperature are identical for all eight glasses. We note that the compositional effect on the Raman spectra is much larger than the temperature effect in the investigated temperature range. However, as shown in the example in Fig. 8, the relative peak intensities depend on the temperature. Particularly, we find that the maximum intensity of the band around 1100 cm^{-1} increases with increasing temperature. The Raman shift of this band also decreases with increasing temperature.

To quantify the effect of temperature on the Raman spectra, we have plotted the maximum intensity and Raman shift of the peak around 1100 cm^{-1} as a function of temperature. An example of this for the Ca-containing glass with $x = 16$ is shown in Fig. 9(a). The intensity increases linearly with temperature, while the Raman shift decreases

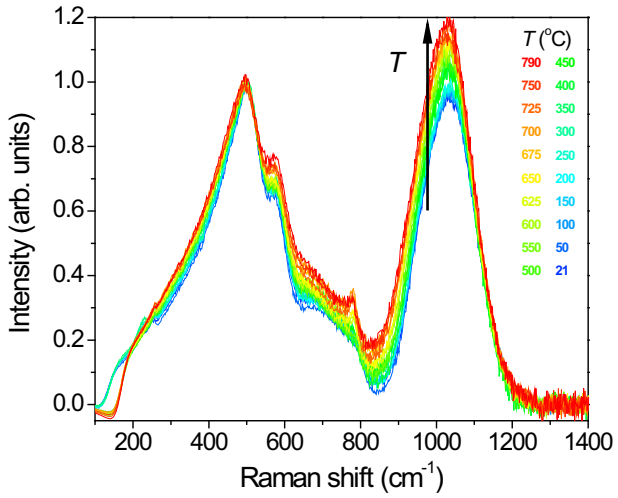

Fig. 8. Example of in situ high temperature Raman spectra of the Ca-containing glass with $x = 16$ measured from room temperature to approximately 100 °C above the glass transition temperature.

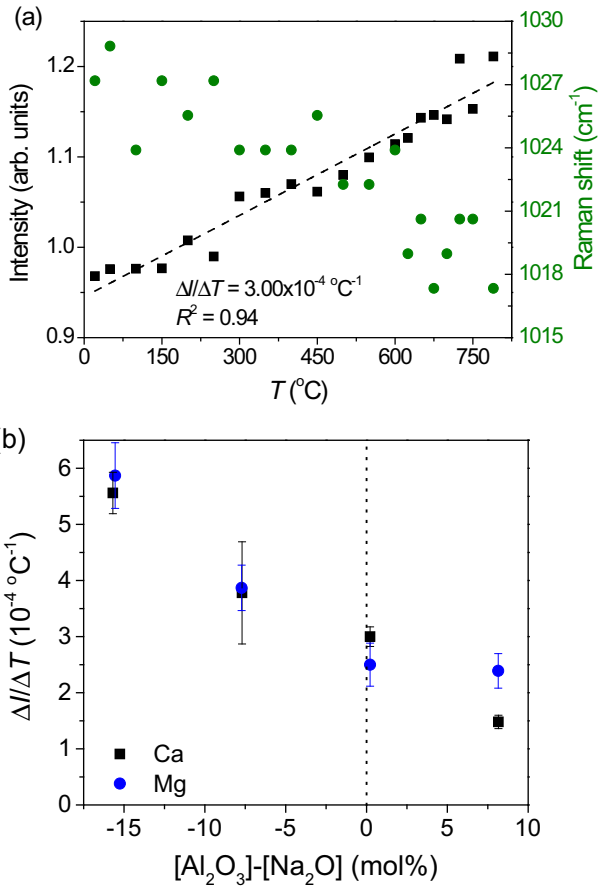

Fig. 9. (a) Temperature dependence of the maximum intensity (black squares) and Raman shift (green circles) of the peak around 1000–1100 cm^{-1} for the Ca-containing glass with $x = 16$. The dashed line represents a linear fit to the intensity data and the temperature derivative of intensity ($\Delta I/\Delta T$) is the slope. (b) Composition dependence of $\Delta I/\Delta T$ for the eight selected glasses. (For interpretation of the references to color in this figure legend, the reader is referred to the web version of this article.)

approximately linearly with temperature. We calculate the temperature derivative of intensity ($\Delta I/\Delta T$) from room temperature to T_g + 100 °C for each of the eight glasses. The composition dependence of $\Delta I/\Delta T$ is shown in Fig. 9(b). $\Delta I/\Delta T$ decreases with increasing $[Al_2O_3]/[SiO_2]$ ratio for both the Ca- and Mg-containing glasses. Hence, as the network becomes more connected with addition of alumina, the temperature sensitivity of the Raman band decreases. However, for $[Al_2O_3] > [Na_2O]$, there is no further change in $\Delta I/\Delta T$ with composition for the Mg-containing glasses. There is no systematic composition dependence of the change in Raman shift with temperature.

4. Discussion

The room temperature Raman spectroscopy data reflect the changing network structure as a function of both $[Al_2O_3]/[SiO_2]$ ratio and Ca^{2+} vs. Mg^{2+}. The shift of the broad band around 1100 cm^{-1} to lower frequencies (Fig. 6(a)) has been ascribed to the reduction in the force constant [5,21,69,70], Al—Si coupling [5,67], and/or superposition of $Si(OAl)_x$ units [64]; all of which reflect substitution of Al^{3+} for Si^{4+} in the glassy network. The Ca- and Mg-containing glasses exhibit essentially the same peak position of the broad high-frequency band for $[Al_2O_3] < [Na_2O]$. In agreement with previous observations [21,25,67], this implies that the size of alkaline earth cation plays only a small role on the structure of the aluminosilicate network. Hence, the $[Al_2O_3]/[SiO_2]$ ratio has much greater influence on the silicon and aluminum speciation in this regime than the substitution of Mg^{2+} by Ca^{2+}, which is also in agreement with the finding of ideal mixing in

some CaO-MgO-Al_2O_3-SiO_2 systems based on viscosity measurements [71]. However, for [Al_2O_3] > [Na_2O], Fig. 6(a) shows a pronounced difference in the Raman peak position when Ca is substituted by Mg. Hence, for [Al_2O_3] < [Na_2O], Na^+ ions are presumably preferred for the charge-stabilization of Al tetrahedra and there is thus no large difference in the aluminosilicate network structure between Ca^{2+} and Mg^{2+}. For [Al_2O_3] > [Na_2O], the alkaline earth cation is now partially responsible for the charge-stabilization of Al^{IV}, which results in significant differences in Q^n distribution. This is observed as a difference in the shape of the 1100 cm^{-1} band. The spectra of the Mg-containing glasses are slightly more intense on the high-frequency side of the peak as seen by the difference in peak position (Fig. 6).

We have found subtle effects of temperature on the peak intensity and Raman shift of the Raman band near ~1100 cm^{-1}. In the glassy state at low temperatures, the structural changes are purely vibrational (anharmonic) in nature on the laboratory timescale. However, at temperatures above the glass transition, structural modifications occur due to increased thermal population of configurational transitions and the supercooled liquid begins to explore additional structural configurations on the laboratory timescale. Even though the effect of temperature on these glasses is small, we find that the polymerized tetrahedral network units (Raman band near 1100 cm^{-1}) become less dependent on temperature at higher [Al_2O_3]/[SiO_2] ratios (Fig. 9(b)). This seems to be in agreement with the increased network connectivity as Al_2O_3 is substituted for SiO_2 and the number of NBOs per tetrahedron decreases. The band near 1100 cm^{-1} also shifts slightly to the low frequency side with temperature, beginning well below the glass transition temperature, which is attributed to bond elongation with temperature due to anharmonicity. However, the low frequency bands due to inter-tetrahedral bending motions do not significantly change peak position or intensity as a function of temperature, indicating that there is little change in the T—O—T angle, i.e., the bond angle bending vibration is relatively harmonic. This behavior is unlike that of pure SiO_2, where the Si—O—Si bending vibrations are highly anharmonic [57]. It has been suggested that this is because the bridging oxygen atoms in modified aluminosilicate networks are coordinated by two T (Si,Al) atoms and one or more network-modifier cations [72], which presumably makes the T—O—T angle more constrained in the systems studied here compared with SiO_2.

5. Conclusions

We have investigated the local structure of sodium aluminosilicate glasses with either magnesium or calcium using room temperature and in situ high temperature Raman spectroscopy. We confirm that Na^+ is preferentially used for charge-stabilizing Al in tetrahedral configuration. We also show that Mg^{2+} is superior to Ca^{2+} in stabilizing the glass structure, evident as violation of the Al-avoidance principle at lower [Al_2O_3] in Mg-containing than in Ca-containing glasses. The Raman spectra also showed differences in Q^n speciation throughout the compositional series. The alkaline earth ions acting as charge-compensators for tetrahedral aluminum are found to have a similar effect on the network structure (Q^n speciation and Al/Si mixing), while they affect the network differently when they are in a modifying role. Our results therefore confirm previous observations for the more simple alkali aluminosilicate and alkaline earth aluminosilicate systems. The improved understanding of the network structure of the quaternary alkali-alkaline earth aluminosilicate glasses is important for understanding physical and thermodynamic properties of glasses and melts.

Acknowledgements

This work was partially funded by Corning Incorporated. L.H. acknowledges the support from NSF under grant DMR-1105238 and DMR-1255378.

References

[1] B.O. Mysen, P. Richet, Silicate Glasses and Melts - Properties and Structure, (2005).
[2] J.F. Stebbins, Dynamics and structure of silicate and oxide melts; nuclear magnetic resonance studies, Rev. Mineral. Geochem. 32 (1995) 191–246.
[3] R.J. Kirkpatrick, R.K. Brow, Nuclear magnetic resonance investigation of the structures of phosphate and phosphate-containing glasses: a review, Solid State Nucl. Magn. Reson. 5 (1995) 9–21, http://dx.doi.org/10.1016/0926-2040(95)00042-O.
[4] G.N. Greaves, S. Sen, Inorganic glasses, glass-forming liquids and amorphizing solids, Adv. Phys. 56 (2007) 1–166, http://dx.doi.org/10.1080/00018730601147426.
[5] B.O. Mysen, D. Virgo, F.A. Seifert, Relationships between properties and structure of aluminosilicate melts, Am. Mineral. 70 (1985) 88–105.
[6] M.J. Toplis, Quantitative links between microscopic properties and viscosity of liquids in the system SiO_2-Na_2O, Chem. Geol. 174 (2001) 321–331, http://dx.doi.org/10.1016/S0009-2541(00)00323-5.
[7] G. Calas, L. Cormier, L. Galoisy, P. Jollivet, Structure – property relationships in multicomponent oxide glasses, C. R. Chim. 5 (2002) 1–13.
[8] S.K. Lee, J.F. Stebbins, Extent of intermixing among framework units in silicate glasses and melts, Geochim. Cosmochim. Acta 66 (2002) 303–309, http://dx.doi.org/10.1016/S0016-7037(01)00775-X.
[9] S.K. Lee, Microscopic origins of macroscopic properties of silicate melts and glasses at ambient and high pressure: Implications for melt generation and dynamics, Geochim. Cosmochim. Acta 69 (2005) 3695–3710, http://dx.doi.org/10.1016/j.gca.2005.03.011.
[10] G.S. Henderson, G. Calas, J.F. Stebbins, The structure of silicate glasses and melts, Elements 2 (2006) 269–273, http://dx.doi.org/10.2113/gselements.2.5.269.
[11] N.M. Vedishcheva, B.A. Shakhmatkin, A.C. Wright, The structure-property relationship in oxide glasses: a thermodynamic approach, Adv. Mater. Res. 39–40 (2008) 103–110, http://dx.doi.org/10.4028/www.scientific.net/AMR.39-40.103.
[12] L. Galoisy, Structure-property relationships in industrial and natural glasses, Elements 2 (2006) 293–297, http://dx.doi.org/10.2113/gselements.2.5.293.
[13] N. De Koker, Structure, thermodynamics, and diffusion in $CaAl_2Si_2O_8$ liquid from first-principles molecular dynamics, Geochim. Cosmochim. Acta 74 (2010) 5657–5671, http://dx.doi.org/10.1016/j.gca.2010.02.024.
[14] S.K. Lee, H.N. Kim, B.H. Lee, H.I. Kim, E.J. Kim, Nature of chemical and topological disorder in borogermanate glasses: insights from B-11 and O-17 solid-state NMR and quantum chemical calculations, J. Phys. Chem. B 114 (2010) 412–420, http://dx.doi.org/10.1021/jp9093113.
[15] F.J. Spera, M.S. Ghiorso, D. Nevins, Structure, thermodynamic and transport properties of liquid $MgSiO_3$: comparison of molecular models and laboratory results, Geochim. Cosmochim. Acta 75 (2011) 1272–1296, http://dx.doi.org/10.1016/j.gca.2010.12.004.
[16] Q. Zheng, M. Potuzak, J.C. Mauro, M.M. Smedskjaer, R.E. Youngman, Y. Yue, Composition – structure – property relationships in boroaluminosilicate glasses, J. Non-Cryst. Solids 358 (2012) 993–1002, http://dx.doi.org/10.1016/j.jnoncrysol.2012.01.030.
[17] E.F. Riebling, Structure of magnesium aluminosilicate liquids at 1700 °C, Can. J. Chem. 42 (1964) 2811–2820.
[18] E.F. Riebling, Structure of sodium aluminosilicate melts containing at least 50 mole % SiO_2 at 1500 C, J. Chem. Phys. 44 (1966) 2857–2867.
[19] Y. Bottinga, D.F. Weill, The viscosity of magmatic silicate liquids; a model calculation, Am. J. Sci. 272 (1972) 438–475.
[20] J.C.C. Chan, M. Bertmer, H. Eckert, Site connectivities in amorphous materials studied by double-resonance NMR of quadrupolar nuclei: high-resolution 11 B ↔ 27 Al spectroscopy of aluminoborate glasses, J. Am. Chem. Soc. 121 (1999) 5238–5248, http://dx.doi.org/10.1021/ja983385i.
[21] F.A. Seifert, B.O. Mysen, D. Virgo, Three-dimensional network structure of quenched melts (glass) in the systems SiO_2-$NaAlO_2$, SiO_2-$CaAl_2O_4$ and SiO_2-$MgAl_2O_4$, Am. Mineral. 67 (1982) 696–717 http://ammin.geoscienceworld.org/content/67/7-8/696.citation.
[22] S. Sen, R.E. Youngman, High-resolution multinuclear NMR structural study of binary aluminosilicate and other related glasses, J. Phys. Chem. B 108 (2004) 7557–7564, http://dx.doi.org/10.1021/jp031348u.
[23] M.J. Toplis, S.C. Kohn, M.E. Smith, I.J.F. Poplett, Fivefold-coordinated aluminum in tectosilicate glasses observed by triple quantum MAS NMR, Am. Mineral. 85 (2000) 1556–1560.
[24] S.H. Risbud, R.J. Kirkpatrick, A.P. Taglialavore, B. Montez, Solid-state NMR evidence of 4-, 5-, and 6-fold aluminum sites in roller-quenched SiO_2-Al_2O_3 glasses, J. Am. Ceram. Soc. 70 (1987) C10–C12, http://dx.doi.org/10.1111/j.1151-2916.1987.tb04859.x.
[25] D.R. Neuville, L. Cormier, D. Massiot, Al environment in tectosilicate and peraluminous glasses: a 27Al MQ-MAS NMR, Raman, and XANES investigation, Geochim. Cosmochim. Acta 68 (2004) 5071–5079, http://dx.doi.org/10.1016/j.gca.2004.05.048.
[26] D.R. Neuville, L. Cormier, D. Massiot, Al coordination and speciation in calcium aluminosilicate glasses: effects of composition determined by 27Al MQ-MAS NMR and Raman spectroscopy, Chem. Geol. 229 (2006) 173–185, http://dx.doi.org/10.1016/j.chemgeo.2006.01.019.
[27] E. Lacy, Aluminum in glasses and melts, Phys. Chem. Glasses 4 (1963) 234–238.
[28] P. Ganster, M. Benoit, W. Kob, J.-M. Delaye, Structural properties of a calcium aluminosilicate glass from molecular-dynamics simulations: a finite size effects study, J. Chem. Phys. 120 (2004) 10172–10181, http://dx.doi.org/10.1063/1.1724815.

[29] M.J. Toplis, D.B. Dingwell, T. Lenci, Peraluminous viscosity maxima in Na_2O·Al_2O_3·SiO_2 liquids: the role of triclusters in tectosilicate melts, Geochim. Cosmochim. Acta 61 (1997) 2605–2612, http://dx.doi.org/10.1016/S0016–7037(97)00126-9.
[30] D. Iuga, C. Morais, Z. Gan, D.R. Neuville, L. Cormier, D. Massiot, NMR heteronuclear correlation between quadrupolar nuclei in solids, J. Am. Chem. Soc. 127 (2005) 11540–11541, http://dx.doi.org/10.1021/ja052452n.
[31] A. Navrotsky, H.D. Zimmermann, R.L. Hervig, Thermochemical study of glasses in the system $CaMgSi_2O_6$-$CaAl_2SiO_6$, Geochim. Cosmochim. Acta 47 (1983) 1535–1538, http://dx.doi.org/10.1016/0016-7037(83)90314-9.
[32] M. Li, B.N. Roy, A. Navrotsky, Thermochemistry of charge-coupled substitutions in silicate glasses: the systems M1/nn + AlO2-SiO2 (M = Li, Na, K, Rb, Cs, Mg, Ca, Sr, Ba,Pb), J. Am. Ceram. Soc. 67 (1984) 606–610.
[33] L. Cormier, D. Ghaleb, D.R. Neuville, J.M. Delaye, G. Calas, Chemical dependence of network topology of calcium aluminosilicate glasses: a computer simulation study, J. Non-Cryst. Solids 332 (2003) 255–270, http://dx.doi.org/10.1016/j.jnoncrysol.2003.09.012.
[34] D.R. Neuville, L. Cormier, A. Flank, V. Briois, D. Massiot, Al speciation and Ca environment in calcium aluminosilicate glasses and crystals by Al and Ca K-edge X-ray absorption spectroscopy, Chem. Geol. 213 (2004) 153–163, http://dx.doi.org/10.1016/j.chemgeo.2004.08.039.
[35] L. Cormier, G.J. Cuello, Mg coordination in a $MgSiO_3$ glass using neutron diffraction coupled with isotopic substitution, Phys. Rev. B: Condens. Matter Mater. Phys. 83 (2011) 1–8, http://dx.doi.org/10.1103/PhysRevB.83.224204.
[36] Y. Tabira, Local structure around oxygen atoms in $CaMgSi_2O_6$ glass by O K-edge EXELFS, Mater. Sci. Eng. B 41 (1996) 63–66.
[37] D. Li, M. Peng, T. Murata, Coordination and local structure of magnesium in silicate minerals in glasses: Mg K-edge XANES study, Can. Mineral. 37 (1999) 199–206.
[38] S. Kroeker, J.F. Stebbins, Magnesium coordination environments in glasses and minerals: new insight from high-field magnesium-25 MAS NMR, Am. Mineral. 85 (2000) 1459–1464.
[39] M.C. Wilding, C.J. Benmore, J.A. Tangeman, S. Sampath, Evidence of different structures in magnesium silicate liquids: coordination changes in forsterite- to enstatite-composition glasses, Chem. Geol. 213 (2004) 281–291, http://dx.doi.org/10.1016/j.chemgeo.2004.08.055.
[40] K. Shimoda, Y. Tobu, M. Hatakeyama, T. Nemoto, K. Koji Saito, Structural investigation of Mg local environments in silicate glasses by ultra-high field 25Mg 3QMAS NMR spectroscopy, Am. Mineral. 92 (2007) 695–698.
[41] K. Shimoda, T. Nemoto, K. Saito, Local structure of magnesium in silicate glasses: a 25Mg 3QMAS NMR study, J. Phys. Chem. B 112 (2008) 6747–6752, http://dx.doi.org/10.1021/jp711417t.
[42] M. Guignard, L. Cormier, Environments of Mg and Al in MgO-Al_2O_3-SiO_2 glasses: a study coupling neutron and X-ray diffraction and Reverse Monte Carlo modeling, Chem. Geol. 256 (2008) 110–117, http://dx.doi.org/10.1016/j.chemgeo.2008.06.008.
[43] N. Trcera, D. Cabaret, S. Rossano, F. Farges, A.M. Flank, P. Lagarde, Experimental and theoretical study of the structural environment of magnesium in minerals and silicate glasses using X-ray absorption near-edge structure, Phys. Chem. Miner. 36 (2009) 241–257, http://dx.doi.org/10.1007/s00269-008-0273-z.
[44] M.M. Smedskjaer, J.C. Mauro, Y. Yue, Ionic diffusion and the topological origin of fragility in silicate glasses, J. Chem. Phys. 131 (2009) 1–9, http://dx.doi.org/10.1063/1.3276285.
[45] W. Loewenstein, The distribution of aluminum in the tetrahedra of silicates and aluminates, Am. Mineral. 39 (1954) 92–96, http://dx.doi.org/10.1002/anie.201004007.
[46] S.K. Lee, G.D. Cody, B.O. Mysen, Structure and the extent of disorder in quaternary (Ca-Mg and Ca-Na) aluminosilicate glasses and melts, Am. Mineral. 90 (2005) 1393–1401.
[47] K.E. Kelsey, J.R. Allwardt, J.F. Stebbins, Ca-Mg mixing in aluminosilicate glasses: an investigation using 17O MAS and 3QMAS and 27Al MAS NMR, J. Non-Cryst. Solids 354 (2008) 4644–4653, http://dx.doi.org/10.1016/j.jnoncrysol.2008.05.049.
[48] S.K. Lee, S. Sung, The effect of network-modifying cations on the structure and disorder in peralkaline Ca-Na aluminosilicate glasses: O-17 3QMAS NMR study, Chem. Geol. 256 (2008) 325–332, http://dx.doi.org/10.1016/j.chemgeo.2008.07.019.
[49] L. Cormier, D.R. Neuville, Ca and Na environments in Na_2O-CaO-Al_2O_3-SiO_2 glasses: influence of cation mixing and cation-network interactions, Chem. Geol. 213 (2004) 103–113, http://dx.doi.org/10.1016/j.chemgeo.2004.08.049.
[50] S.K. Lee, Simplicity in melt densification in multicomponent magmatic reservoirs in Earth's interior revealed by multinuclear magnetic resonance, Proc. Natl. Acad. Sci. 108 (2011) 6847–6852, http://dx.doi.org/10.1073/pnas.1019634108.
[51] M.M. Smedskjaer, S.A. Saxton, A.J. Ellison, J.C. Mauro, Photoelastic response of alkaline earth aluminosilicate glasses, Opt. Lett. 37 (2012) 293, http://dx.doi.org/10.1364/OL.37.000293.
[52] M.M. Smedskjaer, L. Huang, G. Scannell, J.C. Mauro, Elastic interpretation of the glass transition in aluminosilicate liquids, Phys. Rev. B: Condens. Matter Mater. Phys. 85 (2012) 1–10, http://dx.doi.org/10.1103/PhysRevB.85.144203.
[53] M.M. Smedskjaer, J.C. Mauro, J. Kjeldsen, Y. Yue, Microscopic origins of compositional trends in aluminosilicate glass properties, J. Am. Ceram. Soc. 96 (2013) 1436–1443, http://dx.doi.org/10.1111/jace.12298.
[54] M. Guerette, L. Huang, A simple and convenient set-up for high-temperature Brillouin light, J. Phys. D. Appl. Phys. 45 (2012) 275302, http://dx.doi.org/10.1088/0022-3727/45/27/275302.
[55] V.P. Zakaznova-Herzog, W.J. Malfait, F. Herzog, W.E. Halter, Quantitative Raman spectroscopy: principles and application to potassium silicate glasses, J. Non-Cryst. Solids 353 (2007) 4015–4028, http://dx.doi.org/10.1016/j.jnoncrysol.2007.06.033.
[56] W.J. Malfait, W.E. Halter, Structural relaxation in silicate glasses and melts: high-temperature Raman spectroscopy, Phys. Rev. B: Condens. Matter Mater. Phys. 77 (2008) 1–6, http://dx.doi.org/10.1103/PhysRevB.77.014201.
[57] P.F. McMillan, B.T. Poe, P. Gillet, B. Reynard, A study of SiO_2 glass and supercooled liquid to 1950 K via high-temperature Raman spectroscopy, Geochim. Cosmochim. Acta 58 (1994) 3653–3664, http://dx.doi.org/10.1016/0016-7037(94)90156-2.
[58] S.A. Brawer, W.B. White, Raman spectroscopic investigation of the structure of silicate glasses. I. The binary alkali silicates, J. Chem. Phys. 63 (1975) 2421–2432.
[59] S.A. Brawer, W.B. White, Raman spectroscopic investigation of the structure of silicate glasses (II). Soda-alkaline earth-alumina ternary and quaternary glasses, J. Non-Cryst. Solids 23 (1977) 261–278.
[60] T. Furukawa, K.E. Fox, W.B. White, Raman spectroscopic investigation of the structure of silicate glasses. III. Raman intensities and structural units in sodium silicate glasses, J. Chem. Phys. 75 (1981) 3226–3237.
[61] C. Le Losq, D.R. Neuville, Effect of the Na/K mixing on the structure and the rheology of tectosilicate silica-rich melts, Chem. Geol. 346 (2013) 57–71.
[62] T.K. Bechgaard, A. Goel, R.E. Youngman, J.C. Mauro, S.J. Rzoska, M. Bockowski, L.R. Jensen, M.M. Smedskjaer, Structure and mechanical properties of compressed sodium aluminosilicate glasses: role of non-bridging oxygens, J. Non-Cryst. Solids 441 (2016) 49–57, http://dx.doi.org/10.1016/j.jnoncrysol.2016.03.011.
[63] J.D. Kubicki, R.J. Hemley, A.M. Hofmeister, Raman and infrared study of pressure-induced changes in $MgSiO_3$, $CaMgSiO_2$ and $CaSiO_3$ glasses, Am. Mineral. 77 (1992) 258–269.
[64] P.F. McMillan, B. Piriou, A. Navrotsky, A Raman spectroscopic study of glasses along the join silica-calcium aluminate, silica-sodium aluminate, and silica-potassium aluminate, Geochim. Cosmochim. Acta 46 (1982) 2021–2037.
[65] O. Mysen, D. Virgo, A. Seifert, The structure of silicate melts: implications for chemical and physical properties of natural magma, Rev. Geophys. Sp. Phys. 20 (1982) 353–383.
[66] C. Le Losq, D.R. Neuville, P. Florian, G.S. Henderson, D. Massiot, The role of Al^{3+} on rheology and structural changes in sodium silicate and aluminosilicate glasses and melts, Geochim. Cosmochim. Acta 126 (2014) 495–517, http://dx.doi.org/10.1016/j.gca.2013.11.010.
[67] D.R. Neuville, B.O. Mysen, Role of aluminium in the silicate network: in situ, high-temperature study of glasses and melts on the join SiO_2-$NaAlO_2$, Geochim. Cosmochim. Acta 60 (1996) 1727–1737, http://dx.doi.org/10.1016/0016-7037(96)00049-X.
[68] D. Virgo, B.O. Mysen, I. Kushiro, Anionic constitution of 1-atmosphere silicate melts: implications for the structure of igneous melts, Science 208 (1980) 1371–1373 (80-.).
[69] B.O. Mysen, Relationships between silicate melt structure and petrologic processes, Earth Sci. Rev. 27 (1990) 281–365, http://dx.doi.org/10.1016/0012-8252(90)90055-Z.
[70] L. Cormier, D.R. Neuville, G. Calas, Relationship between structure and glass transition temperature in low-silica calcium aluminosilicate glasses: the origin of the anomaly at low silica content, J. Am. Ceram. Soc. 88 (2005) 2292–2299, http://dx.doi.org/10.1111/j.1551-2916.2005.00428.x.
[71] D.R. Neuville, P. Richet, Viscosity and (Ca, Mg) mixing in molten pyroxenes and garnets, Geochim. Cosmochim. Acta 55 (1991) 1011–1021.
[72] I. Daniel, P. Gillet, B.T. Poe, P.F. McMillan, In-situ high-temperature Raman spectroscopic studies of aluminosilicate liquids, Phys. Chem. Miner. 22 (1995) 74–86.

Paper III

Journal of Non-Crystalline Solids 461 (2017) 24–34

Contents lists available at ScienceDirect

Journal of Non-Crystalline Solids

journal homepage: www.elsevier.com/locate/jnoncrysol

Fragility and configurational heat capacity of calcium aluminosilicate glass-forming liquids

Tobias K. Bechgaard [a], John C. Mauro [b], Mathieu Bauchy [c], Yuanzheng Yue [a], Lisa A. Lamberson [b], Lars R. Jensen [d], Morten M. Smedskjaer [a,*]

[a] Department of Chemistry and Bioscience, Aalborg University, Aalborg, Denmark
[b] Science and Technology Division, Corning Incorporated, Corning, USA
[c] Department of Civil and Environmental Engineering, University of California, Los Angeles, USA
[d] Department of Mechanical and Manufacturing Engineering, Aalborg University, Aalborg, Denmark

ARTICLE INFO

Article history:
Received 15 December 2016
Received in revised form 12 January 2017
Accepted 19 January 2017
Available online 31 January 2017

Keywords:
Calcium aluminosilicate glasses
Configurational heat capacity
Liquid fragility
Glass transition
Structure

ABSTRACT

Enabling accurate prediction of the properties of aluminosilicate glasses is important for the development of new glass compositions for high-tech applications. In this study, we use a combined topological and thermodynamic approach to connect the configurational heat capacity ($C_{p,conf}$) with the liquid fragility (m) and glass transition temperature (T_g) of calcium aluminosilicate glass-forming liquids. To study structural and dynamical features of these systems, we choose two representative glass composition series: one at the tectosilicate join with varying SiO_2 content and one with constant CaO content but varying Al_2O_3/SiO_2 ratio. $C_{p,conf}$ is determined using differential scanning calorimetry (DSC), while m and T_g are determined through both DSC and viscosity measurements. The $C_{p,conf}$ model is found to predict the measured data well for most systems, but deviations between the modeled and measured $C_{p,conf}$ values appear for the "strongest" glasses in the tectosilicate series and for the most peraluminous glasses in the constant CaO series. We discuss the structural origins of these model-from-data deviations based on Raman spectroscopy measurements.

1. Introduction

Understanding the composition-structure-property relations of aluminosilicate glasses and melts is important for geological as well as industrial applications. Knowing these relations is important for understanding the behavior of magma dynamics and properties, as 95% of magma composition is covered by the aluminosilicate system [1]. It is also important for the glass industry, since aluminosilicate glasses are used for various commercial applications, e.g., insulation stone wool [2], airplane windshields [3], alkali-free flat panel displays [4], and scratch resistant cover glasses [5,6]. Calcium aluminosilicate glasses are particular interesting to study as they exhibit good glass-forming ability and form the basis for many commercial glasses [7].

The structure of calcium aluminosilicate glasses depends on the ratio among the three components as reported in numerous studies [2,8–12]. The prevailing structural models propose that Al^{3+} is charge-compensated by Ca^{2+} in four-fold confirmation (Al^{IV}) when the ratio $[Al_2O_3]/[CaO] \leq 1$ (i.e., peralkaline compositions), with the remaining Ca^{2+} ions creating non-bridging oxygens (NBOs). Thus, all Al^{3+} atoms are present as Al^{IV} and the glass is NBO-free when the $[Al_2O_3]/[CaO]$ ratio equals 1. However, for calcium aluminosilicates there is evidence from molecular dynamics simulations [13] and nuclear magnetic resonance spectroscopy experiments that up to 6% of the Al^{3+} atoms exist in five-fold coordination in tectosilicate (i.e., $[Al_2O_3] = [CaO]$) compositions [14], suggesting that the model is too simple to describe the composition-structure relations in alkaline earth aluminosilicate glasses. For peraluminous compositions with the ratio $[Al_2O_3]/[CaO] \geq 1$, the 'excess' Al^{3+} will be forced into five- or six-fold coordination to charge-balance Al tetrahedra [9,15,16]. Alternatively oxygen triclusters (three-fold coordinated oxygen) can be formed as proposed in 1964 by Lacy [17].

Viscosity is a property that controls the deformation and flow behavior of glass-forming liquids and, as such, is of primary importance for magmatic liquids. It increases by 12 orders of magnitude upon cooling from the 1 Pa s homogenized liquid (e.g., an industrial glass melt) to the solid glass at the glass transition temperature (T_g). The viscosity vs. temperature relation is composition dependent, and the liquid fragility index m describes how rapidly the dynamics change around T_g. Moreover, understanding the glass transition and relaxation behavior is of both fundamental and industrial interest. Due to the non-equilibrium nature of the glassy state, the glass density depends on the thermal history; this has critical consequences, e.g., for substrate glasses for high-resolution displays that suffer from dimensional

* Corresponding author.
E-mail address: mos@bio.aau.dk (M.M. Smedskjaer).

http://dx.doi.org/10.1016/j.jnoncrysol.2017.01.033
0022-3093/

changes during high-temperature processing [4]. Since the volume relaxation is typically linked with the enthalpy relaxation processes during the glass transition [18], an improved understanding of the composition and structure dependence of enthalpy relaxation would help the design of new glass compositions where relaxation effects can be minimized.

As the supercooled liquid is cooled through the glass transition region, there is a loss of the configurational entropy, and hence, configurational heat capacity ($C_{p,conf}$) as the structural degrees of freedom are lost. While the glassy state primarily contains vibrational degrees of freedom, C_p of the liquid state is the sum of vibrational ($C_{p,vib}$) and configurational contributions [19]. For relatively strong glass systems, such as the calcium aluminosilicates herein with $m < 60$, $C_{p,vib}$ changes only slightly through the glass-liquid transition region, i.e., the glass heat capacity (C_{pg}) is nearly equal to $C_{p,vib}$ of the liquid heat capacity (C_{pl}) at T_g. We can thus make the approximation that $C_{p,conf} \approx C_{pl} - C_{pg} = \Delta C_p$, where ΔC_p is the isobaric heat capacity jump from the glass to the liquid state through glass transition, i.e., the difference between C_{pl} and C_{pg}.

During the last two decades, several attempts [19–27] have been made to develop predictive models of the enthalpy relaxation from the liquid fragility index, using various thermodynamic properties such as the enthalpy of fusion or the configurational entropy. Recently, a model to account for $C_{p,conf}$ in borosilicate glasses was proposed using a combined topological and thermodynamic approach [28]. This was done by defining $C_{p,conf}$ in terms of configurational enthalpy and entropy changes and combining the definition of fragility with the Adam-Gibbs model for equilibrium viscosity. This enables a relation between kinetics (m) and thermodynamics (C_p) (see Ref. [28] for full derivation),

$$\Delta C_p\left[x, T_g(x)\right] = \frac{A(x_R)}{T_g(x)}\left(\frac{m(x)}{m_0} - 1\right), \quad (1)$$

where $A(x_R)$ is a proportionality constant m_0 is the fragility of a strong liquid (15–17), and x is a composition variable. Although the model was found to accurately predict $C_{p,conf}$ in borosilicate glasses, it has not yet been tested for other glass-forming systems.

Previously, the composition dependence of liquid fragility in various aluminosilicate glass-forming liquids has been reported [29–31], but studies of both fragility and $C_{p,conf}$ of calcium aluminosilicate glasses are scarce, limited primarily to the works of Solvang et al. [2,8] and Webb [32]. Their studies show an approximately linear correlation between fragility and $C_{p,conf}$ for sodium aluminosilicate, calcium aluminosilicate, and sodium calcium aluminosilicate glasses. Although Solvang et al. reported data for two glass series with constant NBO/T ratio, the series cover relatively small compositional changes. Webb reported data for only one series of calcium aluminosilicate glasses with changing Al_2O_3/CaO ratio at constant SiO_2 content. Therefore, additional studies are needed to find the general trend about the connection between liquid fragility and $C_{p,conf}$ in calcium aluminosilicate glasses.

In this work, we focus on two series of calcium aluminosilicate glasses covering a large compositional range (Fig. 1). The first series is at the tectosilicate join with varying SiO_2 content, i.e., $(100\text{-}2x)SiO_2$-xAl_2O_3-xCaO glasses with x between 0 and 35. The second series has constant CaO content but varying Al_2O_3/SiO_2 ratio, i.e., $(80\text{-}y)SiO_2$-yAl_2O_3-20CaO glasses with y between 10 and 30. $C_{p,conf}$ is measured using differential scanning calorimetry (DSC), while T_g and m are determined through both DSC and viscosity measurements for selected systems. These results are interpreted in terms of the $C_{p,conf}$ model in Eq. (1) and further discussed on the basis of the atomic packing density and network structure evolution as characterized through density and Raman spectroscopy measurements, respectively.

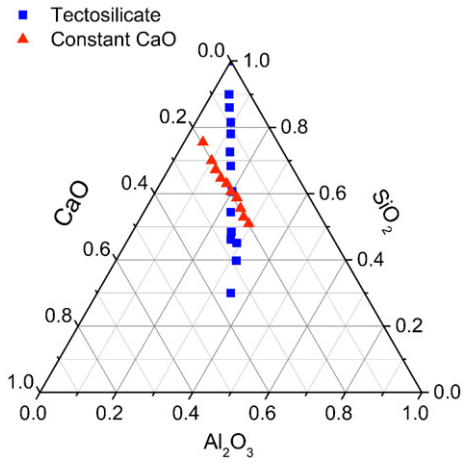

Fig. 1. Analyzed composition of the calcium aluminosilicate glasses under investigation. The tectosilicate series (blue squares) covers the meta-aluminosilicate join, while the constant CaO series (red triangles) covers both peralkaline and peraluminous compositions at a fixed CaO content.

2. Experimental

2.1. Samples preparation

We have prepared a total of twenty-three calcium aluminosilicate glasses in the $(100\text{-}2x)SiO_2$-xAl_2O_3-xCaO and $(80\text{-}y)SiO_2$-yAl_2O_3-20CaO systems, denoted the tectosilicate- and the constant CaO-series, respectively (Fig. 1). The tectosilicate-series covers the intermediate- and high-silica range of meta-aluminosilicate glasses and all glasses in the series will thus be nominally fully polymerized. In the constant CaO-series, the modifier content is kept constant, while Al_2O_3 is substituted for SiO_2, which allows us to study the changes in structure-properties from peralkaline to peraluminous compositions.

To obtain homogenous batches, the raw materials (SiO_2, Al_2O_3, and $CaCO_3$) were mixed for 60 min using a ball mill before being melted in a covered Pt crucible for at least 6 h in air at 1650 °C. To ensure chemical homogeneity, the melts were first quenched and then remelted at 1650 °C for at least 6 h before being quenched on a metal plate. The pure silica glass of the tectosilicate series (x = 0) was obtained commercially (Corning Code 7980). To ensure uniform thermal history, the glasses were annealed for 30 min at their respective glass transition temperatures, which were determined using differential scanning calorimetry (DSC 449F1, Netzsch) at an upscanning rate of 10 K/min (see details below).

The chemical compositions of the glasses were determined using inductively coupled plasma mass spectroscopy and X-ray fluorescence and are given in Tables 1 and 2 for tectosilicate and constant CaO series, respectively. Nominally, all glasses in the tectosilicate series should have $[Al_2O_3]/[CaO]$ ratio = 1, but the actual $[Al_2O_3]/[CaO]$ ratio differs for some glasses, varying between 0.83 and 1.12. The largest discrepancies between nominal and actual compositions are found for x = 5, 7, 28, and 30, which have $[Al_2O_3]/[CaO]$ ratios of 0.83, 0.90, 1.12, and 1.10, respectively. However, this will not affect the investigation of the correlation between configurational heat capacity and liquid fragility as the fitting of data to Eq. (1) is based on measured values of fragility and glass transition temperatures.

2.2. Characterization

The densities (ρ) of the glasses were determined using the Archimedes buoyancy principle with ethanol as the immersion liquid, weighing each sample in air and ethanol ten times. From the measurements of density and chemical composition, the molar volume (V_m) and atomic packing factor (APF) were calculated using Eqs. (2) and (3),

Table 1
Analyzed chemical compositions (in mol%), calculated Al_2O_3/CaO ratio, measured glass transition temperature (T_g), density (ρ), liquid fragility index determined from viscosity data (m_{vis}) and determined by DSC and corrected by Eq. (7) (m), and configurational heat capacity ($C_{p,conf}$) of the tectosilicate glass series, i.e., nominally (100-2x)SiO_2-$x$$Al_2O_3$-$x$CaO. When the total compositions do not add to 100%, the minor impurity oxides are MgO, Fe_2O_3, and TiO_2 (total < 0.7 mol%).

x	Chemical composition (mol%)			$[Al_2O_3]/[CaO]$ (−)	T_g (K)	ρ (g cm^{-3})	m_{vis} (−)	m (−)	$C_{p,conf}$ (J mol^{-1} K^{-1})
	SiO_2	Al_2O_3	CaO						
0	100.0	0.0	0.0	–	1318[a]	2.200	–	–	–
5	89.9	4.6	5.5	0.83	1189	2.299	–	–	12.7
7	86.0	6.6	7.4	0.90	1173	2.345	–	–	12.4
9	81.5	9.2	9.3	1.00	1158	2.401	–	22	13.1
11	78.2	10.6	10.9	0.97	1151	2.418	–	20	13.5
13	72.6	13.5	14.0	0.97	1140	2.523	–	26	17.1
15	69.0	15.9	14.8	1.07	1137	2.538	38	34	18.2
20	60.6	20.1	19.3	1.04	1137	2.628	–	32	20.6
22	54.9	22.6	22.0	1.03	1129	2.666	49	38	24.2
24	48.5	25.9	25.6	1.01	1132	2.734	–	37	25.0
26	46.4	26.7	26.3	1.02	1127	2.722	54	36	26.9
28	45.1	29.0	25.9	1.12	1128	2.764	–	45	29.3
30	39.8	31.6	28.7	1.10	1126	2.788	–	56	29.7
35	30.0	35.0	34.3	1.02	1119	2.812	57	55	33.5

[a] Value is an estimate only due to the wide glass transition of pure SiO_2 glass.

respectively.

$$V_m = \frac{1}{\rho}\sum_i x_i M_i \tag{2}$$

$$\mathrm{APF} = \frac{1}{V_m}\sum_i x_i V_i \tag{3}$$

Here x_i, M_i, and V_i are the mole fraction, molar mass, and ionic volume of oxide i.

Raman spectroscopy was used to study the changes in structure as a function of chemical composition. The Raman scattering spectra was obtained in backscattering geometry using a Renishaw Invia Raman microspectroscope on freshly polished samples. The excitation source was a diode laser with a wavelength of 532 nm. The Raman spectra were baseline-corrected using an asymmetric least square algorithm [33] and deconvoluted in the Fityk software using Gaussian line shapes.

To obtain viscosity and thus liquid fragility data, several methods were used, which include beam bending viscometry, ball penetration viscometry, parallel plate viscometry, and rotational viscometry. Beam bending (BBV) and ball penetration viscometry (BPV) were used in the temperature range just above the glass transition ($\eta = 10^{11}$ Pa s for BBV and $\eta = 10^{10}$– 10^{12} Pa s for BPV), parallel plate viscosity (PPV) was used to determine the softening point ($\eta = 10^{6.6}$ Pa s), and rotational viscometry was used in the high-temperature range ($\eta = 10^2$– 10^5 Pa s). For BBV, BPV, and PPV measurements, sample bars with dimension of approximately 5.5 × 2.5 × 2.5 mm^3, cuboid samples with dimension of 10 × 10 × 5 mm^3, and cylindrical samples with a 6 mm diameter and 5 mm thickness were used, respectively. The samples were flat, parallel, and polished to an optical finish. The standard deviations are 1 K and 2 K for the annealing and softening temperatures, respectively. Crushed samples of ~600 g were used for the rotational viscometry measurements, with an estimated error in log η of ±0.02 (η in Pa s). The fragility of the glass-forming liquid can then be determined by fitting the viscosity vs. temperature data to the MYEGA viscosity model [34],

$$\log\eta = \log\eta_\infty + (12 - \log\eta_\infty)\frac{T_g}{T}\exp\left[\left(\frac{m}{12-\log\eta_\infty} - 1\right)\left(\frac{T_g}{T} - 1\right)\right], \tag{4}$$

where η_∞ is the high-temperature limit of the liquid viscosity, T is the absolute temperature, T_g is the glass transition temperature, and m is the liquid fragility index as defined by Angell [35].

Since the sample sizes were too small for some compositions to measure viscosity data, the fragility was also indirectly determined using DSC. This is based on the premise that the activation energy for viscous flow (and thus m) is governed by the heating/cooling rate dependence of the fictive temperature. Regular DSC upscans were thus performed in Pt crucibles and argon as the purge gas (50 mL/h) at different heating rates subsequent to cooling the glass from well above the glass transition at the same rate. Heating/cooling rates of 10, 15, 20, 25, and 30 K/min and 2, 5, 10, 20, and 30 K/min were used for the tectosilicate and constant CaO series, respectively. The sample mass was either ~50 or ~80 mg depending on the sample preparation method (cutting and drilling, respectively). The liquid fragility index (m) was then determined as described in Ref. [36]:

$$m = \frac{E_g}{RT_g \ln 10}, \tag{5}$$

where R is the ideal gas constant and E_g is the activation energy for equilibrium viscous flow in the glass transition region, which can be calculated from the dependence of the reciprocal DSC upscan rate (q) on the fictive temperature (T_f):

$$\ln\left(\frac{q}{T_f^2}\right) = -\frac{E_g}{RT_f} + \text{constant} \tag{6}$$

Determination of m using Eq. (5) introduces a systematic error in the m data, as Eq. (6) assumes an Arrhenian behavior in a T_f interval in the glass transition range, while the scaling across the temperature range is non-Arrhenian. A correction for the systematic error between the fragilities determined from viscosity (m_{vis}) and DSC (m_{DSC}) was recently presented by Zheng et al. [37]:

$$m_{vis} = 1.289(m_{DSC} - m_0) + m_0 \tag{7}$$

To avoid the systematic error in this work, we use the relation in Eq. (7) to correct the m values determined using DSC from Eqs. (5) and (6).

ΔC_p was determined using DSC with a heating rate of 10 K/min subsequent to cooling at the same rate. The measurement was performed with argon as the purge gas (50 mL/h) in a Pt crucible and the same samples as used for the determination of T_g. The heat capacity curve for each glass was calculated relative to the C_p curve of a sapphire reference material of comparable mass. By determining ΔC_p from the second upscan, we ensure that the measured heat flow reflects the enthalpy response of a sample with a well-defined thermal history. ΔC_p was then determined as illustrated in Fig. 2.

Table 2
Analyzed chemical compositions (in mol%), calculated Al_2O_3/CaO ratio, measured glass transition temperature (T_g), density (ρ), liquid fragility index determined from viscosity data (m_{vis}) and determined by DSC and corrected by Eq. (7) (m), and configurational heat capacity ($C_{p,conf}$) of the constant CaO glass series, i.e., nominally (80-y)SiO_2-yAl_2O_3-20CaO. When the total compositions do not add to 100%, the impurity oxides are MgO, Fe_2O_3, and TiO_2 (total < 0.4 mol%).

y	Chemical composition (mol%)			$[Al_2O_3]$-[CaO] (mol%)	T_g (K)	ρ (g cm^{-3})	m_{vis} (−)	m (−)	$C_{p,conf}$ (J mol^{-1} K^{-1})
	SiO_2	Al_2O_3	CaO						
10	69.6	9.9	20.0	−10.1	1072	2.550	41	46	15.8
12.5	66.9	12.3	20.3	−8.0	1092	2.562	44	49	18.6
15	64.4	15.0	20.2	−5.2	1103	2.587	46	51	18.2
17.5	62.8	17.3	19.5	−2.2	1121	2.593	45	52	21.2
20	60.3	19.7	19.6	0.1	1129	2.617	46	54	20.1
22.5	58.5	22.1	19.0	3.1	1135	2.635	51	60	22.7
25	55.3	24.6	19.6	5.0	1134	2.660	48	59	25.9
27.5	52.7	26.8	20.1	6.7	1135	2.673	48	55	27.0
30	50.7	29.1	19.8	9.3	1135	2.695	–	52	27.2

3. Results and discussion

3.1. Raman spectroscopy

The Raman spectra of aluminosilicate glasses can be divided into three regions: the low frequency-region (250–650 cm^{-1}), the intermediate-frequency region (650–850 cm^{-1}), and the high-frequency region (850–1200 cm^{-1}). The low frequency-region gives information on ring sizes and interconnectivity of the network, the intermediate-frequency region gives information on T-O motions where T is a network-forming cation, and the high-frequency region gives information on the polymerization of the network and on the Al/Si mixing [38]. The Raman spectra of all the glasses in this study are shown in Fig. 3. Raman spectra of some of the glasses in the tectosilicate series (Fig. 3a) have previously been reported and agree well [9,12,39], but here we consider more glasses covering the entire compositional range from 30 to 100 mol% SiO_2. Raman data for glasses in the constant CaO series (Fig. 3b) have not previously been reported to the best of our knowledge.

3.1.1. Tectosilicate series

The glasses in the tectosilicate series exhibit pronounced differences in their Raman spectra as a function of the silica content (Fig. 3a), starting from the pure SiO_2 glass, which exhibits the characteristic features of vitreous silica with peaks at 442, 492, 604, 800, 1060, and 1200 cm^{-1} [40–44]. With simultaneously increasing Al_2O_3 and CaO content, these bands gradually change their intensity and position. The characteristic peaks for SiO_2 glass located at 442, 492, and 604 cm^{-1} are attributed to mixed stretching–bending vibrational modes of Si-O-Si in large-membered (≥5), four-membered, and three-membered rings, respectively [40]. The peak at 442 cm^{-1} has a tail to lower frequencies, probably related to the largest ring sizes [45]. The signals situated at 492 and 604 cm^{-1}, also known as the D_1 and D_2 bands, respectively, are typical features of pure SiO_2 glass as they originate from Si—O—Si vibrations. Addition of Al_2O_3 + CaO decreases the frequency distance between the two low-wavenumber bands (442 and 492 cm^{-1}), and they merge into a single peak around 481 cm^{-1} for a SiO_2 content of 78 mol%. As the Al_2O_3 + CaO content is further increased, the intensity of this peak (now at ~500 cm^{-1}) decreases as a results of the decrease of Si-O-Si units in the overall structural network,

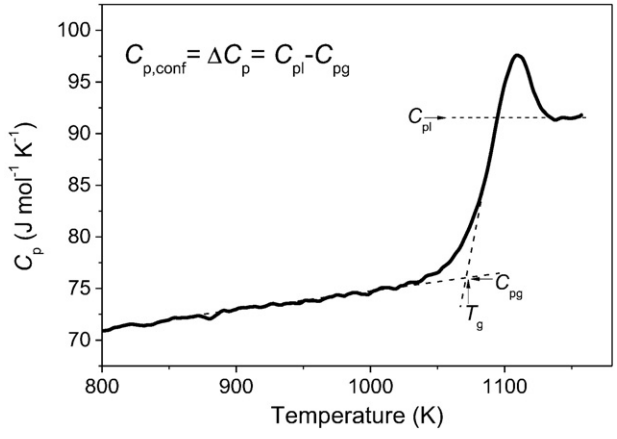

Fig. 2. Illustration of method used for the determination of the configuration heat capacity ($C_{p,conf}$) based on DSC measurements. C_{pl} is determined as the heat capacity in the liquid state, while C_{pg} is the heat capacity at T_g. The present C_p data are for the glass in the constant CaO series with $y = 10$.

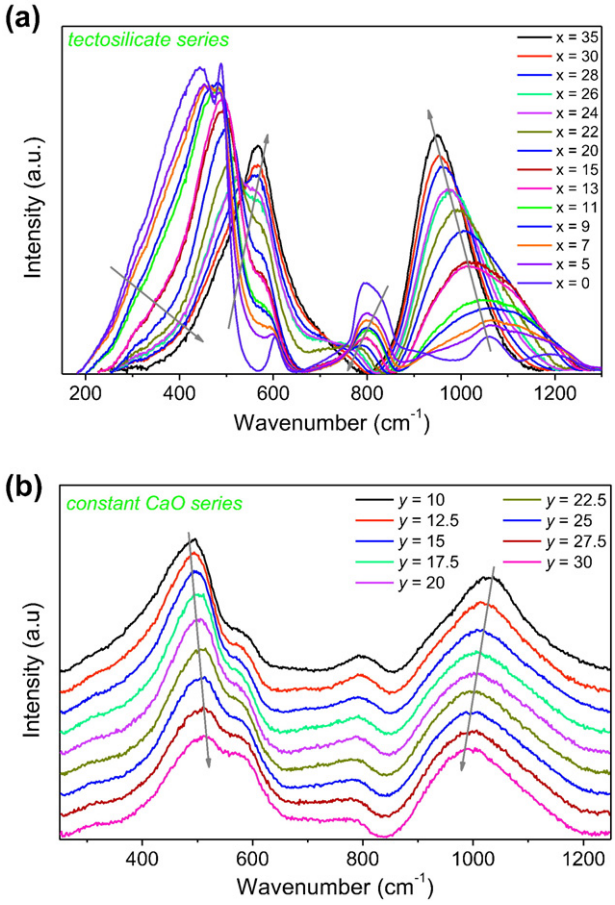

Fig. 3. Raman spectra of the two calcium aluminosilicate glasses series. The individual spectra have been baseline-corrected and adjusted to have the same total area for all bands. Arrows denote directions of increasing x or y. (a) Tectosilicate series with (100-2x)SiO_2-xAl_2O_3-xCaO. (b) Constant CaO series with (80-y)SiO_2-yAl_2O_3-20CaO. The spectra are offset for clarity.

while that of the ~600 cm^{-1} peak increases and the two signals merge into a single peak for the low-Si glasses (<50% SiO_2).

In the intermediate-frequency region, a broad peak can be found around 800 cm^{-1} for the pure SiO_2 glass, which is traditionally ascribed to bending modes of Si—O—Si [40–42,44] or cage motion of Si—O stretching vibrations [9,12,15,38]. With decreasing SiO_2 content, this peak becomes narrower and less intense as the Si-O-Si units are replaced by Si-O-Al units. At lower SiO_2 content (~60 mol%) and with the consequent decrease in average bond strength [46–48], the peak shifts to lower wavenumbers, finally disappears at very low SiO_2 content (<40 mol%). The shift to lower wavenumbers might be related to the presence of AlO_4 tetrahedra [38].

In the high-frequency region, all glasses except pure SiO_2 exhibit a broad peak at ~1000 cm^{-1}, while the pure SiO_2 glass exhibits bands at 1060 and 1200 cm^{-1}, which are ascribed to the stretching modes of Si—O in a fully polymerized silicate network [40–44]. For the $x = 5$ glass with a small amount of Al_2O_3 + CaO (90 mol% SiO_2), these two bands merge into one clearly convoluted peak centered at ~1060 cm^{-1}. This peak consists of several bands originating from stretching modes of Si—O—Si and Si—O—Al units. Due to the aluminum avoidance principle, few or no Al-O-Al units are expected in the low-Al glasses [49]. As the SiO_2 content is further decreased, the peak narrows, becomes more intense, and shifts to lower wavenumbers. The signals in the high-frequency region can be assigned to different stretching vibrations of fully-polymerized tetrahedral network [9] units containing Si^{4+} and Al^{3+}. Naturally, due to the high Al_2O_3 content in the most Al-rich glasses, Al-O-Al units must be present violating the aluminum avoidance. The most intense peak shifts continuously to lower wavenumbers from 1070 cm^{-1} for $x = 5$ to 956 cm^{-1} for $x = 35$ (Fig. 4). The shift to lower wavenumbers is caused by a decrease in force constant [39,46], as Al^{3+} is substituted for Si^{4+} in the tetrahedral network, resulting in an increase in the fraction of $Si(OAl)_x$ units and a decrease in the fraction of $Si(OSi)_x$ units [50]. The peaks in the high-frequency region for the tectosilicate series are deconvoluted in Section 3.1.3 below.

3.1.2. Constant CaO series

In the low-frequency region, several Raman peaks appear around 400–600 cm^{-1} (Fig. 3b), suggesting a polymerized structure [12]. For all the glasses in the constant CaO series, the most intense peak in the low-frequency region appears at ~500 cm^{-1}, which we attribute to Si—O—Si(Al) vibrations. This is consistent with literature, where Si—O—Si(Al) vibrations for various aluminosilicates are reported to be found around 480–500 cm^{-1} [9,51] with the specific position of the peak depending on the glass composition, namely the type of modifier. At ~450 cm^{-1}, a shoulder peak attributed to Si—O—Si bonds can be found in all glasses [38]. As Al_2O_3 is substituted for SiO_2 in the constant CaO series, this peak is expected to be most pronounced for glasses with high SiO_2 content and gradually decrease as the Al_2O_3 + CaO content increases, and this is also the case shown in Fig. 3b. Another shoulder can be found at ~583 cm^{-1} for the peralkaline glasses. The shoulder shifts to ~590 cm^{-1} for the charge-balanced and peraluminous glasses ($y \geq 20$). The increase in intensity of this band with increasing Al_2O_3 content is in agreement with literature and it has been suggested to originate from the presence of rings containing five-fold coordinated Al^{3+} [9]. This is indeed possible as small amounts of Al^{V} are present in peralkaline compositions, and the increase in peak intensity in the peraluminous region could be explained by the lack of charge-balancing Ca^{2+} modifier ions in this composition regime, forcing Al^{3+} to enter five-fold coordination.

In the intermediate-frequency region, a broad low-intensity band is found with maximum at 800 cm^{-1} for the most peralkaline glasses, shifting to lower frequencies as the Al_2O_3 content increases, and finally at 780 cm^{-1} for the most peraluminous glasses. The peak is ascribed to cage motions of both Si—O and Al—O stretching vibrations [9,12,15,38]. As expected, substitution of Al_2O_3 for SiO_2 leads to decrease in peak intensity, peak broadening, and a shift to lower frequencies due to a decrease in the average bond strength [9]. The band around 700 cm^{-1} is reported to be due to AlO_4 tetrahedra and should increase in intensity as the Al_2O_3 content increases [38], and this is indeed the case (Fig. 3b). However, the 700–800 cm^{-1} region is also reported to cover bands due to Al^{3+} in both four-, five-, or six-fold coordination [12] and the intensity of the 700 cm^{-1} band is reported to increase in the peraluminous region, which could be associated with the presence of five- or six-fold coordinated Al species [9]. This is consistent with our results in Fig. 3b and prevailing theories for the structure of peraluminous calcium aluminosilicate glasses [2,8–12].

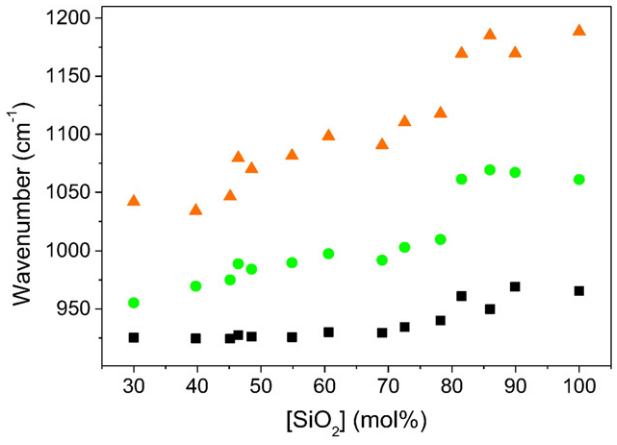

Fig. 4. Raman peak positions for the three bands used in the deconvolution of the high-frequency region as a function of SiO_2 content in the tectosilicate glass series.

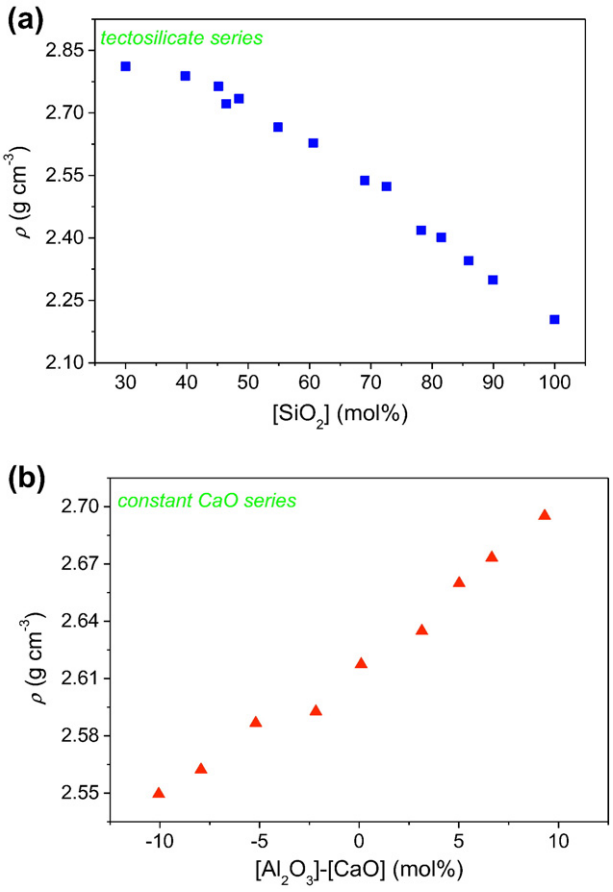

Fig. 5. Density (ρ) plotted as a function of (a) SiO_2 content for the tectosilicate series and (b) [Al_2O_3]-[CaO] for the constant CaO series. Errors associated with ρ are smaller than the size of the symbols.

In the high-frequency region, all glasses in the constant CaO series exhibit a convoluted peak centered around 1000 cm^{-1}. The origin of the peak is Si—O and Al—O stretching [9,12,15,38] in TO_4 (T = Si,Al) units. The peak position shifts to lower frequencies with increasing Al_2O_3 content. This is expected as Al—O stretches should occur at 20–30% lower frequencies than Si—O stretches due to the lower force constant [12].

Unfortunately, unlike the spectra in the tectosilicate series, a deconvolution of the high-frequency region is not possible. The combination of different structural units in peralkaline and peraluminous compositions and the complicated charge-balancing nature of alkaline earth oxides (e.g., the presence of Al^V in peralkaline compositions) lead to a high number of distinct structural units throughout the glass series. The high number of distinct structural units makes it complicated to deconvolute the spectra.

3.1.3. Spectral deconvolution of tectosilicate series

Deconvolution of Raman spectra in the high-frequency region on similar glass compositions can be found in literature [9,12,39]. For example, a tectosilicate calcium aluminosilicate composition is reported to consist of three peaks at 1050, 1150, and 1200 cm^{-1}, while a peak should appear at 1100 cm^{-1} for peraluminous compositions [9]. Elsewhere, the deconvolution is reported to consist of five bands at 925, 1000, 1070, 1140, 1200 cm^{-1} for compositions similar to the ones in this study [12,39].

The deconvolution of our Raman spectra in Fig. 3a leads to bands at 970, 1070, and 1190 cm^{-1} for the pure SiO_2 glass (Fig. 4). As the SiO_2 content decreases throughout the tectosilicate series, the bands all shift to lower wavenumbers. For example, the glass with the lowest SiO_2 content ($x = 35$) exhibits bands at 930, 955, and 1050 cm^{-1}, resembling those reported by Neuville et al. [9]. We note that this is, however, not in agreement with the early work performed by Seifert et al., who reported no compositional effect on the frequency of the bands used for the deconvolution [39]. An example of the deconvolution can be found in Fig. S1 in the Supplementary material for the glass with $x = 30$.

A sudden shift in the position of the high-frequency bands can be observed around 80–85 mol% SiO_2 ($x = 7$–9), as shown in Fig. 4. This suggests that large structural changes occur, which could be related to an abrupt decrease in the number of pure silica rings. Therefore, we emphasize that the three proposed bands do not necessarily represent the same distinct structural units for all glass compositions. For example, the highest frequency band does not represent the same structural unit in glasses with $x = 0$ and 35, as the introduction of Al_2O_3 and CaO allows for forming new and different structural units. However, the deconvolution clearly demonstrates the gradual decrease of the average bond strength as more Al_2O_3 is introduced into the network.

3.2. Atomic packing density

Density exhibits approximate linear composition dependence in both the tectosilicate (Fig. 5a) and constant CaO series (Fig. 5b). In the tectosilicate series, density increases from 2.204 g/cm^3 for the pure silica glass ($x = 0$) to 2.812 g/cm^3 for the glass with the highest Al_2O_3 content ($x = 35$). The density differences between the extremes in

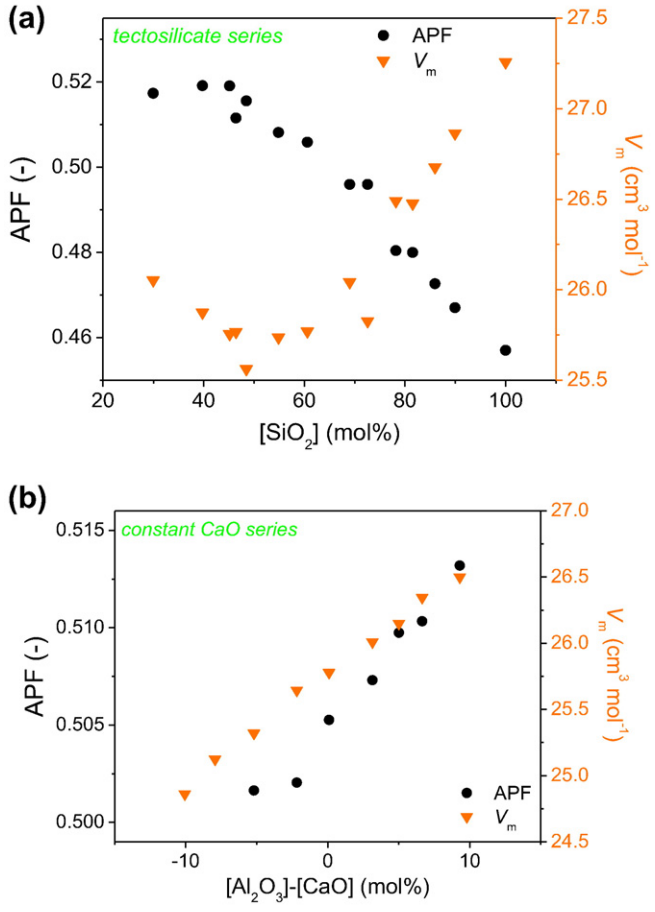

Fig. 6. Atomic packing factor (APF) and molar volume (V_m) plotted as a function of (a) SiO_2 content for the tectosilicate series and (b) [Al_2O_3]-[CaO] for the constant CaO series. Errors associated with APF and V_m are smaller than the size of the symbols. APF is calculated as the ratio between the minimum theoretical volume occupied by the ions and the corresponding molar volume of the glass. Lines are intended as guides for the eyes.

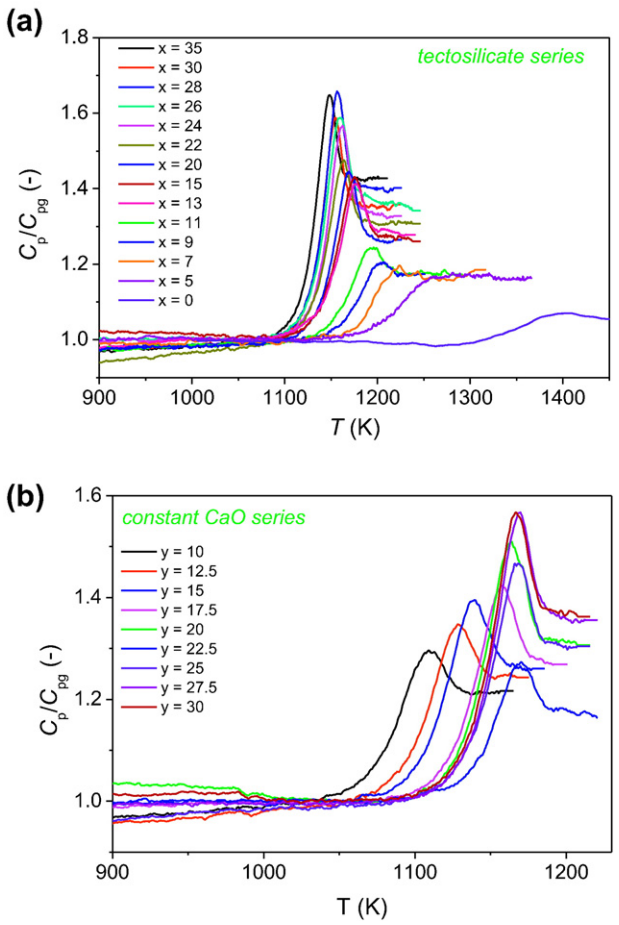

Fig. 7. Differential scanning calorimetry scans for the (a) tectosilicate series and (b) constant CaO series. The data are obtained at 10 K/min subsequent to cooling at the same rate. The measured isobaric heat capacities (C_p) have been normalized by the respective heat capacity at the glass transition (C_{pg}).

compositions are much smaller for the constant CaO series, exhibiting densities of 2.550 and 2.695 g/cm^3 for the glasses with lowest and highest Al_2O_3 content, respectively. Since the molar mass of the glasses changes substantially throughout the two series, we calculate the molar volume (V_m) and the atomic packing factor (APF) to describe changes in the packing density of the glasses (Fig. 6). Molar volume describes the volume occupied by one mole of oxides in the glass. The glasses in the tectosilicate series exhibit a minimum in molar volume around 50–60% SiO_2, suggesting a high packing density in this compositional range (Fig. 6a). The constant CaO series exhibits increasing molar volume with increasing Al_2O_3 + CaO content and thereby a closer packing at low Al_2O_3 + CaO content (Fig. 6b).

APF describes the ratio between the volume occupied by the elements in the glass and the total volume of the glass including free volume. When calculating APF, the elements are assumed to be spherical and the size of the spheres dependent on the coordination number of each species. The coordination numbers are assumed to be 2 for O, 4 for Si, and 6 for Ca [10]. For Al, we estimate the fractions of Al^{IV} and Al^{V} based on the analyzed compositions (Tables 1 and 2) and the ^{27}Al NMR data reported by Neuville et al. [15]. The effective ionic radii have been taken from [52]. For the tectosilicate series, we find APF to be low in glasses with high SiO_2-content and to increase monotonically with increasing Al_2O_3 + CaO content (Fig. 6a), in agreement with literature [53]. This suggests a closer packing as calcium ions occupy the cavities between the network-forming cations. For the constant CaO series, APF increases continuously with increasing Al_2O_3 content (Fig. 6b), as an increasing concentration of calcium is fixed in the proximity of Al^{3+}. In the peraluminous regime, Al^{3+} is introduced in five- or six-fold coordination, causing no apparent change in the trend of APF with Al_2O_3 content.

3.3. Glass transition temperature

For the determination of the glass transition temperature (T_g), we measured the temperature dependence of isobaric heat capacity for both glass series (Fig. 7). As shown in Fig. 8, T_g as determined using DSC is highly dependent on the glass composition. For the tectosilicate series (Fig. 8a), T_g decreases dramatically when Al_2O_3 + CaO is introduced into the network, consistent with literature data [54]. Since all the meta-aluminosilicate glasses are nominally NBO-free, the change in T_g with composition reveals the difference in bond strength as Si—O bonds are strong compared to Al—O bonds [12]. The decrease in T_g with increasing x is particularly pronounced in the high-silica range (down to ~80% SiO_2). In the intermediate-silica range, T_g changes more modestly and only by ~20 K from 72 to 30 mol% SiO_2 (inset of Fig. 8a).

The composition dependence of T_g in the constant CaO series is related to the concentration of NBOs in the network structure (Fig. 8b). In the peralkaline regime, T_g increases approximately linearly with increasing Al_2O_3 content as the role of Ca^{2+} changes from modifying the glassy network to charge-compensating Al^{3+} in four-fold coordination, i.e., the network connectivity increase. In the peraluminous region, T_g is approximately constant, suggesting a constant network connectivity in this compositional regime.

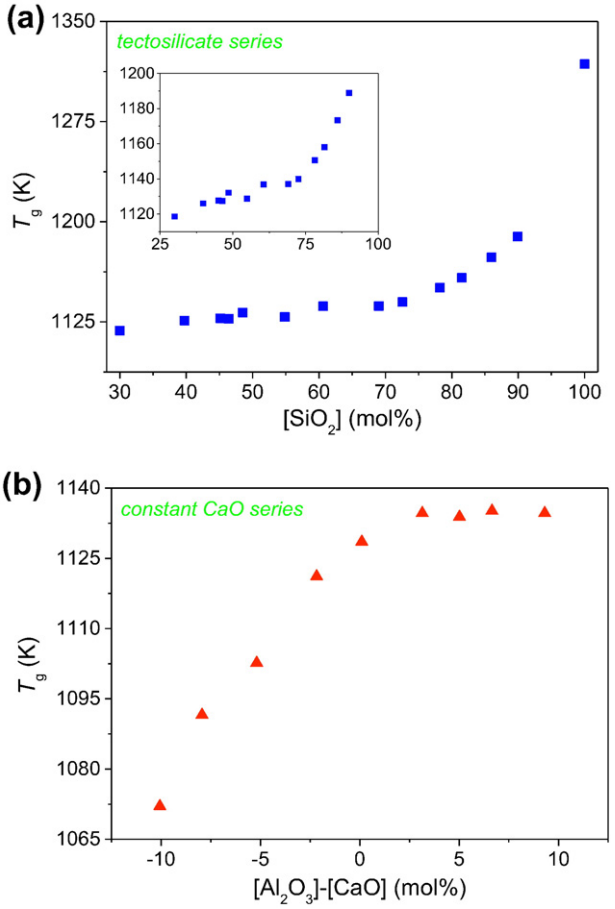

Fig. 8. Glass transition temperature (T_g) determined by differential scanning calorimetry plotted as a function of (a) SiO_2 content for the tectosilicate series and (b) [Al_2O_3]-[CaO] for the constant CaO series. The error associated with T_g is ±2 K. In (a), the inset shows a zoom of the data without pure SiO_2 glass.

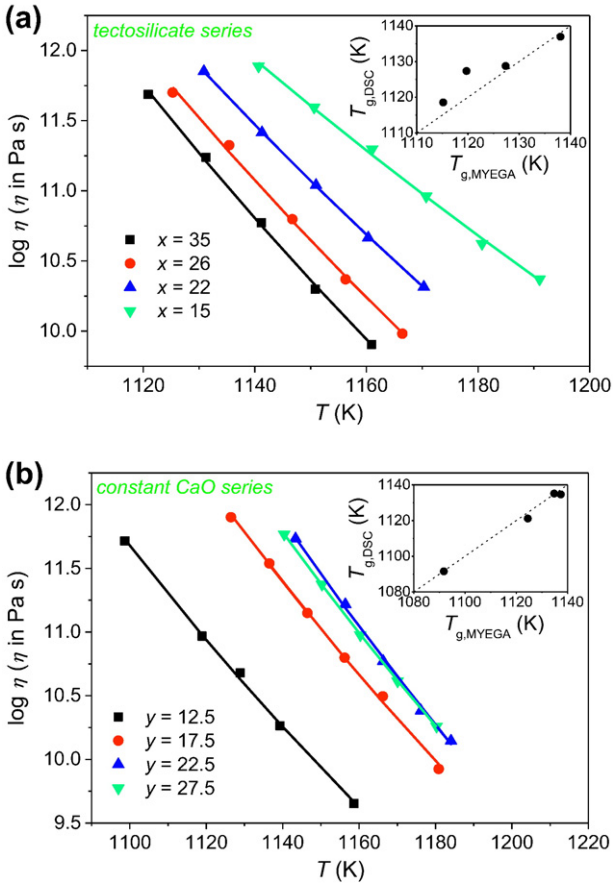

Fig. 9. Logarithmic viscosity (η) in the vicinity of the glass transition temperature (T_g) as a function of temperature for the (a) tectosilicate series and (b) constant CaO series. The lines represent the fits to the MYEGA equation (Eq. (4)). Data have been determined using the BPV technique. The insets in both figures show T_g determined from DSC vs. T_g from the MYEGA fit for the four glasses in both series.

3.4. Viscosity and liquid fragility

To determine the liquid fragility index (m) based on measurements of viscosity, glass samples of at least several grams are typically needed. As such large samples masses are not available for all glasses in this study, we have determined fragility from direct viscosity measurements whenever possible (Eq. (4)) and in addition determined the m values for all glasses using the DSC method (Eqs. (5) and (6)) and corrected the data using Eq. (7). This also allows us to compare the trend in the corrected DSC-determined fragility value, with the precise m values determined from direct viscosity measurements. Viscosity measurements were performed using BPV for four glasses in both the tectosilicate and constant CaO series and using a combination of BBV, PPV, and rotational viscometry for four glasses in the constant CaO series. The combination of experiments performed for each glass was based on available sample mass.

First we consider viscosity data determined in the vicinity of the glass transition using the BPV technique for four compositions in both the tectosilicate (Fig. 9a) and constant CaO series (Fig. 9b). For both series, we find the same trend in T_g (i.e., isokom temperature at $\eta = 10^{12}$ Pa s) with composition as that observed in Fig. 8, where T_g was determined using DSC (see insets in Fig. 9), agreeing with the trend reported in [55]. For the tectosilicate series, the viscosity decreases slightly with decreasing SiO_2 content in the intermediate Si-range. For the constant CaO series, increasing the Al_2O_3 content in the peralkaline regime leads to increased network connectivity, giving rise to large differences in viscosity among the peralkaline glasses. In the peraluminous region, no further increase in connectivity occurs with increasing Al_2O_3 content and the viscosity vs. temperature curve is therefore essentially unaffected by composition even for the high-Al_2O_3 glasses. For four other glasses in the constant CaO series, we present viscosity data covering a large temperature range above the glass transition (Fig. 10). The same trend as in Fig. 9b is observed.

Based on the viscosity data presented in Figs. 9 and 10 and the variation of fictive temperature with heating/cooling rate from DSC (Figs. S2 and S3 in Supplementary material), the liquid fragility index m is calculated and subsequently corrected using Eq. (7) as shown in Fig. 11a for tectosilicate series and in Fig. 11b for constant CaO series. Only low-temperature viscosity data (ball penetration viscometry) has been used for determining m in the tectosilicate series, while a combination of low-temperature and high-temperature viscosity data (beam bending, parallel plate, and rotational viscometry) have been used for the constant CaO series. We note that the compositional trend in fragility is identical for values determined using viscosity or DSC data. The difference in absolute m values is presumably due to the difference in difficulty of determining the fictive temperature using DSC for the different glass compositions. This is in case for the tectosilicate series in particular, as the glasses exhibit relatively small enthalpy overshoot during the glass transition, making it difficult to accurately determine T_f, especially at low heating rates. Moreover, the T_f values are at much higher temperatures for this series, leading to decreased sensitivity of the DSC instrument.

The tectosilicate series exhibits increasing fragility with decreasing SiO_2 content (Fig. 11a) in agreement with the reported effect of Al_2O_3 and CaO on liquid fragility in similar aluminosilicate glass-forming liquids [2,30]. As liquid fragility is a measure of the activation energy for viscous flow at the glass transition and is strongly affected by bond strength and bond order, silica-rich liquids are "strong" because their SiO_2 networks have high bond strengths and exhibit a high degree of short-range order, which only weakens slightly upon increasing temperature. The increasing concentrations of Al_2O_3 and CaO lead to decreasing bond strengths and a decrease in the short-range order, as the presence of CaO results in NBOs [29]. This decrease in network connectivity results in a more flexible and more temperature sensitive network, and hence, an increase in fragility. We note that it has not been possible to determine fragility using the DSC-method for the glasses in the tectosilicate series with high SiO_2 content ($x = 0$, 5, and 7) due to the small overshoots in heat capacity and wide glass transition region for these glasses.

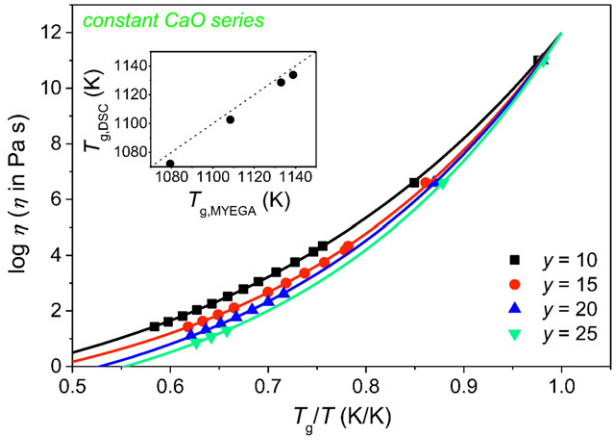

Fig. 10. Logarithmic viscosity (η) as a function of glass transition temperature (T_g) scaled inverse temperature (T_g/T) for glasses in the constant CaO series, illustrating differences in liquid fragility with composition. The lines represent fits to the MYEGA equation (Eq. (4)). Data have been determined using BBV, PPV, and rotational viscometry. Inset shows T_g determined from DSC vs. T_g from the MYEGA fit for the four glasses.

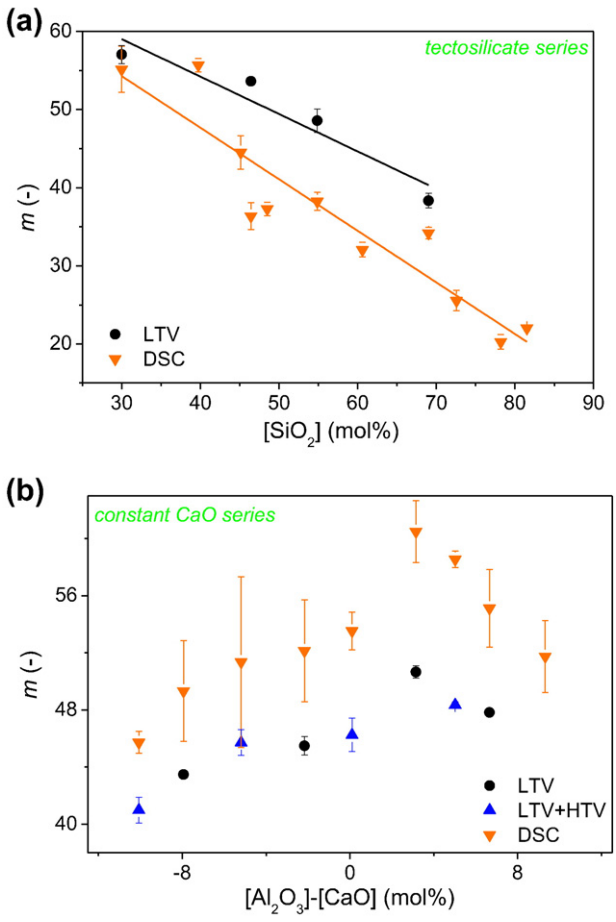

Fig. 11. Liquid fragility index (m) determined by differential scanning calorimetry (DSC) and corrected using Eq. (7), low-temperature viscometry (LTV), and/or high-temperature viscometry (HTV) plotted as a function of (a) SiO_2 content for the tectosilicate series and (b) [Al_2O_3]-[CaO] for the constant CaO series. The errors related to the fragility determined solely by low-temperature viscosity (black bullets) have been checked using different viscosities at infinite temperature ($\log \eta = -1$ to -5) and regardless of the $\log \eta$ value, the error is smaller than 1.5.

In the constant CaO series, the liquid fragility index increases continuously with increasing Al_2O_3 content throughout the peralkaline region (Fig. 11b). A maximum value of m is observed slightly into the peraluminous region, whereupon m decreases with further increase of Al_2O_3 content. This compositional dependence of the fragility is controlled by the network topology. The increase in fragility in the peralkaline region is explained by the increasing Al/Si ratio, resulting in decreasing overall bond strength and increasing disorder [2]. In the peraluminous region, an increase in fragility is expected as an increase in Al^V is also expected, generally leading to longer and weaker bonds [56,57] and also greater number of angular constraint that tend to decrease liquid fragility [58]. This suggests that the angular constraints have a large influence on the fragility of these glasses.

The decrease in liquid fragility in the most peraluminous compositions suggests an increase in the order of the melt, possibly due to the creation of a new structural unit and as such the decrease in fragility in the highly peraluminous compositions could be interpreted as evidence for oxygen tricluster formation. We observe the maximum in fragility when $[CaO]/([CaO] + [Al_2O_3])$ is around 0.47. This value coincides with the maximum in viscosity at constant temperature across the metaluminous join reported by Toplis and Dingwell [59]. They reported a maximum in viscosity when $[CaO] / [CaO] + [Al_2O_3]$ is equal to 0.45–0.48, depending on SiO_2 content and argue that the origin of the maximum and the subsequent decrease in viscosity at more peraluminous composition is oxygen triclusters.

3.5. Configurational heat capacity

The configurational heat capacity ($C_{p,conf}$) for all glasses was determined using DSC as illustrated in Fig. 2. The calorimetric glass transitions and the reduced heat capacities ($C_p/C_{p,g}$) for the two glass series are shown in Fig. The determined values of $C_{p,conf}$ are given in Tables 1 and 2 and shown in Fig. 12. For the tectosilicate series, $C_{p,conf}$ increases approximately linearly with increasing Al_2O_3 + CaO content (Fig. 12a). For the constant CaO series, $C_{p,conf}$ increases linearly with increasing $[Al_2O_3]$ in the peralkaline regime, then exhibits a slightly more pronounced increase in the first peraluminous glasses, and becomes approximately constant for the most peraluminous glasses. The constant configurational heat capacity is not consistent with the study by Webb of calcium aluminosilicate glasses with ~67 mol% SiO_2 and varying Al/Ca ratio, who reported a maximum in $C_{p,conf}$ at the tectosilicate join and decreasing $C_{p,conf}$ for the peraluminous glasses [32].

Next we attempt to predict the composition dependence of $C_{p,conf}$ using Eq. (1). According to the model of Eq. (1), $C_{p,conf}$ is proportional to m and inversely proportional to T_g. Therefore, we would expect a good agreement between data and model for the tectosilicate series, but to a smaller extent for the constant CaO series due to the increase in T_g with $[Al_2O_3]$ in the peralkaline regime (Fig. 8b) and maximum in m in the peraluminous regime (Fig. 11b). Indeed, for the tectosilicate series, the model predicts the data well with just one fitting parameter (A in Eq. (1)) for the relatively fragile glass formers, whereas the largest discrepancies between data and model are found for the strongest glass formers (Fig. 12a). This might be a result of the challenges in

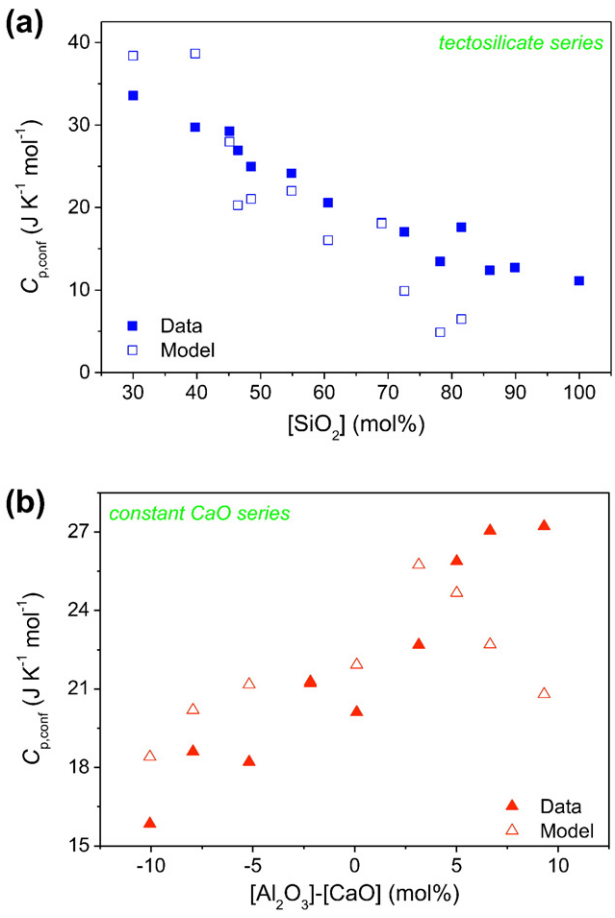

Fig. 12. Configurational heat capacity ($C_{p,conf}$) plotted as a function of (a) SiO_2 content for the tectosilicate series and (b) $[Al_2O_3]$-[CaO] for the constant CaO series. Both $C_{p,conf}$ values determined by differential scanning calorimetry and modeled $C_{p,conf}$ values determined using Eq. (1) are shown.

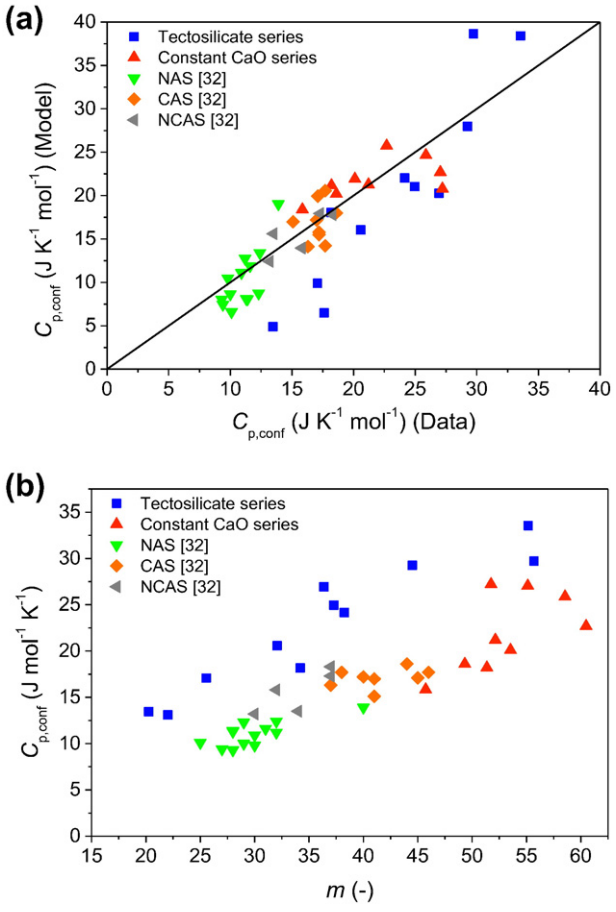

Fig. 13. (a) Modeled vs. measured values of the configurational heat capacity ($C_{p,conf}$) and (b) $C_{p,conf}$ as a function of liquid fragility index (m) for various aluminosilicate glass. The tectosilicate and constant CaO series data are taken from this study, while the data for sodium aluminosilicate (NAS), calcium aluminosilicate (CAS), and sodium calcium aluminosilicate (NCAS) glasses are taken from Ref. [32].

accurately determining m values for strong glass formers by DSC, or because the model is only applicable to less strong glass formers. For the constant CaO series, the model predicts the data well in the peralkaline regime, but discrepancies arise in the peraluminous regime due to the maximum in fragility and/or the constant T_g in the peraluminous region. Considering the Raman spectra of the constant CaO series (Fig. 3b), no major changes in short range order is evident from the high-frequency region. However, a new band or a shift in intensity is evident in the intermediate-frequency region. This band might be ascribed to species with longer and weaker bonds, such as a substantial amount of newly formed five-fold coordinated aluminum [9]. Assuming that $C_{p,conf}$ is related to the short-range order bonding, the changes in structure observed by Raman spectroscopy might explain the constant $C_{p,conf}$ but varying m in the peraluminous region.

The prediction of $C_{p,conf}$ from m and T_g using Eq. (1) has been done using A as a scaling factor, with A connecting the configurational entropy during the glass transition with T_g. The fitted values of A are 16.0 and 11.8 kJ/mol for the tectosilicate series and the constant CaO series, respectively. For comparison, Smedskjaer et al. found A to be 19 kJ/mol for a series of borosilicate glasses [28]. Moreover, using the data from Webb [32] for aluminosilicates, we have determined A to be 12.7, 13.3, and 16.5 kJ/mol for sodium aluminosilicate, calcium aluminosilicate, and sodium calcium aluminosilicate glasses, respectively. The relatively large difference in A values between the constant CaO and borosilicate glass series and the smaller differences between the different aluminosilicate glass series suggest that the chemical composition affects A. Furthermore, the relatively good prediction of $C_{p,conf}$ based on Eq. (1) suggests that the model can be used to predict $C_{p,conf}$ for different glass systems (Fig. 13a). In general, $C_{p,conf}$ and liquid fragility are proportional across different aluminosilicate glass compositions, as illustrated in Fig. 13b.

However, since Eq. (1) cannot account for the full composition dependence of $C_{p,conf}$, other factors could be considered. Recently, it has been proposed that the magnitude of $C_{p,conf}$ is linked to the intermediate-range order (IRO) in borosilicate glasses, with $C_{p,conf}$ increasing with the relative area of the IRO Raman bands [60]. For borate-containing glasses, IRO bands are quite distinct with various borate superstructural units, such as boroxol-rings. On the other hand, for aluminosilicate glasses, the IRO Raman bands are not clearly defined. In general, structural information about IRO in aluminosilicate glasses can be found in the low-frequency region (~200–700 cm^{-1}), which, e.g., describes ring sizes and ring composition, such as the D_1 and D_2 bands for pure SiO_2 rings. For simplicity we use the entire low-frequency region to compare the relative areas of IRO Raman bands throughout both compositional series.

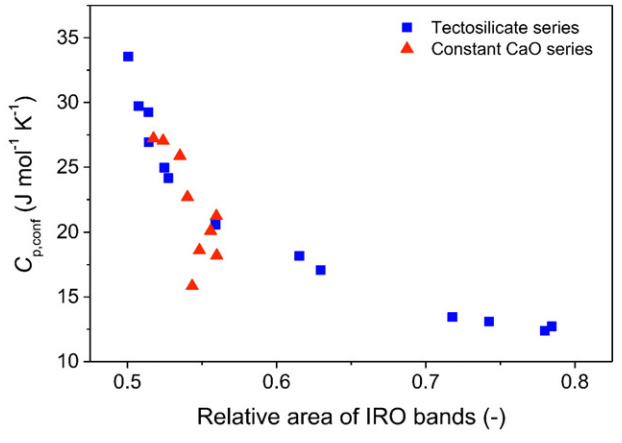

Fig. 14. Dependence of configurational heat capacity ($C_{p,conf}$) on the relative area of the intermediate range order (IRO) Raman bands for the tectosilicate and constant CaO series. The bands assigned to different ring structures in the low-frequency region have been used as an estimate of the extent of IRO.

We note that for the constant CaO series, there is a non-negligible overlap of Raman bands from the low- and intermediate-frequency regions. The Raman spectra in the tectosilicate series shows that $C_{p,conf}$ decreases with an increase in the relative IRO band area, while the constant CaO series exhibits a less systematic trend, perhaps related to the difficulties in deconvoluting the IRO band area (Fig. 14). As such, for the tectosilicate series, it appears that a high intensity of IRO bands reflects a high degree of order, which is related to a small $C_{p,conf}$ as the structural changes occurring during the glass transition are relatively small. This relationship between order and IRO is a result of the Raman intensities of peaks related to short range order, as glasses with uniform bond strengths and low concentrations of NBOs exhibit low intensities (e.g., $x = 0$ in Fig. 3a). The difference in the relationship between $C_{p,conf}$ and IRO band area for the studied aluminosilicate and borosilicate glasses [60] indicates that the origin of the magnitude of $C_{p,conf}$ is highly dependent on chemical composition and not simply extent of IRO.

4. Conclusion

We have investigated the composition dependence of liquid fragility and configurational heat capacity for two series of calcium aluminosilicate glass-forming liquids with varying (Al + Ca)/Si ratio and varying Al/Si ratio at constant CaO content, respectively. For the tectosilicate series we find decreasing glass transition temperature (T_g), increasing liquid fragility, and increasing configurational heat capacity with increasing Al_2O_3 + CaO content. The constant CaO series exhibits increasing T_g with increasing Al_2O_3 content in the peralkaline region, while it becomes constant in the peraluminous region. Measurements of fragility based on both viscometry and calorimetry show a maximum in fragility slightly into the peraluminous region, possibly due to the formation of oxygen triclusters. The configurational heat capacity increases approximately linearly with increasing Al_2O_3 content in this series. We find that the majority of the variation of configurational heat capacity with composition can be predicted based a previously proposed topological/thermodynamic approach, but model-data discrepancies are found for the "strongest" glass formers when configurational heat capacity is not proportional to liquid fragility. Raman spectroscopy measurements confirm the expected structural changes in the two glass series, including the gradual disappearance of pure SiO_2 units as Al_2O_3 + CaO is added in the tectosilicate series, changes in type and size of ring structures, and mixing of Al and Si containing units throughout the aluminosilicate network.

Acknowledgements

We thank Hao Liu (Aalborg University) for valuable discussions. This work was partially funded by Corning Incorporated and the Danish Council for Independent Research under Sapere Aude: DFF-Starting Grant (1335-00051A).

Appendix A. Supplementary data

Supplementary data to this article can be found online at http://dx.doi.org/10.1016/j.jnoncrysol.2017.01.033.

References

[1] B.O. Mysen, Magmatic silicate melts: relations between bulk composition, structure and properties, Magmat. Process. Physicochem. Princ. 375–399 (1987).
[2] M. Solvang, Y. Yue, S.L. Jensen, D.B. Dingwell, Rheological and thermodynamic behaviors of different calcium aluminosilicate melts with the same non-bridging oxygen content, J. Non-Cryst. Solids 336 (2004) 179–188, http://dx.doi.org/10.1016/j.jnoncrysol.2004.02.009.
[3] A.K. Varshneya, Chemical strengthening of glass, Int. J. Appl. Glas. Sci. 1 (2010) 131–142, http://dx.doi.org/10.2307/1711232.
[4] A.J. Ellison, I.A. Cornejo, Glass substrates for liquid crystal displays, Int. J. Appl. Glas. Sci. 1 (2010) 87–103, http://dx.doi.org/10.1111/j.2041-1294.2010.00009.x.

[5] A.K. Varshneya, Chemical strengthening of glass: lessons learned and yet to be learned, Int. J. Appl. Glas. Sci. 1 (2010) 131–142, http://dx.doi.org/10.1111/j.2041-1294.2010.00010.x.

[6] A. Tandia, K.D. Vargheese, J.C. Mauro, A.K. Varshneya, Atomistic understanding of the network dilation anomaly in ion-exchanged glass, J. Non-Cryst. Solids 358 (2012) 316–320, http://dx.doi.org/10.1016/j.jnoncrysol.2011.09.034.

[7] J.E. Shelby, Formation and Properties of Calcium Aluminosilicate Glasses, J. Am. Ceram. Soc. 88 (1985) 155–158.

[8] M. Solvang, Rheological and Thermodynamic Response to Compositional Variation in High Aluminosilicate Melts, Ph.D. thesis, Aalborg University, Denmark, 2002.

[9] D.R. Neuville, L. Cormier, D. Massiot, Al environment in tectosilicate and peraluminous glasses: a 27Al MQ-MAS NMR, Raman, and XANES investigation, Geochim. Cosmochim. Acta 68 (2004) 5071–5079, http://dx.doi.org/10.1016/j.gca.2004.05.048.

[10] D.R. Neuville, L. Cormier, A. Flank, V. Briois, D. Massiot, Al speciation and Ca environment in calcium aluminosilicate glasses and crystals by Al and Ca K-edge X-ray absorption spectroscopy, Chem. Geol. 213 (2004) 153–163, http://dx.doi.org/10.1016/j.chemgeo.2004.08.039.

[11] L.-G. Hwa, S.-L. Hwang, L.-C. Liu, Infrared and Raman spectra of calcium alumino–silicate glasses, J. Non-Cryst. Solids 238 (1998) 193–197, http://dx.doi.org/10.1016/S0022-3093(98)00688-7.

[12] P.F. McMillan, B. Piriou, A. Navrotsky, A Raman spectroscopic study of glasses along the join silica-calcium aluminate, silica-sodium aluminate, and silica-potassium aluminate, Geochim. Cosmochim. Acta 46 (1982) 2021–2037.

[13] M. Bauchy, Structural, vibrational, and elastic properties of a calcium aluminosilicate glass from molecular dynamics simulations: the role of the potential, J. Chem. Phys. 141 (2014) 24507, http://dx.doi.org/10.1063/1.4886421.

[14] M.J. Toplis, S.C. Kohn, M.E. Smith, I.J.F. Poplett, Fivefold-coordinated aluminum in tectosilicate glasses observed by triple quantum MAS NMR, Am. Mineral. 85 (2000) 1556–1560.

[15] D.R. Neuville, L. Cormier, D. Massiot, Al coordination and speciation in calcium aluminosilicate glasses: effects of composition determined by 27Al MQ-MAS NMR and Raman spectroscopy, Chem. Geol. 229 (2006) 173–185, http://dx.doi.org/10.1016/j.chemgeo.2006.01.019.

[16] T.K. Bechgaard, A. Goel, R.E. Youngman, J.C. Mauro, S.J. Rzoska, M. Bockowski, L.R. Jensen, M.M. Smedskjaer, Structure and mechanical properties of compressed sodium aluminosilicate glasses: role of non-bridging oxygens, J. Non-Cryst. Solids 441 (2016) 49–57, http://dx.doi.org/10.1016/j.jnoncrysol.2016.03.011.

[17] E. Lacy, Aluminum in glasses and melts, Phys. Chem. Glasses 4 (1963) 234–238.

[18] K. Adachi, T. Kotaka, Volume and enthalpy relaxation in polystyrene, Polym. J. 14 (1982) 959–970.

[19] L.M. Martinez, C.A. Angell, A thermodynamic connection to the fragility of glass-forming liquids, Nature 410 (2001) 663–667, http://dx.doi.org/10.1038/35070517.

[20] L.M. Wang, C.A. Angell, Response to “Comment on ‘direct determination of the fragility indices of glassforming liquids by differential scanning calorimetry: kinetic versus thermodynamic fragilities’” [J. Chem. Phys. 118, 10351 (2003)] (Journal of Chemical Physics (2003)), J. Chem. Phys. 124 (2006) 10353–10355. doi:10.1063/1.2203634.

[21] C.A. Angell, Strong and fragile liquids, Relaxations Complex Syst. 3–11 (1985).

[22] D.V. Matyushov, C.A. Angell, Two-Gaussian excitations model for the glass transition, J. Chem. Phys. 123 (2005)http://dx.doi.org/10.1063/1.1949211.

[23] D. Huang, G.B. McKenna, New insights into the fragility dilemma in liquids, J. Chem. Phys. 114 (2001) 5621–5630, http://dx.doi.org/10.1063/1.1348029.

[24] G. Ruocco, F. Sciortino, F. Zamponi, C. De Michele, T. Scopigno, Landscapes and fragilities, J. Chem. Phys. 120 (2004) 10666–10680, http://dx.doi.org/10.1063/1.1736628.

[25] F.H. Stillinger, P.G. Debenedetti, Energy landscape diversity and supercooled liquid properties, J. Chem. Phys. 116 (2002) 3353–3361, http://dx.doi.org/10.1063/1.1434997.

[26] C.A. Angell, Ten questions on glassformers, and a real space “excitations” model with some answers on fragility and phase transitions C, J. Phys. Condens. Matter 12 (2000) 6463–6475.

[27] J.D. Stevenson, P.G. Wolynes, Thermodynamic-kinetic correlations in supercooled liquids: a critical survey of experimental data and predictions of the random first order transition theory of glasses, J. Phys. Chem. B 109 (2005) 1–15.

[28] M.M. Smedskjaer, J.C. Mauro, R.E. Youngman, C.L. Hogue, M. Potuzak, Y. Yue, Topological principles of borosilicate glass chemistry, J. Phys. Chem. B 115 (2011) 12930–12946, http://dx.doi.org/10.1021/jp208796b.

[29] M. Moesgaard, R. Keding, J. Skibsted, Y. Yue, Evidence of intermediate-range order heterogeneity in calcium aluminosilicate glasses, Chem. Mater. 22 (2010) 4471–4483, http://dx.doi.org/10.1021/cm1011795.

[30] M. Bouhadja, N. Jakse, A. Pasturel, Stokes-Einstein violation and fragility in calcium aluminosilicate glass formers: a molecular dynamics stud, Mol. Simul. 40 (2014) 251–259, http://dx.doi.org/10.1080/08927022.2013.840893.

[31] G. Gruener, P. Odier, D.D.S. Meneses, P. Florian, P. Richet, Bulk and local dynamics in glass-forming liquids: a viscosity, electrical conductivity, and NMR study of aluminosilicate melts, Phys. Rev. B 64 (2001) 24206, http://dx.doi.org/10.1103/PhysRevB.64.024206.

[32] S.L. Webb, Configurational heat capacity of Na_2O-CaO-Al_2O_3-SiO_2 melts, Chem. Geol. 256 (2008) 91–100, http://dx.doi.org/10.1016/j.chemgeo.2008.04.003.

[33] P.H.C. Eilers, H.F.M. Boelens, Baseline Correction With Asymmetric Least Squares Smoothing, University Medical Centre, Leiden, 2005.

[34] J.C. Mauro, Y. Yue, A.J. Ellison, P.K. Gupta, D.C. Allan, Viscosity of glass-forming liquids, Proc. Natl. Acad. Sci. 106 (2009) 19780, http://dx.doi.org/10.1073/pnas.0911705106.

[35] C.A. Angell, Formation of glasses from liquids and biopolymers Author(s): C.A. Angell Published by: American Association for the Advancement of Science Stable URL: http://www/.jstor.org/stable/2886440, Science 267 (1995) 1924–1935, http://dx.doi.org/10.1126/science.267.5206.1924.

[36] L.M. Wang, V. Velikov, C.A. Angell, Direct determination of kinetic fragility indices of glassforming liquids by differential scanning calorimetry: kinetic versus thermodynamic fragilities, J. Chem. Phys. 117 (2002) 10184–10192, http://dx.doi.org/10.1063/1.1517607.

[37] Q. Zheng, J.C. Mauro, Y. Yue, Reconciling calorimetric and kinetic fragilities of glass-forming liquids, J. Non-Cryst. Solids 456 (2017) 95–100.

[38] C. Huang, E.C. Behrman, Structure and properties of calcium aluminosilicate glasses, J. Non-Cryst. Solids 128 (1991) 310–321, http://dx.doi.org/10.1016/0022-3093(91)90468-L.

[39] F.A. Seifert, B.O. Mysen, D. Virgo, Three-dimensional network structure of quenched melts (glass) in the systems SiO_2-$NaAlO_2$, SiO_2-$CaAl_2O_4$ and SiO_2-$MgAl_2O_4$, Am. Mineral. 67 (1982) 696–717http://ammin.geoscienceworld.org/content/67/7-8/696.citation.

[40] A. Winterstein-Beckmann, D. Möncke, D. Palles, E.I. Kamitsos, L. Wondraczek, Raman spectroscopic study of structural changes induced by micro-indentation in low alkali borosilicate glasses, J. Non-Cryst. Solids 401 (2014) 110–114, http://dx.doi.org/10.1016/j.jnoncrysol.2013.12.038.

[41] F.L. Galeener, Planar rings in vitreous silica, J. Non-Cryst. Solids 49 (1982) 53–62.

[42] F.L. Galeener, Planar rings in glasses, Solid State Commun. 44 (1982) 1037–1040.

[43] E.I. Kamitsos, Reply to “Comment on infrared-reflectance spectra of heat-treated, sol-gel-derived silica”, Phys. Rev. B 53 (1996) 14659–14662, http://dx.doi.org/10.1103/PhysRevB.53.14659.

[44] F.L. Galeener, A.E. Geissberger, Vibrational dynamics in Si_{30}-substituted vitreous SiO_2, Phys. Rev. B 27 (1983) 6199, http://dx.doi.org/10.1017/CBO9781107415324.004.

[45] S.K. Sharma, J.F. Mammone, M.F. Nicol, Raman investigation of ring configurations in vitreous silica, Nature 292 (1981) 140–141.

[46] B.O. Mysen, D. Virgo, F.A. Seifert, Relationships between properties and structure of aluminosilicate melts, Am. Mineral. 70 (1985) 88–105.

[47] B.O. Mysen, Relationships between silicate melt structure and petrologic processes, Earth Sci. Rev. 27 (1990) 281–365, http://dx.doi.org/10.1016/0012-8252(90)90055-Z.

[48] L. Cormier, D.R. Neuville, G. Calas, Relationship between structure and glass transition temperature in low-silica calcium aluminosilicate glasses: the origin of the anomaly at low silica content, J. Am. Ceram. Soc. 88 (2005) 2292–2299, http://dx.doi.org/10.1111/j.1551-2916.2005.00428.x.

[49] W. Loewenstein, The distribution of aluminum in the tetrahedra of silicates and aluminates, Am. Mineral. 39 (1954) 92–96, http://dx.doi.org/10.1002/anie.201004007.

[50] P.F. McMillan, B. Piriou, The structures and vibrational spectra of crystals and glasses in the silica-alumina system, J. Non-Cryst. Solids 53 (1982) 279–298.

[51] D.R. Neuville, L. Cormier, V. Montouillout, P. Florian, F. Millot, J.C. Rifflet, D. Massiot, Structure of Mg- and Mg/Ca aluminosilicate glasses: ^{27}Al NMR and Raman spectroscopy investigations, Am. Mineral. 93 (2008) 1721–1731, http://dx.doi.org/10.2138/am.2008.2867.

[52] R.D. Shannon, Revised effective ionic radii and systematic studies of interatomic distances in halides and chalcogenides, Acta Crystallogr. Sect. A Cryst. Physics, Diffraction, Theor. Gen. Crystallogr. 32 (1976) 751–767.

[53] A. Pönitzsch, M. Nofz, L. Wondraczek, J. Deubener, Bulk elastic properties, hardness and fatigue of calcium aluminosilicate glasses in the intermediate-silica range, J. Non-Cryst. Solids 434 (2016) 1–12.

[54] D.R. Neuville, Propriétés thermodynamiques et rhéologiques des silicates fondus, Ph.D. thesis, Université Paris VII, France, 1992.

[55] Y. Yue, The isostructural viscosity, configurational entropy and fragility of oxide liquids, J. Non-Cryst. Solids 355 (2009) 737–744, http://dx.doi.org/10.1016/j.jnoncrysol.2009.01.032.

[56] M. Bouhadja, N. Jakse, A. Pasturel, Structural and dynamic properties of calcium aluminosilicate melts: a molecular dynamics study, J. Chem. Phys. 138 (2013) 224510, http://dx.doi.org/10.1063/1.4809523.

[57] M. Bouhadja, N. Jakse, A. Pasturel, Striking role of non-bridging oxygen on glass transition temperature of calcium aluminosilicate glass-formers, J. Chem. Phys. 140 (2014)http://dx.doi.org/10.1063/1.4882283.

[58] Q. Zheng, M. Potuzak, J.C. Mauro, M.M. Smedskjaer, R.E. Youngman, Y. Yue, Composition – structure – property relationships in boroaluminosilicate glasses, J. Non-Cryst. Solids 358 (2012) 993–1002, http://dx.doi.org/10.1016/j.jnoncrysol.2012.01.030.

[59] M.J. Toplis, D.B. Dingwell, Shear viscosities of CaO-Al_2O_3-SiO_2 and MgO-Al_2O_3-SiO_2 liquids: implications for the structural role of aluminium and the degree of polymerisation of synthetic and natural aluminosilicate melts, Geochim. Cosmochim. Acta 68 (2004) 5169–5188, http://dx.doi.org/10.1016/j.gca.2004.05.041.

[60] H. Liu, M.M. Smedskjaer, H. Tao, L.R. Jensen, Y. Yue, A medium range order structural connection to the configurational heat capacity of borate – silicate mixed glasses, (2016) 10887–10895. doi:10.1039/c6cp00749j.

Paper IV

Journal of Non-Crystalline Solids 484 (2018) 84–94

Contents lists available at ScienceDirect

Journal of Non-Crystalline Solids

journal homepage: www.elsevier.com/locate/jnoncrysol

Parametric study of temperature-modulated differential scanning calorimetry for high-temperature oxide glasses with varying fragility

Tobias K. Bechgaard[a], Ozgur Gulbiten[b], John C. Mauro[c], Morten M. Smedskjaer[a,*]

[a] Department of Chemistry and Bioscience, Aalborg University, Aalborg, Denmark
[b] Science and Technology Division, Corning Incorporated, Corning, USA
[c] Department of Materials Science and Engineering, The Pennsylvania State University, University Park, USA

ARTICLE INFO

Keywords:
Temperature-modulation
Differential scanning calorimetry
Aluminosilicate glass
Glass transition

ABSTRACT

Differential scanning calorimetry (DSC) has proven to be a highly versatile technique for understanding the glass transition, relaxation, and crystallization behavior of inorganic glasses. However, the approach is challenging when probing glass samples that exhibit overlapping transitions or low sensitivity. To overcome these problems, temperature-modulated DSC (TM-DSC) can be utilized, in which a sinusoidal heating rate is superimposed on the linear heating rate known from standard linear DSC. Until recently, it has only been possible to perform TM-DSC measurements on commercial instruments at temperatures below 973 K, which is insufficient for many oxide glasses of industrial interest, particularly silicate glasses. However, recent commercially available software now enables TM-DSC measurements to be performed at temperatures far exceeding 973 K. To investigate the suitability of using TM-DSC to study glass transition and relaxation behavior in high-temperature silicate systems, we have performed systematic TM-DSC measurements on three different oxide glass systems with varying glass transition temperature and liquid fragility. We find that relatively large underlying heating rates (2–5 K/min) and modulation amplitudes (4–5 K) are needed in order to obtain data with high signal-to-noise ratios. For these combinations of experimental parameters, we also observe a linear response as found using Lissajous curves. Overall, this study suggests that TM-DSC is a promising technique for investigating the dynamics of high-temperature oxide glass systems with a wide range of liquid fragilities.

1. Introduction

Since its invention in 1962 [1], differential scanning calorimetry (DSC) has become an important instrument in the thermal analysis of materials. The technique can be used to identify characteristic temperatures, quantify the heat of thermal events (e.g., phase transitions), and obtain the temperature dependence of the heat capacity [2]. Depending on the calorimeter design, the method can be used to determine heat capacity in the temperature range from 93 to 2673 K, thus covering a diverse range of materials from organic polymers to inorganic crystals and glasses. Due to its versatility, DSC has become a widely used technique for material characterization in research labs and inspection of raw materials or quality control of finished products in industrial facilities [2]. DSC studies have been widely used in the field of glass science to study immiscibility of glass-forming liquids [3], the dependence of the fictive temperature on the thermal history of glass [4–8], glass transition behavior and enthalpy relaxation in hyperquenched glasses [9–11], crystallization behavior and glass stability [12–15], and determination of the fragility index m of glass-forming liquids [16–19].

Traditionally, DSC has been used to measure heat flow (or heat capacity) as a function of a linear heating profile. As such, the programmed temperature profile (T) can be described as:

$$T = T_0 + \beta t \quad (1)$$

where T_0 is the initial temperature at time $t = 0$ and β is the heating rate. Despite its commercial success, linear DSC suffers from some shortcomings in relation to analyzing certain materials with overlapping transitions. For example, these can be found in composite materials of organic polymers with overlapping glass transitions, but also in single phase materials with imperfect crystals where simultaneous melting and recrystallization occur and in metallic glasses with overlapping glass transition and crystallization processes [20–25]. Linear DSC does not offer the ability to separate such overlapping transitions. Moreover, low sensitivity is a challenge, e.g., when studying glasses with high SiO_2 content that exhibit small changes in heat capacity during the glass transition. In linear calorimeters, the sensitivity can only be improved by increasing sample size and/or heating rate,

* Corresponding author.
E-mail address: mos@bio.aau.dk (M.M. Smedskjaer).

https://doi.org/10.1016/j.jnoncrysol.2018.01.022
Received 28 November 2017; Received in revised form 11 January 2018; Accepted 13 January 2018
Available online 21 January 2018

both resulting in decreased resolution due to the larger thermal gradient across the sample and the reduced observation time [26].

To overcome these disadvantages, the temperature-modulated differential scanning calorimeter (TM-DSC) was introduced in 1992 by Reading and co-workers [27–30]. TM-DSC allows for separation of overlapping signals and improved sensitivity at the expense of increased measurement duration [31]. In this approach, a sinusoidal heating rate is superimposed on the linear heating rate, essentially allowing the instrument to use two heating rates. The temperature profile is thus given by

$$T = T_0 + \beta t + A\sin(\omega t) \quad (2)$$

where A is the amplitude of the modulation and ω is the angular frequency of the modulation ($\omega = 2\pi/P$, where P is the period). In modulated DSC, β is the underlying heating rate as the instantaneous heating rate (dT/dt) is now determined by

$$\frac{dT}{dt} = \beta + \omega A\cos(\omega t) \quad (3)$$

The output from a normal linear DSC scan is simply the heat flow signal, while three additional signals, the reversing heat flow, the non-reversing heat flow, and the phase lag, can be obtained by the Fourier transformation of the sinusoidal signals [32,33]. The reversing heat flow describes the temperature dependence of the heat capacity of the sample, while the non-reversing heat flow is related to kinetic events such as relaxation and crystallization. The phase lag describes the time delay between the heat flow signal and the heating rate as a result of thermal inertia of the sample and the instrument. The phase lag is continuous when no transitions occur, but exhibits a peak when the configurational heat capacity of the sample changes. For example, such a phase peak occurs during the glass transition due to the change in configurational entropy [31].

TM-DSC requires three input parameters: average heating rate, oscillation frequency, and the amplitude of the oscillation, complicating the experimental design. Selecting the input parameters can be challenging as the optimal parameters depend on the characteristics of the sample and the investigated phase transition, and changing one parameter affects the most appropriate values of the others. For example, an increase in amplitude requires a decrease in the angular frequency as more time is needed for the heat to flow.

In the glass science community, TM-DSC is currently used to analyze organic, chalcogenide, metallic, and oxide glasses. The applications include easy determination of the glass transition temperature [25,34,35], identifying rigidity transitions [36–39], studying the relaxation behavior during the glass transition [40–46], and determining the liquid fragility index [44–46]. Common to these studies is that the glass transition temperature of the studied samples has been below 973 K. This has been the maximum temperature limit of commercial TM-DSCs, but recently, the TM-DSC technique has become commercially available at temperatures above 973 K. These instruments have a different furnace design than low-temperature (< 973 K) instruments, enabling thermal analysis of, e.g., silicate glasses that exhibit wider glass transitions than any glass measured successfully using a low-temperature TM-DSC [47,48].

The higher operating temperature and wider transitions should require a different set of experimental parameters and result in prolonged measurement time. Therefore, there is an interest in investigating the response of high-temperature silicate glasses to a modulated temperature profile. In this study, we perform systematic TM-DSC experiments on three different glasses to demonstrate how outputs signals are affected as a function of measurement conditions. We choose two calcium aluminosilicate glasses with similar, and relatively high, glass transition temperatures (T_g of 1134 and 1173 K for peraluminous and tectosilicate compositions, respectively), but different liquid fragility indices (m of 48 and 22, respectively). We compare these results with those of a fragile (m = 82) [49] sodium borate glass-forming liquid with lower glass transition temperature (T_g = 748 K). Specifically, we perform 80 different heating scans on the peraluminous calcium aluminosilicate composition and 36 scans on both the tectosilicate calcium aluminosilicate and sodium borate compositions. The experimental conditions have been chosen to show the change in response to changes in the β, A, and P parameters.

2. Experimental section

Three glass compositions were prepared by the melt quench method: two calcium aluminosilicates with nominal compositions (mol %) of $55SiO_2$-$25Al_2O_3$-20CaO (CAS1) and $86SiO_2$-$7Al_2O_3$-7CaO (CAS2) and one sodium borate glass with nominal composition $67B_2O_3$-$33Na_2O$ (NaB). Both the CAS1 and CAS2 glasses exhibit relatively high glass transition temperatures of 1134 and 1173 K, respectively [50], as determined using a 10 K/min heating rate on a standard DSC. The peraluminous CAS1 composition exhibits relatively high fragility index (m = 48), while the tectosilicate CAS2 composition is relatively strong (m < 22) [50]. NaB exhibits a much lower glass transition temperature of 748 K, but higher fragility index of 82.1 [49].

To obtain homogenous glasses, the raw materials (analytical grade SiO_2, Al_2O_3, $CaCO_3$, H_3BO_3, and Na_2O powders with purity > 99.8%) were mixed for 60 min in a ball mill before being melted in air for at least 6 h at 1923 K for CAS glasses and 1373 K for NaB and then quenched. The calcium aluminosilicate glasses were re-melted overnight at 1923 K in air and quenched on a metal plate. All glasses were annealed at their respective T_g for 30 min.

The calorimetric measurements were performed on a Netzsch STA 449F1 Jupiter® calorimeter with the TM-DSC module software extension in Pt-Rh crucibles using argon as the purge gas (flow rate = 50 mL/min). The samples were disc-shaped with a diameter of ~6 mm and thickness of ~0.4 mm, resulting in a mass of ~30 mg. To ensure an optimal heat transfer between sample carrier and samples, the samples were polished to an optical finish on the surface facing the crucible bottom. To evaluate the effect of the three modulation parameters on the calorimetric data, the glasses were scanned using a combination of parameters resulting in a total of 80 scans for CAS1 and 36 for both CAS2 and NaB. For CAS1, the experimental conditions included β = 2, 3, 4, and 5 K/min, A = 1, 2, 3, 4, and 5 K, and P = 90, 120, 150, and 180 s. CAS2 was scanned with β = 3, 5, and 7 K/min, A = 3, 5, and 7 K, and P = 90, 120, 150, and 180 s, while NaB was scanned with β = 2, 3, and 4 K/min, A = 1, 3, and 5 K, and P = 90, 120, 150, and 180 s.

The modulated scans were performed between 1023 and 1238 K, 1053 and 1318 K, and 703 and 793 K for CAS1, CAS2 and NaB, respectively. This was done to cover a wide enough temperature range from the glass to the supercooled liquid. The low temperature limit in the glass corresponds to an average relaxation time, which is much longer than the period of the oscillation. The high temperature limit in the liquid corresponds to an average relaxation time, which is much shorter than the period of oscillation, assuring that no crystallization occurs during the measurement. All upscans were performed subsequent to a linear cooling segment (downscan) with the same β as the subsequent upscan. For example, the temperature profile could be cooling from 1238 to 1023 K with $\beta = -2$ K/min, followed by heating from 1023 to 1238 K with β = 2 K/min, A = 5 K, and P = 150 s. To ensure identical heat transfer, all scans on each glass were performed without opening the furnace tower and thus touching the sample carrier. The phase angle and reversing and non-reversing heat flows were obtained from TM-DSC signals and presented herein without any post corrections. To test the reproducibility of the TM-DSC data, we performed repeated scans for selected experimental conditions on the same sample. The difference in peak position values was always within ± 1 K.

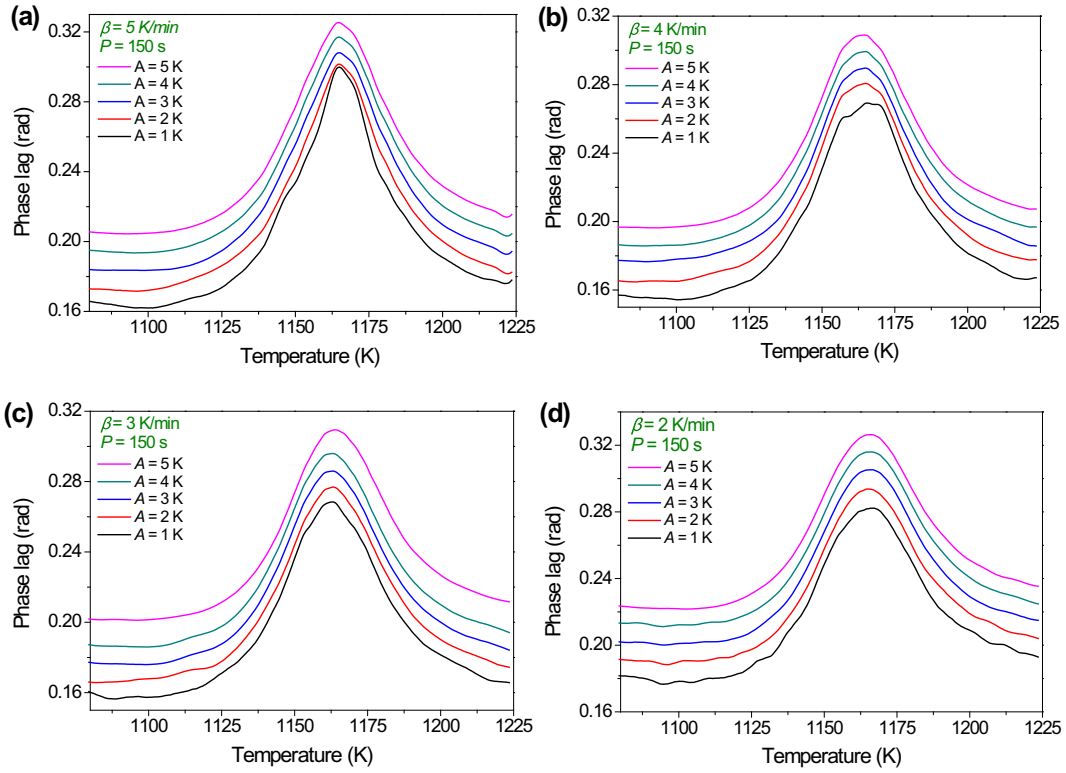

Fig. 1. Raw phase lag for CAS1 during heating through the glass transition with constant modulation period (P = 150 s) and varying modulation amplitude (A) for different heating rates (β): (a) β = 5 K/min, (b) β = 4 K/min, (c) β = 3 K/min, and (d) β = 2 K/min. The phase lag has been offset by 0.01 rad to simplify the comparison of the curves.

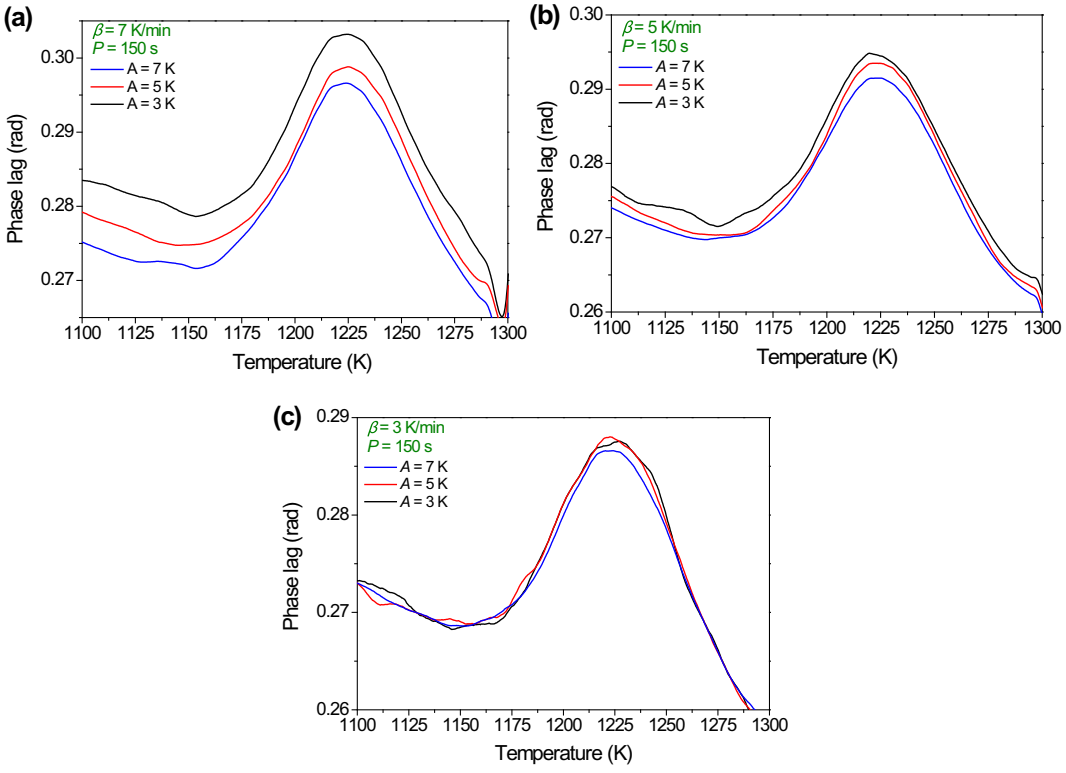

Fig. 2. Raw phase lag for CAS2 during heating through the glass transition with constant modulation period (P = 150 s) and varying modulation amplitude (A) for different heating rates (β): (a) β = 7 K/min, (b) β = 5 K/min, and (c) β = 3 K/min.

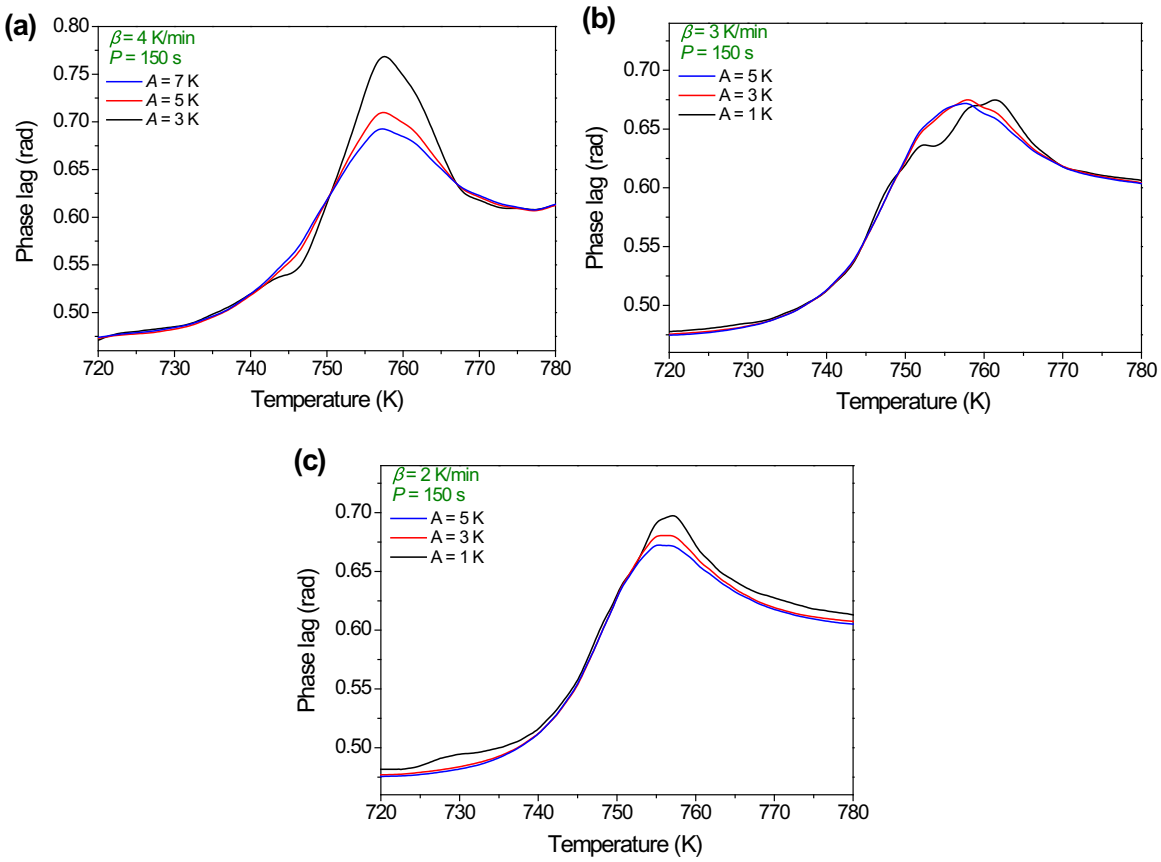

Fig. 3. Raw phase lag for NaB during heating through the glass transition with constant modulation period (P = 150 s) and varying modulation amplitude (A) for different heating rates (β): (a) β = 4 K/min, (b) β = 3 K/min, and (c) β = 2 K/min.

3. Results and discussion

3.1. Phase lag curves

Phase lag between the modulated heating rate and the modulated heat flow is linearly scaled with the imaginary part of the complex heat capacity [51]. Distribution of relaxation times is correlated to the shape of the imaginary part of the complex heat capacity. Therefore, in a single phase glass with a normal distribution of relaxation times, a Gaussian shaped phase lag curve is expected [46,51]. Fig. 1 shows the phase lag for CAS1 for all 20 scans with P = 150 s but varying β and A. The phase lag values in Fig. 1 have been offset by 0.01 rad for each condition for visual clarity. A comparison of the underlying heating rates reveals that for β = 5 K/min, the obtained phase peaks appear asymmetric, noisy, and sharp (Fig. 1a). By decreasing the underlying heating rate to β = 4 K/min, phase peaks become less noisy, more symmetric, and less sharp (Fig. 1b), with further reduction of the heating rate to 3 (Fig. 1c) or 2 K/min (Fig. 1d) resulting in smooth and almost symmetric phase peaks (Fig. 1c and d). Although a high underlying heating rate is desirable to reduce measurement duration, Fig. 1 shows that too high β values results in sharp and distorted phase angles due to the shorter observation time when scanning through the glass transition. Small and smooth heat flow oscillations are required in order to obtain the phase angle from the sinusoidal heat flow data. To achieve this, several modulations must be cycled during the glass transition. Obviously the number of modulation cycles through the glass transition depends on both β and P. For P = 150 s, the number of cycles through the glass transition in Fig. 1 is ~4 and ~4.5 for β = 5 and 4 K/min, respectively. By decreasing the underlying heating rate, the number of cycles increases to ~7 and ~12 for β = 3 and 2 K/min, respectively. By assessing the shape of the phase lag data, our results suggest that high-temperature TM-DSC on this particular silicate glasses should be performed at relatively low heating rate, such as 2 or 3 K/min.

To check the universal validity of such heating rates, we have also collected data for a “stronger” (CAS2) and a more “fragile” (NaB) glass-forming liquid, as presented in Figs. 2 and 3, respectively. For CAS2, scanning with β = 3 K/min yield noisy data, while scans performed at higher underlying heating rates (β = 5 and 7 K/min) appear significantly smoother (Fig. 2). This is especially evident for scans performed with low amplitudes. The relatively high data quality for scans performed at high β values is a result of the wider glass transitions in this glass, allowing more modulations to be cycled during the transition despite the increased underlying heating rate. Fig. 3 show the phase lag curves for NaB composition measured under the same conditions that worked well for CAS1. In general, the data quality and the phase peaks appear noisy and non-smooth with bumps. The low data quality is a result of few modulation cycles during the transition and low signal-to-noise ratio, suggesting that β values of 0.5–1.5 K might be better suited for this glass.

For CAS1, Fig. 1(a–d) also includes scans with five different amplitudes for each underlying heating rate. Independent of β, we find that an amplitude of A = 1 K results in non-smooth phase peaks, especially evident for scans with β = 5 and 4 K/min (Fig. 1a and b, respectively). The obtained phase peaks become smoother with increasing modulation amplitude. A should be high to achieve large changes in instantaneous heating rate (dT/dt), providing increased sensitivity and signal-to-noise ratio of transitions with temperature-dependent heat capacity (such as the glass transition). However, too high amplitudes can simultaneously result in a loss of resolution due to the increase in instantaneous heating rate. In addition, frequency dependent heat capacity describes the response of the glass to small perturbations [52]

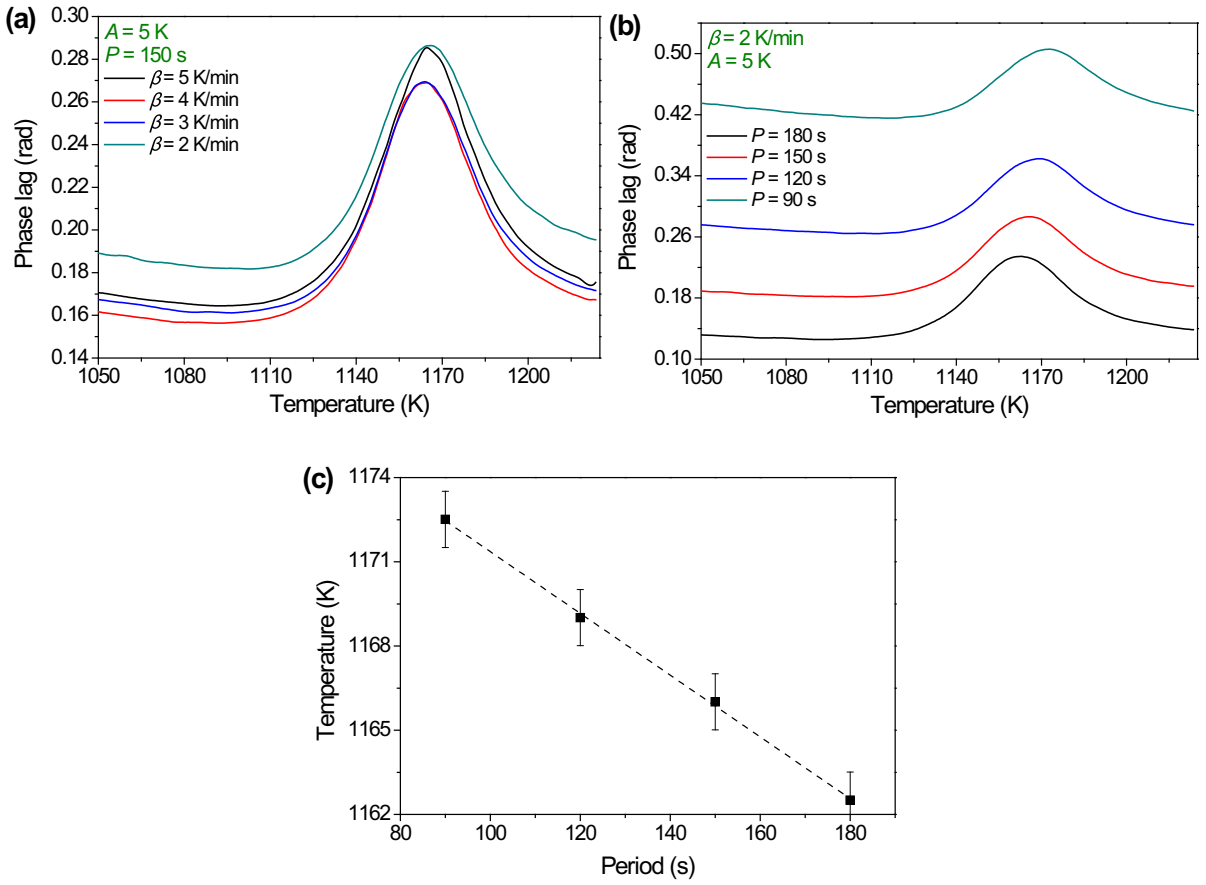

Fig. 4. (a) Underlying heating rate dependence of the phase lag for CAS1 during the glass transition for constant modulation amplitude (A = 5 K) and period (P = 150 s). (b) Frequency dependence of the phase lag for constant underlying heating rate (β = 2 K/min) and modulation amplitude (A = 5 K). (c) Frequency dependence of the peak position of the phase lag. The dashed line in (c) represent the best linear fit (R^2 = 0.9991). The error in the determination of the peak positions is around ± 1 K.

and oscillations with bigger amplitudes cannot satisfy the conditions for small perturbations. The appropriate amplitude value depends on the sample characteristics and the selected period. For CAS2, an amplitude of 3 K results in noisy phase peaks at all the probed combinations of experimental conditions (Fig. 2). This indicates that a higher amplitude is needed for this particular glass, probably due to its low fragility index. Difficulties associated with achieving sufficiently high signal-to-noise ratio for strong glass-forming liquids scanned at low heating rates is also known from standard DSC experiments. By increasing A to 5 or 7 K in this work, the signal-to-noise ratio improves, but for β = 3 K/min, the noise is still substantial for scans obtained at short periods. In general, the data obtained with A = 7 K result in more pointed and less Gaussian-shaped phase peak signals than their A = 5 K counterparts, indicating a loss of resolution. Accordingly, for these high temperature measurements, amplitudes of ~5 K appear to be a good choice for the starting conditions as the resolution decreases at very high amplitudes. We also scanned the fragile NaB at different amplitudes (Fig. 3). The data quality is generally low due to poor combinations of experimental conditions, especially for high β values. However, an amplitude of 5 K still yields the best data quality at low temperatures.

The magnitude of the phase lag also depends on the measurement parameters. As seen in Fig. 4a for CAS1 (and in Fig. S1 in the Supporting Information for CAS2 and NaB), not only the heating rate, but also the combination of parameters and sample properties, determines the magnitude of the instrumental phase lag. By correcting for the instrumental phase lag, the phase lag associated with the glass transition becomes identical [53] (see Fig. S2 in the Supporting Information).

For low-temperature systems, an adequate signal-to-noise ratio can be obtained using amplitudes in the range of 0.5 to 2 K [31], but our results show that phase peaks appear to be significantly smoother when A is increased above 2 K for the high-temperature oxide glasses. That is, all the phase lag data in Figs. 1-3 suggest that larger amplitudes increase the signal-to-noise ratio. This may be related to the differences in temperature control between low- and high-temperature instruments. For the high-temperature scans presented here, the instrumental noise in the heat flow signal is rather large, which might necessitate higher amplitudes. For low-temperature TM-DSC measurements, modulation amplitudes above 2 K tend to decrease the resolution, but we do not observe any change in phase shape for CAS1 or CAS2 when increasing A above 3 K and thus no change in resolution with increasing modulation amplitude (Figs. 1 and 2). Due to the low data quality for NaB in Fig. 3, the effect of A on the resolution cannot be quantified for this glass. In summary, larger amplitudes (4 to 5 K) appear to improve the data quality, unless the temperature is too low for the furnace cooling to follow the specified rate. This problem can occur because commercial high temperature DSCs are typically not equipped with active cooling. We have observed this phenomenon when performing experiments with inappropriate experimental conditions at lower temperatures around 700 K, as shown in Fig. S3 in the Supporting Information.

Fig. 4b shows the frequency dependence (P = 180, 150, 120, and 90 s) of the phase lag for β = 2 K/min and A = 5 K for CAS1. The observed frequency dependence described below is the same for other experimental conditions, as well as for the other compositions CAS2 and NaB (see Fig. S4 in the Supporting Information). The shape of the phase lag obtained at different frequencies is identical and therefore independent of the selected period within the parameter ranges chosen in this study. The magnitude of the transition-induced phase lag, however, decreases with increasing frequency, while the instrumental

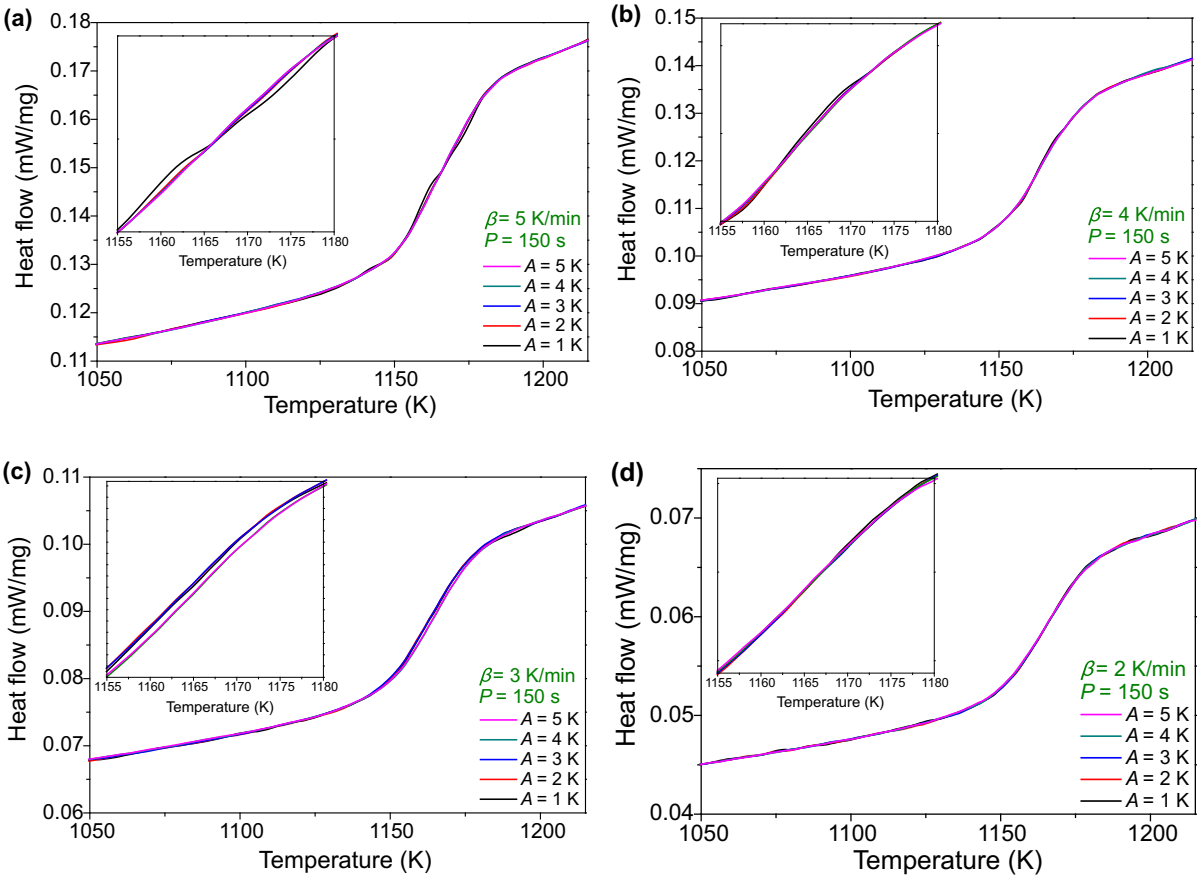

Fig. 5. The reversing heat flow curves for CAS1 during heating through the glass transition for constant modulation period (P = 150 s) and varying modulation amplitude (A) for different underlying heating rates (β): (a) β = 5 K/min, (b) β = 4 K/min, (c) β = 3 K/min, and (d) β = 2 K/min. Insets show enlargements of the glass transition region.

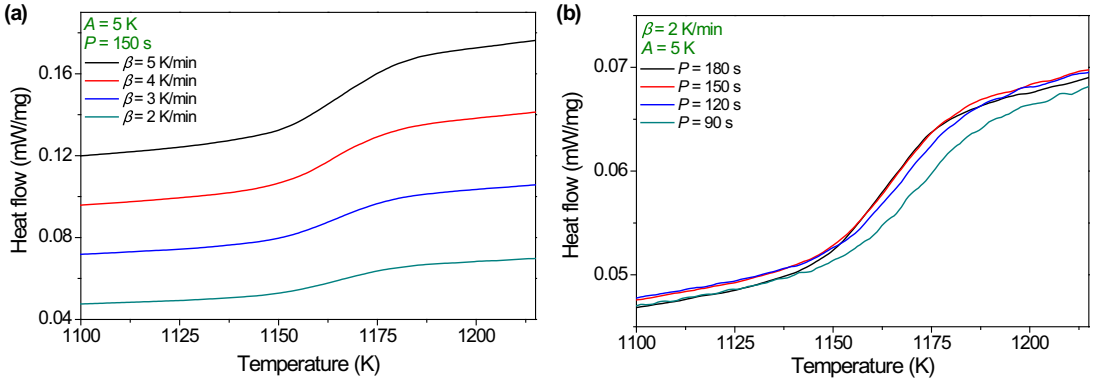

Fig. 6. Comparison of the reversing heat flow curves for CAS1 through the glass transition obtained with varying (a) underlying heating rate for constant modulation amplitude (A = 5 K) and period (P = 150 s) and (b) frequency for constant heating rate (β = 2 K/min) and amplitude (A = 5 K).

phase lag increases with increasing frequency. The results show that smooth phase peaks can be achieved for periods between 90 and 180 s, and possibly for values outside of this range. The range of appropriate period values depend on the other selected parameters and need to be studied in detail. We also observe that increasing the modulation frequency causes a shift of the phase lag peak to higher temperatures, as expected from heat capacity spectroscopy studies [52], where the characteristic relaxation times are shorter [52,54] (Fig. 4c).

3.2. Heat flow curves

Fig. 5 shows the reversing heat flow for 20 scans on CAS1 obtained for P = 150 s with varying heating rate (β = 2, 3, 4, and 5 K/min) and amplitude (A = 1, 2, 3, 4, and 5 K). The magnitude of the reversing heat flow only depends on the heating rate (Figs. 5 and 6a), while the shape is slightly dependent on the combination of β, P, and A parameters, as seen in Fig. 5 (compare, e.g., A = 1 K to the others). This is probably due to a poor combination of modulation parameters. In Fig. 1a, the experimental conditions resulted in a noisy phase peak. Here, it is manifested as a deviation from the expected sigmoidal S-shaped change in the reversing heat flow. An increase of the frequency results in a shift of the step change in the reversing heat flow to slightly lower temperatures (Fig. 6b). As evident from the very similar reversing heat flow curves (Figs. 5 and 6), the reversing heat flow is almost independent of the selected parameters. The same behavior is found for CAS2 and NaB (see Fig. S5 in the Supporting Information). These data are in

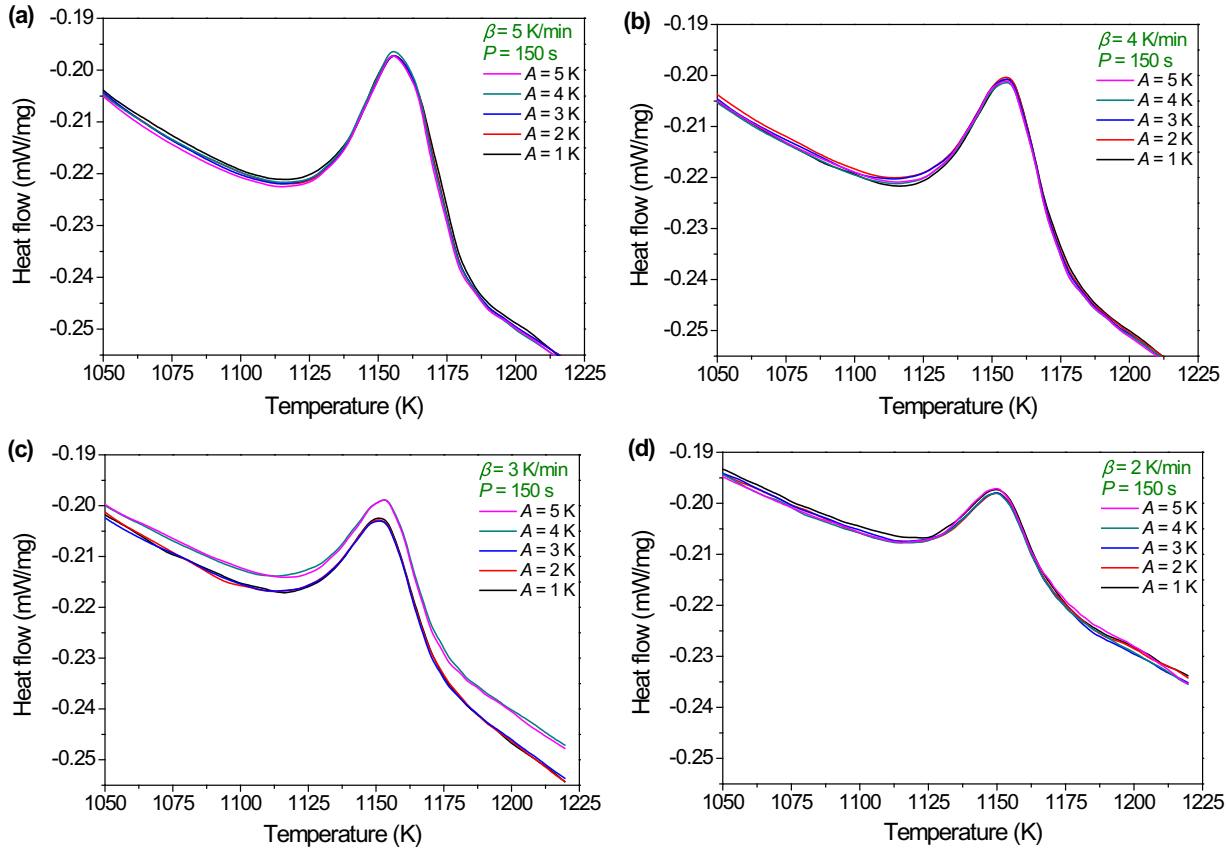

Fig. 7. Non-reversing heat flow curves for CAS1 through the glass transition for constant modulation period (P = 150 s) and varying modulation amplitude (A) for different underlying heating rates (β): (a) β = 5 K/min, (b) β = 4 K/min, (c) β = 3 K/min, and (d) β = 2 K/min.

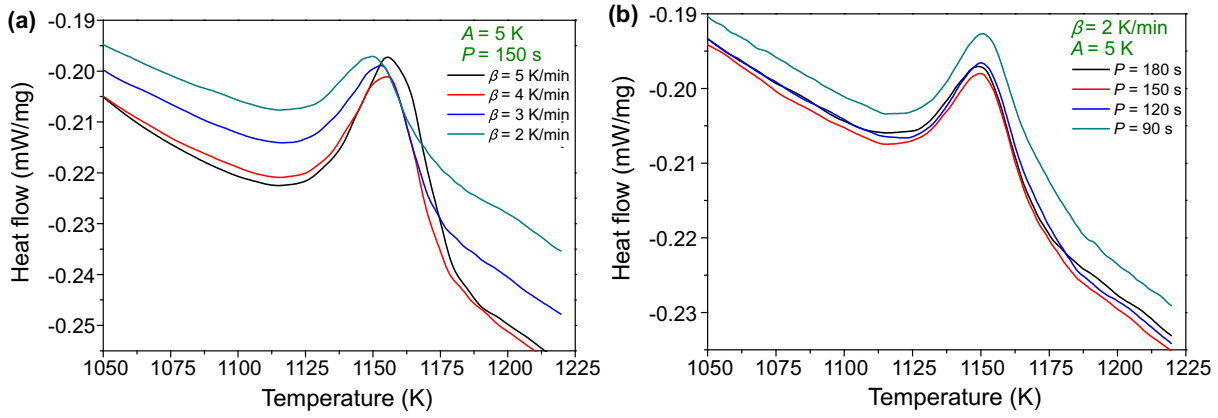

Fig. 8. Comparison of the non-reversing heat flow curves through the glass transition obtained with varying (a) underlying heating rate for constant modulation amplitude (A = 5 K) and period (P = 150 s) and (b) frequency for constant underlying heating rate (β = 2 K/min) and amplitude (A = 5 K).

agreement with theoretical studies in literature, where reversing heat flow curves have been found to be superimposed on each other when obtained at different underlying heating rates [54]. As such, if the reversing heat flow is the only signal of interest for a given study, there is no need for any optimization of the modulation parameters.

The shape and magnitude of the non-reversing heat flow is independent of the amplitude when β and P are kept constant (Fig. 7 for CAS1 and Fig. S6 in the Supporting Information for CAS2 and NaB). On the other hand, the heating rate has a pronounced effect on both magnitude and shape of the non-reversing heat flow signal, with a shift to lower temperatures with increasing heating rate (Fig. 8a) as the heat flow is dependent on the time derivative. However, a linear baseline subtraction makes the shape of the curves approximately identical, while the differences in magnitude are maintained (see Fig. S7 in the Supporting Information). The frequency does not affect the magnitude or position of the peak temperature (Fig. 8b). When analyzing non-reversing heat flow data, the area of the peak is often used as a measure of the energy released by kinetic processes such as relaxation [36–39]. If the absolute values of the heat flow are not of interest in a given study, the experimental parameters do not need to be optimized in order to get accurate data.

3.3. Lissajous curves

In TM-DSC experiments a linear response between heating rate and heat flow is essential, especially when studying glass relaxation

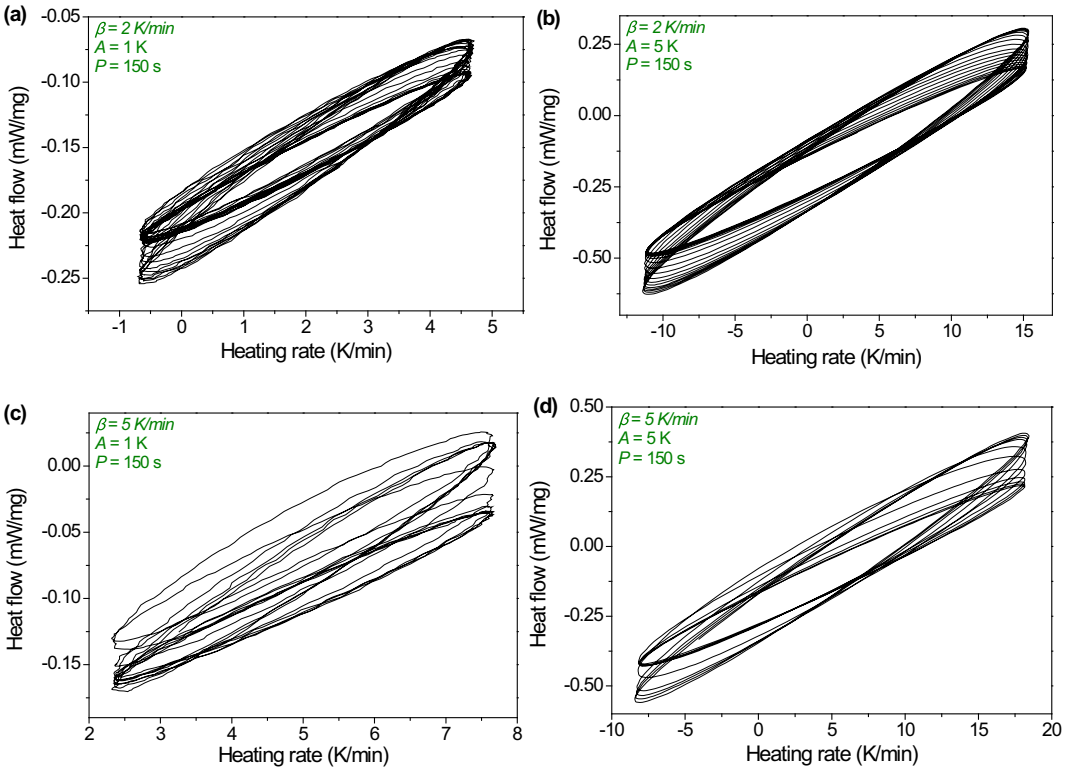

Fig. 9. Lissajous curve for CAS1 for the four extreme combinations of parameters for constant modulation period (P = 150 s): (a) β = 2 K/min and A = 1 K; (b) β = 2 K/min and A = 5 K; (c) β = 5 K/min and A = 1 K; (d) β = 5 K/min and A = 5 K. The data have been smoothed slightly using a Savitzky–Golay algorithm [61].

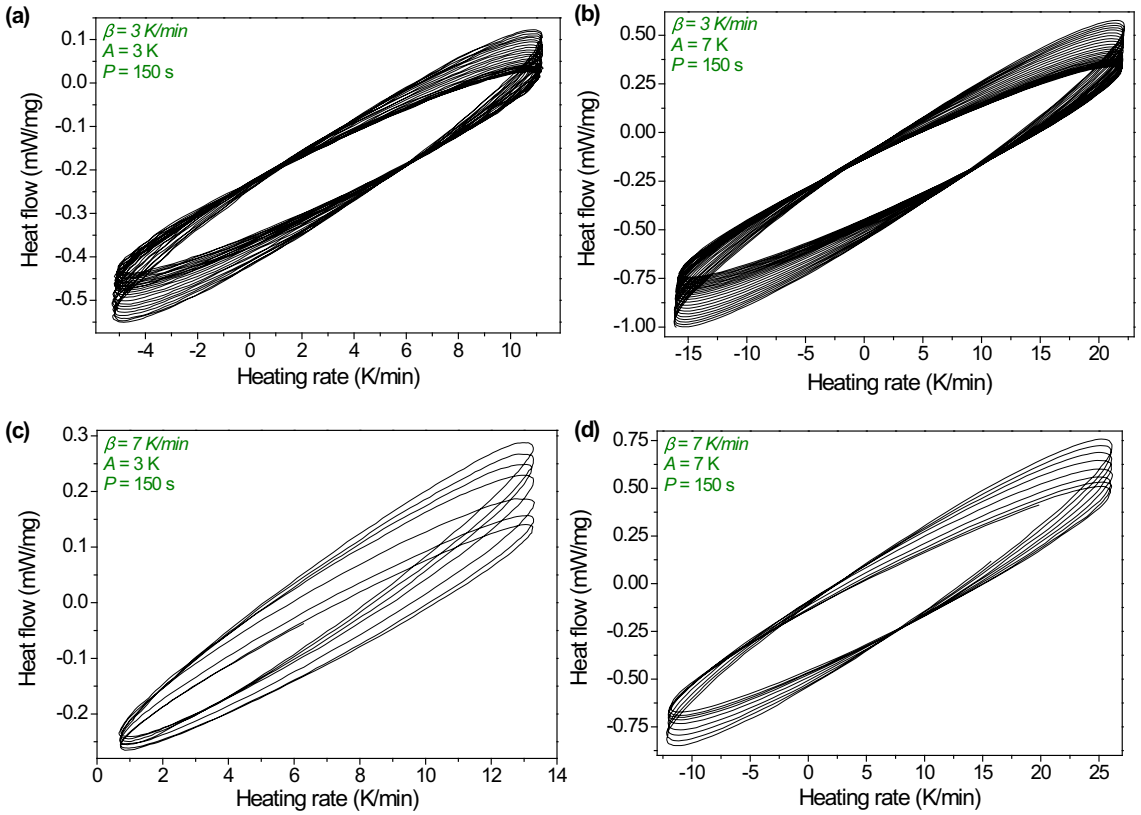

Fig. 10. Lissajous curve for CAS2 for the four extreme combinations of parameters for constant modulation period (P = 150 s): (a) β = 3 K/min and A = 3 K; (b) β = 3 K/min and A = 7 K; (c) β = 7 K/min and A = 3 K; (d) β = 7 K/min and A = 7 K. The data have been smoothed slightly using a Savitzky–Golay algorithm [61].

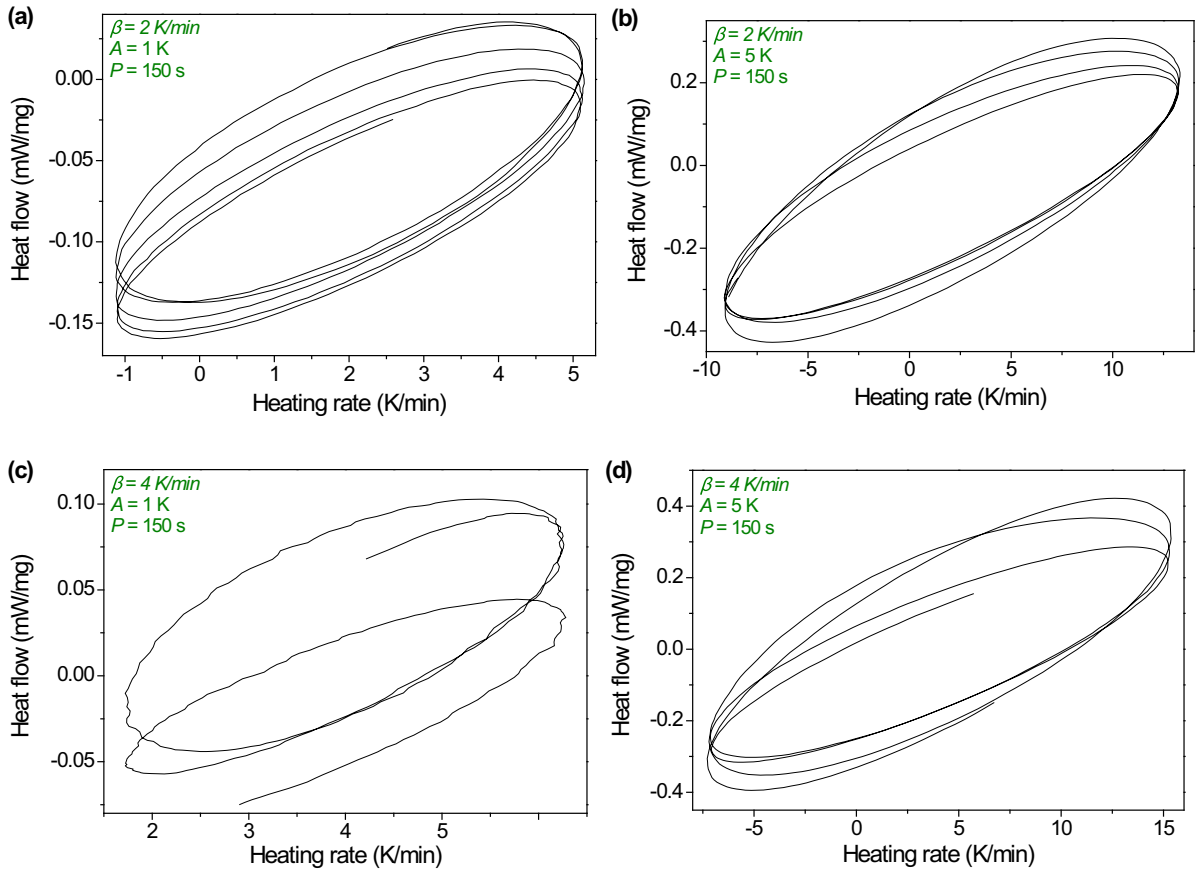

Fig. 11. Lissajous curve for NaB for the four extreme combinations of parameters for constant modulation period ($P = 150$ s): (a) $\beta = 2$ K/min and $A = 1$ K; (b) $\beta = 2$ K/min and $A = 5$ K; (c) $\beta = 5$ K/min and $A = 1$ K; (d) $\beta = 5$ K/min and $A = 5$ K. The data have been smoothed slightly using a Savitzky–Golay algorithm [61].

processes as large enthalpy releases may occur [55–58]. The linearity can be evaluated using Lissajous curves by plotting heat flow as a function of heating rate [59,60]. For ideal heat transfer, all data should fall in a retraceable linear pattern, but due to thermal inertia effects related to the sample thickness, the Lissajous curves adopt an elliptical shape when the response is linear. Since the linear response depends on the specific combination of experimental parameters the measurement conditions need to be optimized to improve the linearity. By decreasing the underlying heating rate and the amplitude, the maximum instantaneous heating rates decrease, resulting in introduction of smaller perturbations and allowing the system to equilibrate faster. The same effect can also be observed by decreasing the modulation frequency.

Lissajous curves of selected combinations of experimental conditions (highest and lowest values of heating rate and modulation amplitude) for CAS1, CAS2, and NaB are shown in Figs. 9, 10, and 11, respectively. The Lissajous curves have been smoothed slightly using a Savitzky–Golay filter [61] for visual clarity without any change in the overall shape. For the CAS1 glass, we find that the Lissajous curves reflect a linear response when they are obtained from scans with low heating rates (Fig. 9a and b) or with simultaneous high underlying heating rate and high modulation amplitude (Fig. 9d). When the underlying heating rate is high and the temperature perturbations are small due to low amplitude, the Lissajous curves do not exhibit linear response (Fig. 9c). Linearity is a result of a sufficient number of modulation cycles during the glass transition, explaining why the lowest underlying heating rates result in linear responses. This can, however, not explain why the high amplitudes also result in a linear response, while this is not the case for the low amplitudes when the underlying heating rate is high. Instead the low signal-to-noise ratio due to the small heat flow perturbations for the low-A, high-β experiment might be responsible for the non-linear response, suggesting that the instrument is not able to control the heat flow perturbations accurately enough to obtain a linear response at low amplitudes. The same response is seen for CAS2 (Fig. 10), although the underlying heating rate are higher for this glass (β between 3 and 7 K/min). These higher underlying heating rates can be used for CAS2, since this glass has a wider glass transition owing to its higher silica content compared to CAS1.

The shapes of the Lissajous curves for NaB (Fig. 11) suggest a linear response for the four shown combinations of experimental conditions, but due to the high heating rates, only a few modulations are cycled through the glass transition. When comparing the curves for the two highest β values (Fig. 11c and d), the positive effect of high amplitude becomes obvious. Even though both Lissajous curves have been smoothed, the signal-to-noise ratio is significantly better in Fig. 11d.

4. Conclusions

We have reported phase angles and both reversing and non-reversing heat flows obtained by temperature modulated differential scanning calorimetry (TM-DSC) for two calcium aluminosilicate glasses and one sodium borate glass. The underlying heating rates have been varied between 2 and 7 K/min, modulation amplitudes varied between 1 and 7 K, and modulation periods varied between 90 and 180 s. We have shown that the best signal-to-noise ratio is achieved for relatively low underlying heating rates (2–3 K) for high-T_g fragile oxide compositions, while stronger liquids can be scanned with larger β values of 5 K and possibly 7 K without any loss in data quality. For the highly fragile low-temperature sodium borate composition, an underlying heating rate of 2 K/min is too high, resulting in noisy data. For all of the probed heating rates, A values of 1–3 K yield phases with a low signal-to-noise ratio, while higher amplitudes result in better data quality. As such, optimization of the experimental conditions involves an interplay

between the liquid's fragility and underlying heating rate, while the best value for the amplitude appears to be less dependent on the glass properties. Furthermore, we have confirmed that the instrument exhibits a linear response between input and output for the tested combinations of experimental parameters. In conclusion, this study therefore suggests that TM-DSC is a promising technique for investigating the dynamic behavior of high-temperature oxide glass systems.

Acknowledgements

This work was funded by Corning Incorporated.

Appendix A. Supplementary data

Supplementary data to this article can be found online at https://doi.org/10.1016/j.jnoncrysol.2018.01.022.

References

[1] M.J. O'Neill, E.S. Watson, Differential microcalorimeter, US3263484 A, (1962).
[2] G. Höhne, W.F. Hemminger, H.-J. Flammersheim, Differential Scanning Calorimetry — an Introduction for Practitioners, Springer-Verlag, Berlin, 1996.
[3] L.E. Tanner, R. Ray, Phase separation in Zr-Ti-Be metallic glasses, Scr. Metall. 14 (1980) 657–662.
[4] A.Q. Tool, Relation between inelastic deformability and thermal expansion of glass in its annealing range, J. Am. Ceram. Soc. 29 (1946) 240–253, http://dx.doi.org/10.1111/j.1151-2916.1946.tb11592.x.
[5] O.S. Narayanaswamy, A model of structural relaxation in glass, J. Am. Ceram. Soc. 54 (1971) 491–498.
[6] C.T. Moynihan, A.J. Easteal, M.A. DeBolt, J. Tucker, Dependence of the fictive temperature of glass on cooling rate, J. Am. Ceram. Soc. 59 (1976) 12–16.
[7] Y. Yue, R. Von Der Ohe, S.L. Jensen, Fictive temperature, cooling rate, and viscosity of glasses, J. Chem. Phys. 120 (2010) 8053–8059, http://dx.doi.org/10.1063/1.1689951.
[8] Y. Yue, J. deClaville Christiansen, S.L. Jensen, Determination of the fictive temperature for a hyperquenched glass, Chem. Phys. Lett. 357 (2002) 20–24.
[9] Y. Yue, C.A. Angell, Clarifying the glass-transition behaviour of water by comparison with hyperquenched inorganic glasses, Nature 427 (2004) 717–720.
[10] C.A. Angell, Y. Yue, L.-M. Wang, J.R.D. Copley, S. Borick, S. Mossa, Potential energy, relaxation, vibrational dynamics and the boson peak of hyperquenched glasses, J. Phys. Condens. Matter 15 (2003) 1051–1068.
[11] Y. Yue, Characteristic temperatures of enthalpy relaxation in glass, J. Non-Cryst. Solids 354 (2008) 1112–1118, http://dx.doi.org/10.1016/j.jnoncrysol.2006.11.027.
[12] V.M. Fokin, A.A. Cabral, R.M.C.V. Reis, M.L.F. Nascimento, E.D. Zanotto, Critical assessment of DTA–DSC methods for the study of nucleation kinetics in glasses, J. Non-Cryst. Solids 356 (2010) 358–367, http://dx.doi.org/10.1016/j.jnoncrysol.2009.11.038.
[13] A.A. Cabral Jr., C. Fredericci, E.D. Zanotto, A test of the Hrubÿ parameter to estimate glass-forming ability, J. Non-Cryst. Solids 219 (1997) 182–186.
[14] C. Fredericci, E.D. Zanotto, E.C. Ziemath, Crystallization mechanism and properties of a blast furnace slag glass, J. Non-Cryst. Solids 273 (2000) 64–75.
[15] M.L.F. Nascimento, L.A. Souza, E.B. Ferreira, E.D. Zanotto, Can glass stability parameters infer glass forming ability? J. Non-Cryst. Solids 351 (2005) 3296–3308, http://dx.doi.org/10.1016/j.jnoncrysol.2005.08.013.
[16] H.E. Kissinger, Reaction kinetics in differential thermal analysis, Anal. Chem. 29 (1957) 1702–1706.
[17] L.-M. Wang, V. Velikov, C.A. Angell, Direct determination of kinetic fragility indices of glassforming liquids by differential scanning calorimetry: kinetic versus thermodynamic fragilities, J. Chem. Phys. 117 (2002) 10184–10192, http://dx.doi.org/10.1063/1.1517607.
[18] Z. Chen, Z. Li, Y. Zhang, R. Liu, Y. Tian, L.-M. Wang, Calorimetric determination of fragility in glass forming liquids: T_f vs. T_g-onset methods, Eur. Phys. J. E. 37 (2014) 52, , http://dx.doi.org/10.1140/epje/i2014-14052-y.
[19] Q. Zheng, J.C. Mauro, Y. Yue, Reconciling calorimetric and kinetic fragilities of glass-forming liquids, J. Non-Cryst. Solids 456 (2017) 95–100.
[20] J. Shi, X. Lu, H. Li, Isothermal crystallization kinetics and melting behavior of PLLA/f-MWNTs composites, J. Therm. Anal. Calorim. 117 (2014) 1385–1396, http://dx.doi.org/10.1007/s10973-014-3885-1.
[21] D.L. Tillier, J. Meuldijk, G.W.H. Höhne, P.M. Frederik, O. Regev, C.E. Koning, About morphology in ethylene–propylene(−diene) copolymers-based latexes, Polymer (Guildf). 46 (2005) 7094–7108, http://dx.doi.org/10.1016/j.polymer.2005.05.095.
[22] K. Ishikiriyama, B. Wunderlich, Melting of poly(oxyethylene) analyzed by temperature-modulated calorimetry, Macromolecules 30 (1997) 4126–4131.
[23] B.B. Sauer, R.S. Mclean, J.D. Londono, B.S. Hsiao, Morphological changes during crystallization and melting of polyoxymethylene studied by synchrotron X-ray scattering and modulated differential scanning calorimetry, J. Macromol. Sci. Part B. 39 (2000) 519–543.
[24] J. Pak, B. Wunderlich, Melting and crystallization of polyethylene of different molar mass by calorimetry, Macromolecules 34 (2001) 4492–4503.
[25] Z.P. Lu, Y. Li, S.C. Ng, Y.P. Feng, K. Lu, Glass transition of rare-earth based metallic glasses: temperature modulated differential scanning calorimetry, J. Non-Cryst. Solids 250–252 ((1999) 689–693, http://dx.doi.org/10.1016/S0022-3093(99)00161-1.
[26] R.M. Saeed, J.P. Schlegel, C. Castano, R. Sawafta, Uncertainty of thermal characterization of phase change material by differential scanning calorimetry analysis, Int. J. Eng. Res. Technol. 5 (2016) 405–412.
[27] M. Reading, D. Elliott, V.L. Hill, Some Aspects of the Modulated Temperature Theory and Practice of Modulated Differential Scanning Differential Scanning Calorimetry: a Novel Approach to Calorimetry, 20 21st Proc. NATAS, 1992, pp. 145–150.
[28] M. Reading, Modulated differential scanning calorimetry—a new way forward in materials characterization, Trends Polym. Sci. 11 (1993) 8.
[29] M. Reading, A. Luget, R. Wilson, Modulated differential scanning calorimetry, Thermochim. Acta 238 (1994) 295–307.
[30] A.A. Lacey, C. Nikolopoulos, M. Reading, A mathematical model for modulated differential scanning calorimetry, J. Therm. Anal. Calorim. 50 (1997) 279–333.
[31] M. Reading, D.J. Hourston, Modulated Temperature Differential Scanning Calorimetry: Theoretical and Practical Applications in Polymer Characterisation, (2006).
[32] J.E.K. Schawe, A comparison of different evaluation methods in modulated temperature DSC, Thermochim. Acta 260 (1995) 1–16.
[33] J.E.K. Schawe, Principles for the interpretation of modulated temperature DSC measurements. Part 1. Glass transition, Thermochim. Acta 261 (1995) 183–194.
[34] H. McPhillips, D.Q.M. Craig, P.G. Royall, V.L. Hill, Characterisation of the glass transition of HPMC using modulated temperature differential scanning calorimetry, Int. J. Pharm. 180 (1999) 83–90.
[35] J.E.K. Schawe, Investigations of the glass transitions of organic and inorganic substances: DSC and temperature-modulated DSC, J. Therm. Anal. Calorim. 47 (1996) 475–484.
[36] D. Selvanathan, W.J. Bresser, P. Boolchand, Stiffness transitions in Si_xSe_{1-x} glasses from Raman scattering and temperature-modulated differential scanning calorimetry, Phys. Rev. B 61 (2000) 61–76.
[37] D.G. Georgiev, P. Boolchand, M. Micoulaut, Rigidity transitions and molecular structure of As_xSe_{1-x} glasses, Phys. Rev. B 62 (2000) 9228–9231.
[38] X. Feng, W.J. Bresser, P. Boolchand, Direct evidence for stiffness threshold in chalcogenide glasses, Phys. Rev. Lett. 78 (1997) 4422.
[39] P. Boolchand, D.G. Georgiev, B. Goodman, Discovery of the intermediate phase in chalcogenide glasses, J. Optoelectron. Adv. Mater. 3 (2001) 703–720.
[40] Y. Matsuda, C. Matsui, Y. Ike, M. Kodama, S. Kojima, Non-debye nature in thermal relaxation and thermal properties of lithium borate glasses studied by modulated DSC, J. Therm. Anal. Calorim. 85 (2006) 725–730, http://dx.doi.org/10.1007/s10973-006-7652-9.
[41] Y. Matsuda, Y. Fukawa, C. Matsui, Y. Ike, M. Kodama, S. Kojima, Calorimetric study of the glass transition dynamics in lithium borate glasses over a wide composition range by modulated DSC, Fluid Phase Equilib. 256 (2007) 127–131, http://dx.doi.org/10.1016/j.fluid.2007.03.011.
[42] P. Lucas, E.A. King, A.D. Horner, B.R. Johnson, S.K. Sundaram, Photostructural relaxation in As–Se–S glasses: effect of network fragility, J. Non-Cryst. Solids 352 (2006) 2067–2072, http://dx.doi.org/10.1016/j.jnoncrysol.2006.03.004.
[43] P. Lucas, E.A. King, O. Gulbiten, J.L. Yarger, E. Soignard, B. Bureau, Bimodal phase percolation model for the structure of Ge-Se glasses and the existence of the intermediate phase, Phys. Rev. B 80 (2009) 214114, , http://dx.doi.org/10.1103/PhysRevB.80.214114.
[44] Y. Matsuda, Y. Fukawa, M. Kawashima, S. Mamiya, S. Kojima, Dynamic glass transition and fragility of lithium borate binary glass, Solid State Ionics 179 (2008) 2424–2427, http://dx.doi.org/10.1016/j.ssi.2008.09.011.
[45] Y. Fukawa, Y. Matsuda, M. Kawashima, S. Kojima, Determination of complex-specific heat and fragility of sodium borate glasses by temperature-modulated DSC, J. Therm. Anal. Calorim. 99 (2010) 39–44, http://dx.doi.org/10.1007/s10973-009-0522-5.
[46] G. Yang, O. Gulbiten, Y. Gueguen, B. Bureau, J.-C. Sangleboeuf, C. Roiland, E.A. King, P. Lucas, Fragile-strong behavior in the As_xSe_{1-x} glass forming system in relation to structural dimensionality, Phys. Rev. B 85 (2012) 144107, , http://dx.doi.org/10.1103/PhysRevB.85.144107.
[47] R. Brüning, On the glass transition in vitreous silica by differential thermal analysis measurements, J. Non-Cryst. Solids 330 (2003) 13–22, http://dx.doi.org/10.1016/j.jnoncrysol.2003.08.051.
[48] C.T. Moynihan, Correlation between the width of the glass transition region and the temperature dependence of the viscosity of high-Tg glasses, J. Am. Ceram. Soc. 76 (1993) 1081–1087.
[49] M.L.F. Nascimento, C. Aparicio, Viscosity of strong and fragile glass-forming liquids investigated by means of principal component analysis, J. Phys. Chem. Solids 68 (2007) 104–110, http://dx.doi.org/10.1016/j.jpcs.2006.09.013.
[50] T.K. Bechgaard, J.C. Mauro, M. Bauchy, Y. Yue, L.A. Lamberson, L.R. Jensen, M.M. Smedskjaer, Fragility and configurational heat capacity of calcium aluminosilicate glass-forming liquids, J. Non-Cryst. Solids 461 (2017) 24–34, http://dx.doi.org/10.1016/j.jnoncrysol.2017.01.033.
[51] O. Gulbiten, J.C. Mauro, P. Lucas, Relaxation of enthalpy fluctuations during sub-Tg annealing of glassy selenium, J. Chem. Phys. 138 (2013) 244504, , http://dx.doi.org/10.1063/1.4811488.
[52] N.O. Birge, S.R. Nagel, Specific-heat spectroscopy of the glass transition, Phys. Rev. Lett. 54 (1985) 2674–2677.
[53] S. Weyer, A. Hensel, C. Schick, Phase angle correction for TMDSC in the glass-transition region, Thermochim. Acta 304 (1997) 267–275.
[54] J.M. Hutchinson, S. Montserrat, The application of temperature-modulated DSC to

the glass transition region II. Effect of a distribution of relaxation times, Thermochim. Acta 377 (2001) 63–84.
[55] J.E.K. Schawe, Modulated temperature DSC measurements: the influence of the experimental conditions, Thermochim. Acta 271 (1996) 127–140.
[56] S.L. Simon, Temperature-modulated differential scanning calorimetry: theory and application, Thermochim. Acta 374 (2001) 55–71.
[57] J.M. Hutchinson, A.B. Tong, Z. Jiang, Aging of polycarbonate studied by temperature modulated differential scanning calorimetry, Thermochim. Acta 335 (1999) 27–42.
[58] S.L. Simon, G.B. McKenna, The effects of structural recovery and thermal lag in temperature-modulated DSC measurements, Thermochim. Acta 307 (1997) 1–10.
[59] B. Wunderlich, Y. Jin, A. Boller, Mathematical description of differential scanning calorimetry based on periodic temperature modulation, Thermochim. Acta 236 (1994) 277–293.
[60] A. Boller, Y. Jin, B. Wunderlich, Heat capacity measurement by modulated DSC at constant temperature, J. Therm. Anal. Calorim. 42 (1994) 307–330.
[61] A. Savitzky, M.J.E. Golay, Smoothing and differentiation of data by simplified least squares procedures, Anal. Chem. 36 (1964) 1627–1639, http://dx.doi.org/10.1021/ac60214a047.

Paper V

Liquid Fragility Determination of Oxide Glass-Formers Using Temperature-Modulated DSC

Tobias K. Bechgaard[1], Ozgur Gulbiten[2], John C. Mauro[3], Yuanzheng Yue[1], Mathieu Bauchy[4], Morten M. Smedskjaer[1,*]

[1] *Department of Chemistry and Bioscience, Aalborg University, Aalborg, Denmark*

[2] *Science and Technology Division, Corning Incorporated, Corning, USA*

[3] *Department of Materials Science and Engineering, The Pennsylvania State University, University Park, USA*

[4] *Department of Civil and Environmental Engineering, University of California, Los Angeles, USA*

* Corresponding author. e-mail: mos@bio.aau.dk

Abstract: Glass-forming liquids exhibit a pronounced diversity in the viscosity-temperature relation. This has been characterized by the liquid fragility index to quantify the extent of the non-Arrhenian flow. Precise and accurate determination of liquid fragility is important for understanding a range of phenomena and controlling industrial glass melting processes. In this study, we use the temperature-modulated differential scanning calorimetry (TM-DSC) to determine liquid fragility of a wide range of oxide compositions, including tellurites, borates, and silicates. We compare our fragility data to those determined using viscometry and the Moynihan DSC approach. We find that TM-DSC is a useful method for determination of fragility, as it exhibits higher sensitivity and provides an easier and more reliable determination of characteristic temperatures compared to the Moynihan approach. Moreover, TM-DSC is faster and requires smaller sample volume compared to the viscometric approach. However, we also observe that TM-DSC tends to either overestimate or underestimate the fragility of very strong and highly fragile compositions, respectively.

Keywords: Oxide glasses, liquid fragility, temperature-modulated DSC

1. Introduction

Accurate knowledge of the viscosity-temperature relationship of glass-forming liquids is of great practical importance for all stages of industrial glass production [1–3], as even small perturbations in temperature can result in significant changes in viscosity. Angell introduced the concept of liquid fragility to quantitatively describe the temperature dependence of liquid and supercooled liquid viscosity [4–7]. Fragility classifies the dynamics of glass-forming liquids in terms of their departure from the Arrhenius temperature dependence of either viscosity or relaxation time [7]. The liquids exhibiting an Arrhenian temperature dependence of viscosity are said to be "strongest", but such ideally strong liquids do not exist in reality. However, the liquids exhibiting the 'nearly' Arrhenian dynamic behavior can be regarded as strong liquids, e.g., silica and germania. In contrast, the liquids showing the non-Arrhenian behavior are termed "fragile" ones. The liquid fragility index m is a liquid-state property that varies with composition (x). It is defined as the slope of the base-10 logarithm of viscosity ($\log_{10}\eta$) versus T_g-scaled inverse temperature (T) curve at T_g, where T_g is the glass transition temperature (corresponding to the viscosity of 10^{12} Pa s) of the liquid:

$$m(x) = \left.\frac{d\log_{10}\eta(T,x)}{d(T_g(x)/T)}\right|_{T=T_g(x)} . \quad (1)$$

The direct determination of fragility is thus from measurements of viscosity as a function of temperature, either in the vicinity of the glass transition utilizing Eq. (1) or by fitting high-temperature viscosity data to, e.g., the MYEGA equation of equilibrium viscosity [8]. However, measurements of viscosity are inherently time-consuming and can be challenging for glass-forming liquids prone to crystallization [9]. In addition, several of the widely-used viscometric methods require samples of specific shapes and volumes, which may be difficult to produce from poor glass-formers. Therefore, indirect methods for determining m using differential scanning calorimetry (DSC) have been established, as these methods only require small sample mass (typically 20-50 mg). Such methods rely on determining the activation energy for structural relaxation by scanning the sample at different heating/cooling rates. The rate dependence of fictive temperature (T_f) is thus used to estimate the activation energy for enthalpy relaxation, which is equivalent to that for shear viscosity, as reported by Moynihan and coworkers [10–13], Kissinger [14], Yue [15], and Wang and coworkers [16,17].

The Moynihan approach has been widely used [9–13], but for relatively strong glass-forming liquids, it is hard to determine T_f since the intercept between the extrapolated straight line of the glass isobaric heat capacity (C_p) curve and the inflection point of the overshoot C_p curve cannot be precisely assigned due to the small C_p jump (Fig. 1). Furthermore, for oxide glasses with high T_g values (e.g., above ~700 °C), the T_f values are determined in a temperature regime, where the sensitivity of most heat-flux DSC instruments is ~60% lower than that at room temperature, resulting in a low signal-to-noise ratio. To overcome these challenges for strong glass-forming liquids with high T_g in the Moynihan approach, we here consider the use of temperature-modulated differential scanning calorimetry (TM-DSC) as an alternative approach for determination of *m*, since TM-DSC allows for increased sensitivity [18].

2. Theory

The TM-DSC experiment is similar to that of the standard DSC, but with a sinusoidal modulation superimposed onto the linear heating segments. Accordingly, the temperature profile in a TM-DSC experiment is given by

$$T = T_0 + \beta t + A\sin(\omega t), \tag{2}$$

where T_0 is the initial temperature at time t = 0, β is the heating rate, A is the amplitude of the modulation, and ω is the angular frequency of the modulating tone ($\omega = 2\pi/P$, where P is the period). A deconvolution of the raw data allows for separation of the calorimetric contributions from the enthalpy relaxation and the heat capacity of the glass itself, identified by the imaginary heat capacity and real heat capacity, respectively [18].

TM-DSC has previously been used to determine the fragility of both chalcogenide and oxide glass-forming systems [19–21]. However, due to instrumental limitations, this has been limited to glasses with low T_g (below ~550 °C), and thus has not been suitable for many high-T_g silicate glasses of industrial importance. In those previous TM-DSC studies, two different approaches have been used. The first one utilizes the frequency dependence of the imaginary part of complex heat capacity data to estimate the activation energy for the structural relaxation, similarly to the Moynihan method

[19]. The other approach approximates the average relaxation time (τ) at a given temperature in order to construct an Angell plot by plotting log τ against T_g/T. Both procedures make use of the frequency dependence of the peak temperature (T_g^{ω}) in the imaginary heat capacity. However, as the imaginary heat capacity (C_p'') curve scales relative to the phase lag (φ) according to Eq. (3) [18], T_g^{ω} can also be determined directly from the phase lag:

$$C_p'' = \left|C_p^*(\omega)\right| \sin\varphi \ . \tag{3}$$

Here, $\left|C_p^*(\omega)\right|$ is the modulus of the complex-specific heat, a non-constant scalar. At temperatures far below and above the glass transition region, the phase lag is zero. At low temperature, the heat transfer occurs through atomic vibrations, while the high-temperature regime is dominated by molecular translations; both have a response much faster than the oscillation frequency. During the glass transition, the relaxation time of the structural rearrangements is on the same order as that of the temperature oscillations, resulting in a time lag between input and output [22]. This time lag can be used to probe the kinetics of the structural processes throughout the glass transition. By increasing the oscillation frequency (i.e., by lowering P), the response can be shifted to higher temperatures. This frequency dependence can be used to determine the activation energy for structural relaxation from the linear relationship between log(ω) and T_g^{ω}, similarly to the Moynihan approach. The activation energy for structural relaxation obtained by this method can be used to calculate the fragility index as in the other methods based on activation energy [19].

The relaxation time procedure is based on considering the glass transition to be a relaxation phenomenon [23], making it possible to determine the fragility of a liquid from the temperature dependence of the structural relaxation time. For molecular glass-formers, the fragility has been determined from the frequency dependence of the dielectric relaxation time [7]. However, as the relaxation of molecular glasses relates to polar atomic motions [24], the dielectric method cannot be applied to non-molecular liquids [25], such as modified silicates with mixed covalent-ionic bonding. Instead, a technique for measuring the structural relaxation time of silicate glasses based on specific heat capacity spectroscopy measurements was proposed in 1985 [26,27], by using the thermal relaxation caused by the isothermal temperature oscillations to measure the structural relaxation time.

Using the frequency dependence of the peak temperature (T_g^{ω}) in the imaginary heat capacity, TM-DSC has successfully been applied to determine *m* of several borate-based glass-forming liquids ($T_g \approx$ 450°C) [20,21,24,28] by converting frequency into relaxation time and using the following equation,

$$m(x) = \left.\frac{d \log_{10}\tau(T,x)}{d\left(T_g(x)/T\right)}\right|_{T=T_g(x)} . \quad (4)$$

In this work, we use the Moynihan DSC approach and the two approaches using TM-DSC to determine the fragility index of glass-forming liquids with a wide range of fragilities (*m* from 25 to 97), covering both tellurite, borate, and silicate glass chemistries [29,30]. Furthermore, we compare the determined *m* values with those from viscometric methods, reported in literature. The discrepancy in *m* among the different procedures is discussed.

3. Experimental procedure

The chemical compositions of the glasses used in this study, covering silicate, borate, and tellurite glasses, are found in Table 1. All glasses were prepared by the melt-quench method. Generally, the raw materials were mixed for 60 min in a ball mill and then melted in a covered crucible in air at 800-1650 °C for at least 6 h before being quenched on a metal plate. The detailed preparation procedure for some of the compositions is reported elsewhere [29,31].

The Netzsch STA 449F1 Jupiter® instrument with the TM-DSC module software extension was used for all the DSC and TM-DSC measurements. Silicate and borate glasses were scanned in Pt-Rh crucibles, while tellurite glasses were scanned in gold crucibles, both using argon as the purge gas (50 mL/min). The mass of the samples was ~20-35 mg. The samples were disc-shaped with diameter of ~4-6 mm and thickness of ~0.4 mm.

The samples were subjected to different heating rates after cooling from well above the glass transition at the same rate. For fragility determination using the Moynihan DSC approach, heating rates between 2 and 30 K/min were used. For the borate composition, the full range of heating rates from 2 to 30 K/min were used. For the silicate glasses, we only used heating rates in the range 10-30 K/min due to issues with instrumental sensitivity, while for tellurite compositions with m>79, the heating rates were limited to 6-14 K/min to minimize the error caused by the Arrhenius approximation

of the calculation of the fragility That is, the Moynihan approach for determining the activation energy assumes a linear dependence of $1/T_f$ on $\log(q_c)$, which is inherently violated by fragile glass-formers. The error caused by the Arrhenius approximation can be decreased by narrowing the heating rate range. The T_f values were here determined as the intercept between the extrapolated glass heat flow and the extrapolated line from the inflection point of the overshoot in heat flow at T_g. The liquid fragility is then determined from the slope of the $\log(1/q_c)$ vs. T_g/T_f plot for each composition.

In order to determine *m* by the two TM-DSC procedures, the frequency dependence of the glass transition is needed. To determine this, the samples were heated to a temperature of ~40-200 K above T_g, cooled to ~40-200 K below T_g with the same rate as the following upscan, and heated with appropriate values for β (0.5, 2, or 5 K/min), A (3 or 5 K), and P (90 to 200 s). An example of a temperature program for an experiment is therefore as follows: (a) heating from room temperature to T_g+150 K with β = 30 K/min, (b) cooling to T_g-100 K with β = -2 K/min, and (c) heating to T_g+150 K with β = 2 K/min, A = 5 K, and P = 150 s. The raw data file from the Netzsch DSC instrument contains the phase lag φ, heat flow amplitude A_{HF}, and heating rate amplitude A_{HR}. From these raw data, the reversing heat flow R_{HF} can be calculated as the ratio of A_{HF} and A_{HR}.

The reversing heat flow is reported directly herein without corrections, while the phase lag has been corrected using the Heat Transfer Correction procedure in the Netzsch Proteus Software, which is a linear two-point correction using one point on either side of the glass transition. To prevent noise from affecting the determination of T_g^{ω}, we fitted a Gaussian function to the top part of the phase signal peak in order to determine the peak temperature. The phase signal does not have a true Gaussian shape, but by limiting the Gaussian fitting to the top part of the peak, the shape is approximately Gaussian. For TM-DSC a linear response between input and output data is important. For the chosen experimental conditions, the samples exhibited a linear response between heat flow vs. heat rate data, evaluated using the procedure reported in Ref. [32].

4. Results and discussion

In the following, we present the *m* values determined by the three procedures described above: i) Moynihan DSC approach, ii) activation energy TM-DSC approach, and iii) relaxation time TM-DSC approach.

(A) Moynihan DSC approach

Fig. 2 shows the logarithmic inverse cooling rate ($\log(1/q_c)$ as a function of the normalized fictive temperature (T_g/T_f) as used in the Moynihan approach for standard DSC. The utilized heating rates (q_c) are not identical for all samples. For example, for high-SiO_2 compositions with low *m* and high T_g (i.e., lower instrument sensitivity at higher temperatures), the useable cooling/heating rates are limited to relative high values, while the q_c values for more fragile compositions are limited to a heating rate range from 6-14 K/min. The heating rate dependence of the fictive temperatures can then be used to approximate the fragility of the glass-forming liquids from the slope of the linear fits in Fig. 2. In general, with this approach, we can accurately determine *m* values when comparing to viscometric data (Figure 8a). However, the vanadium tellurite glasses exhibit discrepancies from the viscometric values reported elsewhere [31].

(B) TM-DSC approaches

Next, we use the two TM-DSC approaches to determine *m* values. Both the activation energy and the relaxation time TM-DSC procedures require quantification of the modulation frequency dependence on the phase lag peak, as obtained from deconvolution of the raw data. Figure 3 shows the reversing heat flow and the uncorrected and corrected phase lag in the glass transition range for the 39.8SiO_2-31.6 Al_2O_3-28.7CaO (mol %) glass composition. The reversing heat flow signal exhibits a step change around 1150 K due to the gained configurational degrees of freedom associated with the transition from the solid glass to the supercooled liquid state.

Simultaneously we observe an asymmetric Gaussian peak in the phase lag signal, associated with the change in the heat transfer during the transition from solid glass to supercooled liquid. From the

phase lag peak, a frequency dependent glass transition temperature (T_g^{ω}) can be determined, where ω is the angular frequency ($\omega = 2\pi/P$ rad/s). The plot of T_g^{ω} vs. T_g is shown in Fig. 4 for all the glasses from Table 1, where T_g is determined as the onset of the glass transition in a linear DSC heating scan at 10 K/min. The compositional trend in the two measures of glass transition temperature is identical. For example, both T_g^{ω} and T_g exhibit high values for glasses with high SiO_2 content and lower values for glasses with low SiO_2 content and the borate tellurite glasses. However, the absolute values of T_g^{ω} and T_g differ due to both different experimental conditions and differences in the procedure for determining the glass transition temperature (e.g., onset vs. peak temperature). Considering the lower heating rate in the TM-DSC compared to DSC experiments, T_g^{ω} should be lower than T_g. However, since T_g^{ω} is determined roughly as the midpoint of the glass transition and T_g is determined as its onset, T_g^{ω} is consistently higher than T_g. As the width of the glass transition is higher for high-SiO_2 glasses compared to the other investigated compositions in this study, the difference between T_g^{ω} and T_g increases as the SiO_2 content increases, in agreement with a previous report [32].

To determine m by the TM-DSC activation energy procedure, we need to consider the frequency dependence of the phase lag peak. Fig. 5 shows the phase lag measured at four different frequencies for the $39.8SiO_2$-$31.6Al_2O_3$-28.7CaO glass. We observe that T_g^{ω} shifts to higher temperature with decreasing modulation frequency as the characteristic relaxation time becomes shorter [26,33]. Analogous to the Moynihan DSC approach, the activation energy for structural relaxation can be determined from the relationship between the characteristic temperature and the corresponding frequency (Fig. 6), with the magnitude of the slope being proportional to that of the fragility index.

In addition to the frequency dependence of the phase lag, the frequency dependent relaxation time procedure requires quantification of the temperate-dependent average relaxation time for the corresponding frequency. When the temperature changes during a modulated scan, the relaxation time changes accordingly. According to Kojima and coworkers, the average relaxation time τ occurs at T_g^{ω}, with $\tau = P/2\pi$ [20,21]. To construct the Angell plot, T_g^{ω} must be normalized by T_g, confirmed as the temperature at equilibrium viscosity $\eta = 10^{12}$ Pa s [34]. From literature studies it is known that at T_g, the shear relaxation time τ is equal to ~100 s [5,35,36]. Using the relation between τ and P, we find

that $T_g^{\omega} = T_g$ when the modulation period is ~628 s. However, it would be inconvenient to perform measurements with such high P value. For β = 2 K/min, the number of periods during the glass transition range would be too few to enable a valid deconvolution of the raw data [18]. A sufficient number of periods would require an underlying heating rate below 1 K/min, resulting in unacceptably long experimental duration. Therefore, an alternative route to obtain $T_g^{\omega} = T_g$ is needed. A linear relationship between T_g^{ω} and τ at each modulation frequency has been reported [26]. By extrapolation we can determine the glass transition temperature ($T_g^{\tau = 100}$) where τ = 100 s. By plotting T_g^{ω} normalized by the determined $T_g^{\tau = 100}$ value as a function of the calculated τ values at each modulation frequency, we obtain an Angell plot (Fig. 7). Using the definition of fragility (Eq. (3)), we can calculate m for each glass-forming liquid.

Finally, we note that the relaxation time is not equal to 100 s at T_g (where η=10^{12} Pa s) for some glass systems, given their difference in shear modulus (G) following the Maxwell relation $\tau = \eta/G$. However, the effect of an error in the relaxation time estimation on m is small. For example, if the data was instead extrapolated to the glass transition temperature with τ = 40 s, the change in m is within ±1-3%. For simplicity, we have therefore used a relaxation time at T_g of 100 s in the fragility determination.

(C) Comparison of fragility methods

All of the fragility values determined by the three methods are shown in Fig. 8. For a few compositions, the calorimetric fragility values differ significantly from those determined using viscometry. As shown in Fig. 8a for the fragilities determined using Moynihan's DSC approach, the m values for the vanadium tellurite compositions ranges from 39 to 82, with all the viscometric m values are around 80. We consider this erroneous estimation to be due to the small difference between fictive temperatures at different heating rates, which in turn is of the same magnitude as the error in temperature when using a DSC. In Figs. 8b and 8c, where the data originate from the same set of frequency-dependent TM-DSC data, the fragilities of the vanadium tellurite compositions are closer to those determined by the viscometric method. However, for the TM-DSC methods, we observe largely underestimated fragility values for the barium titanosilicate and for a borate composition. These

unsystematic errors constitute a significant limitation for using TM-DSC to determine fragility, but it should be noted that the same problem is found using the standard linear DSC method (Fig. 8a). In the following discussion, the largely underestimated (outlier) fragility values (red data points in Figs. 8a-c) are thus neglected. Furthermore, we neglect the data of all the tellurite glasses from Fig. 8a, due to the large variation in the calorimetric *m* values, which is unrealistic considering the similar fragility of those glasses reported in literature [31].

For all three procedures of liquid fragility determination, we observe an approximately linear relationship between viscometric fragility and calorimetric fragility. However, the calorimetric fragilities are generally underestimated when probed by DSC, as all three DSC and TM-DSC procedures assume Arrhenius dynamics around T_g [9]. Since such Arrhenian behavior is only obeyed by the strong glass-forming liquids (such as SiO_2), an inherent error exists in the different procedures for determining fragility, resulting in the underestimation of *m*. To circumvent this systematic problem, Zheng *et al.* [9] have recently suggested to correct calorimetric fragility values (m_{DSC}) to corresponding viscometric fragility (m_{vis}) values using an empirical relation,

$$m_{vis} = 1.289(m_{DSC} - m_0) + m_0, \quad (5)$$

where m_0 is the fragility of a glass-forming liquid exhibiting Arrhenius behavior equal to 14.97 [9]. By using this approach to correct the present data, we obtain the fragility values shown in Fig. 9. Interestingly, for our data, we obtain the fitting coefficients (1.289 from the previous study [9]) of 1.30±0.06 and 1.30±0.07 by using the Moynihan DSC procedure and the activation energy TM-DSC procedure, respectively. We note that both the present study and Ref. [9] include the same vanadium tellurite glasses, but otherwise different compositions. This agreement supports the validity of the correction method proposed in Ref. [9], while it also indicates that we are probing the same type of relaxation using both DSC and TM-DSC measurements. For the relaxation time TM-DSC procedure, which requires the determination of relaxation time, the fitting coefficient is found to be 1.20±0.05, slightly smaller than for the two other procedures. After the correction procedure, the fragility values of both TM-DSC procedures result in the same *m* values.

TM-DSC has two main advantages over linear DSC when determining fragility. First, the superior sensitivity and signal-to-noise ratio at high temperatures of TM-DSC allows for

determination of fragility values of relatively strong glass-forming liquids that typically have higher T_g. Second, in the Moynihan DSC approach, the ease of determining the characteristic onset temperature (i.e., fictive temperature) depends on the width, magnitude, and sharpness of the glass transition and thus fragility. That is, it is typically easier to determine T_f of fragile liquids compared to strong liquids since it is difficult to get a precise tangent line from C_p of the glassy state. On the other hand, the TM-DSC approaches rely on the Gaussian fit to the phase lag curve, allowing a more reliable determination of the characteristic temperature, as the fit to the data uses all available data points compared to only two data points on either side of the glass transition for the Moynihan DSC approach. This difference results in a lower standard error in the fragility values determined by TM-DSC. This can be seen from the size of the error bars in Fig. 10 for a series of fully charge-compensated calcium aluminosilicates.

Using Moynihan's DSC approach to determine fragility of the tectosilicate compositions in Fig. 10, we were unable to determine *m* of the glass-forming liquids with SiO_2 content of more than 82 mol%, such as the glass-forming liquid named Si86 in Fig. 1. However, TM-DSC has been found to enable fragility determination of liquids with SiO_2 content at least up to 90 mol% (Fig. 10), and potentially allow for determination of the fragility of fused SiO_2. Finally, we note that TM-DSC succeeds in reproducing the composition-dependent trend in fragility for the tectosilicates, but the magnitude of the *m* values tends to be underestimated for high-*m* compositions and overestimated for low-*m* compositions (Fig. 10). It should be mentioned that the viscometric fragility data of the liquids with high SiO_2 content were not available and thus are not included in the correction procedure of the TM-DSC data [9]. As Eq. (5) increases the fragility value of all liquids with non-Arrhenius behavior (i.e., with $m > 14.97$), the correction function cannot adequately correct the low-*m* data in this glass series. This suggests that a more advanced correction procedure might be needed for strong glass-forming liquids.

6. Conclusions

We have demonstrated that TM-DSC can be used to determine the liquid fragility index of glass compositions with a large range of glass transition temperatures. The TM-DSC fragility data have been compared to both viscometric data and the well-known DSC data obtained by the Moynihan approach. TM-DSC provides the fragility data with similar accuracy to that obtained by the other two approaches, but with improved precision. Furthermore, TM-DSC enables determination of fragility of relatively strong glass-forming liquids, as the superimposed sinusoidal heating rate increases the sensitivity of the instrument, in contrast to linear DSC. The main disadvantage of the TM-DSC method is the apparent overestimation of the fragility of rather strong liquids and underestimation of the fragility of rather fragile liquids.

Acknowledgements

The purchase of the calorimeter was supported by the Obel Family Foundation.

References

[1] A.K. Varshneya, Fundamentals of Inorganic Glasses, Elsevier, 2011.

[2] P.K. Gupta, J.C. Mauro, Composition dependence of glass transition temperature and fragility. I. A topological model incorporating temperature-dependent constraints, J. Chem. Phys. 130 (2009) 094503. doi:10.1063/1.3077168.

[3] J.C. Mauro, D.C. Allan, M. Potuzak, Nonequilibrium viscosity of glass, Phys. Rev. B. 80 (2009) 094204. doi:10.1103/PhysRevB.80.094204.

[4] C.A. Angell, Strong and fragile liquids, in: K. Ngai, G.B. Wright (Eds.), Relaxations Complex Syst., National Technical Information Service, U.S. Department of Commerce, Springfield, VA 22161, 1985: pp. 3–11.

[5] R. Bohmer, K.L. Ngai, C.A. Angell, D.J. Plazek, Nonexponential relaxations in strong and fragile glass formers, J. Chem. Phys. 99 (1993) 4201. doi:10.1063/1.466117.

[6] C.A. Angell, Formation of Glasses from Liquids and Biopolymers, Science. 267 (1995) 1924–1935. doi:10.1126/science.267.5206.1924.

[7] K. Ito, C.T. Moynihan, C.A. Angell, Thermodynamic determination of fragility in liquids and a fragile-to-strong liquid transition in water, Nature. 398 (1999) 492–495. doi:10.1038/19042.

[8] J.C. Mauro, Y. Yue, A.J. Ellison, P.K. Gupta, D.C. Allan, Viscosity of glass-forming liquids, Proc. Nat. Acad. Sci. 106 (2009) 19780. doi:10.1073/pnas.0911705106.

[9] Q. Zheng, J.C. Mauro, Y. Yue, Reconciling calorimetric and kinetic fragilities of glass-forming liquids, J. Non. Cryst. Solids. 456 (2017) 95–100.

[10] C.T. Moynihan, A.J. Easteal, M.A. DeBolt, J. Tucker, Dependence of the Fictive Temperture of Glass on Cooling Rate, J. Am. Ceram. Soc. 59 (1976) 12–16.

[11] C.T. Moynihan, Structural relaxation and the glass transition, Rev. Mineral. Geochemistry. 32 (1995) 1–19.

[12] C.T. Moynihan, S.K. Lee, M. Tatsumisago, T. Minami, Estimation of activation energies for structural relaxation and viscous flow from DTA and DSC experiments, Thermochim. Acta. 280–281 (1996) 153–162. doi:10.1016/0040-6031(95)02781-5.

[13] A.Q. Tool, Relation Between Inelastic Deformability and Thermal Expansion of Glass in Its Annealing Range, J. Am. Ceram. Soc. 29 (1946) 240–253. doi:10.1111/j.1151-2916.1946.tb11592.x.

[14] H.E. Kissinger, Reaction Kinetics in Differential Thermal Analysis, Anal. Chem. 29 (1957) 1702–1706.

[15] Y. Yue, R. Von Der Ohe, S.L. Jensen, Fictive temperature, cooling rate, and viscosity of glasses, J. Chem. Phys. 120 (2010) 8053–8059. doi:10.1063/1.1689951.

[16] L.-M. Wang, V. Velikov, C.A. Angell, Direct determination of kinetic fragility indices of glassforming liquids by differential scanning calorimetry: Kinetic versus thermodynamic fragilities, J. Chem. Phys. 117 (2002) 10184–10192. doi:10.1063/1.1517607.

[17] V. Velikov, S. Borick, C.A. Angell, The Glass Transition of Water, Based on Hyperquenching Experiments, Science. 294 (2001) 2335–2338.

[18] M. Reading, D.J. Hourston, Modulated temperature differential scanning calorimetry: theoretical and practical applications in polymer characterisation, 6th ed., Springer, 2006.

[19] G. Yang, O. Gulbiten, Y. Gueguen, B. Bureau, J.-C. Sangleboeuf, C. Roiland, E.A. King, P. Lucas, Fragile-strong behavior in the As_xSe_{1-x} glass forming system in relation to structural dimensionality, Phys. Rev. B. 85 (2012) 144107. doi:10.1103/PhysRevB.85.144107.

[20] Y. Matsuda, Y. Fukawa, M. Kawashima, S. Mamiya, S. Kojima, Dynamic glass transition and fragility of lithium borate binary glass, Solid State Ionics. 179 (2008) 2424–2427. doi:10.1016/j.ssi.2008.09.011.

[21] Y. Fukawa, Y. Matsuda, M. Kawashima, S. Kojima, Determination of complex-specific heat and fragility of sodium borate glasses by temperature-modulated DSC, J. Therm. Anal. Calorim. 99 (2010) 39–44. doi:10.1007/s10973-009-0522-5.

[22] O. Gulbiten, J.C. Mauro, P. Lucas, Relaxation of enthalpy fluctuations during sub-Tg annealing of glassy selenium, J. Chem. Phys. 138 (2013) 244504. doi:10.1063/1.4811488.

[23] J.C. Mauro, M.M. Smedskjaer, Statistical mechanics of glass, J. Non. Cryst. Solids. 396 (2014) 41–53. doi:10.1016/j.cell.2013.07.024.

[24] Y. Matsuda, Y. Fukawa, C. Matsui, Y. Ike, M. Kodama, S. Kojima, Calorimetric study of the

glass transition dynamics in lithium borate glasses over a wide composition range by modulated DSC, Fluid Phase Equilib. 256 (2007) 127–131. doi:10.1016/j.fluid.2007.03.011.

[25] L.M. Martinez, C.A. Angell, A thermodynamic connection to the fragility of glass-forming liquids., Nature. 410 (2001) 663–667. doi:10.1038/35070517.

[26] N.O. Birge, S.R. Nagel, Specific-Heat Spectroscopy of the Glass Transition, Phys. Rev. Lett. 54 (1985) 2674–2677.

[27] N.O. Birge, Specific-heat spectroscopy of glycerol and propylene glycol near the glass transition, Phys. Rev. B. 34 (1986) 1631–1642.

[28] Y. Matsuda, C. Matsui, Y. Ike, M. Kodama, S. Kojima, Non-debye nature in thermal relaxation and thermal properties of lithium borate glasses studied by modulated DSC, J. Therm. Anal. Calorim. 85 (2006) 725–730. doi:10.1007/s10973-006-7652-9.

[29] T.K. Bechgaard, J.C. Mauro, M. Bauchy, Y. Yue, L.A. Lamberson, L.R. Jensen, M.M. Smedskjaer, Fragility and configurational heat capacity of calcium aluminosilicate glass-forming liquids, J. Non. Cryst. Solids. 461 (2017) 24–34. doi:10.1016/j.jnoncrysol.2017.01.033.

[30] M.L.F. Nascimento, C. Aparicio, Viscosity of strong and fragile glass-forming liquids investigated by means of principal component analysis, J. Phys. Chem. Solids. 68 (2007) 104–110. doi:10.1016/j.jpcs.2006.09.013.

[31] J. Kjeldsen, A.C.M. Rodrigues, S. Mossin, Y. Yue, Critical V_2O_5/TeO_2 Ratio Inducing Abrupt Property Changes in Vanadium Tellurite Glasses, J. Phys. Chem. B. 118 (2014) 14942–14948. doi:10.1021/jp508910m.

[32] T.K. Bechgaard, O. Gulbiten, J.C. Mauro, M.M. Smedskjaer, Parametric study of temperature-modulated differential scanning calorimetry for high-temperature oxide glasses with varying fragility, J. Non. Cryst. Solids. 484 (2018) 84.

[33] J.M. Hutchinson, S. Montserrat, The application of temperature-modulated DSC to the glass transition region II. Effect of a distribution of relaxation times, Thermochim. Acta. 377 (2001) 63–84.

[34] Y. Yue, Characteristic temperatures of enthalpy relaxation in glass, J. Non. Cryst. Solids. 354

(2008) 1112–1118. doi:10.1016/j.jnoncrysol.2006.11.027.

[35] C.A. Angell, Relaxation in liquid, polymers and plastic crystal - strong/fragile patterns and problems, J. Non. Cryst. Solids. 131 (1991) 13–31.

[36] C.A. Angell, K.L. Ngai, G.B. McKenna, P.F. McMillan, S.W. Martin, Relaxation in glassforming liquids and amorphous solids, J. Appl. Phys. 88 (2000) 3113. doi:10.1063/1.1286035.

Tables and Figures

Table 1. Analyzed chemical compositions (in mol%), measured glass transition temperature (T_g), extrapolated glass transition temperature with τ=100 s ($T_g^{\tau = 100}$), liquid fragility index determined by viscometry (m_{vis}) (literature data [29,30]), and liquid fragility index determined by TM-DSC ($m_{TM\text{-}DSC}$) corrected using Eq. (5),. When the total compositions do not add to 100%, the minor impurity oxides are MgO, Fe_2O_3, and TiO_2 (total <0.7 mol%).

Chemical composition (numbers in mol%)	**T_g (K)**	**$T_g^{\tau = 100}$ (K)**	***m_{vis} (-)***	***$m_{TM\text{-}DSC}$* (-)**
89.9SiO_2-4.6Al_2O_3-5.5CaO	1189	1226	-	27
86.0SiO_2-6.6 Al_2O_3-7.4CaO	1173	1192	-	29
81.5SiO_2-9.2 Al_2O_3-9.3CaO	1156	1177	-	25
78.2SiO_2-10.6 Al_2O_3-10.9CaO	1151	1165	-	25
72.6SiO_2-13.5 Al_2O_3-14.0CaO	1149	1150	-	27
69.0SiO_2-15.9 Al_2O_3-14.8CaO	1143	1149	38	31
60.6SiO_2-20.1 Al_2O_3-19.3CaO	1140	1144	-	30
54.9SiO_2-22.6 Al_2O_3-22.0CaO	1136	1136	49	31
48.5SiO_2-25.9 Al_2O_3-25.6CaO	1136	1137	-	37
46.4SiO_2-26.7 Al_2O_3-26.3CaO	1135	1132	54	36
45.1SiO_2-29.0 Al_2O_3-25.9CaO	1132	1132	-	40
39.8SiO_2-31.6 Al_2O_3-28.7CaO	1132	1131	-	42
30.0SiO_2-35.0Al_2O_3-34.3CaO	1124	1125	57	48
55.3SiO_2-24.6Al_2O_3-19.6CaO	1137	1146	48	40
60.3SiO_2-19.7Al_2O_3-19.6CaO	1131	1140	46	40
64.4SiO_2-15.0Al_2O_3-20.2CaO	1110	1116	46	40
69.6SiO_2-9.9Al_2O_3-20.0CaO	1076	1086	41	39
33Li_2O-67B_2O_3 [a]	769	760	88[b]	30
33Na_2O-67B_2O_3 [a]	747	748	82[b]	98
33BaO-67B_2O_3 [a]	866	865	97[b]	99
40BaO-20TiO_2-40SiO_2 [a]	984	978	71	35
9.7V_2O_5-90.3TeO_2	559	557	81	80
19.9V_2O_5-80.1TeO_2	544	543	80	65
29.2V_2O_5-70.8TeO_2	530	529	80	82
39.6V_2O_5-60.4TeO_2	518	517	79	93
50.2V_2O_5-49.8TeO_2	507	506	85	94

[a] Nominal chemical composition.

[b] Literature values and thus not determined for the specific sample.

Figure 1. (a) Heat flow as a function of temperature obtained at different heating rates for the 86.0SiO_2-6.6 Al_2O_3-7.4CaO (mol%) glass using linear DSC. These data can be used for determination of the activation energy for structural relaxation and thus fragility using the Moynihan approach [10–14,16,17]. Note that it can be challenging to determine the onset temperature (i.e., fictive temperature) due to i) the low sensitivity of the calorimeter at these relatively high temperatures, and ii) the relatively wide glass transition region due to the strong nature of the glass-forming liquid. (b) Example of tangent fitting to the isobaric heat capacity curve, shown for scan with cooling/heating rates of 10 K/min. Small variations in the tangent slopes can result in shifts of the fictive temperature estimation by more than 10 K.

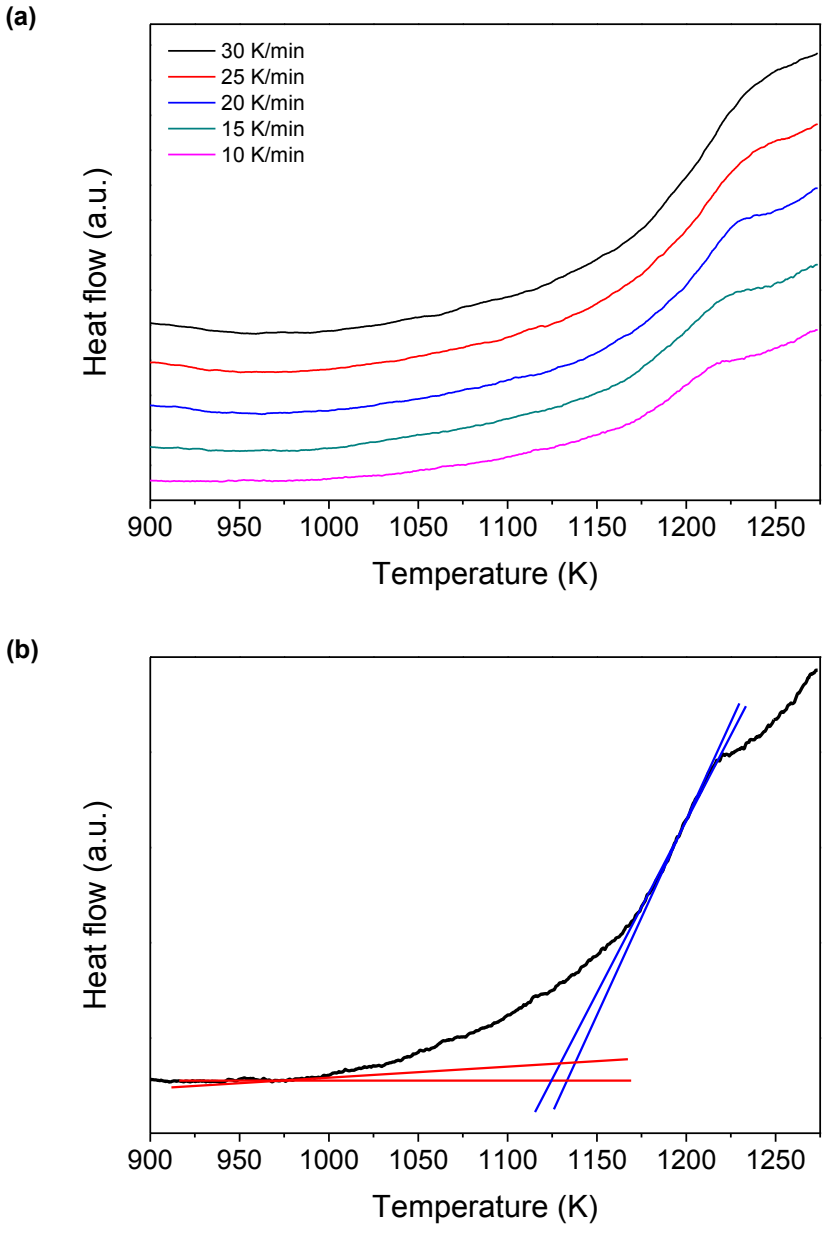

Figure 2. Dependence of the reciprocal rate of logarithmic cooling rate (log $(1/q_c)$) on the reduced fictive temperature (T_g/T_f) for three selected compositions. The fragility can be estimated from the slope of the linear fit. The fragility values given in the legend are from viscometry, with that of the 81.5SiO_2-9.2 Al_2O_3-9.3CaO glass composition unavailable.

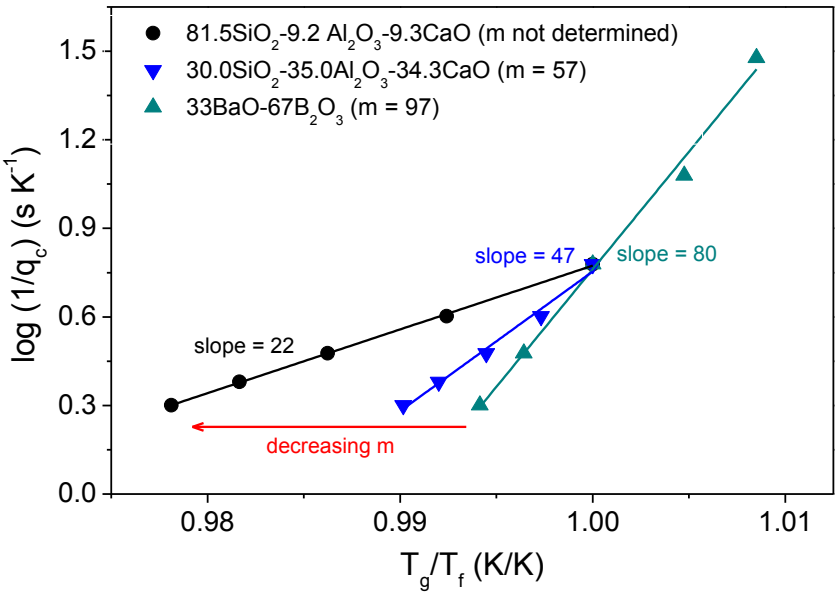

Figure 3. Temperature dependence of the reversing heat flow and phase lag before, during, and after the glass transition for 39.8SiO_2-31.6 Al_2O_3-28.7CaO (mol %) glass with β = 2 K/min, A = 5 K, and P = 180 s. Both the uncorrected and corrected phase lags are shown. The correction used is the Heat Transfer Correction in the Netzsch Proteus software. The determination of T_g^{ω} from a Gaussian fit to the phase lag is also shown.

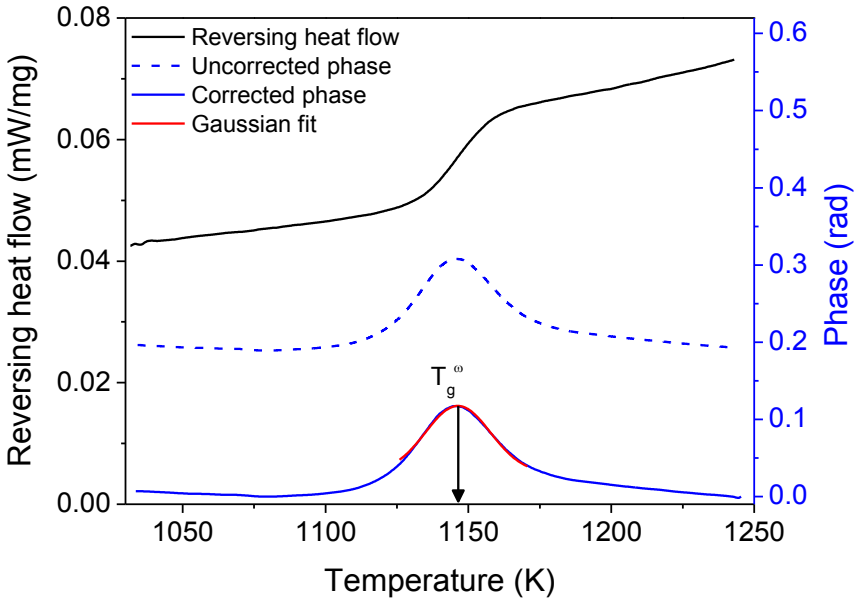

Figure 4. Dependence of the frequency-dependent glass transition temperature (T_g^{ω}, as determined by phase lag TM-DSC data) on the DSC glass transition temperature ($T_{g,DSC}$, as determined by linear DSC using a scanning rate of 10 K/min). Due to the different procedures for determination of the characteristic temperatures, the deviation between the two set of glass transition values increases for strong glass-forming liquids with high T_g. Inset shows the high temperature range with the largest deviation between T_g^{ω} and T_g. The values of T_g^{ω} have been determined from scans with parameters β = 2 K/min, A = 5 K, and P = 180 s.

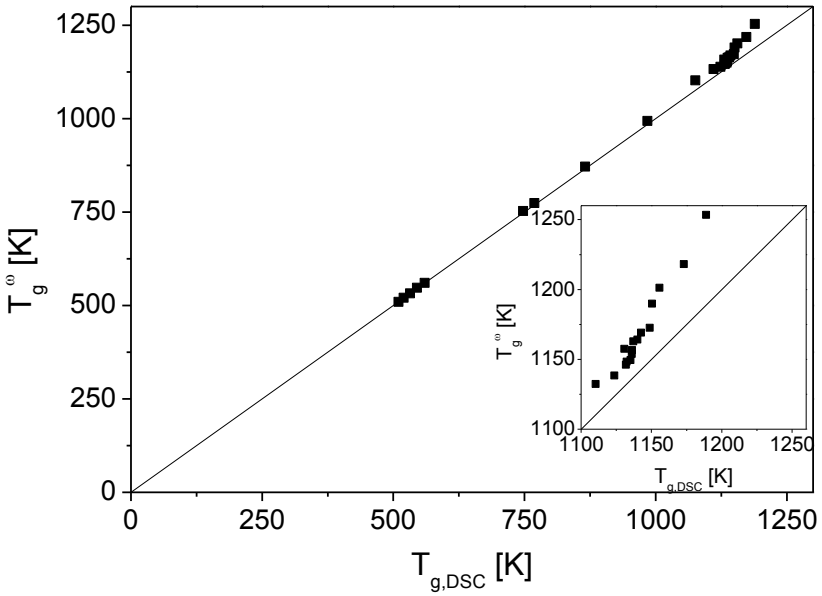

Figure 5. Phase lag as a function of temperature obtained at different frequencies. The phase lag curve and therefore glass transition temperature ($T_g^{(\omega)}$) shifts to higher temperature as the period decreases, i.e., frequency increases. The data are here shown for the $39.8SiO_2$-$31.6Al_2O_3$-28.7CaO (mol %) glass scanned with parameters β = 2 K/min, A = 5 K, and P = 180, 150, 120 and 90 s.

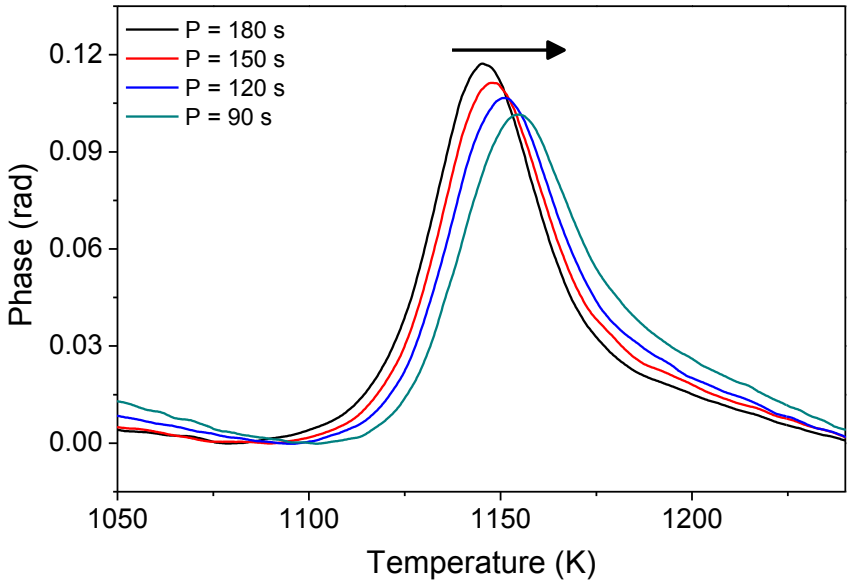

Figure 6. Logarithmic frequency as a function of the inverse phase peak temperature, illustrating the activation energy approach to determine liquid fragility by TM-DSC. The phase lag and therefore the glass transition temperature (T_g^{ω}) shifts to higher temperature as the frequency increases. The data are here shown for 39.8SiO_2-31.6 Al_2O_3-28.7CaO (mol %) glass scanned with parameters β = 2 K/min, A = 5 K, and P = 180, 150, 120 and 90 s. The fragility values given in the legend are from viscometry, with that of the 81.5SiO_2-9.2 Al_2O_3-9.3CaO (mol %) glass composition unavailable.

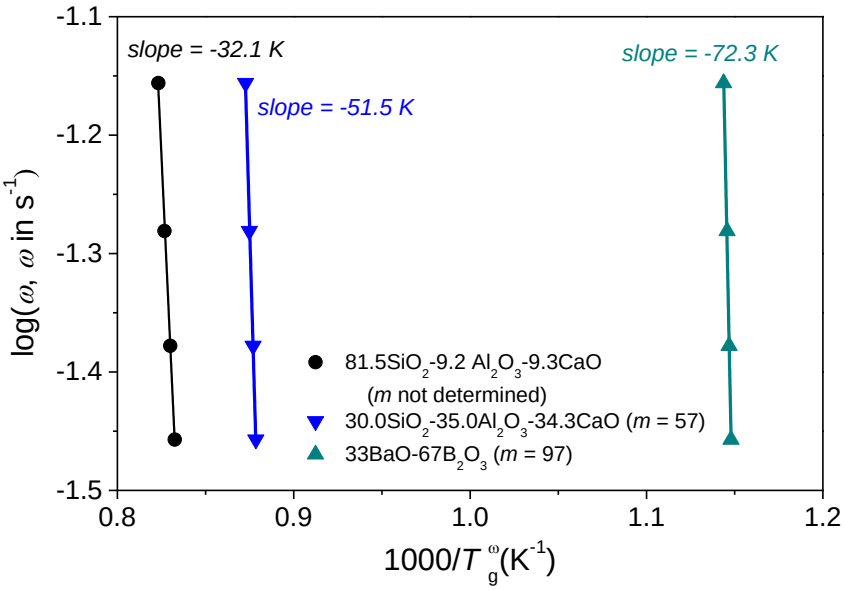

Figure 7. Angell plot of three selected compositions showing the relaxation time slightly above the glass transition temperature. The relaxation times have been determined using $\tau = 1/\omega = P/2\pi$ rad/s. The straight lines represent linear fits to the data. The fragility values given in the legend are from viscometry, with that of the 81.5SiO_2-9.2 Al_2O_3-9.3CaO (mol %) glass composition unavailable.

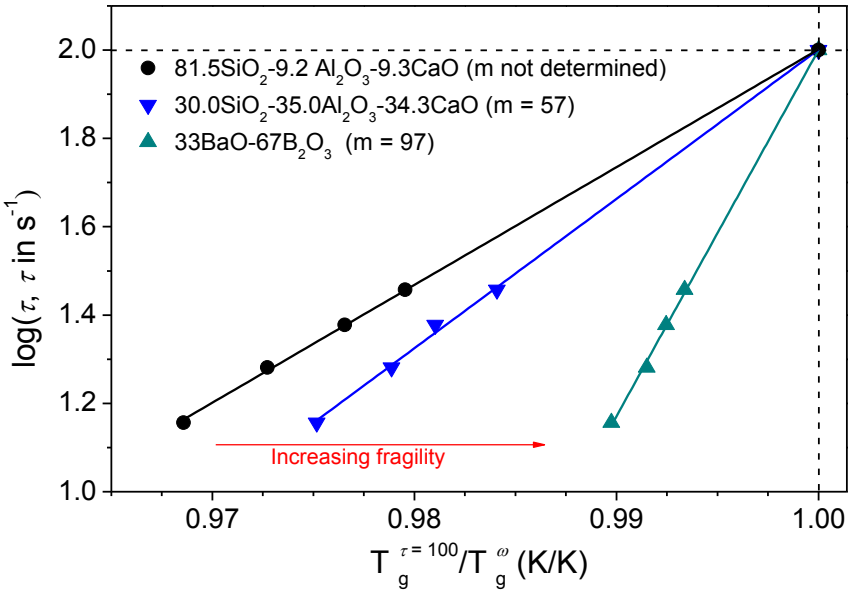

Figure 8. Fragility values determined by (a) Moynihan's DSC approach (m_{DSC}), (b) activation energy TM-DSC procedure ($m_{TM\text{-}DSC,\ activation\ energy}$), and (c) relxation time TM-DSC procedure ($m_{TM\text{-}DSC,\ relaxation\ time}$) as a function of the fragility determined using viscometry (m_{visco}). The m values are reported directly from the activation energy or relaxation time plot without any further correction. For each data set, some compositions (shown in red) exhibit m values far from the viscometric values. In (a), these glasses are tellurites with low T_g, while for (b) and (c), it is barium titanosilicate and lithium borate glasses. Viscometric fragilities are taken from Refs. [29,30].

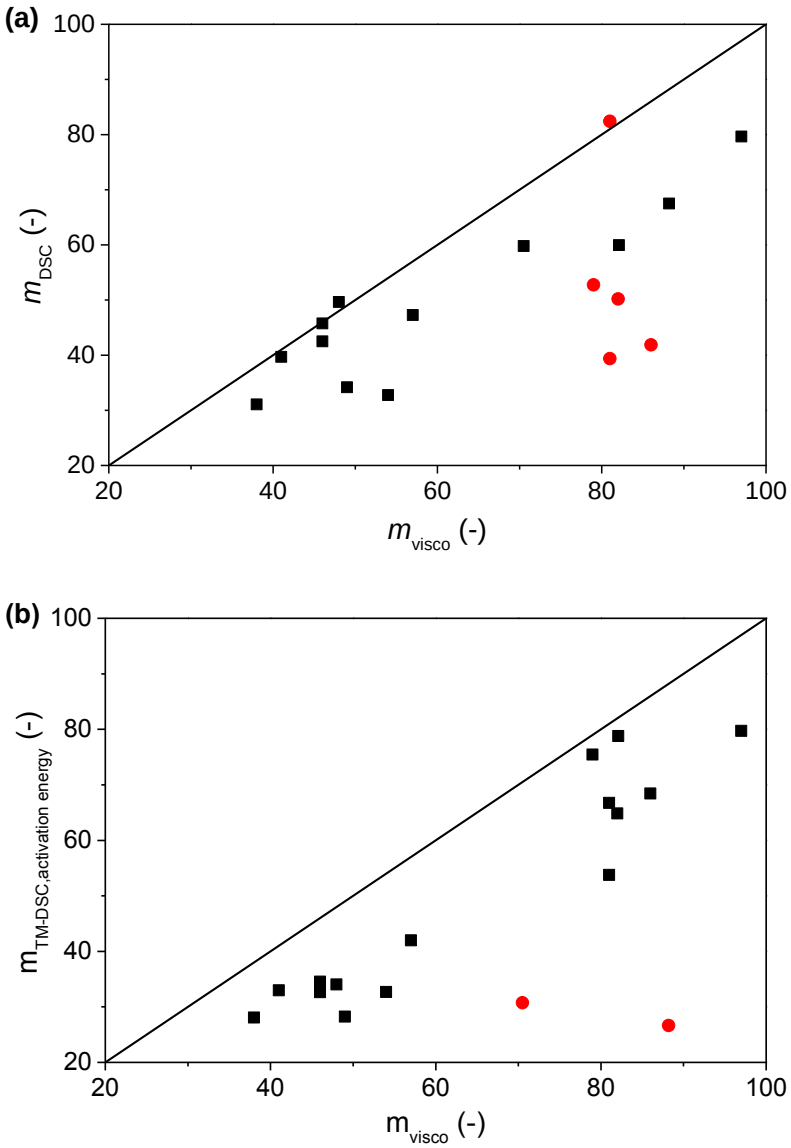

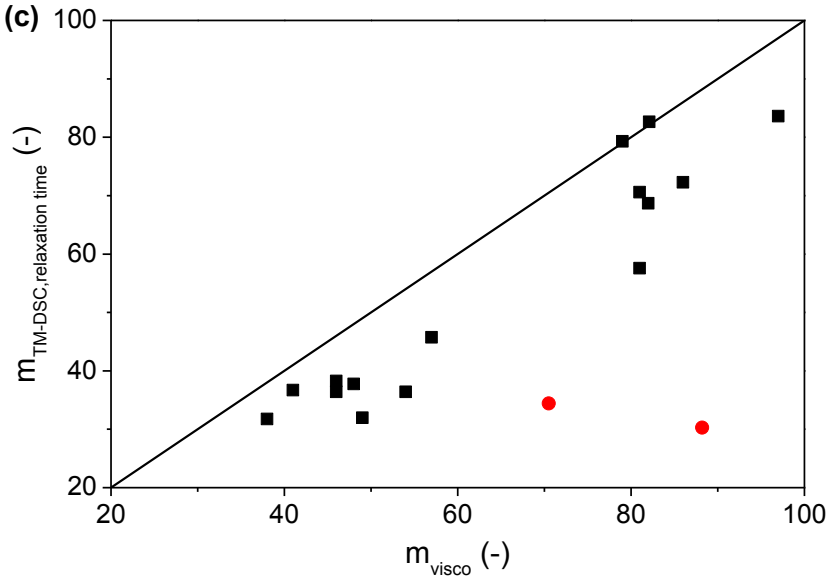
(c)
100
80
60
40
20
20
40
60
80
100
m TM-DSC,relaxation time (-)
m visco (-)

Figure 9. Corrected fragility values (*m*) determined by the Moynihan's DSC approach and two TM-DSC procedures as a function of the fragility determined using viscometry (m_{visco}). The correction has been made using the procedure presented by Zheng *et al.* [9]. The fitting coefficients are 1.30±0.06, 1.30±0.07, and 1.20±0.05 for Moynihan DSC approach, activation energy TM-DSC procedure, relaxation time TM-DSC procedure, respectively. These values are close to those presented in Ref. [9]. We note that the *m* values determined by the two TM-DSC approaches become identical after the correction, with a tendency to underestimate *m* of strong glass-forming liquids and overestimate *m* for more fragile compositions.

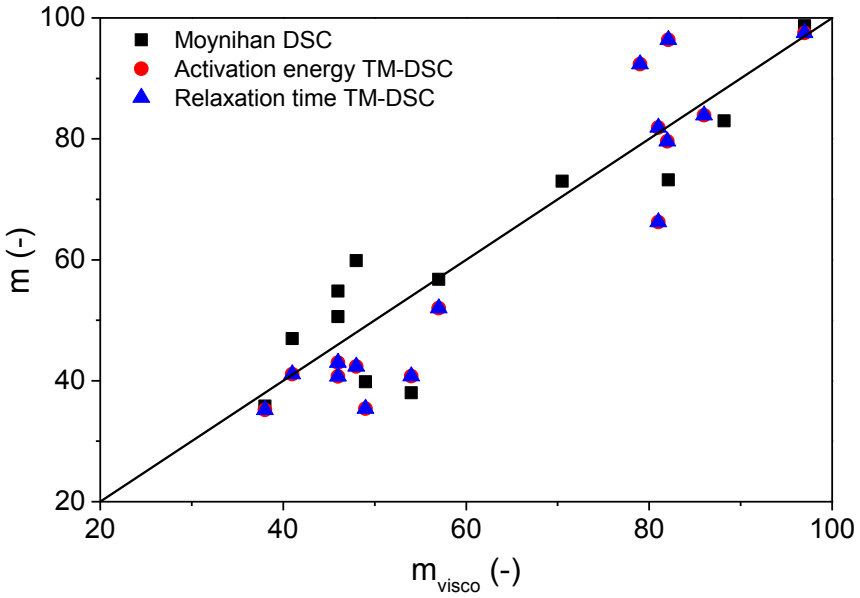

Figure 10. Fragility values (*m*) of tectosilicate calcium aluminosilicate glass series obtained by viscometric and calorimetric methods as a function of the SiO_2 content (see Table 1). The calorimetric fragilities have been corrected. The fragilities determined by the two TM-DSC methods are superimposed. The absolute values of the fragility probed by both DSC and TM-DSC approaches are both underestimated compared to the viscometric data. Note that *m* values obtained by TM-DSC exhibit smaller standard errors than those obtained by DSC. Viscometric data are taken from Ref. [29].

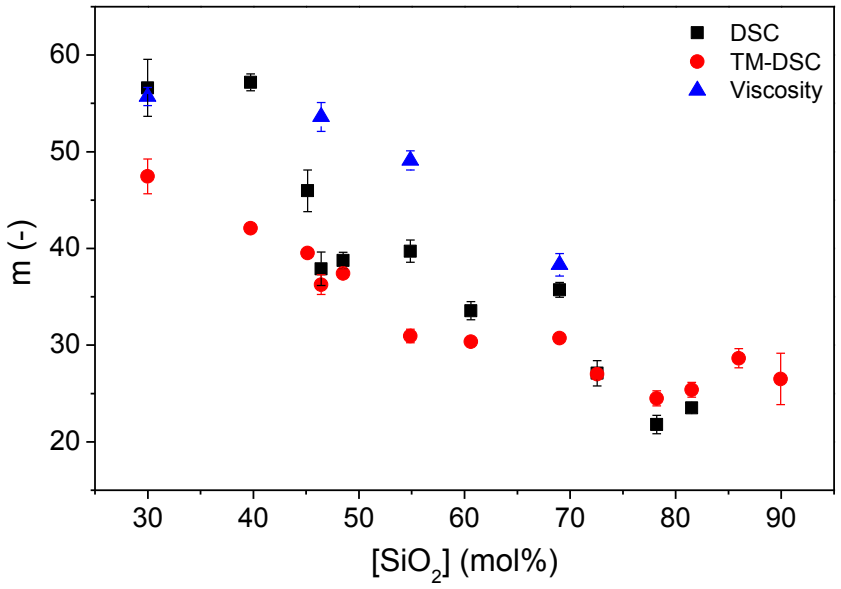

Paper VI

Journal of Non-Crystalline Solids 491 (2018) 64–70

Contents lists available at ScienceDirect

Journal of Non-Crystalline Solids

journal homepage: www.elsevier.com/locate/jnoncrysol

Time and humidity dependence of indentation cracking in aluminosilicate glasses

Tobias K. Bechgaard[a], John C. Mauro[b], Morten M. Smedskjaer[a,*]

[a] Department of Chemistry and Bioscience, Aalborg University, 9220 Aalborg, Denmark
[b] Department of Materials Science and Engineering, The Pennsylvania State University, University Park, PA 16802, USA

ARTICLE INFO

Keywords:
Oxide glass
Indentation
Crack initiation
Crack resistance
Environmental effect

ABSTRACT

The inherent brittleness and poor crack resistance of oxide glasses have always been among their main limitations for many advanced applications. As the formation of cracks leads to amplification of applied tensile stresses and ultimately catastrophic failure, there is an interest in understanding the compositional and structural dependence of crack initiation and growth. The resistance to cracking can conventionally be measured using instrumented indentation that mimics the real-life damage for certain applications. Wada introduced a method to evaluate the crack resistance by counting the number of initiated cracks as a function of the applied load. Experiments have shown that the environmental humidity and the time period between indentation and crack counting both affect the crack resistance value, but unfortunately these parameters are not always reported in literature studies. Here we perform a systematic study of the time and humidity dependence of crack initiation in calcium aluminosilicate glasses. Depending on the experimental conditions (time and humidity), the crack resistance of an aluminosilicate glass can vary by more than a factor of two. Furthermore, the observed radial/median cracks can initiate several hours after indentation. These results therefore indicate the need for a standardized procedure for determination of crack resistance to allow comparison of data from different research groups. We suggest including a sufficiently long waiting period (such as 24 h) between indentation and crack counting, as the majority of the crack initiation will then have occurred.

1. Introduction

Although they are among the manmade materials with the highest intrinsic strength [1], a major drawback of oxide glasses for many applications is their inherent brittleness [1–4]. The practical strength of glass is compromised by the presence of surface flaws, which act as stress intensifiers ultimately leading to brittle fracture since oxide glasses do not have a stable shearing mechanism to dissipate the stresses [5]. Glass scientists have attempted to decrease the risk of catastrophic failures through both compositional design and various post-treatments (e.g., thermal tempering, lamination, partial crystallization, and ion exchange) [6].

Sharp point contact is a primary failure mode for cover glasses in personal electronic devices. Since Vickers indentation can be used to replicate these failure conditions and due to its reproducibility and ease of sample preparation/measurement, it is a suitable method for evaluation of the cracking behavior of glasses for many industrial applications [7]. In Vickers indentation, a diamond pyramid with a defined pyramidal shape with the opposite faces having an angle of 136° is loaded onto the surface of a flat, polished sample. By measuring the size of the resulting indentation relative to the applied force on the sample, hardness can be obtained. The test can also be used to study the crack initiation and growth behavior of glass. Traditionally, the cracking behavior is quantified through the relationship between indentation load and crack initiation probability. The resistance to crack initiation is typically quantified using the approach of Wada et al. [8], in which crack resistance (CR) is taken as the indentation load which on average generates two radial/median cracks from the indent corners. CR can thus be viewed as a measure of the resistance to surface damage, but its determination is not straightforward. For example, indentation cracks are difficult to detect when they are located beneath the surface, aligned with the indentation edge, or too small to be observed using optical microscopy [9].

In addition to the indentation load, the chemical composition and any post-treatment of the glass [8,10] also affect the generation of cracks. Moreover, the experimental conditions, including indentation time [11,12], indenter tip geometry (including wear of the indenter tip) [13], and surrounding environment have a profound effect on the

* Corresponding author.
E-mail address: mos@bio.aau.dk (M.M. Smedskjaer).

https://doi.org/10.1016/j.jnoncrysol.2018.04.009
Received 5 February 2018; Received in revised form 20 March 2018; Accepted 2 April 2018
Available online 06 April 2018
0022-3093/

cracking behavior of glasses. For example, the “less-brittle” soda-lime-silica glass of Sehgal and Ito features a crack resistance of 3.5 kgf when measured in pure nitrogen atmosphere [14], but only 1.0 kgf when measured in air [15]. The origin of the relation between crack initiation and atmospheric humidity is not fully elucidated in literature, but the possible mechanisms responsible for water-assisted crack initiation could be related to a reaction between gaseous water and strained Si—O bonds in the indent [16,17]:

$$\equiv Si–O–S\equiv + H_2O \rightarrow 2\equiv SiOH$$

This is the idealized reaction for pure silica glass, but a similar hydrolysis reaction has been reported for Al—O bonds [16]. An introduction of modifiers such as alkali or alkaline-earth cations yields dangling bonds in the glass structure, which can facilitate a more rapid hydrolysis reaction. Moreover, the hydrolysis reaction rate is reported to increase when the glass is under compressive stress [18], probably due to the energetically unfavorable strained bonds. An alternative explanation relates to the entrance of water into the glass during indentation, resulting in a weakening of the glass structure [19–21], which has been reported, e.g., as reduced elastic moduli [18]. Water does not significantly enter most silicate glasses at room temperature due to a low diffusion rate; hence the proposal of a stress-assisted entry [19]. Water entry has been reported to be the cause of low crack resistance [17].

The influence of water vapor on other glass mechanical properties has been thoroughly described, including the influence of water vapor on crack propagation [3,22,23] and glass fatigue [2,4,24]. The influence of liquid water on crack initiation has also been reported [20], although most literature studies have investigated the effect of water on pre-existing cracks. Striepe et al. [24] showed that water vapor increases the crack initiation probability, with the largest change for dense glasses with lower fictive temperature. Despite the reported dependence of crack initiation on humidity, there is no standard testing procedure for determining CR in the literature. From a set of 32 papers on indentation crack resistance of oxide glasses [15,24,26–55], approximately half of the studies reported the atmospheric conditions or immersion medium, while the rest contained either no information about the humidity or merely stated that the experiment was conducted under “ambient conditions” (Fig. 1). However, this information is insufficient, since ambient conditions can cover relative humidity (RH) values down to ~30% in the winter and up to ~80% in the summer in our laboratory in northern Europe. Furthermore, Lawn et al. [25] investigated crack initiation for soda-lime silicate glasses as a function of contact time and atmospheric environment, observing delayed cracking up to 600 s after unloading of the indenter. That is, the time period between indent imprinting and crack counting also influences the determined crack resistance, as cracks can initiate over time, presumably due the kinetics of stress-corrosion hydrolysis.

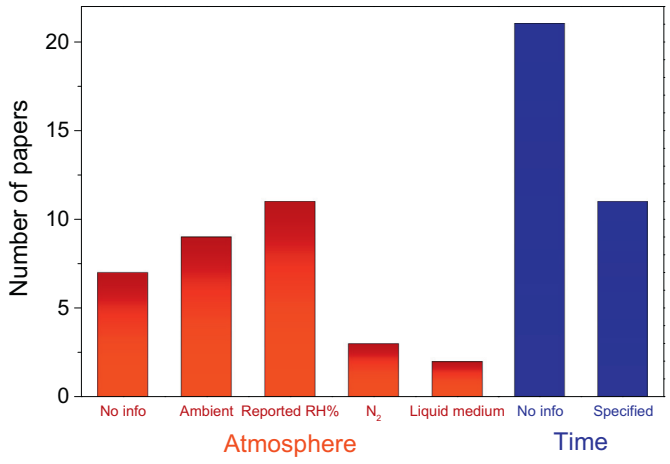

Fig. 1. Summary of the experimental conditions reported in literature studies used when determining crack resistance, including the atmospheric conditions and the time between indentation and counting of the number of cracks. Although not always adequately described, the atmospheric conditions are more often reported than the time between indentation and crack counting. The data have been obtained from Refs. [15, 24, 26–55]. The data were found among the papers referring to Wada's original work, using combinations of the keywords “crack”, “crack resistance”, and “crack initiation” for oxide glasses.

In the aforementioned set of 32 papers, approximately one third specify the period between indent imprinting and crack counting (Fig. 1), with no explicit reasoning given for the choice and inclusion of short waiting periods (< 30 s) to allow fast data collection or long waiting periods (24 h). To our knowledge, only the paper by Scannell et al. [36] has recently investigated the time dependence of crack initiation, as they reported that crack initiation ceased two hours after indentation for soda-titania-silicate glasses [36]. The dwell time during indentation, which is the time the indenter is held at maximum load, is 15 s in two-thirds of these 32 papers. Dwell time has been shown to affect glass hardness [11,12,20], but to the best of our knowledge, the relationship between crack initiation and dwell time has not been reported in the literature. No reason is given for the choice of dwell time in any of the 32 papers. We note that the recommended dwell time for Vickers hardness measurements is 10–15 s according to ASTM E384 [56], which could be the reason for the common use of 15 s dwell time in crack resistance measurements.

In this work, we investigate the combined humidity and time dependence of crack initiation to improve the understanding of stress-release and cracking behavior of oxide glasses and develop an experimental testing protocol for determining the crack resistance. We evaluate the time dependence by continuously monitoring the crack initiation for at least 6 h following indentation, enabling accurate determination of the time of crack initiation. As in most laboratories, the indenter instrument is not placed under a controlled atmosphere, and we therefore evaluate the humidity dependence of indentation cracking by performing the experiments during winter (relative humidity of 39 ± 8%) and summer (relative humidity of 70 ± 9%). The experiments are performed on two calcium aluminosilicate glasses (one tectosilicate and one peralkaline composition).

2. Experimental section

The synthesis of the tectosilicate $60.3SiO_2$–$19.7Al_2O_3$–19.6CaO and peralkaline $66.9SiO_2$–$12.3Al_2O_3$–20.3CaO (measured compositions, in mol%) glasses was done using the melt-quench procedure, as described in detail elsewhere [57]. The quenched glasses were cut and ground to an optical finish before being annealing for 30 min at their respective glass transition temperature T_g of 1092 and 1129 K, as previously reported in Ref. [57]. The glasses were named according to their nominal Al_2O_3 content, i.e., Al20 and Al12. Using an ultrasonic thickness gauge, Young's modulus and Poisson's ratio were determined to be 91 ± 1 GPa and 0.25 ± 0.01, respectively, for Al20 and 83 ± 2 GPa and 0.25 ± 0.01, respectively, for Al12.

The crack initiation probability was measured using a Vickers microindenter (Duramin 5, Struers A/S) in air at 22–24 °C. Only radial/median cracking from the corners of the indents was observed in these glasses. The indents were performed at loads of 0.49, 0.98, 1.96, 2.94, 4.91, and 9.81 N using a dwell time of 15 s. Images of the indents were collected using optical microscopy every 10 s for the first 2–3 h after the initial indentation and every 5 min for up to 6–8 h after indentation (Fig. 2). We set $t = 0$ at the end of the 15 s dwell time, when the indenter pyramid starts to unload. The first observation is made at $t = 15$ s, as this is the time needed for turning from indenter to camera mode on our instrument. The setup allows us to accurately determine the time at which indentation cracking occurs, as exemplified in Fig. 3. In this case, no cracks were visible immediately following unloading of the indenter, but after 343 s the first crack appears, followed by three

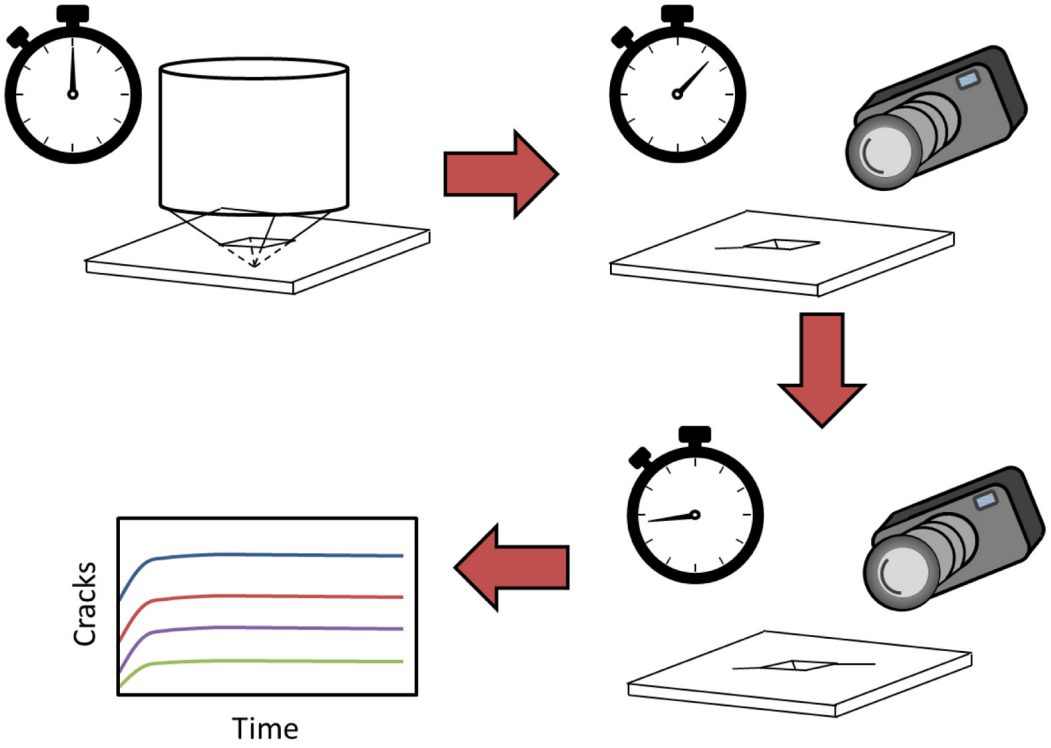

Fig. 2. Schematic of the experimental procedure for determination of the time (t) dependence of crack initiation. At time $t_0 = 0$, the indenter is unloaded after a 15 s dwell time, leaving the imprint exposed to the atmosphere. For $t > 0$, images of the imprint are continuously collected, allowing accurate determination of the time of each crack initiation. The data have been collected continuously for 6 h. After the experiment is finished, the data are averaged for a minimum of 20 indentations on the same glass and plotted as crack initiation probability vs. time.

additional cracks in the following 40 s. The relative humidity (RH) was recorded at the beginning of each experiment and the data were sorted into two groups: low (LRH) and high relative humidity (HRH) of 39 ± 8% and 70 ± 9%, respectively. The variation in RH during the experiments was recorded for a few cases. Generally, RH increases < 5% during the day of measurement, i.e., significantly less than the difference between the low and high RH groups.

3. Results and discussion

Crack initiation probability (CIP) was first determined immediately following the micro-indentation (~35 s) and then 24 h after the indentation for the two glasses. These data are shown in Fig. 4 by plotting the load dependence of CIP. CIP exhibits a pronounced dependence on the Al_2O_3 content in the glasses, with a higher Al_2O_3 content leading to a higher resistance to crack initiation, consistent with data reported in literature [44]. That is, the higher concentration of NBOs in the Al12 glass results in a network more prone to deform through shear flow than densification, decreasing the crack resistance. By comparing otherwise identical experiments obtained in environments with different humidity, we observe that CIP is sensitive to the atmospheric water vapor (Fig. 4), as CIP increases with increasing humidity for both Al12 and Al20. This increase is ascribed to a glass-water reaction water entering the glass [19,20]. The humidity-induced increase in CIP is dependent on a combination of the indentation load and number of cracks initiated at that load. For very low (< 1 N) and very high loads (> 5 N), the residual stress is either too low for crack initiation, or so high that most indent corners feature cracking, respectively. For the intermediate indentation loads most affected by humidity, CIP is > 20 percentage points higher under high-humidity conditions than under low-humidity conditions. Increased time between indentation and crack counting also increases CIP (Fig. 4). This phenomenon is in agreement with the delayed fracture reported by Lawn et al. [25]. We also observe that when residual stress triggers the initiation of one crack, more cracks initiate around the same indent subsequently as if the stress release results in a chain-initiation of cracks. An example of this is shown in Fig. 3, in which no cracks initiate within the first 343 s, where after four cracks appear within 50 s.

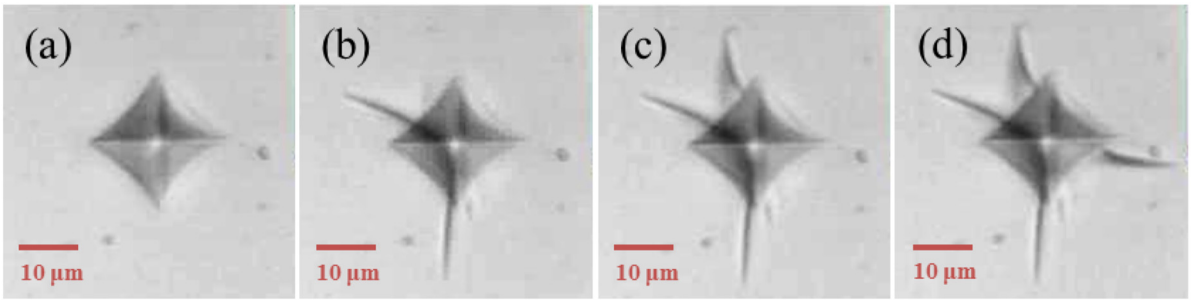

Fig. 3. Images of an indent at four different times after indentation, showing the time dependence of crack initiation for the Al20 glass using a load of 1.96 N with RH = 37.2%. The images show an indent (a) right after imprinting and after 343 s (identical), (b) after 353 s, (c) after 363 s, and (d) after 393 s.

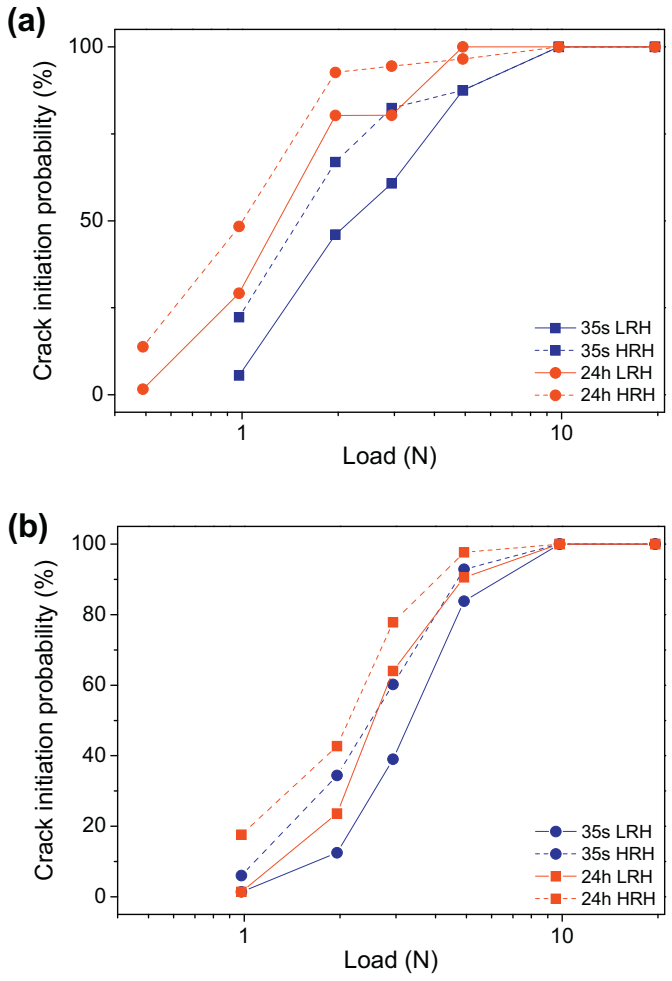

Fig. 4. Effect of varying the indentation load on the crack initiation probability for (a) Al12 and (b) Al20 for low relative humidity (LRH) (full line) and high relative humidity (HRH) (dashed line) conditions counted after 35 s (blue line) and 24 h (red line). (For interpretation of the references to colour in this figure legend, the reader is referred to the web version of this article.)

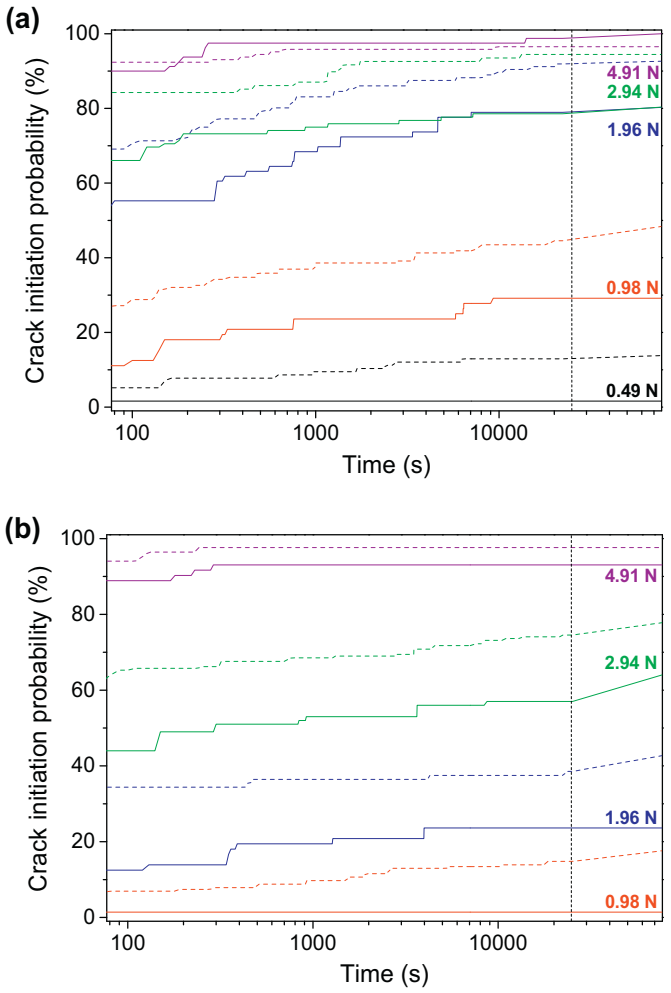

Fig. 5. Crack initiation probability over an extended time period at various loads and humidities for (a) Al12 and (b) Al20 glasses. The applied loads are 0.49 (black), 0.98 (red), 1.96 (blue), 2.94 (green), and 4.91 N (purple). The solid lines represent data obtained under low humidity conditions, while the dashed lines are obtained at high humidity conditions. The development in crack initiation probability between 22,200 and 76,500 s has been extrapolated. The vertical dashed lines represent the end of the continuous data collection. (For interpretation of the references to colour in this figure legend, the reader is referred to the web version of this article.)

Table 1
Crack resistance (CR) determined under low (LRH) and high relative humidity (HRH) conditions for Al12.5 and Al20 glasses. The cracks have been counted after both 35 s and 24 h. The error in CR is within ± 0.2 N.

	CR of Al12 (N)		CR of Al20 (N)	
	35 s	24 h	35 s	24 h
LRH	2.5	1.4	3.4	2.6
HRH	1.7	1.0	2.6	2.1

The crack resistance (CR) is often used to compare the resistance of glasses against radial/median crack formation in different glass compositions or after different post-treatments. Indeed, the two different compositions in this study exhibit different CR values, with Al20 being more resistant to crack initiation (Table 1). This compositional difference between Al12 and Al20 is the same as described above for the CIP data, as CR is determined from the CIP vs. load plot. However, the absolute value of CR is dependent on other factors besides chemical composition. For Al12, CR is 2.2 N in a low-humidity environment if the cracks are counted after 35 s, and decreases to 1.6 N under the more humid experimental conditions. The equivalent CR values for Al20 are 3.4 N and 2.6 N, respectively. By performing crack counting after 24 h, the difference between low and high humidity conditions is reduced, with CR values of 1.4 and 1.0 N, respectively, for Al12 and 2.6 and 2.1 N, respectively, for Al20. The time of crack counting influences the determined CR values, as the longer initiation period allows for the formation of more cracks, leading to substantially lower CR values. This time dependence of CR highlights the importance of using the same period between indentation and counting when comparing CR of different glasses.

To further study the time dependence of crack initiation, we have counted the number of cracks every 10 s for several hours. The time dependence of CIP is then plotted in Fig. 5a for Al12 and Fig. 5b for Al20 at different indentation loads and under both low and high relative humidity. We observe that crack initiation can occur for both glass compositions and both environments if the load is sufficiently high. For both samples and environments, the rate of crack initiation decreases with time. That is, the crack initiation rate (i.e., slope of CIP vs. time) is relatively high within the first ~300 s after the indentation, but a substantial number of cracks continue to initiate up to 3 h after indentation. While most of the long-term cracking has ceased after 2 h, in agreement with the findings of Scannell et al. [36], we observe that cracks continue to initiate for many hours, although the crack initiation

rate decreases with time. For a few experiments, we counted the cracks continuously for a 24 h period and observed crack initiation after > 19 h. The decreasing crack initiation rate with time is related to the stress release following initiation of cracks, leading to decreasing residual stress around indents with time.

As is evident from Fig. 4, the relative humidity affects the measured value of CIP immediately following indentation. We also observe that indentations performed under high humidity conditions lead to higher CIP values within the first 15 s compared to those under low humidity conditions (Fig. 5), which is due to the stress corrosion reactions [18]. However, for the high humidity experiments, the initiation of new cracks at the longest times is relatively small, presumably because the high initial CIP value leave fewer uncracked indent corners, from which cracks can initiate subsequently. For the low humidity experiments, the rate of crack initiation within the first few minutes is lower than at higher humidity, but the rate at longer times is larger. As such, the difference in CIP between the two humidity conditions decreases with increasing time, although a significant difference remains after 24 h (Fig. 5). To study this further, we revisited some of the indents made at different loads 1.5 year after the original indentations. The samples were stored in a plastic bag in our lab and exposed to varying humidity. An increase in crack initiation probability from 44% after 24 h to 47% after 1.5 years is observed, suggesting that the majority of crack initiation occurs within the first 24 h.

To further analyze the time-dependence of crack initiation, we next attempt to identify an equation to describe these kinetics. For example, a diffusion-controlled reaction should exhibit a square-root dependence on time. We thus attempted to fit the experimental in Fig. 5 using a variety of functional forms, including stretched exponential functions, power functions, etc. This also included treating the problem in terms of reactions kinetics with a reactant (e.g., environmental humidity) and product (probability of crack initiation) with varying "concentrations". The underlying physics governing the kinetics mechanism are probably highly complicated, involving the interplay between glass composition, load, humidity, time, etc. However, as an initial attempt to understand the time-dependence of crack initiation, we found the best fit (also considering that the number of adjustable parameters should be a small as possible) to be a power function of type

$$y = At^{-1/n}, \quad (1)$$

where y is the percentage of uncracked indent corners, t is time, and A and n are interrelated composition, humidity, and load dependent constants. A depends on the total concentration of initiated cracks, while n controls the time-dependent curvature of the crack-time dependence. We note that the model does not have the right limiting behavior at initial time as the crack initiation probability approaches infinity for $t \rightarrow 0$. However, the function reproduces both the steepness at short times as well as the time-dependence of cracking for a wide load range and for both compositions and humidity levels (Fig. 6a). Based on these quantitative descriptions of the time-dependence of crack initiation, we find that the A parameter systematically decreases with increasing load and humidity (Fig. 6b). A is also smaller for glass Al12 compared to Al20. These trends in A are in agreement with the qualitative assessment of the crack initiation data (Fig. 5). The n parameter describing the steepness of the curve is also load dependent, but its dependence on composition and humidity is not systematic (Fig. 6c). This may be because n and A are interrelated and a complex, convoluted function of load, humidity, and composition, or because the model does not accurately capture the discrete evolution of the data. Accordingly, the errors associated with the fitting parameters are relatively large. More work is thus needed to improve the fundamental understanding of crack initiation and its composition dependence.

The observed influence of both humidity and time of crack counting on crack initiation emphasizes the need for standardized protocols for determination of crack resistance. We therefore recommend that all measurements of crack resistance are performed under similar humidity conditions for internal comparison and that the average relative humidity is reported. Ideally, the measurements are performed in a closed environment with a controlled humidity such as a glovebox. Using a

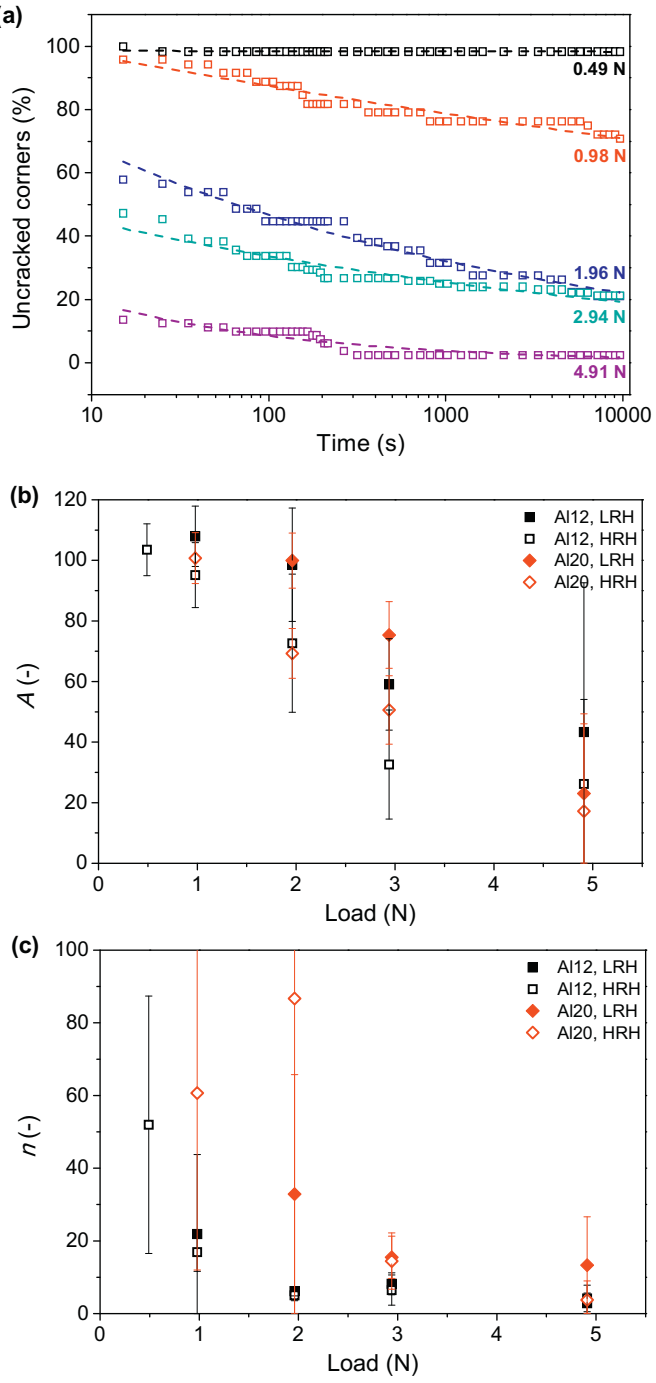

Fig. 6. (a) Time dependence of the number of uncracked indent corners for Al12 glass in low relative humidity conditions. The applied loads are 0.49 (black), 0.98 (red), 1.96 (blue), 2.94 (green), and 4.91 N (purple). The open symbols represent data acquired by the procedure shown in Fig. 2, while the dashed lines are the model fits to Eq. (1). The data used for fitting have been restricted to 49 data points within the first 10,000 s. The fits for other experimental conditions (relative humidity and glass composition) are similar. (b,c) Load dependence of the (b) A and (c) n fitting parameters in Eq. (1) used for the modeling the time dependence of the crack initiation data. We have omitted the A and n values for loads that do not create any cracks as their time-dependence cannot be captured by the model. (For interpretation of the references to colour in this figure legend, the reader is referred to the web version of this article.)

glovebox with nitrogen atmosphere would simplify the data comparison, but it would not simulate real-world cracking conditions where humidity is present. Our results also suggest that cracks should not be counted within the first 5 min, as small variations in the time between t_0 and the time of crack counting will result in an erroneous determination of crack initiation probability and crack resistance. It appears that 3 h is a more appropriate minimum waiting time between indentation and crack counting, but for practical purposes, a waiting period of 24 h might be the best option. In addition to time and humidity, the chemical composition of the glass also needs to be considered, as the reactivity between atmospheric water and glass greatly depends on the type of network former. Borate glasses tend to be rather hygroscopic, while the reactivity between aluminosilicate glasses and water is lower. The role of the chemical composition on the rate of crack initiation should be addressed when designing comparable experiments of glasses of different compositions. The present results indicate that to compare different chemical compositions accurately, cracks should be counted after a sufficiently long waiting period to allow the majority of crack initiation to have occurred, e.g., 24 h.

Finally, we note that the reported time-dependence of crack initiation may also be of importance for determination of frangibility. In a frangibility experiment, delayed failure is needed to isolate cracking due to the release of internally stored energy from impact induced cracking [58]. Typically, the specimen is observed for 60 s, but the present results show that cracks can initiate at much longer timescales. A revision of the experimental procedure for frangibility testing could thus also be needed.

4. Conclusions

The damage resistance of oxide glasses is often evaluated by measuring the crack resistance using Vickers micro indentation. Although the cracking behavior and the number of initiated crack is highly dependent on atmospheric water vapor and of the time between imprinting and crack counting, these experimental conditions are not always reported in literature studies. We have shown that the crack resistance decreases dramatically for two calcium aluminosilicate glasses when the experiments are performed under high-humidity rather than low-humidity conditions and when cracks are counted after 24 h compared to 35 s. Furthermore, we report quantitative data on the crack initiation rate obtained by continuous collection of images of indents for 6 h and find that most of the radial/median crack initiation ceases after 3 h, but with examples of crack initiation after > 19 h.

Acknowledgements

This work was partially funded by Corning Incorporated.

References

[1] L. Wondraczek, J.C. Mauro, J. Eckert, U. Kühn, J. Horbach, J. Deubener, T. Rouxel, Towards ultrastrong glasses, Adv. Mater. 23 (2011) 4578–4586, http://dx.doi.org/10.1002/adma.201102795.
[2] J.E. Ritter, C.L. Sherburne, Dynamic and static fatigue of silicate glasses, J. Am. Ceram. Soc. 54 (1971) 601–605, http://dx.doi.org/10.1017/CBO9781107415324.004.
[3] C.R. Kurkjian, P.K. Gupta, R.K. Brow, The strength of silicate glasses: what do we know, what do we need to know? Int. J. Appl. Glas. Sci. 1 (2010) 27–37, http://dx.doi.org/10.1111/j.2041-1294.2010.00005.x.
[4] S.M. Wiederhorn, L.H. Bolz, Stress corrosion and static fatigue of glass, J. Am. Soc. Ceram. 53 (1970) 543–548, http://dx.doi.org/10.1111/j.1151-2916.1970.tb15962.x.
[5] A.A. Griffith, The phenomena of rupture and flow in solid, Philos. Trans. R. Soc. Lond. Ser. A 221 (1921) 163–198.
[6] A.K. Varshneya, Fundamentals of Inorganic Glasses, Society of Glass Technology, Sheffield, 2011.
[7] J.J. Price, G.S. Glaesemann, D.A. Clark, T.M. Gross, K.L. Barefoot, A mechanics framework for ion-exchanged cover glass with a deep compression layer, SID Symp. Dig. Tech. Pap. 40 (2009) 1049–1051.
[8] M. Wada, H. Furukawa, K. Fujita, Crack resistance of glass on Vickers indentation, Proc. Int. Congr. Glas. 10th, 11 1974, pp. 39–46.
[9] T. Rouxel, S. Yoshida, The fracture toughness of inorganic glasses, J. Am. Ceram. Soc. 100 (2017) 4374–4396, http://dx.doi.org/10.1111/jace.15108.
[10] H. Ishikawa, N. Shinkai, Critical load for median crack initiation in Vickers indentation of glasses, J. Am. Ceram. Soc. 65 (1982) 124–127.
[11] J. Suwanprateeb, A comparison of different methods in determining load- and time-dependence of Vickers hardness in polymers, Polym. Test. 17 (1998) 495–506, http://dx.doi.org/10.1016/S0142-9418(97)00040-8.
[12] O. Yoldas, T. Akova, H. Uysal, Influence of different indentation load and dwell time on Knoop microhardness tests for composite materials, Polym. Test. 23 (2004) 343–346, http://dx.doi.org/10.1016/S0142-9418(03)00104-1.
[13] T.M. Gross, Deformation and cracking behavior of glasses indented with diamond tips of various sharpness, J. Non-Cryst. Solids 358 (2012) 3445–3452, http://dx.doi.org/10.1016/j.jnoncrysol.2012.01.052.
[14] J. Sehgal, S. Ito, A new low-brittleness glass in the soda–lime–silica glass family, J. Am. Ceram. Soc. 81 (1998) 2485–2488, http://dx.doi.org/10.1111/j.1151-2916.1998.tb02649.x.
[15] T.M. Gross, M. Tomozawa, A. Koike, A glass with high crack initiation load: role of fictive temperature-independent mechanical properties, J. Non-Cryst. Solids 355 (2009) 563–568, http://dx.doi.org/10.1016/j.jnoncrysol.2009.01.022.
[16] T.A. Michalske, S.W. Freiman, A molecular mechanism for stress corrosion in vitreous silica, J. Am. Ceram. Soc. 66 (1983) 284–288.
[17] T.M. Gross, M. Tomozawa, Crack-free high load Vickers indentation of silica glass, J. Non-Cryst. Solids 354 (2008) 5567–5569, http://dx.doi.org/10.1016/j.jnoncrysol.2008.09.015.
[18] M. Tomozawa, Stress corrosion reaction of silica glass and water, Phys. Chem. Glasses 39 (1998) 65–69.
[19] M. Tomozawa, W.-T. Han, W.A. Lanford, Water entry into silica glass during slow crack growth, J. Am. Ceram. Soc. 74 (1991) 2573–2576, http://dx.doi.org/10.1111/j.1151-2916.1991.tb06801.x.
[20] K. Hirao, M. Tomozawa, Microhardness of SiO2 glass in various environments, J. Am. Ceram. Soc. 70 (1987) 497–502.
[21] M. Tomozawa, K. Hirao, Diffusion of water into oxides during microhardness indentation, J. Mater. Sci. Lett. 6 (1987) 867–868, http://dx.doi.org/10.1007/BF01729041.
[22] S.M. Wiederhorn, Influence of water vapor on crack propagation in soda-lime glass, J. Am. Ceram. Soc. 50 (1967) 407–414.
[23] C. Gurney, Delayed fracture in glass, Proc. Phys. Soc. 59 (1947) 169.
[24] S. Striepe, J. Deubener, M.M. Smedskjaer, M. Potuzak, Environmental effects on fatigue of alkaline earth aluminosilicate glass with varying fictive temperature, J. Non-Cryst. Solids 379 (2013) 161–168, http://dx.doi.org/10.1016/j.jnoncrysol.2013.08.005.
[25] B.R. Lawn, T.P. Dabbs, C.J. Fairbanks, Kinetics of shear-activated indentation crack initiation in soda-lime glass, J. Mater. Sci. 18 (1983) 2785–2797, http://dx.doi.org/10.1007/BF00547596.
[26] I. Hasdemir, S. Striepe, J. Deubener, K. Simon, A 2000-year perspective on indentation crack resistance and brittleness of glass, J. Non-Cryst. Solids 408 (2015) 51–56, http://dx.doi.org/10.1016/j.jnoncrysol.2014.10.012.
[27] P. Sellappan, T. Rouxel, F. Celarie, E. Becker, P. Houizot, R. Conradt, Composition dependence of indentation deformation and indentation cracking in glass, Acta Mater. 61 (2013) 5949–5965, http://dx.doi.org/10.1016/j.actamat.2013.06.034.
[28] H. Morozumi, S. Yoshida, J. Matsuoka, Composition dependence of crack formation probability in aluminoborosilicate glass, J. Non-Cryst. Solids 444 (2016) 31–37, http://dx.doi.org/10.1016/j.jnoncrysol.2016.04.030.
[29] H. Morozumi, H. Nakano, S. Yoshida, J. Matsuoka, Crack initiation tendency of chemically strengthened glasses, Int. J. Appl. Glas. Sci. 6 (2015) 64–71, http://dx.doi.org/10.1111/ijag.12089.
[30] G.A. Rosales-Sosa, A. Masuno, Y. Higo, H. Inoue, Crack-resistant Al_2O_3–SiO_2 glasses, Sci. Rep. 6 (2016) 23620, , http://dx.doi.org/10.1038/srep23620.
[31] C. Hermansen, J. Matsuoka, S. Yoshida, H. Yamazaki, Y. Kato, Y. Yue, Densification and plastic deformation under microindentation in silicate glasses and the relation to hardness and crack resistance, J. Non-Cryst. Solids 364 (2013) 40–43.
[32] A. Koike, S. Akiba, T. Sakagami, K. Hayashi, S. Ito, Difference of cracking behavior due to Vickers indentation between physically and chemically tempered glasses, J. Non-Cryst. Solids 358 (2012) 3438–3444, http://dx.doi.org/10.1016/j.jnoncrysol.2012.02.020.
[33] Y. Kato, H. Yamazaki, Y. Kubo, S. Yoshida, J. Matsuoka, T. Akai, Effect of B_2O_3 content on crack initiation under Vickers indentation test, J. Ceram. Soc. Jpn. 118 (2010) 792–798, http://dx.doi.org/10.2109/jcersj2.118.792.
[34] Y. Kato, H. Yamazaki, S. Yoshida, J. Matsuoka, Effect of densification on crack initiation under Vickers indentation test, J. Non-Cryst. Solids 356 (2010) 1768–1773, http://dx.doi.org/10.1016/j.jnoncrysol.2010.07.015.
[35] S. Striepe, M.M. Smedskjaer, J. Deubener, U. Bauer, H. Behrens, M. Potuzak, R.E. Youngman, J.C. Mauro, Y. Yue, Elastic and micromechanical properties of isostatically compressed soda – lime – borate glasses, J. Non-Cryst. Solids 364 (2013) 44–52, http://dx.doi.org/10.1016/j.jnoncrysol.2013.01.009.
[36] G. Scannell, L. Huang, T. Rouxel, Elastic properties and indentation cracking behavior of Na_2O-TiO_2-SiO_2 glasses, J. Non-Cryst. Solids 429 (2015) 129–142.
[37] S. Yoshida, Y. Nishikubo, A. Konno, T. Sugawara, Y. Miura, J. Matsuoka, Fracture- and indentation-induced structural changes of sodium borosilicate glasses, Int. J. Appl. Glas. Sci. 3 (2012) 3–13, http://dx.doi.org/10.1111/j.2041-1294.2011.00077.x.
[38] M. Barlet, J.-M. Delaye, T. Charpentier, M. Gennisson, D. Bonamy, T. Rouxel, C.L. Rountree, Hardness and toughness of sodium borosilicate glasses via Vickers's indentations, J. Non-Cryst. Solids 417–418 (2015) 66–79, http://dx.doi.org/10.1016/j.jnoncrysol.2015.02.005.

[39] K.G. Aakermann, K. Januchta, J.A.L. Pedersen, M.N. Svenson, S.J. Rzoska, M. Bockowski, J.C. Mauro, M. Guerette, L. Huang, M.M. Smedskjaer, Indentation deformation mechanism of isostatically compressed mixed alkali aluminosilicate glasses, J. Non-Cryst. Solids 426 (2015) 175–183.
[40] R. Limbach, A. Winterstein-Beckmann, J. Dellith, D. Möncke, L. Wondraczek, Plasticity, crack initiation and defect resistance in alkali-borosilicate glasses: from normal to anomalous behavior, J. Non-Cryst. Solids 417 (2015) 15–27, http://dx.doi.org/10.1016/j.jnoncrysol.2015.02.019.
[41] S. Striepe, M. Potuzak, M.M. Smedskjaer, J. Deubener, Relaxation kinetics of the mechanical properties of an aluminosilicate glass, J. Non-Cryst. Solids 362 (2013) 40–46, http://dx.doi.org/10.1016/j.jnoncrysol.2012.11.017.
[42] G.D. Sorarù, M. Guglielmi, R. Dal Maschio, Influence of sol-gel coatings on crack initiation by vickers indentation in soda-lime glass, J. Non-Cryst. Solids 100 (1988) 440–446.
[43] M.N. Svenson, T.K. Bechgaard, S.D. Fuglsang, R.H. Pedersen, A.O. Tjell, M.B. Østergaard, R.E. Youngman, J.C. Mauro, S.J. Rzoska, M. Bockowski, M.M. Smedskjaer, Composition-structure-property relations of compressed borosilicate glasses, Phys. Rev. Appl. 2 (2014) 1–9, http://dx.doi.org/10.1103/PhysRevApplied.2.024006.
[44] A. Pönitzsch, M. Nofz, L. Wondraczek, J. Deubener, Bulk elastic properties, hardness and fatigue of calcium aluminosilicate glasses in the intermediate-silica range, J. Non-Cryst. Solids 434 (2016) 1–12.
[45] T.K. Bechgaard, A. Goel, R.E. Youngman, J.C. Mauro, S.J. Rzoska, M. Bockowski, L.R. Jensen, M.M. Smedskjaer, Structure and mechanical properties of compressed sodium aluminosilicate glasses: role of non-bridging oxygens, J. Non-Cryst. Solids 441 (2016) 49–57, http://dx.doi.org/10.1016/j.jnoncrysol.2016.03.011.
[46] K. Januchta, R.E. Youngman, A. Goel, M. Bauchy, S.J. Rzoska, M. Bockowski, M.M. Smedskjaer, Structural origin of high crack resistance in sodium aluminoborate glasses, J. Non-Cryst. Solids 460 (2017) 54–65, http://dx.doi.org/10.1016/j.jnoncrysol.2017.01.019.
[47] S. Yoshida, A. Hidaka, J. Matsuoka, Crack initiation behavior of sodium aluminosilicate glasses, J. Non-Cryst. Solids 344 (2004) 37–43, http://dx.doi.org/10.1016/j.jnoncrysol.2004.07.019.
[48] A. Talimian, V.M. Sglavo, Can annealing improve the chemical strengthening of thin borosilicate glass? J. Non-Cryst. Solids 465 (2017) 1–7, http://dx.doi.org/10.1016/j.jnoncrysol.2017.03.038.
[49] K. Januchta, R.E. Youngman, A. Goel, M. Bauchy, S.L. Logunov, S.J. Rzoska, M. Bockowski, L.R. Jensen, M.M. Smedskjaer, Discovery of ultra-crack-resistant oxide glasses with adaptive networks, Chem. Mater. 29 (2017) 5865–5876, http://dx.doi.org/10.1021/acs.chemmater.7b00921.
[50] S. Kapoor, N. Lönnroth, R.E. Youngman, S.J. Rzoska, M. Bockowski, L.R. Jensen, M.M. Smedskjaer, Pressure-driven structural depolymerization of zinc phosphate glass, J. Non-Cryst. Solids 469 (2017) 31–38, http://dx.doi.org/10.1016/j.jnoncrysol.2017.04.011.
[51] S. Kapoor, X. Guo, R.E. Youngman, C.L. Hogue, J.C. Mauro, S.J. Rzoska, M. Bockowski, L.R. Jensen, M.M. Smedskjaer, Network glasses under pressure: permanent densification in modifier-free Al_2O_3-B_2O_3-P_2O_5-SiO_2 systems, Phys. Rev. Appl. 7 (2017) 1–16, http://dx.doi.org/10.1103/PhysRevApplied.7.054011.
[52] S. Striepe, N. Da, J. Deubener, L. Wondraczek, Micromechanical properties of (Na,Zn)-sulfophosphate glasses, J. Non-Cryst. Solids 358 (2012) 1032–1037, http://dx.doi.org/10.1016/j.jnoncrysol.2012.01.045.
[53] G.A. Rosales-Sosa, A. Masuno, Y. Higo, H. Inoue, Y. Yanaba, T. Mizoguchi, T. Umada, K. Okamura, K. Kato, Y. Watanabe, High elastic moduli of a 54Al_2O3-46Ta2O5 glass fabricated via containerless processing, Sci. Rep. 5 (2015) 1–8, http://dx.doi.org/10.1038/srep15233.
[54] S. Sperimentale, Crack nucleation in ultrathin blown silicate glasses, J. Non-Cryst. Solids 80 (1986) 481–486.
[55] Y. Hayashi, Y. Fukuda, M. Kudo, Investigation on changes in surface composition of float glass—mechanisms and effects on the mechanical properties, Surf. Sci. 507 (2002) 872–876, http://dx.doi.org/10.1016/S0039-6028(02)01365-1.
[56] A. International, ASTM Standard, Standard Test Method for Knoop and Vickers Hardness of Materials, (2011).
[57] T.K. Bechgaard, J.C. Mauro, M. Bauchy, Y. Yue, L.A. Lamberson, L.R. Jensen, M.M. Smedskjaer, Fragility and configurational heat capacity of calcium aluminosilicate glass-forming liquids, J. Non-Cryst. Solids 461 (2017) 24–34, http://dx.doi.org/10.1016/j.jnoncrysol.2017.01.033.
[58] Z. Tang, Y.Z. Mauro, C. Gee, D.L.J. Duffy, T.E. Meyer, M.B. Abrams, K.A. Walker, J.C. Mauro, Methods for measurement and statistical analysis of the frangibility of strengthened glass, Front. Mater. 2 (2015) 1–8, http://dx.doi.org/10.3389/fmats.2015.00050.

Paper VII

Optical Materials 67 (2017) 155–161

Contents lists available at ScienceDirect

Optical Materials

journal homepage: www.elsevier.com/locate/optmat

Photoelastic response of permanently densified oxide glasses

Tobias K. Bechgaard [a], John C. Mauro [b], Lynn M. Thirion [b], Sylwester J. Rzoska [c], Michal Bockowski [c], Morten M. Smedskjaer [a, *]

[a] Department of Chemistry and Bioscience, Aalborg University, Aalborg, Denmark
[b] Science and Technology Division, Corning Incorporated, Corning, USA
[c] Institute of High-Pressure Physics, Polish Academy of Sciences, Warsaw, Poland

ARTICLE INFO

Article history:
Received 23 December 2016
Received in revised form
30 March 2017
Accepted 31 March 2017
Available online 8 April 2017

Keywords:
Photoelastic response
Stress optic coefficient
Hot compression
Densification
Oxide glass

ABSTRACT

The stress-induced birefringence (photoelastic response) in oxide glasses has important consequences for several applications, including glass for flat panel displays, chemically strengthened cover glass, and advanced optical glasses. While the effect of composition on the photoelastic response is relatively well documented, the effect of pressure has not been systematically studied. In this work, we evaluate the effect of hot isostatic compression on the photoelastic response of ten oxide glasses within two commonly used industrial glass families: aluminosilicates and boroaluminosilicates. Hot isostatic compression generally results in decreasing modifier-oxygen bond lengths and increasing network-former coordination numbers. These structural changes should lead to an increase in the stress optic coefficient (C) according to the model of Zwanziger et al., which can successfully predict the composition and structure dependence of C. However, in compressed glasses, we observe the opposite trend, viz., a decrease in the stress optic coefficient as a result of pressurization. We discuss this result based on measured changes in refractive index and elastic moduli within the context of atomic and lattice effects, building on the pioneering work of Mueller. We propose that the pressure-induced decrease in C is a result of changes in the shear modulus due to underlying topological changes in the glass network.

1. Introduction

Glasses are inherently isotropic due to their lack of long-range order. However, under a deviatoric stress the glass can exhibit an anisotropic response, including optical birefringence. The magnitude of this stress-induced birefringence can be quantified by the stress optic coefficient (C), which is the proportionality constant between birefringence and applied stress:

$$\delta = C\sigma l, \tag{1}$$

where δ is the difference in the optical path length for light polarization along the stress axis and the orthogonal direction, σ is the applied uniaxial stress, and l is the sample thickness. When the uniaxial stress is applied to the glass, it changes its dielectric response in both the stress direction and in the orthogonal direction. The resulting birefringence is proportional to this difference.

For advanced optical applications, small amounts of birefringence can be a serious problem [1–4]. Typically standard network formers (e.g., SiO_2, B_2O_3, and P_2O_5) lead to a large positive birefringence (thus large positive C value), while traditional network modifiers (e.g., Na_2O and CaO) act to decrease the birefringence only slightly, leading to positive birefringence for standard oxide glass compositions. To obtain zero-stress optic glasses, the positive birefringence originating from the typical glass formers has traditionally been counterbalanced by the addition of PbO, which affects the birefringence negatively [5–7]. However, recent health and environmental regulations that aim at reducing the usage of lead due to its toxicity have necessitated research in the compositional and structural origins of the photoelastic response [2,8,9]. This research has led to the development of new lead-free glass compositions, exhibiting zero-stress optic response when strained anisotropically [2,7,9–13].

In the 1930s, Mueller proposed that the stress optic response of a material arises from lattice distortions and atomic polarizability [14,15]. Building on Mueller's concepts, Zwanziger and co-workers [2] proposed an empirical model to predict the birefringence in oxide glasses from the ratio between the cation-anion bond length (d) and the cation coordination number (N_c) of the glass

* Corresponding author.
E-mail address: mos@bio.aau.dk (M.M. Smedskjaer).

http://dx.doi.org/10.1016/j.optmat.2017.03.060
0925-3467/

components. Based on the available literature data, they discovered that a d/N_c ratio of approximately 0.5 Å leads to a zero-stress glass, while negative and positive birefringence occurs when the ratio is above and below 0.5 Å, respectively. Mathematically, the empirical condition for $C = 0$ is

$$\sum_i x_i \left(\frac{d}{N_c}\right) \approx 0.5\text{Å}, \quad (2)$$

where the sum is over all the components i in the glass, and x_i is their respective mole fraction.

In their initial work, Zwanziger and co-workers used bond lengths and coordination numbers from crystallographic data, resulting in good qualitative agreement between model and data [2]. Later studies have supported their original findings by using more accurate bond lengths and coordination numbers in the actual glasses based on simulations [16,17] and experimental structural probes such as Mössbauer spectroscopy [17], nuclear magnetic resonance spectroscopy [7,8,17], Raman spectroscopy [9,18], extended X-ray absorption fine structure [18], and X-ray diffraction [7]. These findings support the original approach for estimating the stress optic response of oxide glasses, but they also show that detailed structural information is required to enable accurate predictions of the composition dependence of C.

The importance of d and N_c in controlling the stress optic response originates from their effect on the elastic response of a glass subjected to anisotropic stress. The bond length correlates positively with bond metallicity [19]. A more metallic bond is less directional and is thus free to be distorted in both the direction of the anisotropic stress and in the orthogonal direction. The coordination number also affects the deformation mechanism. Structural units with high coordination numbers tend to be distorted isotropically, whereas structural units with low coordination numbers are more susceptible to anisotropic distortion. Accordingly, glasses with tailored stress response can be produced by balancing the distortion mechanisms through glass composition design.

To further clarify the structural and topological origins of the photoelastic response of oxide glasses, here we investigate the effect of hot compression at 1 GPa on C in two families of industrial oxide glasses, covering a range of aluminosilicate and boroaluminosilicate compositions. Compression is performed at high pressure-high temperature conditions (typically near the ambient T_g), enabling permanent and isostatic densification at modest pressure (~1 GPa) of bulk samples (cm^3). Due to the high viscosity of the glass at ambient conditions, the glass structure is captured permanently in the densified state as a result of the pressure-quench [20]. This, in turn, enables *ex situ* measurements of pressure-induced changes in mechanical and optical properties [21]. Although the dependence of the photoelastic effect on density and pressure has previously been discussed to some extent [22,23], this study will clarify the role of permanent network densification and pressure-induced structural transformations on photoelasticity. This is because the hot compression method is known to induce permanent changes in oxide glass structures, including modifier-oxygen bond lengths and cation coordination numbers [24]. As such, this approach enables us to test the underlying assumptions of the Zwanziger model (Eq. (2)), i.e., whether the effects of bond length and coordination number on C are indeed causal relations. Furthermore, we compare the pressure-induced changes in C with the changes in elastic moduli, since a recent study showed that the resistance of a material to elastic shear deformation is related to birefringence [25]. For this work, we choose ten different glass compositions with significantly different initial C values (from 1.86 to 6.22 nm MPa^{-1} cm^{-1}, see Table 1) in the borosilicate and aluminosilicate families, as these glasses are known to exhibit different but well-understood structural responses to hot isostatic compression [21,26–29]. For example, hot compression at 1 GPa can result in pronounced structural changes in borosilicate glasses (e.g., $B^{III} \rightarrow B^{IV}$) [28], while the structural changes in aluminosilicate glasses (e.g., $Al^{IV} \rightarrow Al^{V}$) are more modest at this pressure range [26].

2. Experimental section

The total of 10 different silicate glasses (Table 1) were prepared by mixing the appropriate amounts of raw materials, then melting the mixtures overnight in a covered Pt crucible in air at 1650 °C, and finally quenching the melts on metal plates. The glass transition temperatures (T_g) of the glasses were determined by beam bending viscometry, and the glasses were annealed for 30 min at their respective T_g. After thermal annealing, all glasses were subjected to hot isostatic compression (see Ref. [21] for details) at 1 GPa for 30 min at the ambient pressure T_g value, which was well above the structural relaxation time at this temperature. The samples were compressed in a nitrogen gas pressure chamber, which contains a multizone cylindrical furnace. Following the 30-min compression at T_g, the system was first cooled and then decompressed at around 60 K min^{-1} and 30 MPa min^{-1}, respectively.

The Archimedes buoyancy principle was used for determination of glass density ρ of both annealed and compressed samples. Ethanol was used as the immersion liquid and each sample was weighed ten times in both air and ethanol. From the density data, we calculated the plastic compressibility (β) and the molar volume (V_M) as

Table 1
Sample code and oxide components, glass transition temperature (T_g), plastic compressibility (β), density (ρ), stress optic coefficient (C), refractive index (n), shear modulus (G), and Young's modulus (E) of the glasses in this study. The errors associated with the measured values are ±0.003 GPa for β, ±0.002 g cm^{-3} for ρ, <1% for C, ±0.0001 for n, and <1% for G and E.

Glass ID	Oxide components	T_g (K)	β (GPa^{-1})	ρ (g cm^{-3})		C (nm MPa^{-1} cm^{-1})		n (–)		G (GPa)		E (GPa)	
				ambient	1 GPa	ambient	1 GPa	ambient	1 GPa	ambient	1 GPa	ambient	1 GPa
SAP1	SiO_2, Al_2O_3, P_2O_5, Na_2O, ZnO	935	0.023	2.519	2.578	3.22	3.07	1.505	1.517	27.4	29.6	66.8	72.8
SAP2	SiO_2, Al_2O_3, P_2O_5, Na_2O, ZnO	858	0.020	2.571	2.623	3.17	3.03	1.514	1.526	28.2	29.6	68.9	72.8
SAB1	SiO_2, Al_2O_3, B_2O_3, CaO	827	0.064	2.190	2.340	4.88	3.90	1.480	1.512	20.9	26.0	51.6	64.4
SAB2	SiO_2, Al_2O_3, B_2O_3, CaO	891	0.066	2.223	2.381	4.66	3.73	1.490	1.522	22.1	27.6	54.6	68.2
SAB3	SiO_2, Al_2O_3, B_2O_3, CaO	921	0.070	2.218	2.386	4.45	3.78	1.490	1.520	22.5	27.2	54.7	65.8
SABP1	SiO_2, Al_2O_3, B_2O_3, P_2O_5	903	0.057	2.203	2.337	4.43	3.82	1.473	1.500	23.0	27.6	55.4	66.7
SAB4	SiO_2, Al_2O_3, B_2O_3	746	0.070	2.119	2.280	5.28	4.14	1.477	1.511	19.1	24.9	47.4	61.4
SABP2	SiO_2, Al_2O_3, B_2O_3, P_2O_5	703	0.066	2.073	2.219	6.22	4.90	1.462	1.494	15.3	19.7	37.1	47.8
SA1	SiO_2, Al_2O_3, MgO, CaO	1088	0.008	2.918	2.941	1.86	1.81	1.664	1.670	42.1	42.7	107.1	109.1
SA2	SiO_2, Al_2O_3, MgO, CaO	1097	0.012	2.907	2.941	1.86	1.80	1.653	1.659	41.2	42.0	105.4	107.5

$$\beta = -\frac{1}{V_0}\frac{\Delta V}{\Delta P}, \quad (3)$$

$$V_M = \frac{1}{\rho}\sum_i x_i M_i, \quad (4)$$

where V_0 is the sample volume before compression, $\Delta V/\Delta P$ is the change in volume as a response to the change in pressure, and x_i and M_i are the mole fraction and molar mass of oxide i, respectively. The plastic compressibility quantifies the permanent relative change in volume as a response to pressure. Consequently, the elastic component of the compression is not considered, as the density measurements are performed *ex situ* following cooling and decompression.

Shear modulus (G) and Young's modulus (E) were determined using resonant ultrasound spectroscopy for all glasses. Glass samples of about 10 × 8 × 6 mm^3 with polished surfaces were used to gather resonance spectra from 100 to 300 kHz. For each sample, the first five resonant peaks in the frequency domain resulting from excited resonant eigenmodes were used to calculate the elastic moduli. The errors of the reported elastic moduli do not exceed ±1%. Refractive index n of the pre- and post-compressed glasses was measured at the sodium D-line (589.3 nm) using prism coupling refractometry on optically polished samples.

The stress optic coefficient for each glass was determined by a diametral compression method. Two cylindrical samples (diameter: 12.7 mm; height: 7 mm) with parallel faces and an optical finish were prepared for each glass composition. Each sample was then loaded under diametral compression to ~55 kg force and an interference figure was viewed through crossed polarizers using a polarized light microscope at 546 nm (using a green filter with 10 nm bandwidth). The interference figure, or Maltese cross, was visually centered, and retardation measurements were made using a calcite magnesium prism containing Berek compensator. The stress optic coefficient was subsequently calculated using Eq. (1). The average of two samples was recorded as the measured value of C for each composition. The difference in measured C values between the two samples was always less than 0.5%.

3. Results

Table 1 compiles the measured glass transition temperature (T_g), density (ρ), plastic compressibility (β), stress optic coefficient (C), refractive index (n), shear modulus (G), and Young's modulus (E) data for all pre- and post-compressed samples.

The ten glasses densify to different extents upon 1 GPa compression at T_g, thus resulting in different plastic compressibility values ranging from 0.008 to 0.070 GPa^{-1}. Initial density and molar volume values are plotted as a function of plastic compressibility in Fig. 1. Plastic compressibility (i.e., magnitude of the volume densification) scales approximately linearly with the initial density and the initial molar volume. That is, glasses with a high initial density and a low initial molar volume show larger resistance to compaction when compressed isostatically at high temperatures, while glasses with low densities and high molar volumes generally show less resistance towards compaction.

Upon hot compression, all the glasses permanently densify and thus exhibit increased values of elastic moduli and refractive index, while the stress optic coefficient is always found to decrease as a result of compression (Table 1). The extents of these changes in mechanical and optical properties depend on the glass composition. Fig. 2 shows the dependence of the initial C values of the annealed (pre-compressed) glasses and the pressure-induced

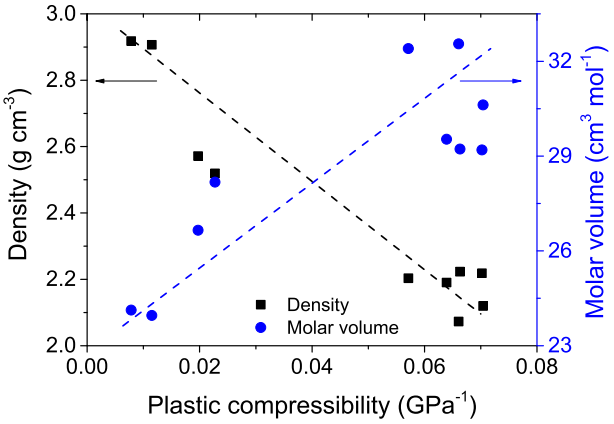

Fig. 1. Dependence of density (black squares) and molar volume (blue circles) of the annealed (not-compressed) glasses on the plastic compressibility (Eq. (3)). The errors in density and molar volume are smaller than the size of the symbols. Dashed lines are guides for the eye. (For interpretation of the references to colour in this figure legend, the reader is referred to the web version of this article.)

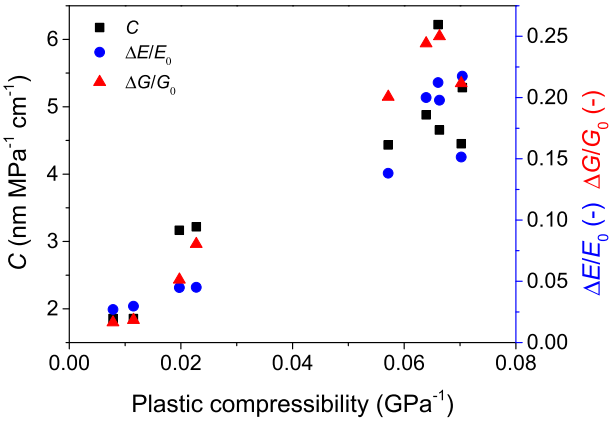

Fig. 2. Stress optic coefficient (C) of the annealed (not-compressed) glasses (black squares) and the pressure-induced relative changes in Young's ($\Delta E/E_0$) (blue circles) and shear moduli ($\Delta G/G_0$) (red triangles) as a function of the plastic compressibility (Eq. (3)). (For interpretation of the references to colour in this figure legend, the reader is referred to the web version of this article.)

relative changes in Young's ($\Delta E/E_0$) and shear moduli ($\Delta G/G_0$) on the plastic compressibility. The observed positive correlation among these properties indicates that the ability of an oxide glass to deform and its photoelastic response may be intimately connected. Fig. 3 shows an approximately linear relationship between the pressure-induced change in stress optic coefficient ($\Delta C/C_0$) and those of Young's ($\Delta E/E_0$) and shear moduli ($\Delta G/G_0$), pointing to potentially common structural and topological origins of the elastic and photoelastic properties.

4. Discussion

4.1. Apparent mismatch between data and Zwanziger model

The Zwanziger et al. model of Eq. (2) can be used to predict the composition dependence of the stress optic coefficient (C) [2,7–13,16–18]. If the average cation-oxygen bond length decreases and/or the average coordination number increases, it results in a more positive value of C. Based on previous work in the literature, hot isostatic compression of oxide glasses generally results in decreasing modifier-oxygen bond lengths and increasing network-

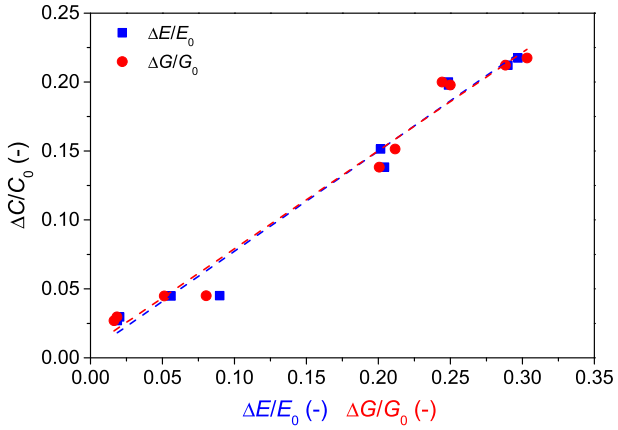

Fig. 3. Relationship between pressure-induced relative change in stress optic coefficient ($\Delta C/C_0$) and the pressure-induced relative changes in both Young's ($\Delta E/E_0$) (blue squares) and shear ($\Delta G/G_0$) moduli (red circles). R^2 values for both linear fits (dashed lines) are 0.98. (For interpretation of the references to colour in this figure legend, the reader is referred to the web version of this article.)

former coordination numbers. That is, in pressure/temperature conditions similar to the ones applied in this study, increases in boron [27–29] and aluminum [24,26,30,31] coordination numbers have been reported. The extent of the conversions of B^{III} to B^{IV} and of Al^{IV} to Al^{V} or Al^{VI} have been found to depend on the non-bridging oxygen (NBO) content through the equilibria $B^{III} + NBO \rightleftharpoons B^{IV}$ [24,32] and $Al^{IV} + NBO \rightleftharpoons Al^{V}$ [26,30]. For the network modifiers, no pressure-induced changes in coordination numbers are expected. For example, hot compression has been found not to affect the Na coordination using ^{23}Na nuclear magnetic resonance spectroscopy [29].

The cation-anion bond lengths are expected to change during hot compression. Decreasing bond lengths have been reported for both alkali (Na–O bonds [24,27,29,33]) and alkaline earth [31] oxides, while the reported pressure-induced increases in coordination numbers of the network-forming cations [24,26,30,32] should increase the bond length of the newly formed higher-coordinated species to accommodate them in the coordination sphere. For example, increases in Si–O and Al–O bond lengths have been reported for glasses quenched at 6–10 GPa [30], but considering the large pressure-induced decrease in volumes (defined as the plastic compressibility, see Table 1), we expect an overall decrease in the average bond length in all glasses under investigation.

Based on the pressure-induced structural changes discussed above, we would expect an increase in C when the glasses are compressed according to Eq. (2). That is, the decrease in the modifier cation-oxygen bond length and the increase in network-former coordination number should result in a decrease in the sum of the ratio between average bond length and average coordination number, which in turn should lead to an increase in C. However, we observe the opposite trend, viz., a pronounced decrease in C for all ten glass compositions as a result of compression (Table 1). This suggests that other factors besides d and N_c are important when considering the pressure dependence of C. Since the applied pressure is relatively small, it is possible that the changes in d and N_c are also relatively small. However, even if this is the case, our conclusion that C is governed by other factors beyond d and N_c remains the same due to the large pressure-induced change in C (up to 22%). Indeed, the data in Figs. 2 and 3 suggest that the pressure-induced decrease in C is related to the overall network densification rather than specific structural changes. We should thus also note that the results in this study suggest that it is possible to tailor the value of C of bulk glasses not only through composition design, but also through compression. This could enable the design of glasses with pressure-tailored photoelastic response from a wider compositional range, possibly also including new zero-stress oxide glasses through proper composition design and pressure treatment.

4.2. Understanding photoelasticity from lattice and atomic effects

To understand the apparent mismatch between our data and Eq. (2), we consider the work of Mueller [14,15] and Matusita et al. [34,35]. In this seminal work on photoelasticity, Mueller conjectured that birefringence in glasses and crystals is a result of two factors, which he termed the lattice effect and the atomic effect. Both effects contribute to the photoelastic response of a material and depend on its structure and composition. The lattice effect describes the change in atomic positions as a response to stress and can most easily be explained using a crystal lattice due to the simpler ordered structure. In the direction of the stress, the lattice planes will move closer together, whereas the lattice planes normal to the stress direction will maintain the same separation distance in an ideal crystal. The atomic effect describes the distortion of the electronic structure around every atom in the material as a response to stress; this is controlled by the polarizability. The sum of the atomic and lattice effects describes the strain-optical properties of a material through the Pockels strain optical coefficients.

The atomic effect is the cause of positive birefringence, whereas the lattice effect is the cause of negative birefringence [14]. As such, understanding these effects is of great importance for compositional studies of photoelastic properties since the lattice effect is highly influenced by composition, whereas the atomic effect is fairly independent of composition for oxide glasses, as it mostly depends on the type of anion present in the material [34,35]. Based on experimental data, the atomic and lattice effects can be extracted from the relation [34–36],

$$p_{12} - p_{11} = \frac{4\pi(n^2+2)^2}{9n^4}\sum_j N_j\left(a_{11}^{ij} - a_{12}^{ij}\right) - \frac{2(n^2-1)^2}{5n^4}, \qquad (5)$$

where p_{12} and p_{11} are the Pockels strain-optical coefficients, n is the refractive index, N_j is the concentration of the j-ion, and a_{11}^{ij} and a_{12}^{ij} are the elements of the nonlinear polarizability. The first term on the right-hand side of Eq. (5) represents the atomic effect, while the second term represents the lattice effect. Using the calculated $p_{12} - p_{11}$ values (see further explanation below and Table 2) and the experimentally determined refractive indices (Table 1), we are able to determine the effect of hot compression on the lattice and atomic effects (Fig. 4). The atomic effect is essentially unaffected by compression, while a minor pressure-induced change is observed for the lattice effect, probably due to the atoms in the compressed

Table 2
Strain-optical coefficients ($p_{12} - p_{11}$) determined using Eq. (6) and data in Table 1.

Glass ID	$(p_{12} - p_{11})$	
	ambient	1 GPa
SAP1	0.1035	0.1044
SAP2	0.1029	0.1009
SAB1	0.1257	0.1175
SAB2	0.1241	0.1169
SAB3	0.1211	0.1172
SABP1	0.1278	0.1252
SAB4	0.1253	0.1193
SABP2	0.1219	0.1158
SA1	0.0678	0.0663
SA2	0.0667	0.0662

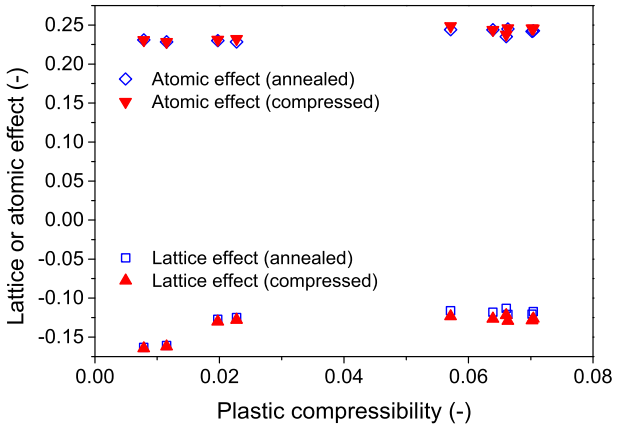

Fig. 4. Contributions to the strain-optic coefficient from the lattice and atomic effects for as-prepared and compressed glasses as a function of the plastic compressibility. The two effects are calculated from Eq. (5) using the experimentally determined stress optic coefficient and refractive index values from Table 1.

glasses being in closer proximity to each other. However, the overall effect of permanent densification on the strain-optical properties of the glasses is negligible.

When predicting C from structural data using the Zwanziger model, the aim is to obtain zero-stress glasses by balancing bond lengths and average coordination number. It can be shown from literature data for a lead borate glass that the condition d/N_c ~0.5 Å is fulfilled when $(p_{12} - p_{11}) = 0$ [7,35], i.e., when the atomic and lattice effects have been balanced to achieve a glass without a photoelastic response (Fig. 5), in agreement with recent work on the elasto-optic coefficients of borate, phosphate, and silicate glasses [37]. Actually $(p_{12} - p_{11})$ is found to be equal to 0 slightly above 0.5 (≈0.52), as predicted from the positive stress optic response of TeO_2 with $d/N_c = 0.5$ Å [2]. As the permanent densification does not result in significant changes in $(p_{12} - p_{11})$, the pressure-induced decrease in C must be caused by changes in other factors that affect the photoelastic response.

4.3. Relation with elastic moduli and refractive index

The measured values of plastic compressibility and elastic moduli of the glasses are closely related to their chemical compositions. In general, glasses consisting solely of network formers, such as pure SiO_2 glass, will have a high molar volume due to the large free volume in the structure, whereas glasses containing large amounts of modifiers will have a low molar volume as they obtain a more close-packed structure as the modifiers occupy interstitial sites between the network formers, decreasing the free volume. This relationship among composition, free volume, and molar volume affects the properties of the glasses. We observe that the annealed (pre-compressed) glasses with large molar volumes exhibit low E and G values (Table 1), as their open structures exhibit a large elastic response compared to glasses with low molar volumes. The latter glasses exhibit larger values of E and G due to their compact structures, which are more resistant to elastic deformations.

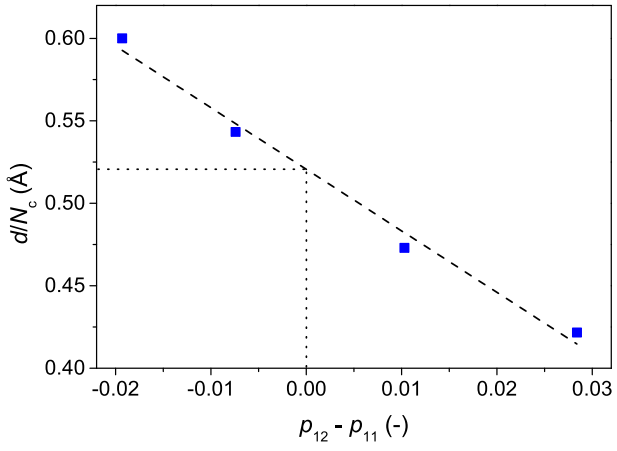

Fig. 5. Relationship between d/N_c from the Zwanziger et al. model (Eq. (2)) and the Pockels strain optical coefficient $(p_{12} - p_{11})$. Data are taken for lead borate glasses from Refs. [7] and [35]. Here $(p_{12} - p_{11})$ is equal to 0 when $d/N_c = 0.52$ Å, which is in agreement with the prediction of zero-stress glasses having a d/N_c slightly higher than 0.5 [2].

Since the pressure dependence of C is not a result of changing strain-optical coefficients, we next discuss whether the photoelastic response and the response to hot compression have similar origins, even though the former is an elastic response and the latter is a plastic response. Both experiments involve a strain of the glass structure, with the magnitude of the strain depending on the flexibility of the glass. For glasses with large elastic moduli, both plastic compressibility (i.e., permanent densification as a result of hot compression) and the photoelastic response are found to be small, while these values are larger for glasses with lower elastic moduli (Table 1). This can also be seen by the larger pressure-induced changes in the elastic moduli for the high-molar volume glasses. Moreover, the magnitude of C can be related to the plastic compressibility and the elastic moduli of the glasses (Fig. 2). The glasses with larger elastic moduli and low plastic compressibility exhibit larger resistance to deformation, resulting in a small deformation under stress and thereby a low C value and vice versa for glasses with low elastic moduli and high plastic compressibility. In compressed glasses, the free volume has decreased, resulting in a smaller response to stress, in turn yielding a decrease in C for all compositions upon hot compression.

C is directly connected to shear modulus (G) through the relation [38],

$$C = \frac{n^3}{4G}(p_{12} - p_{11}). \quad (6)$$

As such, a complicated relationship between C and G could be explained by large changes in $(p_{12} - p_{11})$ among different compositions and thus by structural features, especially influenced by modifiers and non-bridging oxygens [34]. However, for the glasses in the current study, we observe a simple linear relationship between C and G (Fig. 6), i.e., the relatively small pressure-induced changes in n (Table 1) and $(p_{12} - p_{11})$ (Table 2) result in an approximate proportionality between C and G. Considering only the glasses with a G value below 30 GPa, we find that C and G are linearly related ($R^2 = 0.997$). However, the two glasses with larger G values do no follow this linear trend. This could be ascribed to the high modifier content (>50 mol%) in these glasses, which increases the lattice effect as evident from Fig. 4, thereby illustrating the crucial importance of composition in the design of zero-stress glass compositions.

The small pressure-induced changes in n (<2.2%) is in agreement with literature data of other hot compressed oxide glasses [29]. Compared to the small pressure-induced change in $(p_{12} - p_{11})$ observed here (<4.6%), Matusita et al. [34,35] observed larger changes in $(p_{12} - p_{11})$ due to compositional and structural changes (up to 43%), e.g., when substituting a modifier for glass former. As such, changing the chemical composition of the glasses introduces a large change in the electron clouds in the glasses, thus modifying

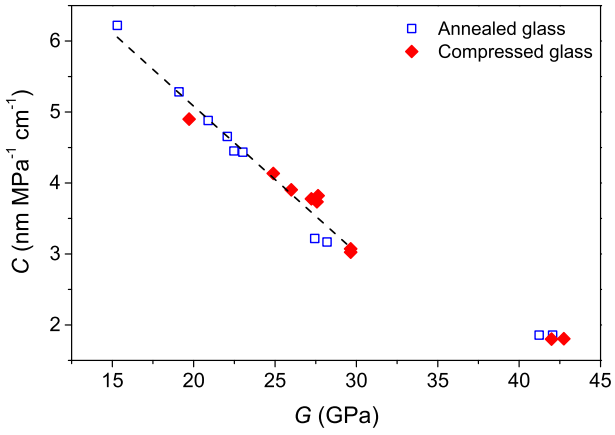

Fig. 6. Dependence of the stress optic coefficient (C) on the shear modulus (G) for annealed (not-compressed) and compressed glasses. The dashed line ($R^2 = 0.997$) represent the linear dependence of C on G when the pressure-induced change in Pockels strain-optical coefficients is negligible, which is not the cause for glasses with high modifier content (SA1 and SA2 in Table 1).

the value of $(p_{12} - p_{11})$. In the present study, the change in $(p_{12} - p_{11})$ originates from distortions of electron clouds induced by compression, which are rather small compared to the compositional effects (Fig. 4 and Table 2). Therefore, the only major property change on the right-hand side of Eq. (5) is in the shear modulus.

Based on the above, we infer that the pressure-induced decrease in C is primarily governed by the increase in shear modulus according to Eq. (6), which in turn is proportional to the plastic compressibility (Fig. 1). This suggests that the extent of the pressure-induced decrease in C is governed by—and can be predicted by—the extent of volume densification of the glass. Furthermore, from the considerations of the effect of densification on $(p_{12} - p_{11})$, we are able to compare the prediction of C from Zwanziger's model based on d/N_c to the pressure-induced change in the *strain*-optical coefficient of the glasses in this study. Based on the purely structural considerations in Section 4.1, we should expect the C value of glasses to generally increase when d/N_c decreases as a result of hot compression. Consequently the magnitude of $(p_{12} - p_{11})$ is expected to increase due to densification. However, our calculations show that $(p_{12} - p_{11})$ can either decrease or increase depending on the glass composition. This could be due to a change in bond metallicity as the density increases, which changes the bond polarizability. Alternatively, densification might not lead to the expected decreasing bond length but rather to a total increase in average bond length to accommodate the high-coordinated species generated by hot compression. Regardless of which is the correct explanation, the Zwanziger et al. model fails to account for the impact of pressure on C as the elastic properties of the glass has a large influence on the magnitude of C.

4.4. Comparing pressure- and compressive stress-induced changes in C

For many modern applications, post-treatment of glasses is needed to achieve enhanced properties. For example, improved damage resistance can be achieved by chemical strengthening via ion exchange, where, e.g., a sodium-containing glass is submerged into a molten potassium salt, allowing exchange of the sodium ions in glass surface with the potassium ions in the liquid salt [39,40]. Due to the size difference, this results in the generation of a compressive stress (CS) at the glass surface, and the magnitude of CS greatly influences the mechanical performance [41–44]. It is thus important to be able to determine CS accurately, which is typically based on optical birefringence measurements, in turn requiring accurate knowledge of C of the glass. However, during ion exchange, the properties of the glass change and understanding the effect of these changes on C is therefore critically important.

Both the atomic effect on photoelasticity and the shear modulus should change during ion exchange, in turn affecting C. As described by Matusita et al., changing the chemical composition of a material will change its strain-optical coefficients [34,35]. However, considering the rather small (~2.7%) decrease in $(p_{12} - p_{11})$ observed between $33Na_2O–67SiO_2$ and $33K_2O–67SiO_2$ end-member glasses [34], the ion exchange in the surface is not expected to have a significant effect on the strain-optical properties. However, the shear modulus does increase as the large potassium ion is substituted into the interstice left by the smaller sodium ion without any plastic deformation [39]. This results in an increase in the elastic moduli of the compressed surface layer, affecting the magnitude of C as described by Eq. (6). The change in C can only be determined accurately with knowledge of the ion exchange-induced change in the shear modulus, e.g., through Brillouin spectroscopy or using molecular dynamics simulations [45]. If the change in shear modulus is not accounted for, an artificially high value of surface compressive stress may be obtained.

5. Conclusions

We have determined the density, elastic moduli, and stress optic coefficient (C) of ten different oxide glasses before and after hot compression. An unexpected decrease in the stress optic coefficient has been observed as a result of this compression. This result is the opposite of what may be inferred using the model of Zwanziger et al., which links stress-optic coefficient with glass structural features. Compression normally leads to decreasing modifier-oxygen bond lengths and increasing network-forming coordination numbers, which, according to the Zwanziger model, should lead to increases in the stress optic coefficient. This disagreement between experimental data and the model prediction can be understood on the basis of the atomic and lattice effects described by Mueller and a model for photoelasticity. We find that densification only has a small influence on the strain-optic properties, which in turn have small influence on the pressure-induced change in C. The pressure-induced change in shear modulus, however, has a pronounced influence on how C changes as a response to densification. That is, we found that the stress optic coefficient is a linear function of the shear modulus for densified glasses with similar modifier content due to the atomic affect. When comparing glasses with large differences in modifier content, the differences in the lattice effect must also be accounted for.

Acknowledgements

This work was partially funded by Corning Incorporated and the Danish Council for Independent Research under Sapere Aude: DFF-Starting Grant (1335-00051A). S.J.R. acknowledges the support from the National Science Center of Poland under Grant No. UMO-2011/03/B/ST3/02352.

References

[1] Y.S. Choi, J.U. Yun, S.E. Park, Flat panel display glass: current status and future, J. Non. Cryst. Solids 431 (2016) 2–7.
[2] M. Guignard, L. Albrecht, J.W. Zwanziger, Zero-stress optic glass without lead, Chem. Mater 19 (2007) 286–290, http://dx.doi.org/10.1021/cm062208a.
[3] K. Kusama, T. Matano, Y. Ohashi, M. Kobayashi, K. Nagamoto, P-72: is the photo-elasticity of PSAs for LCD panels reducible?, in: SID Symp. Dig. Tech. Pap, 2008, pp. 1457–1460.

[4] K. Kurosawa, K. Yamashita, T. Sowa, Y. Yamada, Flexible fiber faraday effect current sensor using flint glass fiber and reflection scheme, IEICE Trans. Electron 83 (2000) 326–330.
[5] F. Pockels, Über die Änderung des optischen Verhaltens verschiedener Gläser durch elastische Deformation, Ann. Phys. 312 (1902) 745–771.
[6] A.I. Rabukhin, Photoelastic constants of germanate glasses containing lead and bismuth oxides, Glas. Ceram. 51 (1994) 15–18.
[7] V. Martin, B. Wood, U. Werner-Zwanziger, J.W. Zwanziger, Structural aspects of the photoelastic response in lead borate glasses, J. Non. Cryst. Solids 357 (2011) 2120–2125, http://dx.doi.org/10.1016/j.jnoncrysol.2011.01.042.
[8] M. Guignard, U. Werner-Zwanziger, J.W. Zwanziger, Glass-former/glass-modifier interactions and the stress-optic response, J. Non. Cryst. Solids 354 (2008) 79–83, http://dx.doi.org/10.1016/j.jnoncrysol.2007.06.096.
[9] M. Guignard, J.W. Zwanziger, Zero stress-optic barium tellurite glass, J. Non. Cryst. Solids 353 (2007) 1662–1664, http://dx.doi.org/10.1016/j.jnoncrysol.2007.01.038.
[10] M. Itadani, A. Saitoh, Y. Masaoka, H. Takebe, Low photoelastic and optical properties in RO–SnO–P2O5 (R = Zn, Ba, Sr) glasses, Opt. Lett. 41 (2016) 45–48.
[11] A. Saitoh, K. Nakata, G. Tricot, Y. Chen, N. Yamamoto, H. Takebe, Zero photoelastic and water durable ZnO–SnO-P2O5–B2O3 glasses, Apl. Mater 3 (2015) 46102, http://dx.doi.org/10.1063/1.4917347.
[12] N. Yamamoto, A. Saitoh, H. Takebe, Zero photoelastic zinc tin phosphate glass without lead oxide, Opt. Lett. 37 (2012) 4203–4205.
[13] J. Galbraith, J.W. Zwanziger, Designing glass with non-dispersive stress-optic response, J. Non. Cryst. Solids 433 (2016) 82–86.
[14] H. Mueller, Theory of photoelasticity in amorphous solids, J. Appl. Phys. 6 (1935) 179–184.
[15] H. Mueller, The theory of photoelasticity, J. Am. Ceram. Soc. 21 (1938) 27–33.
[16] M.M. Smedskjaer, S.A. Saxton, A.J. Ellison, J.C. Mauro, Photoelastic response of alkaline earth aluminosilicate glasses, Opt. Lett. 37 (2012) 293, http://dx.doi.org/10.1364/OL.37.000293.
[17] V. Martin, U. Werner-Zwanziger, J.W. Zwanziger, R.A. Dunlap, Correlation of structure and photoelastic response in tin phosphate glass, Int. J. Appl. Glas. Sci. 2 (2011) 282–289, http://dx.doi.org/10.1111/j.2041-1294.2011.00049.x.
[18] J.G. Thorbahn, J.W. Zwanziger, Compositional dependence of the stress-optic response in zinc tellurite glasses, J. Non. Cryst. Solids 381 (2013) 48–53, http://dx.doi.org/10.1016/j.jnoncrysol.2013.09.016.
[19] S. Wemple, Optical oscillator strengths and excitation energies in solids, liquids, and molecules, J. Chem. Phys. 67 (1977) 2151–2168.
[20] S. Kapoor, L. Wondraczek, M.M. Smedskjaer, Pressure-induced densification of oxide glasses at the glass transition, Front. Mater 4 (2017) 1, http://dx.doi.org/10.3389/fmats.2017.00001.
[21] M.M. Smedskjaer, S.J. Rzoska, M. Bockowski, J.C. Mauro, Mixed alkaline earth effect in the compressibility of aluminosilicate glasses, J. Chem. Phys. 140 (2014) 54511, http://dx.doi.org/10.1063/1.4863998.
[22] M.E. Lines, Photoelastic trends from halides to pnictides by a bond-orbital method, J. Appl. Phys. 60 (1986) 1472–1478, http://dx.doi.org/10.1063/1.337274.
[23] P.Y. Yu, M. Cardona, Intrinsic piezobirefringence of several semiconducting chalcogenides, J. Phys. Chem. Solids 34 (1973) 29–56.
[24] J. Wu, J. Deubener, J.F. Stebbins, L. Grygarova, H. Behrens, L. Wondraczek, Y. Yue, Structural response of a highly viscous aluminoborosilicate melt to isotropic and anisotropic compressions, J. Chem. Phys. 131 (2009) 1–10, http://dx.doi.org/10.1063/1.3223282.
[25] M.M. Smedskjaer, M. Potuzak, X. Guo, J.C. Mauro, Compositional control of the photoelastic response of silicate glasses, Opt. Mater. (Amst) 35 (2013) 2435–2439.
[26] T.K. Bechgaard, A. Goel, R.E. Youngman, J.C. Mauro, S.J. Rzoska, M. Bockowski, L.R. Jensen, M.M. Smedskjaer, Structure and mechanical properties of compressed sodium aluminosilicate glasses: role of non-bridging oxygens, J. Non. Cryst. Solids 441 (2016) 49–57, http://dx.doi.org/10.1016/j.jnoncrysol.2016.03.011.
[27] M.N. Svenson, T.K. Bechgaard, S.D. Fuglsang, R.H. Pedersen, A.O. Tjell, M.B. Østergaard, R.E. Youngman, J.C. Mauro, S.J. Rzoska, M. Bockowski, M.M. Smedskjaer, Composition-structure-property relations of compressed borosilicate glasses, Phys. Rev. Appl. 2 (2014) 1–9, http://dx.doi.org/10.1103/PhysRevApplied.2.024006.
[28] M.B. Østergaard, R.E. Youngman, M.N. Svenson, S.J. Rzoska, M. Bockowski, L.R. Jensen, M.M. Smedskjaer, Temperature-dependent densification of sodium borosilicate glass, RSC Adv. 5 (2015) 78845–78851, http://dx.doi.org/10.1039/C5RA16219J.
[29] M.M. Smedskjaer, R.E. Youngman, S. Striepe, M. Potuzak, U. Bauer, J. Deubener, H. Behrens, J.C. Mauro, Y. Yue, Irreversibility of pressure induced boron speciation change in glass, Sci. Rep. 4 (2014) 3770, http://dx.doi.org/10.1038/srep03770.
[30] S.K. Lee, G.D. Cody, Y. Fei, B.O. Mysen, Nature of polymerization and properties of silicate melts and glasses at high pressure, Geochim. Cosmochim. Acta 68 (2004) 4189–4200, http://dx.doi.org/10.1016/j.gca.2004.04.002.
[31] J.R. Allwardt, J.F. Stebbins, B.C. Schmidt, D.J. Frost, A.C. Withers, M.M. Hirschmann, Aluminum coordination and the densification of high-pressure aluminosilicate glasses, Am. Mineral. 90 (2005) 1218–1222, http://dx.doi.org/10.2138/am.2005.1836.
[32] L.S. Du, J.R. Allwardt, B.C. Schmidt, J.F. Stebbins, Pressure-induced structural changes in a borosilicate glass-forming liquid: boron coordination, non-bridging oxygens, and network ordering, J. Non. Cryst. Solids 337 (2004) 196–200, http://dx.doi.org/10.1016/j.jnoncrysol.2004.03.115.
[33] S.K. Lee, J.F. Stebbins, The distribution of sodium ions in aluminosilicate glasses: a high-field Na-23 MAS and 3Q MAS NMR study, Geochim. Cosmochim. Acta 67 (2003) 1699–1709, http://dx.doi.org/10.1016/S0016-7037(02)00026-7.
[34] K. Matusita, C. Ihara, T. Komatsu, R. Yokota, Photoelastic effects in silicate glasses, J. Am. Ceram. Soc. 67 (1984) 700–704.
[35] K. Matusita, R. Yokota, T. Kimijima, T. Komatsu, Compositional trends in photoelastic constants of borate glasses, J. Am. Ceram. Soc. 67 (1984) 261–265.
[36] N.F. Borrelli, R.A. Miller, Determination of the individual strain-optic coefficients of glass by an ultrasonic technique, Appl. Opt. 7 (1968) 745–750, http://dx.doi.org/10.1364/AO.7.000745.
[37] J. Galbraith, L. Chapman, J.W. Zwanziger, M. Aldridge, J. Kieffer, Elasto-optic coefficients of borate, phosphate, and silicate glasses: determination by brillouin spectroscopy, J. Phys. Chem. C 120 (2016) 21802–21810, http://dx.doi.org/10.1021/acs.jpcc.6b07202.
[38] A.K. Varshneya, Fundamentals of Inorganic Glasses, 2011.
[39] A.K. Varshneya, Chemical strengthening of glass: lessons learned and yet to be learned, Int. J. Appl. Glas. Sci. 1 (2010) 131–142, http://dx.doi.org/10.1111/j.2041-1294.2010.00010.x.
[40] A.K. Varshneya, Chemical strengthening of glass, Int. J. Appl. Glas. Sci. 1 (2010) 131–142, http://dx.doi.org/10.2307/1711232.
[41] Z. Tang, M.B. Abrams, J.C. Mauro, L.R. Zoeller, N. Venkataraman, G. Hu, High-speed camera study of stage III crack propagation in chemically strengthened glass, Appl. Phys. A Mater. Sci. Process 116 (2014) 471–477, http://dx.doi.org/10.1007/s00339-014-8370-y.
[42] Z. Tang, M.B. Abrams, J.C. Mauro, N. Venkataraman, T.E. Meyer, J.M. Jacobs, X. Wu, A.J. Ellison, Automated apparatus for measuring the frangibility and fragmentation of strengthened glass, Exp. Mech. 54 (2014) 903–912, http://dx.doi.org/10.1007/s11340-014-9855-5.
[43] Z. Tang, Y.Z. Mauro, C. Gee, D.L.J. Duffy, T.E. Meyer, M.B. Abrams, K.A. Walker, J.C. Mauro, Methods for measurement and statistical analysis of the frangibility of strengthened glass, Front. Mater 2 (2015) 1–8, http://dx.doi.org/10.3389/fmats.2015.00050.
[44] J.C. Mauro, M.M. Smedskjaer, Unified physics of stretched exponential relaxation and Weibull fracture statistics, Phys. A Stat. Mech. Its Appl. 391 (2012) 6121–6127, http://dx.doi.org/10.1016/j.physa.2012.07.013.
[45] K.D. Vargheese, A. Tandia, J.C. Mauro, Molecular dynamics simulations of ion-exchanged glass, J. Non Cryst. Solids 403 (2014) 107–112.

ISSN (online): 2446-1636
ISBN (online): 978-87-7210-341-9

AALBORG UNIVERSITY PRESS